

Measurements of Electron Beam-Induced Spin-Relaxation in Frozen-Spin Hydrogen-Deuteride (HD)

Thomas R. O'Connell, Ph.D.

University of Connecticut, 2022

Targets of solid hydrogen-deuteride (HD) can be prepared in a frozen-spin state with spin-relaxation times (T_1) in excess of a year. The present work has studied their potential use in experiments with electron beams. Polarization relaxation rates have been measured during exposure to sub-nanoAmp currents of 9.7 MeV electron beams from the recently commissioned Upgraded Injector Test Facility (UITF) at Jefferson Lab (JLab). These UITF measurements can be used to anticipate the expected performance at the GeV energies typical of JLab experiments, since the energy deposition in a target is almost independent of beam energy. An in-beam dilution refrigerator equipped with superconducting solenoids has been used to maintain solid HD samples at ~ 0.1 K and ~ 1 tesla, and internal NMR coils have been used to monitor hydrogen polarization. Spin-relaxation in two frozen-spin targets, with initial H-polarizations of 40% and 34%, have been tracked while exposed to beams under varying conditions of current, dose, beam duty factor and temperature. At a fixed accumulated dose, the spin-relaxation rates drop with current, suggesting depolarization by the charge cloud of the beam. Imposing a duty factor on the otherwise continuous UITF beam, with forced millisecond scale gaps, has shown no obvious correlation to polarization loss rates. After an accumulated dose of $\sim 2 \mu\text{C}/\text{cm}^2$, beam-off spin-relaxation rates drop from their immeasurably long pre-irradiation values to the order of weeks (with beam-on T_1 values typically an order of magnitude shorter), reflecting a buildup of paramagnetic charge centers within the HD lattice. The accumulated polarization loss was approximately proportional to dose in both targets, dropping to $1/e$ of their initial values after $\sim 6 \mu\text{C}/\text{cm}^2$. Thermal equilibrium polarizations of targets not in the frozen-spin state (with intentionally short T_1) have been used to deduce the *in situ* temperature of solid HD while under electron bombardment. A model for depolarization by beam-associated paramagnetic impurities largely accounts for the data, and suggests that improvements in heat removal could lead to significant increases in the in-beam T_1 .

Measurements of Electron Beam-Induced Spin-Relaxation in Frozen-Spin Hydrogen-Deuteride (HD)

Thomas R. O'Connell

B.S. University of Connecticut, 2008

M.S. University of Connecticut, 2015

A Dissertation

Submitted in Partial Fulfilment of the Requirements

For the Degree of

Doctorate of Philosophy

at the

University of Connecticut

2022

Copyright by
Thomas R. O'Connell

2022

APPROVAL PAGE

Doctor of Philosophy Dissertation

Measurements of Electron Beam-Induced Spin-Relaxation in Frozen-Spin Hydrogen-Deuteride (HD)

Presented by

Thomas R. O'Connell, B.S., M.S.

Major Advisor: _____
Kyungseon Joo

Associate Advisor: _____
Andrew M. Sandorfi

Associate Advisor: _____
Peter Schweitzer

University of Connecticut

2022

For my Grandmom, who I am eternally grateful for instilling in me a love of science and learning of new things. And for my best friend Hillary for always supporting me no matter what life throws my way.

Acknowledgements

Despite many setbacks and other challenges in life, I would not have made it this far if it had not been for several amazing individuals. My academic journey would not have been possible without Dr. Kyungseon Joo. He has continuously stuck by and supported me the whole way. I am so grateful for him making my dream of being a scientist come true.

The eHD experiment would not have been possible without the tireless leadership and dedication of Dr. Andrew Sandorfi. Andy has been a constant source of knowledge, compassion, and inspiration in my life. Dr. Xiangdong Wei has been a true mentor and friend over the years. From teaching me how to properly solder to operating NMR systems, I have learned so much from him. I will always appreciate Dr. Tsuneo Kayaga's kindness and for taking the time to teach me about how to condense HD ice crystals and use cryogenic equipment. Dr. Charles Hanretty was instrumental in the beamline design for the eHD target and was always willing to jump in to help me when I had questions. Although Dr. Michael Lowry retired during the eHD experiment, the years he shared his knowledge of cryogenic systems and polarized targets with me have been indispensable. Gary Dezern taught me more about tools, constructing experimental equipment, and proper equipment maintenance than all the years of technology education classes I have ever taken. Finally, I could always count on Kevin Wei's help. Whether it was to physically help me with tasks I couldn't perform or to discuss analysis code, he wouldn't hesitate to lend a hand.

I am eternally grateful for the love and support from my friends and family over the years. In particular, I would like to thank Dr. Dwight Ligham. After several failed surgeries, many doctors believed I reached my maximum medical improvement and that I would be unable to return to Jefferson Lab. Dr. Ligham was never willing to settle for that. He offered me hope through an experimental procedure using my own stem cells to repair parts of my damaged spine, which allowed me to take part in the eHD experiment.

Contents

1	Introduction	1
1.1	Physics Motivation	1
1.2	Thomas Jefferson National Accelerator Facility	2
1.3	Upgraded Injector Test Facility	4
1.4	Overview of Polarized Targets	6
2	The HDice Target at Jefferson Lab	9
2.1	General description	9
2.2	Previous HDice Target Design and History	9
2.3	Improved eHD Target Cell at UITF	14
2.4	HD Material	15
2.5	Target Production and Cryostats	16
2.5.1	Target Production Overview	17
2.5.2	Production Dewar	19
2.5.3	HD Ice Production	22
2.5.4	Transfer Cryostat	24
2.5.5	Dilution Refrigerator	26
3	Depolarization Mechanisms and Mitigating Measures	30
3.1	Electron Beam Heating Depolarization	30
3.2	HD Temperature Control Improvements	31
3.3	Hyperfine Mixing	33
3.4	Hyperfine Mixing Prevention	33
3.5	HD Material Chemical Reactions	34
3.6	Minimizing Chemical Reactions within HD	34

4	Experimental Setup at UITF	35
4.1	UITF Layout	35
4.1.1	Cave 1: The KeV Region	36
4.1.2	Cave 2: The MeV Region	37
4.2	DAQ Area	43
4.3	Target Loading and Unloading Procedure	45
4.4	Experimental Runs at UITF	47
4.4.1	Run 1: Aperture Target	48
4.4.2	Run 2A: Unpolarized Target	51
4.4.3	Run 3A: Polarized Target	54
4.4.4	Run 3B: Polarized Target	55
4.4.5	Run 2B: Unpolarized Target	58
5	Polarimetry	60
5.1	Polarimetry Overview	60
5.2	Nuclear Magnetic Resonance	62
5.3	Adiabatic Fast Passage	64
5.4	NMR Setup	65
5.4.1	NMR Apparatus	65
5.4.2	Fast Resonance Scan	67
5.4.3	Field Scan	69
5.5	Measuring NMR Signals	70
5.5.1	Treating Raw Signal Data	71
5.5.2	Kramers-Kronig Relations	73
5.5.3	Phase Test and Correction	75
5.5.4	Discrete Fourier Transform Filtering	77
5.5.5	Baseline Correction	78
5.6	Signal Integration	81
5.6.1	Sliding Window Technique	81
5.6.2	Peak Center Determination and Raw Signal Measurement	82
5.6.3	RF Power Scaling	83
5.6.4	TE Signal Measurement and Polarization Calculation	86

6	Analysis	88
6.1	HDice Runs 2A and 2B	88
6.1.1	Aspects of Runs 2A & 2B	89
6.1.2	HD Temperature Monitoring	89
6.2	HDice Runs 3A and 3B	93
6.2.1	Aspects of Run 3A	93
6.2.2	Results with eHD Target #60	95
6.2.3	Aspects of Run 3B	96
6.2.4	Results with eHD Target #66	98
6.2.5	Spiral Raster Correction	99
6.2.6	Dose Determination	104
6.2.7	Corrected eHD Run 3A Results for the Core and Ring Sections	109
6.2.8	Corrected Run 3B Results for the Core and Ring Sections	112
6.2.9	Relaxation Time Determination	114
6.2.10	Modeling the HD Polarization Loss in Run 3A	124
6.2.11	Modeling the HD Polarization Loss in Run 3B	131
6.2.12	Comparison to Mano and Honig	133
6.2.13	Projected Performance with a Colder Target	136
7	Conclusions	138
7.1	Summary and Outlook	138
A	Error Analysis	142
A.1	Error Estimation on Polarization Calculation	142
A.2	Error Estimation on Runs 3A and 3B Corrected Results	145
B	Unpolarized eHD Target Raw NMR Signal Area Data	147
C	Run 3A and 3B Run Conditions	150
D	Polarized eHD Target Raw NMR Signal Area Data	160
E	Polarized eHD Target Polarization Data	173

F	T1 Fitted Plots	186
F.1	Run 3A Beam Off T1 Plots	186
F.2	Run 3A Beam On T1 Plots	189
F.3	Run 3B Beam Off T1 Plots	193
F.4	Run 3B Beam On T1 Plots	196

List of Figures

1.1	An aerial view of the Thomas Jefferson National Accelerator Facility, also commonly known as JLab [3].	3
1.2	HDice target polarization values during the g14 experiment at Hall B [4]. . . .	4
1.3	The energy deposited into the HDice target by electrons at various energies. Around approximately 10 MeV, the energy deposited into the target levels off with the rest of the energy lost as bremsstrahlung.	5
1.4	The image above shows a simulated electron beam as it passes through the magnetic fields of the IBC solenoid. The beam quickly spreads out as it enters the IBC and hits the target region.	6
2.1	HDice target cell schematic. The Kel-F shells are attached to the copper ring with epoxy. Most of volume within the outer shell is filled with solid HD, taking the form of a 50 mm long and 15 mm diameter cylinder	10
2.2	Layout of the HDice target cell used during g14. From left to right, a bundle consisting of 14 Al wires, a sectional view of the Kel-F pieces that attach to the ring, a completed target cell, and a target cell after 60 bundles are soldered and the wires separated to be positioned.	11
2.3	Hydrogen polarization $P(H)$ during the second electron beam period in March 2012, with 0.29 tesla holding field during exposures. Shaded vertical bands indicate beam-on periods [10].	13
2.4	The progression of the eHD target cell. Displaying from left to right: the individual target cell components, the wires bundles combed into position after being soldered to the copper ring, and the completed target cell after the outer shell has been attached.	14

2.5	Spin exchanges between ortho-H ₂ (and para-D ₂) and H (and D) nuclei in the HD molecule.	15
2.6	The layout of the HDice lab, containing the cryogenic devices used in target production. Note: the Storage Dewar (SD) was not used for the eHD experiment, but was stored in the HDice lab.	17
2.7	A schematic diagram summarizing the HDice target life cycle.	18
2.8	The Production Dewar - a cryostat used for HD crystal formation with a temperature of 4.2 K and a magnetic field up to 2 T [13].	20
2.9	The image on the right is of the transfer cryostat - a cryostat used to move targets with a temperature of 2 K and a magnetic field of 0.12 T. The image to the left is a diagram showing the internal components of the TC [15].	25
2.10	The dilution refrigerator. The left side shows the top of the DF with the TC mounted on top. Most of the DF was located in the pit below aluminum safety plate. On the right is a schematic of the DF's components in the pit [16].	27
3.1	The polarization of atomic electrons dropped significantly during g14 due to the increased HD temperatures.	31
3.2	Differences in thermal conductivity between the aluminum wire purities used in g14 and eHD.	32
3.3	Raster magnet driving currents as sampled by Pearson probes.	33
4.1	Layout of the Upgraded Injector Test Facility at Jefferson Lab.	35
4.2	The electron gun's primary light source for operation is a 780nm laser delivered via fiber optic cable from a fiber laser amplifier. Electron beams were directed to the QCM after exiting the electron gun.	36
4.3	UITF Beamline components in the KeV Region (Cave 1).	37
4.4	Beamline components in the MeV Region of the accelerator (Cave 2).	38
4.5	The IBC, a cryostat used to hold and use targets in beam experiments. The image on top shows the IBC installed in the UITF beamline. The image below is a diagram showing the main internal components [18].	39
4.6	As electrons pass through the in-beam cryostat the fields shown in the above figure are used to control the distribution of electrons.	40

4.7	As electrons (in red) pass through the in-beam cryostat from left to right in the figure there is significant spreading and scattering.	41
4.8	UITF Beam Dump at the end of the accelerator. The left panel shows the dump connected to the IBC with a gate valve, the middle panel is a schematic of the dump solenoid, and the left panel is a simulation of how the electrons are affected by the fields when passing through the dump.	41
4.9	First time a MeV beam was seen on the YAG viewer located at the beam dump. The image of the YAG screen with beam on it was obtained with an in-beam camera.	42
4.10	The electronic system of the Halo detector is made up of a FPGA box connected to 32 identical SiPMs, each connected to its own independent channel amplifier. Four step-up power supplies are each connected to eight SiPMs/amplifier pairings to supply the proper voltage bias for the SiPMs to operate. Additionally, a raspberry pi computer is connected to the FPGA to read and manage the digitized rates.	44
4.11	The halo-gtk in operation. The top right displays the beam location in real time when the accelerator is in operation. The top left has tabs which change the display on the left from displaying the channel rates over time, the rates per channel, or to the position of each event detected. The bottom displays individual channel rates of the detectors.	45
4.12	Target loading at the UITF. The left shows the IBC as it it was being rotated vertically for loading. The right shows the UITF ceiling tiles removed allowing the TC to be attached to the crane, lifted, and mounted to the vertical IBC. . .	46
4.13	The aperture target used in Run 1.	49
4.14	The HALO detector output was calibrated by putting the beam through the arcs of the aperture target using the halo-gtk during Run 1. The left panels show the beam position on the YAG viewers which were used to verify the position determined using the halo-gtk program, seen in the right panels.	50
4.15	Oscilloscope output of signals from one Halo detector, triggered by the gun laser, during $DF = 2/3$ operations.	57
5.1	The $S = 1/2$ energy level splitting.	61

5.2	NMR Signals before and after performing the Adiabatic Fast Passage on Target #60.	65
5.3	The NMR rack located in Cave 2 of the UITF. On the left is the schematic and on the right is a photo of the actual rack. From bottom to top the rack contains the main solenoid power supply, NMR computer, lock-in amplifier, radio-frequency generator, switching box, and amplifier.	66
5.4	Fast Resonance Scan example in the IBC during the eHD experiment. Each peak represents resonances corresponding to standing waves in the cables.	68
5.5	Field Scan in the IBC during the eHD experiment.	71
5.6	The difference between a single NMR sweep (left) and multiple sweeps averaged together (right) during a scan to cancel the noise and isolate the signal.	72
5.7	Comparison of target TE up absorption signals with polarized target up absorption signals. The top row corresponds to Run 3A's target #60, while the bottom corresponds to target #66 of Run 3B. The TE signals on the left panels are an average of 450 sweeps in the PD, prior to polarization in the DF. These pre-frozen-spin line shapes are broadened by jitter in the timing of the 450 sweeps. The right panels are single sweeps in the PD after the HD has reached a frozen-spin state.	73
5.8	Example of an NMR signal being broken up into its absorption (left plot) and dispersion spectra (right plot). Both signals are from a single sweep in the PD over the hydrogen line in target #60, with $P_H = 38\%$, just prior to the start of Run 3A.	74
5.9	On the left plot is an example of when there is a phasing issue. The plot of the left is of the raw signal data. The right plot shows the absorption signal after applying a -13° phase rotation to isolate the pure absorption signal.	76
5.10	The plot above shows the results of the Phase test. The phase correction angle producing the maximum signal area is -15° for NMR Scan IBC 73688717.	77
5.11	Noise filtering of raw NMR absorption signal. (a) Start with a raw signal. (b) The raw signal is converted to the frequency domain using the DFT. (c) High frequency noise is removed. (d) The filtered signal is converted back to the time domain.	79

5.12	Polynomial baseline corrections to the raw NMR signals. Up to a 9 th order polynomial fit (green) is applied to the tails of the raw data (blue). The fitted baseline is then subtracted out from the raw data resulting in a cleaner, treated signal (red).	80
5.13	Periodic baseline corrections to the raw NMR signals. The determined repeating noise pattern is approximately 1900 channels wide, highlighted in the purple box. This pattern is isolated and repeated (green) to fit the periodic background of the raw signal tails (blue). The fit is then removed from the raw data resulting in a cleaner, treated signal (red) for analysis.	80
5.14	The sliding window technique as used on an NMR scan from the PD. A window 600 data channels wide was swept across the signal data. The window started from the left and swept right in intervals of 1 data channel. During each interval, the 600 points were summed together representing the area value under the curve within the specific windowed region.	82
5.15	The results of the sliding window technique on PD Scan #73506764. The plateau in the center consists of the many individual area under the curve measurements performed by the window. Taking a weighted mean of the center points provides a NMR signal measurement with less error than just a single measurement. . . .	83
5.16	Center Peak Determination: The top plot shows the sliding window results where linear fits were applied to the sides of the plateau to locate the plateau center. In the plot below is the same plot, but zoomed in to show the center determination (dashed red line).	84
6.1	Runs 2A and 2B beam-off NMR Signal Measurements * temperature of the HD. The Run 2A data was normalized to the Run 2B. The fit is from using Equation 6.27.	91
6.2	Comparison of HD temperature versus average beam current during Run 2 with the IBC Mixing Chamber at ~70 mK and the Mixing Chamber heater off. The left plot shows derived temperature calibration curve using data from Run 2A and 2B. The plot on the right is the calibration curve previously derived by Kevin Wei [24] using Run 2B data only.	92

6.3	Sample of monitored HALO counts and accumulated dose as a function of time from the pico-ammeter during Run 3A . This data was taken for the second 250pA beam condition of Run 3A on November 24, 2020. The red spikes correspond to time periods where NMR measurements were taken.	94
6.4	Target #60 polarization and accumulated dose as a function of time.	95
6.5	Run 3A initial polarization versus accumulated dose.	96
6.6	Sample of monitored HALO counts and accumulated dose as a function of time from the pico-ammeter during Run 3B. This data was taken during the third 125pA, third 83pA, fourth 125pA, and the 250pA beam conditions of Run 3B on December 12, 2020.	97
6.7	Run 3B initial polarization versus experimental run time.	99
6.8	Run 3B initial polarization versus accumulated dose.	99
6.9	The radiation intensity near a HARP BPM just before the entrance to the IBC, plotted as a function of the position of three thin wires that are passed through the beam, at different angles to the beam axis.	100
6.10	The image on the left shows a cross-sectional view of the target, where the regions experiencing different dose rates are labeled as Skin, Ring, and Core Regions. The figure to the right is a side view of the target regions.	100
6.11	Run 3A demonstrated changes in the rate of polarization loss in different regions, separated by the vertical black dashed lines.	101
6.12	Run 3B demonstrated changes in the rate of polarization loss in different regions, separated by the vertical black dashed lines.	102
6.13	Run 3A shifted NMR Signal data with the projected ring only signals within Region I. The left plot shows the results of extrapolating the ring signals from the data and methods described within this chapter. On the right, the plot shows the previous work done determining the ring signals in Region I done by by Kevin Wei [24].	102
6.14	Run 3B shifted NMR Signal data with the projected ring only signals within Region I plotted.	104
6.15	Run 3A NMR signals with overnight data and the projected ring signals. The left plot is of the signals derived from Section 6.2.6, while the right plot is a reference of previous work done by K. Wei [24].	105

6.16	Run 3B NMR Signals with overnight data and the projected ring signals are plotted on the right.	105
6.17	Run 3A core section polarization values as a function of accumulated total target dose. In both plots, the data were shifted up to simulate continuous running without overnight periods. The left plot is of the polarization values derived from Section 6.2.6, while the right plot is a reference of previous work done by K. Wei [24].	110
6.18	Run 3A core section polarization values as a function of the core section accumulated dose. In both plots, the data were shifted up to simulate continuous running without overnight periods. The left plot is of the polarization values derived from Section 6.2.6, while the right plot is a reference of previous work done by K. Wei [24].	110
6.19	Run 3A ring section polarization values as a function of accumulated total target dose. The left plot is of the polarization values derived from Section 6.2.6, while the right plot is a reference of previous work done by K. Wei [24].	111
6.20	Run 3A ring section polarization values as a function of ring section accumulated dose. These plots show the ring data before removing the overnight scans and the data shifts to simulate continuous beam running. The left plot is of the polarization values derived from Section 6.2.6, while the right plot is a reference of previous work done by K. Wei [24].	111
6.21	Run 3A core section polarization values as a function of the core section accumulated dose with the overnight periods removed and data shifts to simulate continuous beam use. The left plot is of the polarization values derived from Section 6.2.6, while the right plot is a reference of previous work done by K. Wei [24].	112
6.22	Run 3A ring section polarization values as a function of the ring section accumulated dose with the overnight periods removed and data shifts to simulate continuous beam use. The left plot is of the polarization values derived from Section 6.2.6, while the right plot is a reference of previous work done by K. Wei [24].	112

6.23	Run 3B core polarization versus total target accumulated dose on the left with the ring polarization versus total target accumulated dose on the right. Note the removal of the high and low holding field points were removed from the ring data.	113
6.24	Run 3B core polarization versus accumulated core dose/area on the left with the ring polarization versus ring dose/area on the right. Note the removal of the high and low holding field points were removed from the ring data.	113
6.25	Run 3B core polarization versus core dose per area (left) and ring polarization versus ring section dose per area (right). Both plots have the overnight periods removed and data shifts to simulate continuous beam use.	114
6.26	The polarization values from the run condition with 0.25 nA and at 161 mK (a temperature elevated by a resistive heater) are fitted to Equation 2.1 and divided by the initial polarization for the beam condition to find the relative change in polarization.	115
6.27	The relative change in polarization during a Run 3B overnight, no beam condition at the IBC base temperature. The polarization values were fitted to Equation 2.1 and divided by the initial polarization for that overnight condition to find the relative change in polarization.	116
6.28	Comparing the T_1 values between the beam-on and beam-off NMR measurements of the core section of Run 3A.	118
6.29	Comparing the T_1 values between the beam-on and beam-off NMR measurements of the Ring section of Run 3A.	119
6.30	Comparing the T_1 values between the beam-on and beam-off NMR measurements of the core and ring sections of Run 3B. Note: Two T_1 values with errors larger than the values were suppressed.	122
6.31	Comparing the Run 3A and 3B T_1 values between different beam-on currents. The effect of current on the T_1 can be seen in the plot.	122
6.32	Relaxation times as function of average beam current at an accumulation of $5.0\mu C/cm^2$	123
6.33	Comparison of relaxation time, T_1 values, from 125pA average beam current (top) and the 125pA peak beam current (bottom).	124
6.34	Comparison of relaxation time, T_1 values, from 250pA CW beam current (left) and the 250pA peak beam current (right).	124

6.35	The fitted α values of Run 3A's core section, determined from the different beam conditions.	127
6.36	The fitted α values of Run 3A's core and ring sections, determined from the different beam conditions.	127
6.37	Run 3A core (left) and ring (right) sections measured polarization along with the simulated values from using the fitted α values found for each of the beam conditions.	128
6.38	Run 3A core section measured polarization along with the simulated values from using the global α	128
6.39	Run 3A ring section measured polarization along with the simulated values from using the global α	129
6.40	Run 3A measured polarization values along with the simulated values from using the global α , 948 ± 32 (pA/S)($1/\mu C^2$)($1/T^3$), from the weighted mean of the individual core and ring global α values. The core section is represented by the plot of the left with the ring section plotted on the right.	131
6.41	The fitted α values of Run 3B's core section, determined from the different beam conditions.	132
6.42	The left plot shows Run 3B's core section measured and simulated polarization values using each beam condition's fitted α . The ring section equivalent is on the right. The ring made up less than $\sim 7\%$ of the total target, which received much less dose than the core during each condition, and thus no polarization loss when beam was on. The overnight drops in polarization dominate the ring polarization loss.	132
6.43	Run 3B's target core and ring section measured and simulated polarization values using the global α	133
6.44	Run 3A and 3B core section relaxation times compared to those from Mano and Honig [27]. Equation 6.37 was used to scale those initial T_1 values to match the same HD temperature and magnetic field conditions during the eHD experiment. The blue bar represents scaling Mano and Honig's results between Run 3A and 3B conditions. Run 3A had a higher holding field, but higher T_{HD} due to running the mix heater on.	135

F.1	The T_1 extraction of the first no beam run condition at 160 mK. The fitted T_1 value for the core section is 9.154 ± 2.644 days and 11.106 ± 2.955 days for the ring section.	186
F.2	The T_1 extraction of the second no beam run condition at 160 mK. The fitted T_1 value for the core section is 0.942 ± 0.018 days and 1.608 ± 0.038 days for the ring section.	187
F.3	The T_1 extraction of the third no beam run condition at 70 mK. By this point in the experimental run, the core section polarization was depleted, which leaves just the ring section polarization. The fitted T_1 value is 19.405 ± 1.213 days for the ring section.	187
F.4	The T_1 extraction of the fourth no beam run condition at 70 mK. By this point in the experimental run, the core section polarization was depleted, which leaves just the ring section polarization. The fitted T_1 value is 4.267 ± 0.181 days for the ring section.	188
F.5	The T_1 extraction of the first beam-on run condition with 125pA on the target at 160 mK. The fitted T_1 value for the core section is 5.631 ± 2.769 days and 7.113 ± 3.823 days for the ring section.	189
F.6	The T_1 extraction of the second beam-on run condition with 125pA CW on the target at 160 mK. The fitted T_1 value for the core section is 1.479 ± 0.050 days and 1.759 ± 0.070 days for the ring section.	190
F.7	The T_1 extraction of the first beam-on run condition with 250pA CW on the target at 160 mK. The fitted T_1 value for the core section is 0.501 ± 0.008 days and 1.533 ± 0.063 days for the ring section.	190
F.8	The T_1 extraction of the second beam-on run condition with 250pA CW on the target at 239 mK. The fitted T_1 value for the core section is 0.235 ± 0.113 days and 1.067 ± 0.060 days for the ring section.	191
F.9	The T_1 extraction of the third beam-on run condition with 125pA CW on the target at 70 mK. By this point in the experimental run, the core section polarization was depleted, which leaves just the ring section polarization. The fitted T_1 value is 1.759 ± 0.070 days for the ring section.	191

F.10	The T_1 extraction of the fourth beam-on run condition with 125pA CW on the target at 70 mK. This run had an average magnetic holding field of 0.45T, instead of 1.04T like the rest of Run 3A. By this point in the experimental run, the core section polarization was depleted, which leaves just the ring section polarization. The fitted T_1 value is 1.759 ± 0.070 days for the ring section.	192
F.11	The T_1 extraction of the first no beam run condition at 70 mK. The fitted T_1 values are not available due to the polarization effectively not changing with such a low accumulated dose. Without any measurable decrease in polarization, the T_1 values are infinite.	193
F.12	The T_1 extraction of the second no beam run condition at 70 mK. The fitted T_1 value for the core section is 10.104 ± 4.488 days and 3.281 ± 0.872 days for the ring section.	194
F.13	The T_1 extraction of the third no beam run condition at 70 mK. The fitted T_1 value for the core section is 2.816 ± 0.037 days and 2.666 ± 0.776 days for the ring section.	194
F.14	The T_1 extraction of the fourth no beam run condition at 70 mK. The fitted T_1 value for the core section is 3.260 ± 1.190 days and 11.861 ± 7.47 days for the ring section.	195
F.15	The T_1 extraction of the fifth no beam run condition at 70 mK. By this point in the experimental run, the core section polarization was depleted, which leaves just the ring section polarization. The fitted T_1 value is 21.110 ± 15.380 days for the ring section.	195
F.16	The T_1 extraction of the first beam-on run condition of 83pA average, 250pA peak current on the target at 70 mK. The fitted T_1 value for the core section is 5.631 ± 2.769 days and 29.888 ± 59.835 days for the ring section.	196
F.17	The T_1 extraction of the second beam-on run condition of 125pA average, 188pA peak current on the target at 72 mK. The fitted T_1 value for the core section is 3.783 ± 0.846 days and 33.763 ± 111.160 days for the ring section.	197
F.18	The T_1 extraction of the third beam-on run condition of 125pA average, 188pA peak current on the target at 72 mK. The fitted T_1 value for the core section is 6.630 ± 18.624 days and 1.533 ± 0.063 days for the ring section.	197

F.19	The T_1 extraction of the fourth beam-on run condition of 167pA average, 250pA peak current on the target at 73 mK. The fitted T_1 value for the core section is 1.401 ± 0.084 days and 1.067 ± 0.06 days for the ring section.	198
F.20	The T_1 extraction of the fifth beam-on run condition of 83pA average, 250pA peak current on the target at 72 mK. The fitted T_1 value for the core section is 5.170 ± 2.313 days and 0.637 ± 0.082 days for the ring section.	198
F.21	The T_1 extraction of the sixth beam-on run condition of 167pA average, 250pA peak current on the target at 73 mK. The fitted T_1 value for the core section is 0.512 ± 0.033 days and 7.286 ± 4.605 days for the ring section.	199
F.22	The T_1 extraction of the seventh beam-on run condition of 125pA CW current on the target at 73 mK. The fitted T_1 value for the core section is 0.913 ± 0.250 days and 3.133 ± 2.980 days for the ring section.	199
F.23	The T_1 extraction of the eighth beam-on run condition of 83pA average, 125pA peak current on the target at 74 mK. The fitted T_1 value for the core section is 1.931 ± 6.101 days and 1.849 ± 132.400 days for the ring section.	200
F.24	The T_1 extraction of the eighth beam-on run condition of 125pA average, 375pA peak current on the target at 78 mK. The fitted T_1 value for the core section is 1.931 ± 6.101 days and 0.419 ± 0.0535 days for the ring section.	200
F.25	The T_1 extraction of the ninth beam-on run condition of 250pA CW current on the target at 78 mK. The fitted T_1 value for the core section is 0.443 ± 0.067 days and not available due to no measurable change in polarization during the time period.	201
F.26	The T_1 extraction of the ninth beam-on run condition of 125pA CW current on the target at 73 mK. Unlike most run conditions, this condition included setting the holding field to 0.45T. By this point in the experimental run, the core section polarization was depleted, which leaves just the ring section polarization. The fitted T_1 value is 0.535 ± 0.234 days for the ring section.	202
F.27	The T_1 extraction of the ninth beam-on run condition of 125pA CW current on the target at 70 mK. Unlike most run conditions, this condition included setting the average holding field to 1.04T. By this point in the experimental run, the core section polarization was depleted, which leaves just the ring section polarization. The fitted T_1 value is 13.879 ± 46.152 days for the ring section.	203

F.28	The T_1 extraction of the ninth beam-on run condition of 500pA CW current on the target at 70 mK. By this point in the experimental run, the core section polarization was depleted, which leaves just the ring section polarization. The fitted T_1 value is 0.592 ± 0.177 days for the ring section.	204
F.29	The T_1 extraction of the ninth beam-on run condition of 333pA average, 500 peak current on the target at 81 mK. By this point in the experimental run, the core section polarization was depleted, which leaves just the ring section polarization. The fitted T_1 value is 0.630 ± 0.136 days for the ring section.	205
F.30	The T_1 extraction of the ninth beam-on run condition of 500pA average, 750 peak current on the target at 101 mK. By this point in the experimental run, the core section polarization was depleted, which leaves just the ring section polarization. The fitted T_1 value is 0.797 ± 0.426 days for the ring section.	206

List of Tables

4.1	The eHD Run Schedule.	47
4.2	Run 2A summary of conditions in which NMR measurements were taken at the UITF. The simulated beam conditions were taken during overnight, no beam periods after running a particular beam current condition. The Mixing Chamber heater was turned on and adjusted to increase the Mixing Chamber temperature until it matched the same temperature reached during the actual beam interactions. This in turn would heat the HD sample up to the temperature it was during beam on operations.	53
4.3	Run 2B summary of overnight beam off conditions for NMR measurements taken at the UITF.	58
4.4	Run 2B summary of conditions in which beam on NMR measurements were taken at the UITF.	59
5.1	Thermal equilibrium polarization values from PD for eHD Targets #66 and #60.	86
6.1	Characteristics of eHD Targets #62 and #60 used in Runs 2A and 2B respectively.	89
6.2	Summery of Target #60 information.	93
6.3	Summery of Target #66 information.	97
6.4	Properties of the core and ring sections of Runs 3A, 3A (Reference) [24], and 3B.	109
6.5	The Run 3A T_1 values from fitting the polarization data of the core section for the no beam run conditions are listed above. Due to the NMR measurements being taken during no beam periods, the temperature of the HD is the same as the Mixing Chamber. The core polarization is depleted entirely before the last two sets of measurements were taken so there are no T_1 values available.	117

6.6	The Run 3A T_1 values from fitting the polarization data of the ring section for the no beam run conditions. The Mixing Chamber and HD temperatures are the same due to these being beam-off measurements.	117
6.7	The Run 3A T_1 values from fitting the polarization data of the core section for beam-on run conditions. There is no T_1 value for the core section after the fourth row because all the core polarization is gone by this run condition.	117
6.8	The Run 3A T_1 values from fitting the polarization data of the ring section for beam-on run conditions.	118
6.9	The Run 3B T_1 values from fitting the polarization data of the core section for beam-off run conditions.	119
6.10	The Run 3B T_1 values from fitting the polarization data of the ring section for beam-off run conditions.	120
6.11	The Run 3B T_1 values from fitting the polarization data of the core section for beam-on run conditions.	120
6.12	The Run 3B T_1 values from fitting the polarization data of the ring section for beam-on run conditions.	121
B.1	Summary of Run 2A raw down absorption and dispersion NMR signal measurements.	147
B.2	Summary of Run 2A raw up absorption and dispersion NMR signal measurements.	148
B.3	Summary of Run 2B raw down absorption and dispersion NMR signal measurements.	148
B.4	Summary of Run 2B raw up absorption and dispersion NMR signal measurements.	149
C.1	Run 3A summary of conditions in which NMR measurements were taken at the UITF.	153
C.2	Run 3B summary of conditions in which NMR measurements were taken at the UITF.	159
D.1	Summary of the Run 3A NMR signal measurements from the down absorption and dispersion NMR signals, Part 1.	161

D.2	Summary of the Run 3A NMR signal measurements from the down absorption and dispersion NMR signals, Part 2.	162
D.3	Run 3A Raw NMR Up Sweep Signal Area Measurements	163
D.4	Summary of the Run 3A NMR signal measurements from the up absorption and dispersion NMR signals, Part 1.	163
D.5	Summary of the Run 3A NMR signal measurements from the down absorption and dispersion NMR signals, Part 2.	164
D.6	Summary of the Run 3B NMR signal measurements from the down absorption and dispersion NMR signals, Part 1.	165
D.7	Summary of the Run 3B NMR signal measurements from the down absorption and dispersion NMR signals, Part 2.	166
D.8	Summary of the Run 3B NMR signal measurements from the down absorption and dispersion NMR signals, Part 3.	167
D.9	Summary of the Run 3B NMR signal measurements from the down absorption and dispersion NMR signals, Part 4.	168
D.10	Summary of the Run 3B NMR signal measurements from the up absorption and dispersion NMR signals, Part 1.	169
D.11	Summary of the Run 3B NMR signal measurements from the up absorption and dispersion NMR signals, Part 2.	170
D.12	Summary of the Run 3B NMR signal measurements from the up absorption and dispersion NMR signals, Part 3.	171
D.13	Summary of the Run 3B NMR signal measurements from the up absorption and dispersion NMR signals, Part 4.	172
E.1	Summary of Run 3A polarization values from the raw down absorption and dispersion NMR signals, Part 1.	174
E.2	Summary of Run 3A polarization values from the raw down absorption and dispersion NMR signals, Part 2.	175
E.3	Summary of polarization values from the raw up absorption and dispersion NMR signals, Part 1.	176
E.4	Summary of Run 3A polarization values from the raw up absorption and dispersion NMR signals, Part 2.	177

E.5	Summary of Run 3B polarization values from the raw down absorption and dispersion NMR signals, Part 1.	178
E.6	Summary of Run 3B polarization values from the raw down absorption and dispersion NMR signals, Part 2.	179
E.7	Summary of Run 3B polarization values from the raw down absorption and dispersion NMR signals, Part 3.	180
E.8	Summary of Run 3B polarization values from the raw down absorption and dispersion NMR signals, Part 4.	181
E.9	Summary of Run 3B polarization values from the raw up absorption and dispersion NMR signals, Part 1.	182
E.10	Summary of Run 3B polarization values from the raw up absorption and dispersion NMR signals, Part 2.	183
E.11	Summary of 3B polarization values from the raw up absorption and dispersion NMR signals, Part 3.	184
E.12	Summary of 3B polarization values from the raw up absorption and dispersion NMR signals, Part 4.	185

Glossary of Symbols

α - Proportionality constant of T_1 expression

$$\beta = B^3 \exp\left(\frac{2\mu_e B}{kT}\right)$$

A_C - Cross sectional area of the core section

A_R - Cross sectional area of the ring section

A_T - Total cross sectional area of the entire target

B - Magnetic holding field strength

C_e - Concentration of paramagnetic centers

D_C - Dose received by the core section from the beam

D_R - Dose received by the ring section from the beam

D_{rel} - Relative dose received since start of run condition

D_T - Dose received by the entire target from the beam

ΔB_p - Nuclear line width

f - Proportionality constant between the core and ring section doses

\hbar - Reduced Planck's constant

k - Boltzmann constant, $k = 1.3806 * 10^{-23} J/K$

P_0 - Initial polarization

P_C - Polarization of the core section

P_e - Polarization of unpaired electrons

P_R - Polarization of the ring section

P_{TE} - Thermal Equilibrium Polarization

S_C - Portion of the NMR signal correlated to the core section

S_C^0 - Initial value of the NMR signal correlated to the core section

S_R - Portion of the NMR signal correlated to the ring section

S_R^0 - Initial value of the NMR signal correlated to the ring section

S_{skin}^0 - Initial value of the NMR signal correlated to the skin section

T_1 - Polarization relaxation time, or spin-lattice relaxation time

T_1^H - Polarization relaxation time of hydrogen

τ_e - Correlation time of the oscillating field in the sample material

μ_e - Magnetic moment of electron, $\mu_e = 9.2847 * 10^{-24} J/T$

μ_p - Magnetic moment of proton, $\mu_p = 1.4106 * 10^{-26} J/T$

List of Acronyms

AFP - Adiabatic Fast Passage

BPM - Beam Position Monitor

CEBAF - Continuous Electron Beam Accelerator Facility

CLAS - CEBAF Large Acceptance Spectrometer

CW - Continuous Wave

D - Deuterium or Deuteron

DF - Dilution Refrigerator

DFT - Discrete Fourier Transform

DNP - Dynamic Nuclear Polarization

FRS - Fast Resonance Scan

H - Hydrogen, or proton

HD - Hydrogen Deuteride

IBC - In-Beam Cryostat

IDFT - Inverse Discrete Fourier Transform

IGH - Intelligent Gas Handling system

IPS - Intelligent Power Supply

JLab - Jefferson Lab

LEGS - Laser Electron Gamma-ray Source

NMR - Nuclear Magnetic Resonance

PD - Production Dewar

RF - Radio Frequency

TC - Transfer Cryostat

TE - Thermal Equilibrium

UITF - Upgraded Injector Test Facility

Chapter 1

Introduction

1.1 Physics Motivation

Study of transversity phenomena is one of the flagship experimental programs with the 12 GeV Continuous Electron Beam Accelerator Facility (CEBAF) and CEBAF Large Acceptance Spectrometer (CLAS12) at Jefferson Lab. Development of transversely polarized targets for use with electron beams is essential to the experimental transversity program at the 12 GeV upgraded JLab. However, one of the main problems with transversely polarized targets in an electron beam is that the electrons can be deflected by the magnetic holding fields accompanying such targets. These holding fields create challenging background conditions. To mitigate these conditions, a magnetic chicane can be installed upstream of the target and arranged in such a way that the target's magnetic holding field bends the electron beam back onto the beam axis. A consequence to using a chicane is that bremsstrahlung created in the target material will be peaked along the direction of the incoming electrons, which will then be at several degrees to the detector axis. In general, one can either arrange to have the electron beam or the target bremsstrahlung centered at 0° , but not both. Polarized Hydrogen Deuteride (HD) targets in the frozen spin mode have been developed for use in nuclear and particle physics. Initially the HDice target was used for measuring spin sum rules [1] at the Laser Electron Gamma-ray Source (LEGS) facility at Brookhaven National Facility, and then more recently used for the g-14 run period in Hall B at Jefferson Lab [2].

In light of its success with photon beams, a systematic study of the response of frozen-spin HD to charged-particle beams was initiated. This study focused on the target's response to electron beams, because of the potential application to highly-rated experiments in Hall

B. This thesis reports some of the results of these e^+HD experiments. There are numerous advantages of using frozen-spin HD (HDice target). Using the transversely polarized HD target in a frozen-spin state that requires only relatively small holding fields would greatly mitigate background issues. It has the lowest dilution factor among all other solid targets, having only one neutron and two protons; all of which are polarizable. The proton and deuteron (D) spins can be transferred between each other as desired with radio frequency (RF) transitions. Since HDice can maintain high polarization for a very long period of time, it can be made in advance and used for long complex experiments without changing experimental conditions. This results in greatly reducing systematic errors. Although the HDice target has been shown to successfully work under a high intensity photon beam, it has yet to be demonstrated that the target could stand an electron beam of reasonably high current (nA). During the g-14 run period in 2012, the first short test using an electron beam showed that even though there was no evidence of permanent target damage, preserving the target polarization for a long period of time with an electron beam requires several improvements. These improvements were implemented and a full scale test of an electron beam on a Hydrogen Deuteride target (known as the eHD experiment at Jefferson Lab) ran from September 11, 2020 to March 15, 2021.

1.2 Thomas Jefferson National Accelerator Facility

The eHD experiment described in this thesis was carried out in the Upgraded Injector Test Facility (UITF) at the Thomas Jefferson National Accelerator Facility (JLab), Virginia, USA. Located in the High Bay Area of the Test Lab, the UITF was home to the accelerator and In-Beam Cryostat for the duration of experiment. The goals of the HDice test program at the UITF were to identify the beam and target parameters required to have an in-beam polarized HD spin relaxation time maintained at about two weeks (which is approximately the minimum frequency for target exchanges while running an experiment with electron beams). Experimental run conditions comprised of circularly polarized electron beam incident on a solid HD target that is longitudinally polarized along the beam axis. Producing the electron beam requires the use of a 200kV gun and a cryo-booster module as part of the accelerator. Target temperatures and polarizations were maintained by holding the target within IBC during beam run times.

When the lab was founded in 1984, it was initially named the Continuous Electron Beam Accelerator Facility. This was until 1996, when the lab was renamed to Jefferson Lab. CEBAF



Figure 1.1: An aerial view of the Thomas Jefferson National Accelerator Facility, also commonly known as JLab [3].

now refers to the accelerator at Jefferson Lab. The national laboratory's mission is to study the fundamental structure of nuclear matter using CEBAF. It can provide electron beams to four experimental Halls simultaneously. The energies provided can reach up to ~ 11 GeV with a 100% duty cycle for Halls A, B, and C. Hall D has the ability to reach up to ~ 12 GeV.

Hall B housed CLAS until 2012 when construction of the 12 GeV CEBAF upgrade began. The last experiment to use CLAS was g14, which used the previous polarized frozen-spin HD targets. Afterwards, it was replaced with the improved CLAS12 to be used with the upgraded beam energies as well as multiple scheduled experiments using HD ice targets contingent on the results of eHD.

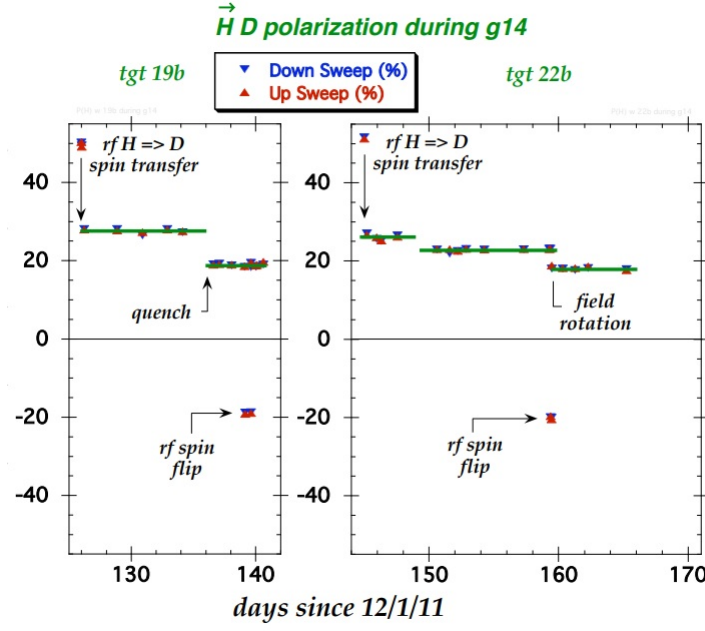


Figure 1.2: HDice target polarization values during the g14 experiment at Hall B [4].

1.3 Upgraded Injector Test Facility

Preparations were made to run experimental tests on frozen, polarized HD targets with an electron beam at the Upgraded Injector Test Facility. This facility was commissioned for research and development of the HDice target with electron beams. The energy deposited in the target is shown by the solid blue curves in Figure 1.2 (as calculated with two different simulation codes), and is essentially independent of energy. Compared to 10 MeV, the deposited energy is only 30% higher at 10 GeV. In contrast, the total energy loss (dashed red curves) is a strong function of energy, but this is due to bremsstrahlung that leaves the material unaffected.

Several electron beam tests were performed with 9.7 MeV on polarized and non-polarized HD targets. The energy deposited into the target during electron beam runs becomes independent of the electron beam energy at ~ 10 MeV and further increases in beam energy is all lost as bremsstrahlung radiation as seen in Figure 1.3. This justifies a comparison between the tests performed at UITF with tests done in experimental Hall B where the beam energy can go as high as 10 GeV. Since the ionization and energy deposition into the target are approximately independent of the beam energy at 10 MeV, results from tests at UITF can be extrapolated to predict the target's behavior in Hall B. However, many qualities of a 10 MeV electron beam needed to be considered before being used at UITF that are not issue using the higher energy beam.

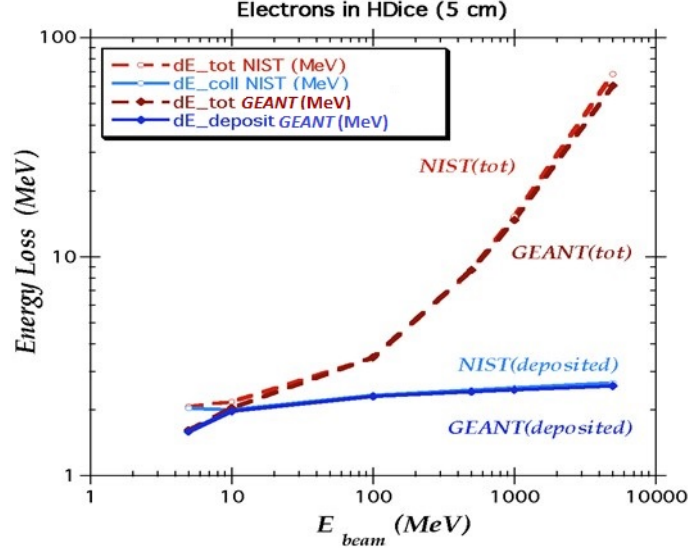


Figure 1.3: The energy deposited into the HDice target by electrons at various energies. Around approximately 10 MeV, the energy deposited into the target levels off with the rest of the energy lost as bremsstrahlung.

Although the energy deposition is nearly the same for a 10 MeV and 10 GeV beam, there were still differences that caused issues that needed to be address to properly conduct the low energy tests. One such issue was how the electron beam behaves as it passed through various beamline components and the IBC. The electron beam began to spread out over a much larger area as it entered the IBC. This is due to the beam passing through the IBC solenoid fields, as see in Figure 1.4. Additionally, beam also scattered off the IBC radiation baffle. Without corrections, the beam would spray all over the place after entering the IBC.

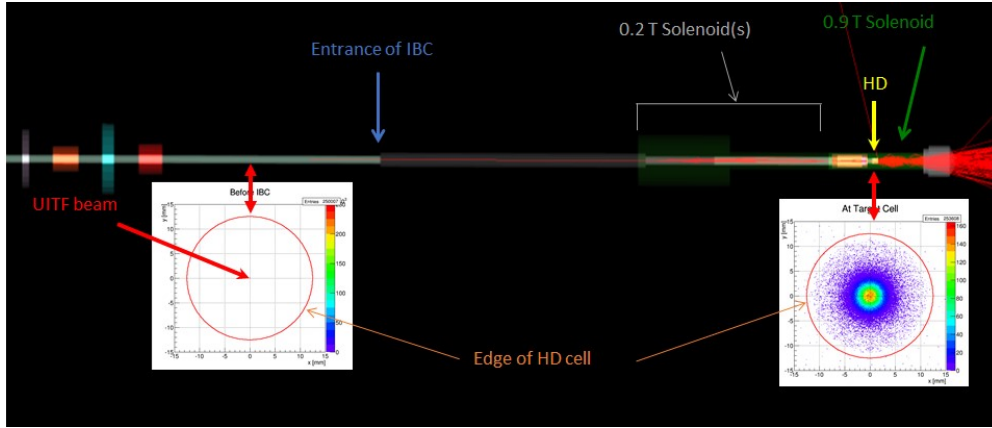


Figure 1.4: The image above shows a simulated electron beam as it passes through the magnetic fields of the IBC solenoid. The beam quickly spreads out as it enters the IBC and hits the target region.

1.4 Overview of Polarized Targets

Efficient polarized targets require a high polarization, a fast polarization build up rate, a slow polarization loss rate, and the possibility for the target to be able to reverse its polarization direction. Many targets meet those criteria at some level of success. A few of them used at Jefferson Lab will be described in this section.

One type of polarized targets relies on Dynamic Nuclear Polarization (DNP). Common materials used for this target are ammonia (NH_3) [5], butanol ($\text{C}_4\text{H}_9\text{OH}$), and lithium hydride (^7LiH), as well as their deuterated counterparts (ND_3 , $\text{C}_4\text{D}_9\text{OD}$ and ^6LiD) [6]. These are solid state targets that can achieve very high polarizations for the hydrogen (H) species within the molecules (80-90% for protons and 40-80% for deuterons). However, their polarizations are highly diluted due to the presence of other heavier nuclei, which create undesired backgrounds. The polarization can build up within a few hours by inducing radio-frequency transitions between nucleons and electron energy levels. However, those materials are diamagnetic substances (all electrons paired), thus it is necessary to dope the material to introduce free electrons (paramagnetic radicals) into the target material. The doping is made for ammonia and lithium hydride targets by irradiation, while the addition of a chemical dopant is used in butanol targets. In the case of the FROzen Spin Target (FROST) in Hall B, the butanol is mixed by weight with 5% of H_2O and 0.5% of TEMPO3. The FROST is a frozen spin mode target operating at 50 mK, in a holding field of 0.56 T, and has to be repolarized every few days.

Another target commonly used in Jefferson Lab's Hall A is a gaseous helium-3 polarized

target. It is a good substitute to a polarized free neutron target, which cannot be realized due to the short lifetime of free neutron (~ 15 minutes) and its neutral charge. Indeed, both proton spins in the ^3He nucleus form anti parallel pairs. The nucleons are predominantly in a S-wave, thus the spin of the neutron aligns with the one of the ^3He nucleus. The advantage of the ^3He target over the previous (DNP-type) targets is that the ^3He target is almost pure ^3He , only including an impurity in the form of a small amount of nitrogen ($\sim 1\%$). An obvious drawback of this target is its low density (typically 1% of a solid target) due to its gaseous nature. However, this is compensated in part by using a longer target cell and higher beam current. Fortunately, ^3He target uses current of $10\mu\text{C}$, contrarily to the FROST target (which can only be run with photon beam) and DNP-type targets that typically use about 10 nA. Although higher currents of about 0.1 mA were achieved in Hall C at a price of larger overhead due to the necessary very frequent anneals [6]. The target is polarized by optical pumping, and the typical target polarization is about 40%. New techniques of hybrid optical pumping now allow polarization to reach about 65% [7].

In 2008, the HD target has been added to Jefferson Lab's collection of polarized targets in Hall B. This target was transferred from and original developed at Brookhaven National Laboratory. Only a few other HD targets have been developed across the world. For instance, the Hydile target at GRAAL in France [8] and in Japan with the new HD target at Spring-8 [9]. The HD target is a solid state target consisting of 99.9% pure HD molecules, where both the proton and deuteron are polarized. It allows studying both nuclei in the exact same experimental configuration ideally with scattering only from nuclei (H and D) of interest. Unlike the DNP-type targets, the HD target is polarized by a "brute force" method. The HD target takes approximately 3 months to reach a long enough polarization life-time. Thus, the target cannot be repolarized during an experimental run. However, the target can also achieve extremely long relaxation times (resulting in a very low polarization loss rate), which is usually enough to perform weeks of experiment. Like FROST, the HD target is a frozen spin target operating at 50 mK.

The HDice target offers unique opportunities to study nucleons. Unlike other targets, the HDice target ideally contains only protons and deuterons, which can both be polarized in principle up to up to 60% H and 15% D, or 30% for both H and D with the current setup at Jefferson Lab. Other types of targets contain additional nuclei that cannot be polarized. For instance, ammonia targets (NH_3 and ND_3) contain nitrogen, which creates an undesirable

background. Therefore, with an HD target such unwanted background is significantly reduced. Another advantage of an HD target is that it can hold its polarization while in “frozen-spin mode” for a relatively long time; on the order of several months to years under the proper experimental conditions (HD temperature < 500 mK and a holding field of ~ 1 T).

Chapter 2

The HDice Target at Jefferson Lab

2.1 General description

The HDice target is composed of Hydrogen-Deuteride in the solid phase, grown slowly to yield a volume approximating a single crystal. It is primarily made of HD molecules in the solid state, but also includes a few H₂ and D₂ impurities. The impurities are essential in the polarization process of the target. The target polarization is achieved by subjecting each HD crystal to a low temperature of around 10 mK while positioned in a strong magnetic holding field of 15 Tesla.

As discussed in Section 1.4, the HDice target offers unique opportunities to study nucleons. Unlike other targets, the HDice target ideally contains only protons and deuterons. Therefore, with an HD target unwanted background from larger atoms is significantly reduced. Another advantage of an HD target is that it can hold its polarization while in “frozen-spin mode” for a relatively long time; on the order of several months to years under the proper experimental conditions.

2.2 Previous HDice Target Design and History

The first HDice target cell used with beam at Jefferson Lab consisted of an outer shell, an inner shell, aluminum wires, and a copper ring as shown in 2.1. The shells were made of a fluoropolymer, PCTFE (Polychlorotrifluoroethylene), otherwise known as Kel-F. At low temperatures around 10 mK, Kel-F offered useful characteristics like low permeation and low deformation. Kel-F also provides good mechanical, chemical, and radiation resistances. The

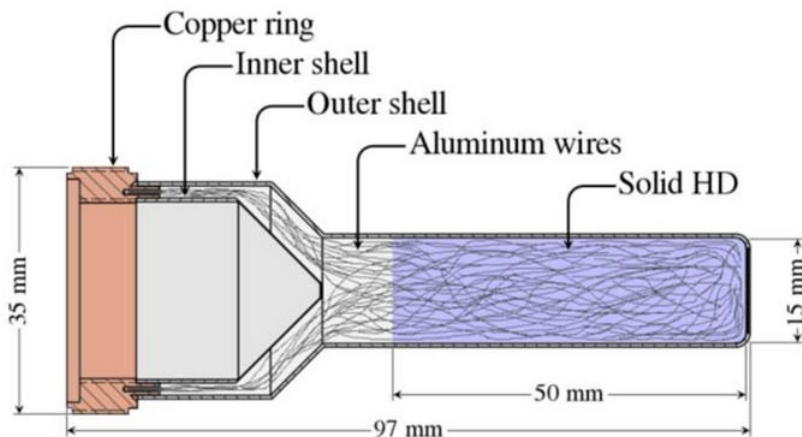


Figure 2.1: HDice target cell schematic. The Kel-F shells are attached to the copper ring with epoxy. Most of volume within the outer shell is filled with solid HD, taking the form of a 50 mm long and 15 mm diameter cylinder

most important feature is that the molecular structure of the Kel-F shells do not contain any hydrogen or deuterium atoms. A consequence of this was no background interference to the crystal's hydrogen or deuterium measured NMR signals. The NMR signal on Fluorine, which is at about 5% higher field than H at the same frequency, provided a reliable magnetic field calibration.

The g14 HDice target cell contained 740 aluminum wires with a 99.9998% or 4N purity rating. These wires were put together in bundles of 14 twisted together at one end and free on the other. Then the twisted end of a bundle was placed in each of the 60 holes in the copper ring and soldered into place. The wires were then carefully combed out in order to be evenly distributed within the target. During this process, the center of the ring was clear of any wires allowing for the inner Kel-F shell to be inserted in the ring and secured with a vacuum tight seal of epoxy. Before the outer Kel-F shell was lowered down onto the target ring, the wires were positioned to run along the inner shell before being straightened to run parallel to the long side of the outer shell. Different stages of the target cell during the production process can be seen in Figure 2.2.

These wires were first necessary to remove heat from the target generated during the polarization process. Secondly, the wires conducted out heat produced by beam interactions or energy level transitions. Unfortunately, wires being in the path of the beam were unavoidable for the amount of heat removal required by the HD crystal. The material used for the wires had to be chosen carefully. Aluminum has good thermal conductivity, low density, and a low



Figure 2.2: Layout of the HDice target cell used during g14. From left to right, a bundle consisting of 14 Al wires, a sectional view of the Kel-F pieces that attach to the ring, a completed target cell, and a target cell after 60 bundles are soldered and the wires separated to be positioned.

nucleon count, making it an excellent choice to limit background interactions with the beam. The aluminum wire that was used was of 4N purity and the best available at the time.

The copper ring ensured the support of the target by threading the target into place and efficiently dissipating the heat from the target crystal brought by the aluminum wires into the cryostat's copper cold-finger. Unlike the wires, the ring was not in the way of the beam or in the sight of a detector. As a result, copper with its superior heat transfer could be used instead of Aluminum. The outside threads of the ring were right-handed allowing the target to be mounted to the cold-finger, while the inner left-handed threads allow for the installation and removal of the target.

An opportunity to see the interaction between an HDice target and electron beam arose during Hall B's g14 experiment. The experiment focused on HDice targets with a photon beam. However, a glitch in the the IBC holding field power supply lead to the system incorrectly assuming a quench occurred, which lead to the power supply ramping down the holding field. By the time the issue was corrected, the target within the IBC had lost a significant amount of its polarization and was no longer ideal to continue using in the planned experiment. The decision was made not to immediately remove the target, but to use this target with an electron beam to see what knowledge could be gained for future target development.

The two runs from g14 using electron beams with polarized HD were conducted in 2012.

Although conducted under less than ideal conditions, beams were rastered over the targets allowing for studies to be conducted with different rastered areas, HD temperatures, and holding fields. Target polarization values were monitored with NMR measurements indicating several signal loss mechanisms at work. The beam raster system used in these tests was inadequate and resulted in significant heating of the target material. This heat could not be removed from the g14 target cells that had been optimized for photon running. Polarization losses occurred due to a combination of this heat and ionization through Moller scattering. These effects were further compounded by ionization screening of the NMR RF response.

Electron beams were used with the target between March 29, 2012 and April 1, 2012. During this period, a g14 target was used with a 5 pass, 5.5 GeV beam. Two target exposures to electron beams were carried out, interspersed with periods of NMR measurements. The magnetic field was about 0.29 T which allowed field-sweep NMR data to be collected during the irradiation periods. A graphical history of the H polarization is shown in Figure 2.3. The target cell cross section is shown to the right of the plotted polarization history and the different colored ellipsoids show the size of the rastered beam on target. The first and second doses of the March run period differed in current by a factor of 10 (100 pA vs 1 nA). This period concluded with a search for radiation damage by turning off the IBC's holding field for an hour. The intention was to zero the polarization, restore the holding field, and then scan using NMR to see if any polarization grew back. After the field was zeroed at the end of the last dose, the H polarization did in fact start to grow back, but it stopped at about half of the expected Thermal Equilibrium (TE) value. The D polarization showed a qualitatively similar behavior to H, although the signal loss rates with beam appeared higher.

As mentioned earlier, the two 2012 electron beam runs were carried out in far less than optimal conditions. These conditions mainly affected to temperature of the HD sample within the target cell. One such condition was that the only available raster at the time was the Hall B Spiral Raster. This raster was responsible for sweeping the beam over the face of the target during beam on conditions. If the beam was not rastered, it would have focused most of its intensity on a specific area of the target. All the heat generated from the beam interaction would be in this particular spot. This would cause the HD target temperature to not be uniform throughout the entire target, create separate regions of the target with different polarization values, and could potentially melt a hole through the target. By moving the position of the beam spot around, these issues can be minimized. Unfortunately, the Hall B Spiral Raster

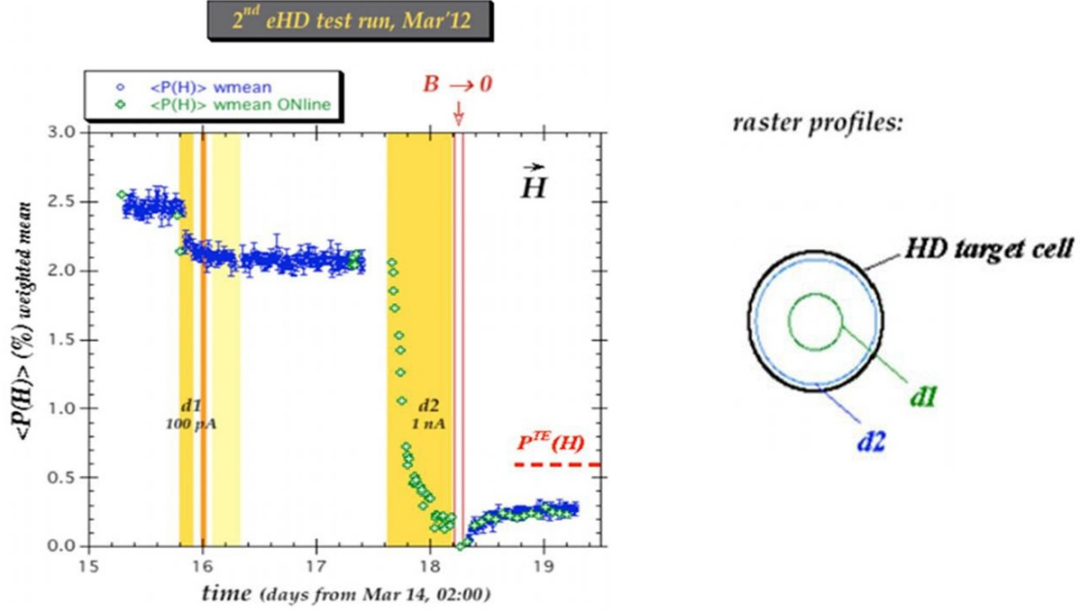


Figure 2.3: Hydrogen polarization $P(H)$ during the second electron beam period in March 2012, with 0.29 tesla holding field during exposures. Shaded vertical bands indicate beam-on periods [10].

ended up being too slow for use with electrons and ended up increasing the HD temperature from ~ 70 mK to ~ 1.3 K. This large increase in temperature contributed heavily to the rate of target depolarization.

The second issue related to the increased HD temperature was that g14 target cells were optimized for the photon experiment and not one using electrons. The target cells could not efficiently conduct electron beam-heating out of the HD crystal. If the target design accounted for removing an increased heat load from an electron beam, then it could have, at least in part, compensated for the "slow" raster discussed previously.

A third issue that arose from the setup involved Hyperfine Mixing. The creation of HD^+ ions by the beam and the interactions with the spin of these ions' unpaired electrons (Hyperfine Mixing) can account for most of the observed polarization losses. These losses are expected to be greatly reduced when the unpaired electrons are highly polarized, a condition that could not be achieved in with the 2012 experimental setup as a result of the high target temperatures. It was determined that straight forward improvements in the target cell design and the raster system could drop the internal HD temperature significantly. Nonetheless, given the many competing processes in play, further testing would be essential to improve results with electron beams.

2.3 Improved eHD Target Cell at UTF

The improved target cell design used during the eHD experiment similarly consisted of an outer shell, an inner shell, aluminum wires, and a copper ring as seen in Figure 2.4. The shells were also made of Kel-F and attached to a copper ring using the same type of epoxy. The differences between target cell designs were in the wire material, how the wires are attached to the copper ring, and the size of the Kel-F outer shell. Instead of wire bundles consisting of 12 wires of 4N9 aluminum, the new bundles are made of 24 wires of 5N9 aluminum. The diameter of the wires were increased from 0.002" to 0.003" for eHD. To match the new Kel-F outer shell length of 25mm, the wires were trimmed shorter. The bundles were placed in the first 2 holes on the copper ring with the third hole being left unfilled. This pattern was continued completely around the ring resulting in 960 total wires. These changes led to the desired increase in heat removal capacity for the target, which was required after observing target performance during g14.

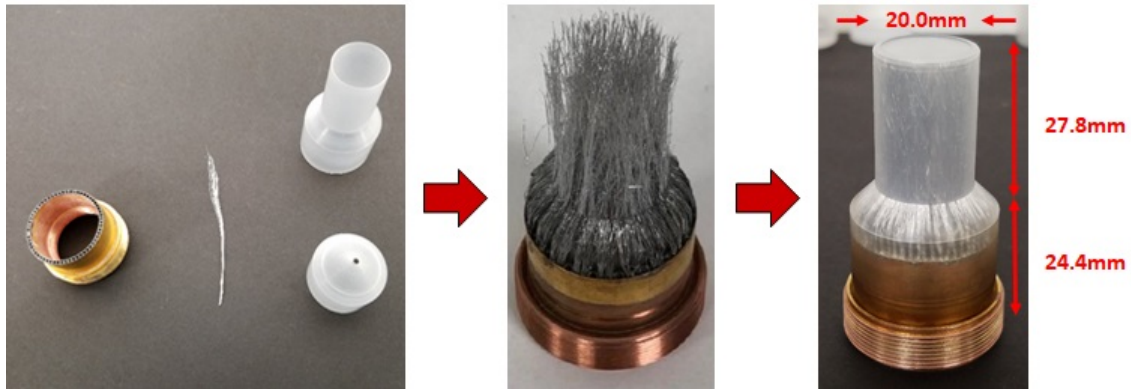


Figure 2.4: The progression of the eHD target cell. Displaying from left to right: the individual target cell components, the wires bundles combed into position after being soldered to the copper ring, and the completed target cell after the outer shell has been attached.

Each HD crystal formed in one of the new cells was an approximately 12.5 mm long, 19 mm diameter cylinder with more aluminum wires of higher purity to provide additional heat removal. The crystal condensation process is described further in this 2.5.3. Larger diameter crystals allowed more surface area for the rastered beam to move across, which allowed for longer times between the beam hitting the same spot of the target face. This contributed greatly to keeping the HD temperature around 150mK during beam on periods as opposed to the temperature being closer to 1.3K seen at the end of g14.

2.4 HD Material

One of the most important parameters of the HD material is its relaxation time, T_1 , which is the recovery time of the polarization to the thermal equilibrium given via:

$$P(t) = P_{te} + (P_0 - P_{te}) * \exp\left(\frac{-t}{T_1}\right), \quad (2.1)$$

where $P(t)$ is the polarization at time t , P_0 is the initial polarization at $t = 0$, and P_{te} is the thermal equilibrium. In the case of pure HD, the relaxation times for both H and D are very long (more than several years). A long relaxation time would usually be considered a great advantage due to the polarization being held for the duration of an experiment. However, it would also be a problem since it would take decades to reach the desired polarization.

In 1967, A. Honig [11] suggested that the relaxation time could be adjusted by adding a small amount of ortho-H₂ and para-D₂ impurities to the pure HD. The HD protons and ortho-H₂ nuclei have comparable Larmor frequency values that allow them to exchange energy by cross relaxation as shown in Figure 2.5. Ortho-H₂ and para-D₂ are the names corresponding to rotational states J ($J = 1$) of H₂ and D₂. The names of the rotational states of J ($J = 0$) are para-H₂ and ortho-D₂. Ortho refers to the group of states of higher nuclear spin degeneracy while para refers to the lower state [12].

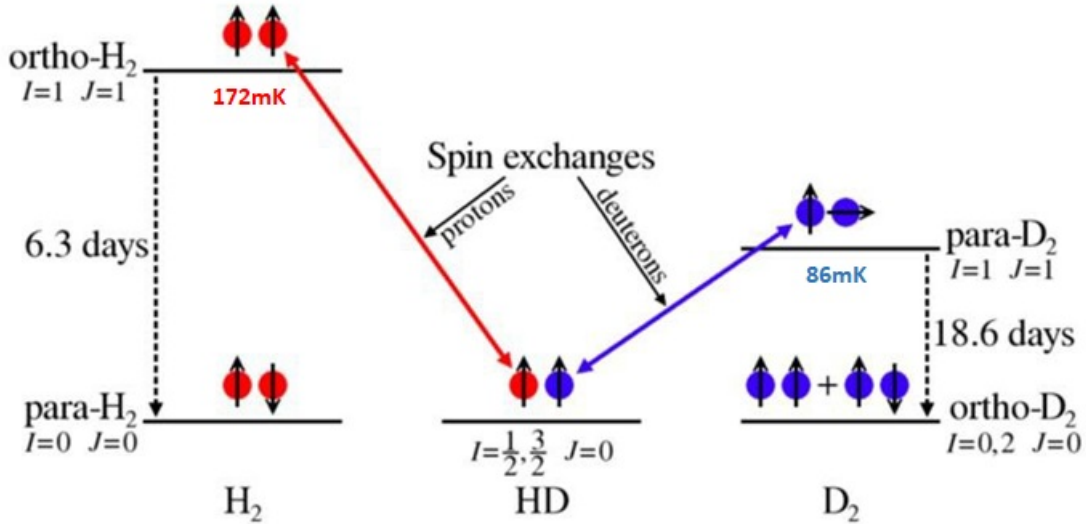


Figure 2.5: Spin exchanges between ortho-H₂ (and para-D₂) and H (and D) nuclei in the HD molecule.

At room temperature, ortho-H₂ amounts to 75% of the H₂ content and para-D₂ amounts to

33% of the D2 content. By following the Fermi-Dirac distribution for H and the Bose-Einstein distribution for D, the populations of ortho-H2 and para-D2 decay at the liquid helium temperature with lifetimes of 6.3 days and 18.6 days, respectively as shown in Figure 2.5. Consequently, the HD relaxation times depend on these populations, and will increase as the concentrations of ortho-H2 and para-D2 decrease. Therefore, high populations with short relaxation times during the polarization phase are possible. Then once the HD is polarized, we still achieve long relaxation times when it is being operated or stored at low temperature due to the decay of those same populations.

In practice, the impurities did not need to be added because commercial HD gas already contains about 1.5% of H2 and 0.5% of D2, which both are two orders of magnitude too high for the HDice target. Thus, the HD gas used in the making of the targets used at UITF was first distilled to the desired purified level before being injected into the target cells.

2.5 Target Production and Cryostats

A cryostat is a device used to store an experimental sample or piece of equipment at constant, low cryogenic temperatures. The use of multiple cryostats was necessary to successfully produce a polarized, single crystal made from hydrogen-deuterium gas. All cryostats used in the creation of an HDice target, with the exception of the transfer cryostat, contain a copper cold-finger, superconducting magnets, a cooling system, and several layers of thermal shielding. In general, the cryostats were similar in design. However, the differences that will be explained in each cryostat's respective section.

The following is the list of all the cryogenic devices required to make and use the HDice target:

1. The Production Dewar (PD): a cryostat used for crystal formation and polarimetry with a temperature of 4.2 K (capable of as low as ~ 2 K) and a magnetic field up to 3 T.
2. The Dilution Refrigerator (DF): a cryostat used to polarize targets with a temperature of 10 mK and a magnetic field of 15 T.
3. The Transfer Cryostat (TC): a cryostat used to transfer targets between the other cryostats with a temperature of 2 K and a magnetic field of 0.1 T.
4. The In-Beam Cryostat (IBC): a cryostat used to operate the target under a particle beam

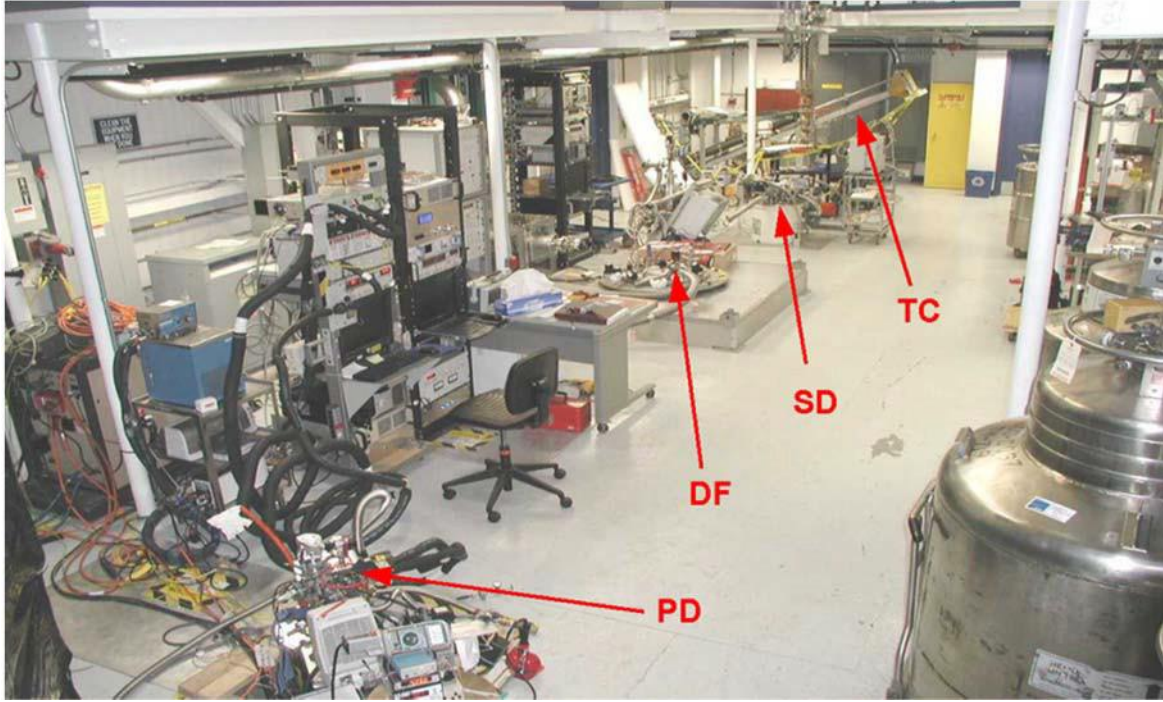


Figure 2.6: The layout of the HDice lab, containing the cryogenic devices used in target production. Note: the Storage Dewar (SD) was not used for the eHD experiment, but was stored in the HDice lab.

with a temperature range of 50 mK to 300 mK, a longitudinal magnetic field up to 1.1 T, and a transverse magnetic field up to 0.07 T.

2.5.1 Target Production Overview

HDice target production began with target cell assembly. The completed cell was connected to the gas injection manifold via vacuum line and inserted into the PD. The HD gas was bled into the cell condensed in the cell through an injection tube glued to the cell with a low temperature RTV silicone sealant, and installed on top of the PD. Prior to the HD gas injection, the target cell was vacuum pumped and leak checked. The target cell was then slowly cooled down by lowering the tube in the PD. As the tube was lowered, the HD gas condensed from liquid, then solid. Initially, the HD did not form a single crystal, but rather a snowy mixture. The tube was then slowly raised until the HD reached its triple point, where it existed multiple states. The tube was then slowly lowered again, which allowed the HD triple point mixture to almost instantaneously go into a solid state forming a single HD crystal.

Once the crystal was formed, a polarization calibration was performed at thermal equilibrium before it was transfer red to the DF for the next stage of the production process. The transfer

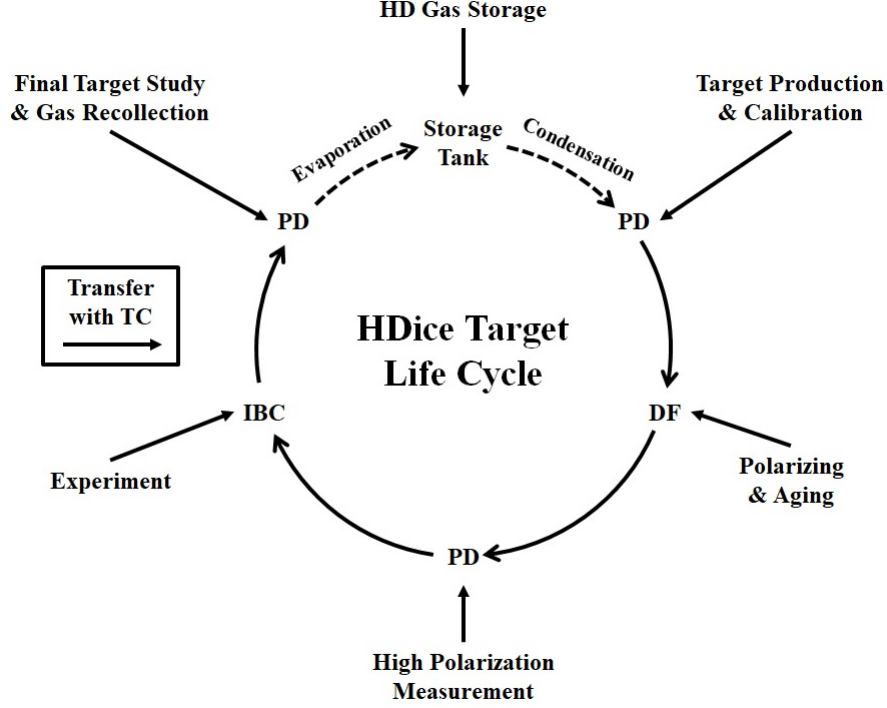


Figure 2.7: A schematic diagram summarizing the HDice target life cycle.

of the target cell from one cryostat to another was a critical time in the life of a HD target. Any issue during the transfer could have lead to an unrecoverable loss of target polarization or the loss of HD material in the cell. The transfer consisted of extracting the cell from a cryostat and inserting it into another cryostat. The extraction of the cell started by connecting the TC to the first cryostat. The TC tube was lowered until it reached the cell. Engaging the threaded screw driver tool within the TC with the inner left-handed threads of the target cell's copper ring, the target was released from the first cryostat and collected into the TC. Once the cell was in the TC, it was transferred to the next cryostat as quickly as possible. The TC was not an ideal place for the target to be stored long term because its cryogenic supply was limited and it's magnetic field was low. As a result, the target could suffer from a higher rate of polarization loss the longer it rests in the TC.

The targets were polarized in the DF using a “brute force” method. The target was placed in a high magnetic field and subjected to a low temperature to age until the polarization reached its thermal equilibrium. While the target was aging, the relaxation time of the cell was increasing exponentially. This polarizing process started as soon as target was transferred to the DF. The process began by setting the magnetic field to 15 T while lowering the temperature down to 10 mK. As the HD polarized, the $J=1$ H₂ and D₂ species decayed to their $J=0$ ground states. Heat

was released during the decays. Thus, immediately achieving the optimal thermal equilibrium polarization condition was not possible. As long as heat from decay was produced, the thermal equilibrium polarization was lower than it would be in the optimal 10 mK and 15 T condition.

After aging for ~ 3 months, each target was polarized. The targets remained in the DF until one was required for tests in the IBC. When the time came to use a target, it was moved back to the PD. Here the H and D polarization measurements were performed to verify that the polarization was high. At this point the target was ready to be used in the IBC with beam.

Once the experimental use of the cell was over, the target was transferred back to the PD with the TC for final polarization measurements. Afterwards the HD was retrieved by evaporating the target in the PD. This process was just the reverse of the condensing procedure mentioned earlier. As the necessary mixture of HD gas is difficult to make, the preference was to retrieve gas so it could be reused in future targets. This can be done as long as the gas sample's H₂ and D₂ concentrations are still acceptable. Those concentrations can change over time due to the HD recombining into H₂ and D₂ ($2 \text{ HD} \rightarrow \text{H}_2 + \text{D}_2$). The recombination may be accelerated due to the irradiation of the HD or the presence of chemical compound acting as a catalyst.

2.5.2 Production Dewar

The Production Dewar was the first cryostat required in making the solid HD target for the eHD experiment. It was designed as a top loading, variable temperature cryostat with a superconducting magnet inside. The production dewar was an integral component of the HDice target system. It was used to freeze the HD gas to produce an ice crystal target. The PD was also used to vaporize old targets for gas recollection of each target after completing their respective beam run periods. Most of the PD was situated in a pit within the HDice lab with an aluminum safety plate installed around it at floor level. The PD itself consisted of several layers and components, which are shown in Figure 2.8.

In order for the PD to perform its tasks, it held the target at temperatures from just under 2K up to room temperature. To accomplish this range, the cryostat was constructed in layers. Each layer acted as different temperature shields. The outermost layer was the cryostat vacuum chamber. Located within this isolation vacuum space, was the Liquid Nitrogen (LN₂) reservoir, the liquid helium (LHe) reservoir, and vari-temp space. The outer wall of this vacuum space was exposed to the ambient temperature of the HDice lab. The vacuum greatly reduced any heat

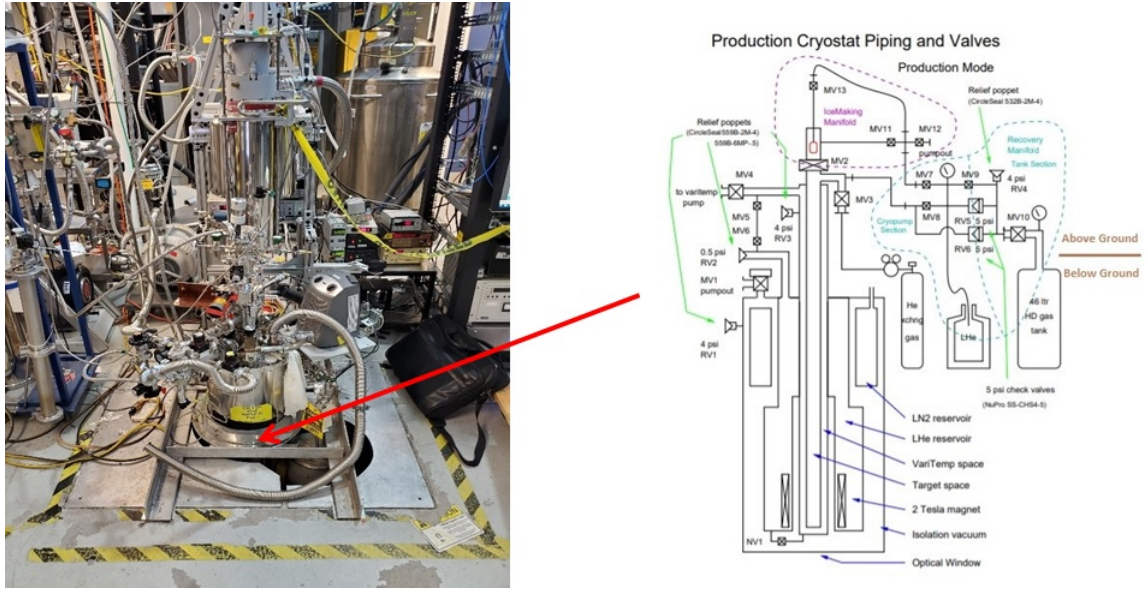


Figure 2.8: The Production Dewar - a cryostat used for HD crystal formation with a temperature of 4.2 K and a magnetic field up to 2 T [13].

transfer from the outside to the next layer, the LN2 reservoir. The reservoir's shape was toroidal, wrapping around the inside of the vacuum space. It was filled through a liquid nitrogen transfer port located externally on top of the cryostat. Due to the temperature of liquid nitrogen, the LN2 reservoir acted as an 80K shield from the heat being transferred through the vacuum space. Between the LN2 reservoir and the next layer of thermal shielding known as the LHe reservoir, was an additional vacuum space. Like the LN2 reservoir, there was a LHe transfer fill port located on top of the cryostat. The liquid helium stored in the reservoir provided a shielding temperature of around 4 K.

While the aforementioned layers allowed a target to reach a temperature of 4 K, the target temperature needed to go to approximately 2 K to measure an aged target’s final polarization through the use of nuclear magnetic resonance (NMR) measurements. A further description of the NMR system used with the PD is provided in Section 5.4.1. The varitemp space was the toroidal layer located between the LHe reservoir and where the target is stored, known as the target space. It was isolated from the LHe reservoir by vacuum. This region allowed the target to reach lower than liquid helium temperatures. Liquid helium or warm helium vapor entered the varitemp space through a capillary coming from the LHe reservoir. The varitemp space was connected to a pump by a valve located on top of the PD. While the varitemp space was pumped on, the reduced pressure resulted in lowering the boiling point of stored liquid helium from 4.2 K to ~ 1.5 K.

Located within the target space contained the target pedestal, which was responsible for holding the target once it was threaded into the pedestal. Besides holding the target securely within the cryostat, the pedestal contained both the target NMR coil and a shutter opener. The shutter opener was used to open the 80 K radiation shutter of the transfer cryostat. Details on the shutter opener are discussed further under in 2.5.4. Due to the target vacuum space sharing a wall with the varitemp space, the temperature of the target could be controlled by pumping directly on the varitemp space. Thermistors mounted on the target pedestal sent signals to external readouts to measure the temperature of the target space.

Mounted within the LHe reservoir was a submerged superconducting magnet necessary for both target polarization measurements and maintaining the polarization of a completed target. Although the target polarization process took place in the Dilution Refrigerator and is discussed in 2.5.5, polarization measurements were done afterwards in the PD. To make these measurements, the cryostat's superconducting magnet generated a 2 Tesla holding field at 4.2K. The maximum possible energy stored within the magnet was 1.7 kilojoules given a full field current of 39.71 Amperes and an inductance of 2.2 Henries.

The PD and DF superconducting magnets were both equipped with a persistent current switch. These switches were pieces of coil that connect both ends of the superconducting coils. The switch allowed the magnet power supply to be connected to the superconducting magnet only when the magnet field strength required to be changed. At all other times, the switch was left open to prevent anyone from accidentally changing magnet settings during operation. The purpose of this feature was to prevent accidental damage to both the magnet and surrounding system components as well as maintain target polarization.

Two auxiliary components of the PD were the gas recovery and ice making manifolds. The gas recovery manifold included connections for storage tanks to act as expansion volume for the HD gas. The tanks were selected and installed in the gas recovery manifold prior to any HD being introduced to the PD. Prior to a target being made, the tank was filled with the HD gas used to make a crystal. The tank was also used in recollecting the HD gas of a target after its experimental run. In order to recollect as much of the evaporated gas as possible, a cryopumping system was built into the gas recovery manifold. The cryopump was made up of thin wall stainless steel tube approximately 3m in length and 3mm diameter. The tube was inserted into a small dewer of liquid helium, which lowered the pressure within the tube. The pressure differential caused the HD gas to flow into the tube and condense, removing it from

the from the PD. The ice making manifold consisted of a combination of three valves, a vacuum lock, and interconnecting tubing. It connected to the target space of the PD through a gate valve located on the top of the PD. The manifold was also connected to the target cell through a small capillary.

2.5.3 HD Ice Production

The following procedure describes the steps required in the formation of HD ice within a target cell. Production began with a target-less PD running operating at 4K with both the gas manifold and gas recovery manifold connected to the PD. The gas recovery manifold was connected to a tank of HD gas. The liquid helium levels in the LHe reservoir and vari-temp space were equalized while an exchange gas was injected into the target space. The cooling capacity to condense a target was provided by this exchange gas.

Next, an empty target cell was connected to the PD's gas recovery manifold by attaching the cell to one end of the target injection tool known as the injection tool. This injection tool provided the line for HD gas to flow into the target cell. The other end of the tool was attached to the gas recovery manifold by a vacuum line. Once the target cell was attached to the injection tool, it was mounted to a gate valve on top of the PD. The volume within the target as well as the volume surrounding the target in the gate valve were vacuum pumped down. At this stage, the RTV seal used between the target cell copper ring and the injection tool was checked for leaks. The target cell's pressure was monitored while it sits vacuum pumped for approximately 30 minutes to confirm the target seal was good and the procedure could continue.

After the seal is confirmed to good, the pressures in both volumes were vacuum pumped down to a pressure better than 1×10^{-5} barr. HD gas was then bled only into the target cell until the pressure in the cell reached 0.5 bar. The gate valve could then be opened and the target cell could begin to be lowered down into the PD. As the target cell was lowered, the target cell temperature decreased. As a result of the cooling, a low pressure region was created in the target cell. The HD gas began to flow into the target cell due to this differential. As the pressure in the cell dropped, additional HD gas was bled into the cell. The target cell continued to be lowered until it was approximately 10 cm above the liquid helium level in the reservoirs. At this point, the target cell was cool enough for the HD gas to rapidly condense.

The target was then pulled back up 1 cm while the increase in target pressure was being monitored. If there was little to no change in pressure, the target was pulled up another 1 cm. This continued until the pressure within the target cell was back to an order of 0.5 bar and stable. The target was then lowered about 1 cm again until the pressure drops down to .4 bar. At this point, the rest of the HD gas flowed from the sample tank to the target until the target reached a pressure of 0.26 bar. Although solid HD was now present within the target cell, it was not a single crystal, but more snow.

To form a crystal of HD from the HD mixture in the target cell, the triple point of HD needed to be located. This was achieved by carefully monitoring the pressure of the target cell as the remaining HD in condensed and the target's heat input decreased. Adjusting the vertical position of the injection tool acted as the temperature/pressure control. If the target pressure fell below 0.13 bar, the snowy HD mixture didn't melt. When this occurred, the target position was slowly moved back up in 3 mm increments until the pressure raises back to 0.15 bar. This was the location of the HD triple point; the position where the HD within the target cell simultaneously existed in solid, liquid, and gas states. Having the HD at its triple point was the only way to form a single, solid crystal out of HD. Once the triple point was located, the target resumed being slowly lowered into the PD over the course of 5 minutes. Again, the pressure of the target cell was carefully observed until it reached 0.125 bar. At this pressure a solid, single crystal of HD rapidly condensed from the triple point mixture without forming a snowy substance made up of multiple crystals.

After the crystal was formed, the valve connecting the gas manifold line to the injection tool was closed with all the HD condensed into the target cell. The target was then lowered all the way down until it touched the pedestool that it was be threaded into for NMR analysis. The valve connecting the line to the gas manifold was shut and the HD gas line removed from the back of the injection tool. By doing this, the injection tool essentially became just an 8-foot-long screw driver used to thread the target cell into the pedatstool. The injection tool was then rotated clockwise half a turn to engage the threads.

When the threads were properly engaged, the tool couldn't move vertically. The target was then slowly threaded into the pedestool while the temperature of the target space was constantly monitored. As the target was threaded in, the friction between the sets of copper rings generated heat and caused the target cell to warm up. If the target was threaded too quickly, the HD ice could begin to melt, altering the structure of the crystal. Threading slowly

enough avoided this issue. The target was threaded by hand until a torque wrench was required to finish.

The torque wrench was necessary to break the temporary RTV seal between the copper target ring and the injection tool. By continuing to turn the tool clockwise after the break, the M26x1 lefthand threads that connected the injection tool to the target cell released. The target was now threaded firmly in the PD, while the injection tool is released. As the tool was brought up to be removed, a heat gun was used directly on the double sliding seal to prevent the o-rings from freezing to the cold injection tool as it moved upwards. Once the tool was all the way up, the gate valve to the target sample space was closed, isolating the target within the PD. Once the injection tool was removed from the PD, the ice making manifold and required pumps can also be removed. With the removal of the last tools, the HD crystal forming process was complete.

2.5.4 Transfer Cryostat

The transfer cryostat played a critical role in transporting the HD target during production. Targets must be condensed in the PD, but the PD's superconducting solenoid maximum field was only 2 tesla. For this reason, the targets needed to be transferred to the DF and stored in a 15 tesla field. Polarized, fully aged targets were then required to move back to the PD for NMR measurements to determine the target's starting polarization before being transferred to IBC for experimental usage. After the experiment, the target was transferred back to the PD to evaporate the HD ice and recollect the gas. The TC was the piece of equipment that provided the target with its mobility [14].

In order to transfer a target, the TC needed to be able to extend a left-handed screw thread into a cryostat and thread into the inner threads of the target for removal or installation. More so, the TC needed to cool these screw threads down to 2 K to match the target temperature before making contact with the target. Matching the temperatures prevented melting of the target, lose of polarization, and cross threading. In order to further maintain target polarization, the TC had an internal rare-earth magnet that provided a constant, uniform magnetic field for the target.

In order to understand how the TC accomplished it's tasks, an overview of the cryostat's systems is necessary. The transfer cryostat was a series of concentric cylindrical volumes sheathing one another similar to the other cryostats used during target production. The center most

Transfer Cryostat Piping and Valves

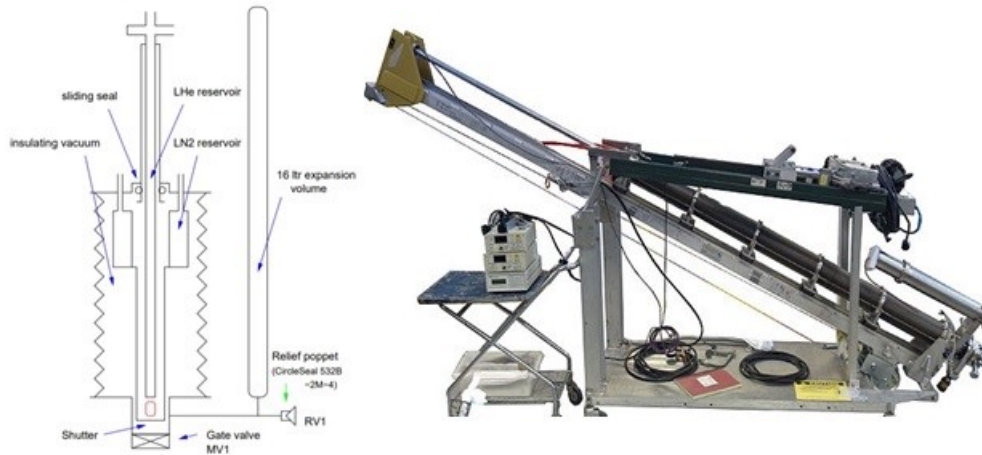


Figure 2.9: The image on the right is of the transfer cryostat - a cryostat used to move targets with a temperature of 2 K and a magnetic field of 0.12 T. The image to the left is a diagram showing the internal components of the TC [15].

volume was the liquid helium (LHe) reservoir. This space provided a target with cooling down to 4K. Like the other cryostats, a vacuum space surrounded the outside of the LHe reservoir. The reservoir was directly filled via transfer line connecting the TC's LHe fill port. Both temperature and liquid level sensors were located within the reservoir to track when a refill was necessary. The temperature sensors were also monitored to ensure the target temperature didn't rise high enough for the target to melt.

Outside of the vacuum space surrounding the LHe reservoir, was a second cryogen reservoir. This reservoir differed in that it was toroidal in shape instead of being a cylinder and that was filled with liquid nitrogen. As with the other cryostats, the liquid nitrogen reservoir acted as an 80K thermal shield. Unlike the other cryostats, attached at the bottom of this shield was a permanent magnet array set in an Holbach configuration. The array provided a transverse 0.12 Tesla holding field for a polarized target while held in the TC. Underneath the magnet array was a spring-loaded, multiple leaf shutter that closed to isolate the target from room temperature radiation once a target was inside the TC. When the top of the bellows of the TC was lowered down on top of another cryostat, the lowered portion of the LN2 reservoir and shutter extruded downwards through the bellows to the cryostat's gate valve.

Surrounding both liquid cryogen reservoirs and target was a space known as the insulating vacuum. It protected both reservoirs and the target from room temperature. While the other cryostats had insulating vacuums, the TC's was unique in that it's insulating vacuum outer wall

consisted of highly compressible bellows. The bellows allowed the TC to compressed downwards so that the inside LHe tube, which acts as the screw driver shaft, could insert into the attached cryostat. A sliding seal was located on top of the bellows. As the bellows compressed and relaxed, the seal could be moved accordingly. The compressible bellows and sliding seal were required to allow vertical movement and rotation of the target for installation and removal. Once the TC was mounted to the target space gate valve of any cryostat, the bellows were compressed to allow for the downward vertical movement of a target along with the liquid cryogen reservoirs.

Besides the cryostat portion, the TC had an externally attached support frame consisting of an aluminum backbone and a winch. The full weight of the TC as well as it's moving parts were supported and guided by the aluminum backbone, which spanned nearly the entire length of the cryostat. A linear track was attached to the top of the backbone. There were four small carts that rode along the track in order to guide and support the bellows motion. A winch located at the bottom of the backbone was used to control the vertical movement of the LHe tube. In addition to controlling movement, the winch cables also helped maintain the vacuum force on the inside of the bellows.

There were two additional custom built pieces of equipment necessary to assist in both storing and safely moving the transfer cryostat. When a target is being moved from the HDice lab to UITF or when the TC is not in use, the TC rested in an aluminum cradle on a large cart. The cart also held the target cell temperature and liquid helium level electronic readouts. The second piece of equipment was a lifting arm used with a crane to position the TC above another cryostat for connection. The lifting arm contained a motorized counter weight system that allowed the cryostat to be held at any angle between 0° and 90° to horizontal. The advantage to having this range of motion was that it allowed for a gentle placement of the TC on top of the production cryostat, dilution refrigerator, and in-beam cryostat.

2.5.5 Dilution Refrigerator

The Dilution Refrigerator was vital in polarizing the HDice crystal after being condensed in and transferred from the PD by the TC. It was capable of storing up to 3 frozen HD targets (although only two were made) at a temperature around 10mK with a magnetic holding field of 15 tesla. These were the conditions required to store and age an HD ice target until it reached its maximum polarization. The main refrigerator unit was a Kelvinox Model 1000 from Oxford

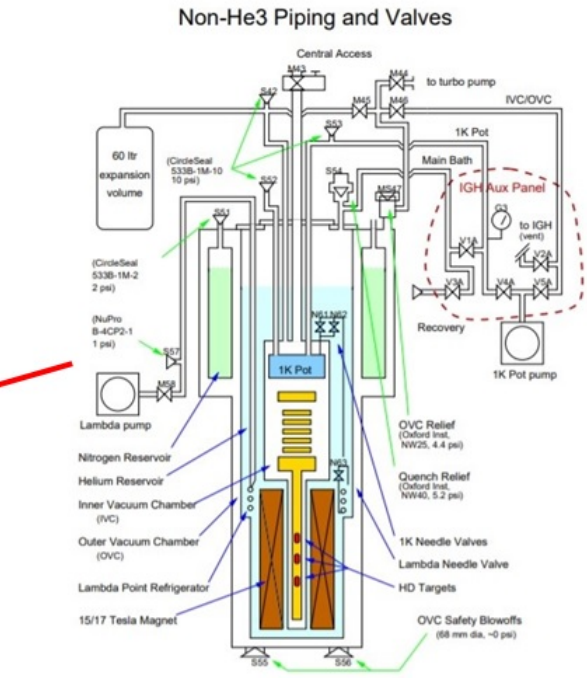


Figure 2.10: The dilution refrigerator. The left side shows the top of the DF with the TC mounted on top. Most of the DF was located in the pit below aluminum safety plate. On the right is a schematic of the DF's components in the pit [16].

Instruments. It contained a custom-built superconducting magnet system capable of providing a maximum field of 17 Tesla.

The DF required axillary equipment to operate the main dilution refrigeration unit. To provide the cooling power to cool a target down to 10 mK, many pumps were needed along with a mixture of helium-3/helium-4 gas. The gas mixture was used in the DF still for cooling below 1.2 K. It circulated throughout the system via the use of the pumps, which were physically located on a large stand in the room behind the DF. The pumps' lines ran to the Intelligent Gas Handling system (IGH) through an access port in the wall behind the DF. The IGH was the system that regulated the flow rates of gas mixtures and pump rates for vacuum spaces. This system and controls were contained in a large rack located to the left of the DF. On the same rack were additional controls for the lambda refrigerator, used in cooling the DF's main superconducting solenoid. Additionally located on the rack was an Intelligent Power Supply (IPS) to power the system. The IGH was connected directly to a PC located on the right side of the DF. This allowed remote access and monitoring of the IGH system through a LabView VI.

The cryostat contained two insulating vacuum spaces, a LHe reservoir, and LN reservoir arranged similarly to those in the previously discussed cryostats. Contained within the LHe reservoir was the lambda point refrigerator necessary for lowering the target temperature below the of liquid helium. It consisted of a spiral coil of tubing in which liquid helium was fed through into the LHe reservoir. The coil was attached to a pump that pumped on the liquid helium to create the evaporative cooling necessary to lower the main solenoid temperature to 2.2 K. Controls for the lambda refrigerator rotary pump were accessed manually on the front panel of the IGH as well as remotely on the PC connected to the IGH.

The DF's superconducting magnet was located in the LHe reservoir, where it was mounted to the bottom of this volume while submerged in the provided liquid helium. The magnet was a solenoid made of niobium-titanium (Nb-Ti) and niobium-tin (Nb-Sn) alloys. To produce the desired field of 15 Tesla at 4.2K, the solenoid current was set to 94.51 amps. The energy stored in the solenoid was more than enough to rapidly boil off the entire supply of liquid helium within the reservoir. Great care was taken to ensure there was always enough helium to keep the solenoid submerged to prevent a magnet quench.

The dilution refrigerator contained a secondary superconducting magnet known as the transfer solenoid. This solenoid's task was to provide a holding field to maintain target polarization as a target is transferred to/from the TC. As mentioned earlier, a polarized target must always be subject to a magnetic field in order to maintain its polarization. Although the main solenoid had a fringe field that extended outwards, it alone couldn't provide a field strong enough to maintain polarization as the target moved outside the main solenoid region. The transfer solenoid provided the additional field strength needed in the region between the main superconducting solenoid and Halbach magnet inside the TC.

The dilution unit consisted of several components that worked together to lower the target temperature in stages. Liquid helium supplied from the LHe reservoir to the dilution unit provided the initial cooling of 4.2 K. From here the liquid helium was fed into a copper canister, known as the 1K Pot, and pumped on with a rotary pump attached via the IGH. The temperature produced by pumping on the canister was approximately 1.2 K, hence the name 1K Pot. The remaining components that make up the dilution unit were mounted below the 1K Pot and were part of recirculating He3/He4 system used for cooling below 1.2 K. This system composed of the mixing chamber, the still, and the various heat exchangers used to connect the two together.

After the 1K pot, the mixture enters a spiral heat exchanger where the temperature drops to about 160 mK. Next, it then enters the mixing chamber. The two helium isotopes split into two phases, a dilute and a concentrated phase. The dilute phase occurs in the mixing chamber where the ^3He (a Fermi fluid) bubbles through the ^4He , which removes heat from the ^4He Boson superconducting liquid. This is where the temperature drops to ~ 10 mK. The ^3He exits the Mixing Chamber and collects in the Still during the concentrated phase, at about 600 mK. The DF's coldfinger was directly connected to the Still allowing for direct cooling. The DF's coldfinger differed from the others mentioned in that it had the capability to store up to three targets at once. Here the targets required to be stored a minimum of 3 months to polarize. The targets used in the eHD experiment ended up aging for over a year due to delays in the experimental run schedule.

Chapter 3

Depolarization Mechanisms and Mitigating Measures

As mentioned in Section 2.2, the opportunity to use electron beams with the g14 HDice target provided valuable insight for future target design. Three potential depolarization mechanisms were identified during the g14 electron tests. Although identified, how much each mechanism contributed to the depolarization of the target was unclear. It became necessary to mitigate each as much as possible to develop a target that could be used for future electron beam experiments. The depolarization mechanisms addressed were electron beam heating, Hyperfine mixing of spin states, and chemical reactions within the HD.

3.1 Electron Beam Heating Depolarization

Electron beam heating results in HD target depolarization due to the HD temperature and the electron polarization of the target material. The electron beam passing through the target could increase the HD temperature, creating unpaired electrons. If these electrons are only partially polarized, their spins can flip between their magnetic substates. When this occurs, a changing magnetic field is generated. This field could have Fourier components at Hydrogen and Deuterium's Larmor frequencies resulting in the loss of their polarizations. The depolarization can begin in a particular region of the target and then spread throughout the target.

During g14 electron beam runs, the target holding fields were 0.9 and 0.3 Tesla with the HD temperatures reaching as around 1.4K. These fields and HD temperatures resulted in an electron polarization of HD sample being between 20% and 50%. This electron polarization

resulted in the target's T_1 being on the order of ~ 4 hours.

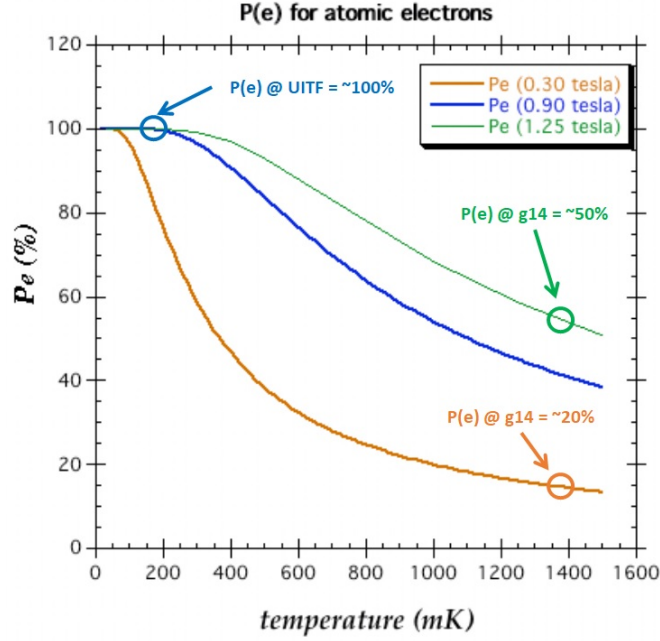


Figure 3.1: The polarization of atomic electrons dropped significantly during g14 due to the increased HD temperatures.

3.2 HD Temperature Control Improvements

The beam heating issues were mitigated during the eHD experiment through improved target temperature controls. The first of these controls was the improved target design. During g14, the target cell was optimized for heat removal with photon beams. The new design involved changing the dimensions of the HD ice crystal to allow for more uniform temperature control across a target the eHD cell contains about 40% as much HD as in g14. During g14, the cylindrical crystal dimensions were length of 50mm and diameter of 15mm. For the eHD target, the crystal dimensions were 12.5mm for length and 19mm for diameter. Complete details on the new target cell design are found in Section 2.3.

The eHD target's larger surface area allowed for more aluminum wires, used to remove heat from the HD ice, to be inserted into the target. During g14, the target cells contained 720 aluminum wires soldered into the target ring. This number was increased to 960 for the eHD target. Besides increasing the number of wires to improve the heat removal capacity, the purity of the aluminum use was improved from a rating of 4N9 to 5N9 (99.99% to 99.999% purity). Improving the purity increased the thermal conductivity by an order of magnitude as seen in

Figure 3.2. This improvement was measured at Jefferson Lab by Dr. Xiangdong Wei and Dr. Andrew Sandorfi.

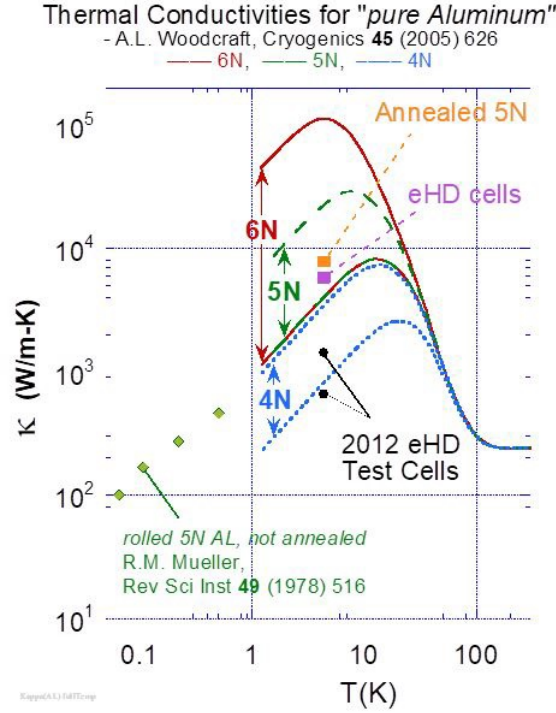


Figure 3.2: Differences in thermal conductivity between the aluminum wire purities used in g14 and eHD.

Besides improvements to the HD target design, an improvement to the raster used during beam operations also contributed to better HD temperature control. The raster used during g14 experiment was replaced with a faster, spiral raster. This improved raster had a frequency modulation of ~ 14 KHz and an amplitude modulation that created the spiral pattern of ~ 1 KHz. The currents driving the raster magnets, as sampled by Pearson probes, are shown in the following Figure 3.3. The beam width fills in the gaps in the spiral.

It was responsible for distributing the electron beam evenly across the surface area of the target. By sweeping the beam quickly and evenly across the target, the raster prevented the beam from resting too long on any one region of the target. This mitigated the problem of a particular area heating up, depolarizing, and then depolarizing the neighboring regions.

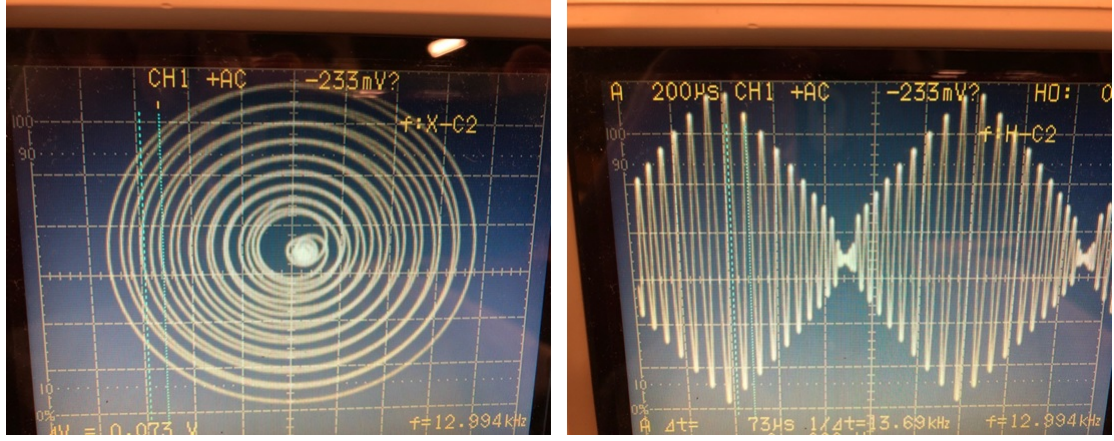


Figure 3.3: Raster magnet driving currents as sampled by Pearson probes.

3.3 Hyperfine Mixing

The second mechanism for depolarization is from hyperfine mixing. As mentioned in the previous section, the ionization that accompanies beam heating can result in unpaired electrons, which can cause target depolarization through the mixing of hyperfine spin states. The magnetic moment of these electrons is anti-parallel to the direction of the IBC holding field. The magnetic moments of the hydrogen and deuterium are parallel to the same holding field. The total angular momentum of the H (or D) atom is the sum of the nuclear and the electron spin. Since the two are opposite, there are two ways of combining the spin projections to get the same absolute value. Since total angular momentum is conserved, the wave-function becomes a mix of two states with the same total angular momentum but opposite nuclear spin. Thus, the polarization becomes diluted.

3.4 Hyperfine Mixing Prevention

Hyperfine mixing can be prevented by orienting the spin of the target nuclei to be in parallel with that of the spin of the electrons. Doing so creates a unique state in which hyperfine mixing cannot occur within the sample. After the target is initially polarized, the spin of the hydrogen and deuterium nuclei orient to be parallel to the magnetic holding field. By flipping the spins of the hydrogen and deuterium nuclei to be anti-parallel, the unique state that prevents hyperfine mixing is achieved. The NMR procedure for flipping or reorienting the spins is known as Adiabatic Fast Passage and is described further in Section 5.3.

3.5 HD Material Chemical Reactions

A third polarization mechanism arises from chemical reactions within the HD sample of the target. During beam periods, the chemical composition of the HD can change due to beam interactions ionizing the HD molecules. This ionization leads to highly mobile HD^+ molecules. The following chemical reactions can occur:



When H_2 molecules form, ortho- H_2 also occurs and reduces the T_1 of the target. This in turn can negatively affect the target polarization during experimental runs. Further impacting the target polarization is the heat generated from the exothermic reactions between the chemical compounds in the target once the beam has stopped. These reactions can cause significant spikes in the HD sample temperature. Thus as the HD^+ molecules react to neighboring molecules, the target polarization is diluted.

3.6 Minimizing Chemical Reactions within HD

The elevated HD temperatures during the g14 electron beam runs resulted in chemical reactions that could occur within the HD. These reactions created ions that acted as paramagnetic centers that could then interact with surrounding HD material to depolarize it. To reduce the occurrence of these reactions as much as possible, all (or as much as possible) of the molecular electrons needed to be as polarized. Like the other depolarization mechanisms, the chemical reactions are related to the HD temperature. As seen in Figure 3.1, the total electron polarizations during g14 were only 20% and 50%.

Since the electron polarization was tied to the HD temperature, the changes made to the target cell design as well as the new raster accomplished this goal. By keeping the HD temperature to under 250mK during beam operations, approximately all the electrons remained polarized. The production of ortho- H_2 could still occur as a depolarization mechanism, but according to the previous work of Mano and Honig [11], the affect on the rest of the polarized HD was minor. Thus, the focus was on keeping the electrons polarized as much as possible.

Chapter 4

Experimental Setup at UITF

4.1 UITF Layout

UITF is located in the High Bay Area of the Test Lab. Figure 4.1 shows the layout of the facility during the eHD experiment. Prior to the upgrades required for running with eHD targets, it was called the Injector Test Facility. It was capable of delivering 200 keV beams in what later became known as Cave 1. The upgrade added an accelerator cavity and the area known as Cave 2.

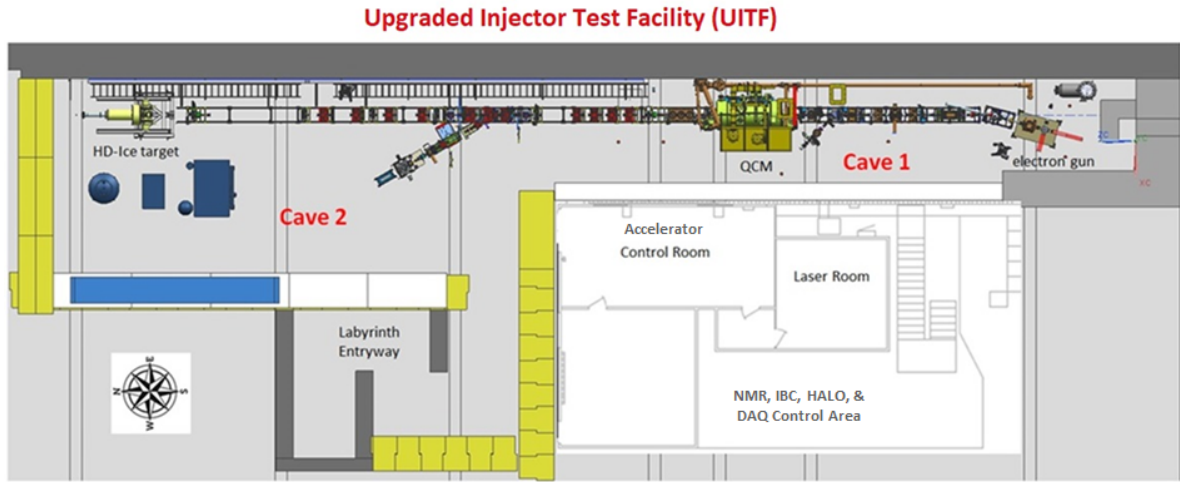


Figure 4.1: Layout of the Upgraded Injector Test Facility at Jefferson Lab.

Cave 1 is where the keV region of the accelerator is located. This is also where the electron gun generates the beam. Once formed the beam accelerates up to 250 keV as it approaches Cave 2. A dedicated beam dump for the keV energy beam is located right before the Quarter Cryo Module (QCM). When not being sent to the beam dump, the electron beam can be sent

through the QCM to accelerate up to 10 MeV. The beam then continues into Cave 2 where related instrumentation, additional beam dumps, and the HDice target are located.

4.1.1 Cave 1: The KeV Region

Located within Cave 1 was the electron gun, the quarter cryomodule (QCM), and the kilo electron volts beam energy region of the accelerator. Cave 1 by itself could function as a gun test stand. However, when beam was sent to Cave 2, it was accelerated to an energy that exceeds the potential energy applied to the gun. When this occurred the UITF was considered a fully operational accelerator.

The electron beam was first generated from the first component in the beam line, the electron gun. To produce the beam, the gun used a laser set to pulse at 750MHz with a gallium arsenide puck. As the laser struck the disk, an electron beam was produced by the stimulated emissions of electrons. The gallium arsenide puck was coated with a thin layer of cesium to lower the potential barrier above the conduction band. To polarize the electrons in the conduction band,

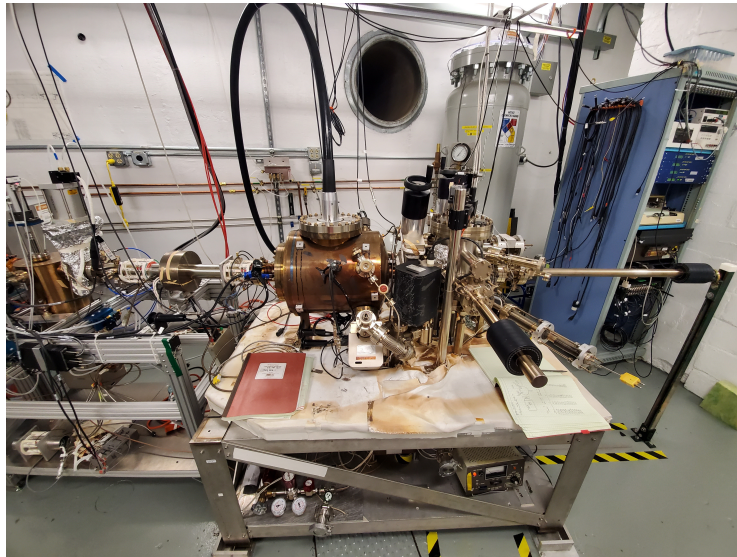


Figure 4.2: The electron gun's primary light source for operation is a 780nm laser delivered via fiber optic cable from a fiber laser amplifier. Electron beams were directed to the QCM after exiting the electron gun.

polarized light of a particular frequency was shined on the puck causing the electrons to emit in clusters. These clusters of electrons were then directed along the beam line through the use of dipole steering magnets and quadrupole magnets for focusing the beam (controlled by the beam operator in the Control Room). Between the electron gun and QCM, the electron beam energy

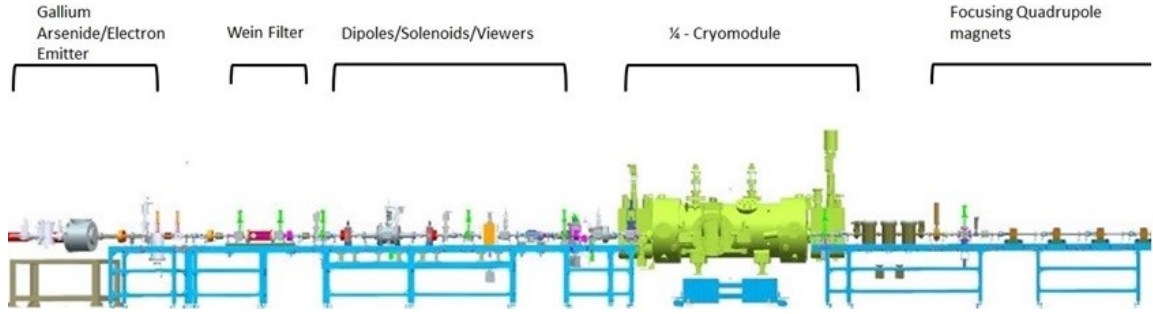


Figure 4.3: UITF Beamline components in the KeV Region (Cave 1).

was initially 250keV. Several beam position monitors (BPMs) and viewers were used to track the beam as it moved downstream from the gun. Standard YAG (yttrium aluminium garnet) crystal screens were used as beam position monitors along the beamline in Cave 1. YAG screens provided good spatial resolution, which made them useful for beam profile measurements. The screens were moved into the path of the beam via pneumatic arms controlled by a PC in the UITF Control Room.

The BPMs allowed for the aligning of the beam throughout Cave 1. Faraday cups installed along various locations of the beam line could be placed to block the beam from going further downstream during beam alignment. When the aligned beam passed through the QCM, the electron energy increased from 250KeV to 9.7MeV. As the electrons passed through the QCM, the oscillating electric fields within accelerated the electrons increasing the beam energy. This works the same way as the other linear accelerators work, located at Jefferson Lab. After passing through the QCM, the 9.7MeV beam continued to be directed and focused down stream to Cave 2. Like before the QCM, the beam was controlled through the use of more dipole and quadrupole magnets.

4.1.2 Cave 2: The MeV Region

Upon exiting Cave 1, the electron beam was either deflected into a dump by a dipole magnet to measure energy, or sent to the IBC to run beam on target. Due to the size requirements of the IBC, the beam line was required to be elevated as it entered Cave 2. The elevation of the beam to the IBC was accomplished through the use of a vertical chicane.

Like the Cave 1 region of UITF, Cave 2 had a series of dipole and quadrupole magnets to manipulate the beam. These were necessary before and after the vertical chicane. After the beam is directed past the vertical chicane, it passes through the raster. The raster was

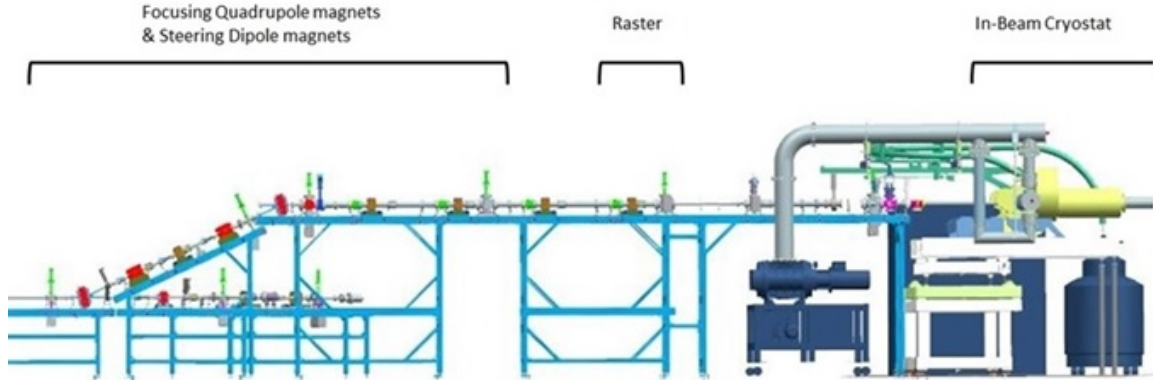


Figure 4.4: Beamline components in the MeV Region of the accelerator (Cave 2).

responsible for spreading the beam out into a spiral pattern, which was to be swept across the upstream face of the target. To do this, the raster consisted of two coils that each generated oscillating magnetic fields. One coil was responsible for vertical moment while the other was took care of the horizontal. Combining the use of both coils created a spiral pattern to reduce localized heating.

After passing through the raster, the beam traveled towards the IBC. Right before the IBC was another Faraday cup. It was inserted when tuning the focus, position, or Raster at a higher current. Inserting the cup prevented any beam from accidentally hitting the copper target ring when tuning. Hitting the ring was very undesirable as the beam would rapidly heat up the copper. This heat could then be transferred into the target via the aluminum wires resulting in the target warming up.

The primary function of the In-Beam Cryostat was to hold an HD ice target during beam operations while maintaining the target's polarization [17]. To achieve this, the IBC was capable maintaining a target temperature between 50mK and 1.5K with a magnetic holding field of 1.1 Tesla. An equally crucial requirement was that the IBC must be able to move from a vertical target loading orientation to a horizontal beam running position and vice versa. To do this, the IBC had to be positioned higher than the beam line in Cave 1. Thus the need for a vertical chicane.

The IBC design was similar to the DF for maintaining targets, but with two major difference. The first involved the IBC's ability to change orientations for loading. The second being that the IBC relied on just liquid helium as a cryogen to provide its cooling power. There is no nitrogen bath to cool system components or act as a thermal shield. Instead, cold He gas at about 80 K is used to cool a separate thermal shield that surrounds the magnet and dilution

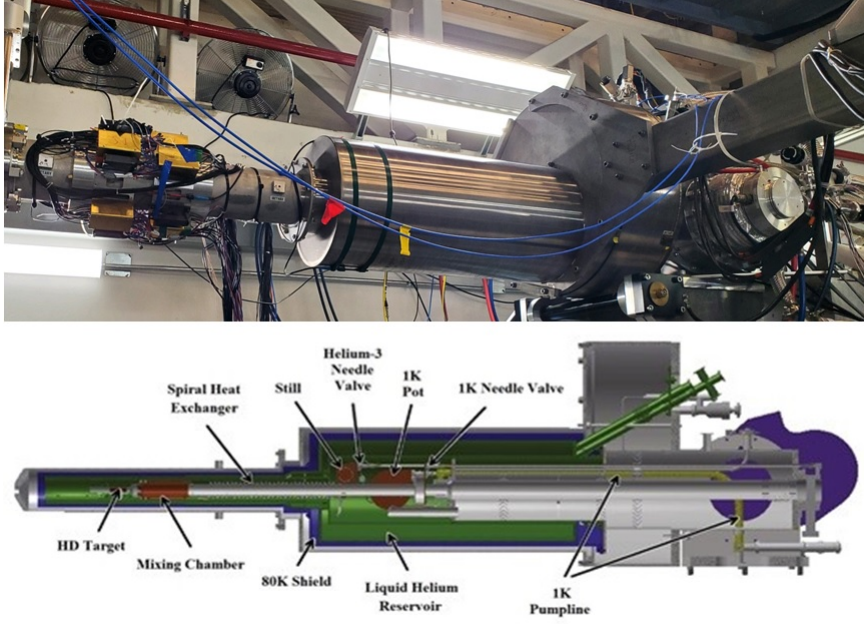


Figure 4.5: The IBC, a cryostat used to hold and use targets in beam experiments. The image on top shows the IBC installed in the UTF beamline. The image below is a diagram showing the main internal components [18].

unit.

Surrounding the target region was the main superconducting solenoid, which was submersed in the surrounding liquid helium bath. This main solenoid provided a constant magnetic holding field up to 1.1 Tesla. The field was required to maintain a target's polarization. A superconducting solenoid located in the helium bath was used during target transfers to provide a holding field for the region between the IBC main solenoid and the TC's Holbach magnet.

Located further within the IBC was a 1K pot, still, and mixing chamber used with a series of pumps. A He^3/He^4 mixture was circulated through those inner parts by the pumps to provide cooling for HDice target. This cooling is accomplished same way as in the DF and is described Section 2.5.5. Like the DF, the IBC coldfinger allowed a secure location for a target cell to be placed into the cryostat and be cooled down to the required temperatures. It was made from 99.999% copper tube with a M35x1, right-handed threaded section where the target cell is screwed into just like the DF. As the cooling system reduced the coldfinger temperature, the attached cell would cool through direct thermal contact.

As the beam traveled through the IBC, it interacted with the target inside. The interactions resulted in electrons scattering off the target and out of the IBC. These scattered electrons were detected by a system of scinillators that made up the HALO detector. This detector acted as a

BPM at the position of the target and will be discussed further in Section 4.2. The number of detected particles indicated whether the beam was in the center of the target. To further help focus the beam so that it went through the center of the target, holding fields were included around the target as seen in Figure 4.6.

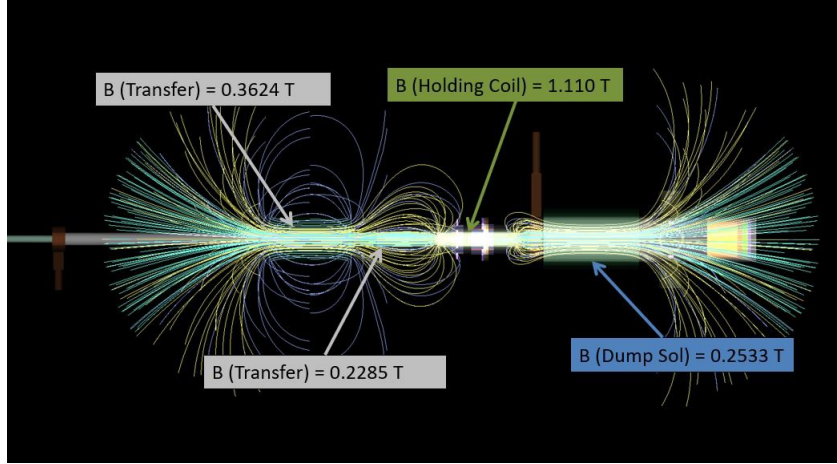


Figure 4.6: As electrons pass through the in-beam cryostat the fields shown in the above figure are used to control the distribution of electrons.

The holding field around the target was a combination of fields of three magnetics known as the transfer solenoid, main solenoid, and dump solenoid. Due to the beam energy being on the order of 10MeV at UITF instead of 10GeV like in Hall B, the magnets were able to control the spread of incoming and outgoing electrons. In Hall B, the beam energy is high enough for the electrons to travel along the beam path with significantly less scattering of the electrons along the way.

The spreading of the target at UITF at around 10MeV was countered through refocusing of the beam on the target face by using the magnetic fields. The fields were set to focus the electron beam at a node that was located on the upstream face of the target as seen in Figure 4.7. The outgoing electrons were also focused, but not for the same reason. Eventually the beam would terminate in the beam dump located at the end of the beam line. By focusing the exiting electrons back along the beam line, most end up safely in the beam dump instead of scattering out into the UITF.

Located at the end of the beamline was the beam dump, where the scattered beam was redirected back along the beam axis after the beam scattered off the target in the IBC. It consisted of a large magnet solenoid with an operational current of 318 Amps generating a central holding field of 0.250 Tesla with a maximum operational limit of 350 Amps and field

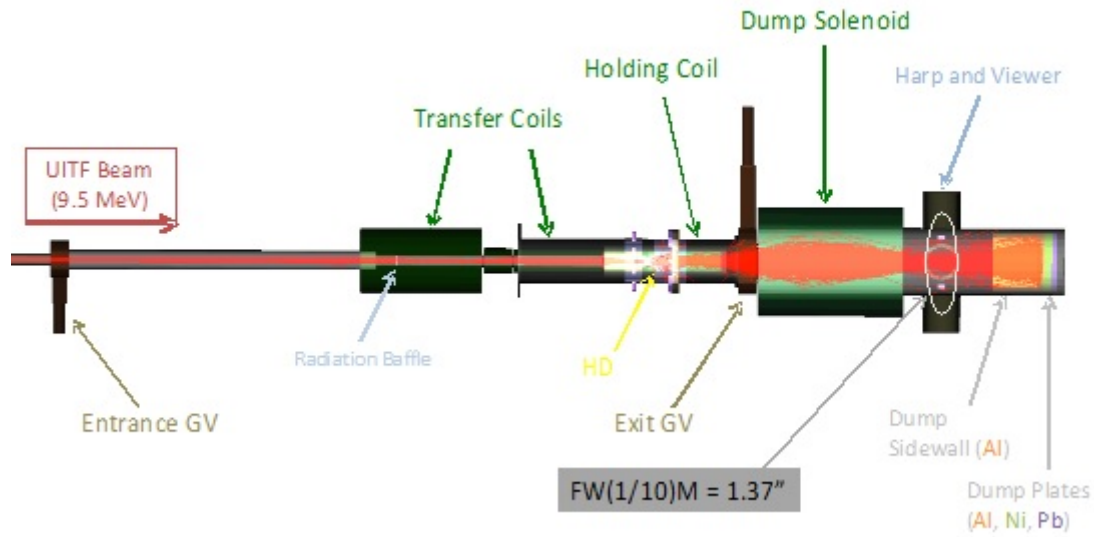


Figure 4.7: As electrons (in red) pass through the in-beam cryostat from left to right in the figure there is significant spreading and scattering.

of 0.275 Tesla. This magnet was wound using a square copper conductor that has a central water-cooling hole. The conductor was made up of four 2-layer coils that were connected in series and weighed approximately 400 pounds. The solenoid was fixed on top of a stand so that the beam line passed through its center. The magnet was operated remotely from a PC in the Data Acquisition (DAQ) Area set up in the Test Lab.

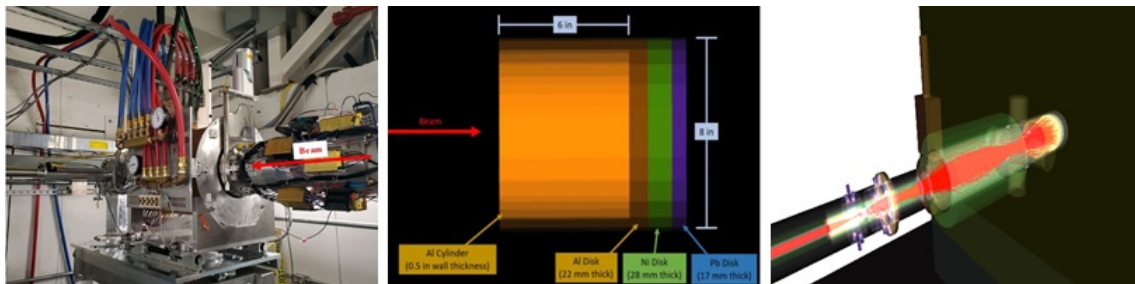


Figure 4.8: UITF Beam Dump at the end of the accelerator. The left panel shows the dump connected to the IBC with a gate valve, the middle panel is a schematic of the dump solenoid, and the left panel is a simulation of how the electrons are affected by the fields when passing through the dump.

Included in the beam dump was a camera and YAG viewer installed to view and determine the distribution of the electron beam at the end of the beamline. Prior to experimental Run 1, YAG viewers were used successfully to view the beam position along the KeV region of

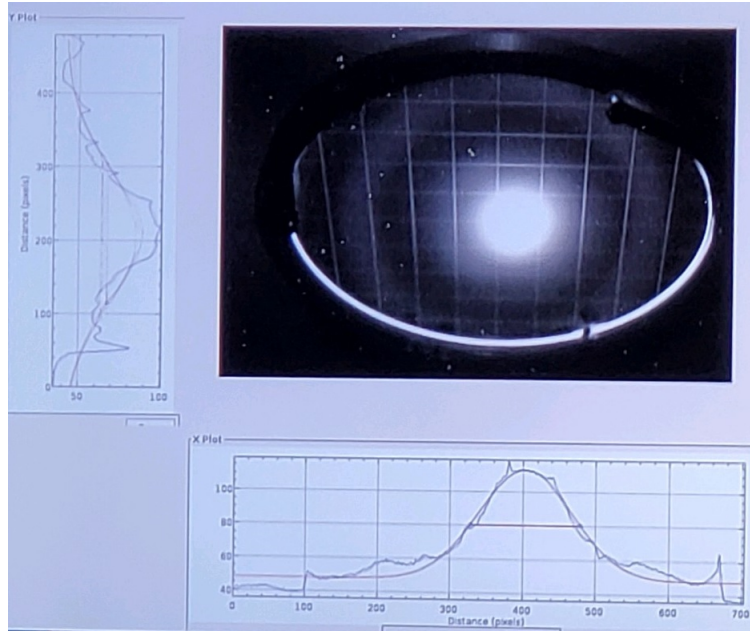


Figure 4.9: First time a MeV beam was seen on the YAG viewer located at the beam dump. The image of the YAG screen with beam on it was obtained with an in-beam camera.

the accelerator. In this region the YAGs were 29mm outer diameter by 0.25mm thick. These stopped the keV beam producing significant amounts of light. An attempt to use these types of BPMs for the MeV region had never been tested prior to the eHD experiment. Two custom built YAG viewers were specifically constructed and used as BPMs at the beam dump. At 10 MeV, the electrons would lose very little energy in a 0.25mm thick YAG. The Dump YAGs had a 100mm outer diameter to accommodate the rastered beam and a thickness of 2.0mm to guarantee sufficient light to make low currents visible. A video camera set above the beam and perpendicular to the viewing arm, could observe the scintillation light from one of these screens. Only one screen could be inserted into the beam at a time. Both screens had distance markings etched onto the crystal to provide a method for determining how far off axis the beam might have drifted. The live video feed of the beam positioned on the grid allowed for the beam steering magnet corrections to be seen instantly and ensured users could quickly steer the beam back to normal operating parameters. Additionally, a pico-ammeter was installed on the beam dump, below the viewer location to monitor the current received at this location.

4.2 DAQ Area

The Data Acquisition Area was located outside the Caves of the UITF. Originally, the DAQ area was to be incorporated into the Control Room. Since the eHD experiment took place during the Covid-19 pandemic, Jefferson Lab instituted several health and safety policies including strict social distancing of at least 6 feet. As a result, there wasn't enough room for more than two operators to be in the Control Room at once. However, approximately eight operators were required to run all the systems during beam on operations. An area of the Test Lab was then sectioned off and designated as the DAQ Area, which acted as an auxiliary control room. Here was where the controls for the raster, NMR system, IBC, and Halo detector were located. Each set of controls were on its own designated PC in the DAQ area.

The NMR and IBC controls consisted of custom LabView programs. Ethernet cables connecting the systems in Cave 2 to the remote PCs in the DAQ Area allowed the controls to be mirrored and accessed safely outside the UITF. Occasionally the remote access to the systems would be broken during beam operations, requiring a stoppage in beam for access to reboot the local PCs connected to the NMR and IBC systems in Cave 2. NMR scans were able to then be taken while beam was going through the target rather than stopping the beam to make the measurements. The flow rates and thus internal IBC temperatures were regulated through the use of the IBC LabView program. In addition to this, the program allowed monitoring of the HD target temperature through measuring the mixing chamber temperature in the IBC.

As mentioned earlier, the beam scattering effect was mitigated by tuning the beam energy to approximately 9.5 MeV. Doing so fixed the electron beam behavior to a node at a single point on the face of the target cell. The result was that the electrons scattered off the HD crystal when the beam first made contact. The Halo detector system was a beam position monitoring system set up on the outside of the IBC around the region where a target rests during beam runs. The controls for operating the Halo system were located on a Halo only designated PC in the DAQ Area.

The system consisted of 32 scintillators with each scintillator coupled to a Silicon Photo Multiplier (SiPM) and its own Printed Circuit Board (PCB) amplifier. Each amplifier had one input connected to a SiPM along with a digital and analog output. RG-174 cables connected the analog output to the Fast Analog to Digital Converter (FADC) box for data acquisition. Using the same type of cables, the digital outputs were connected to a Field-Programmable Gate

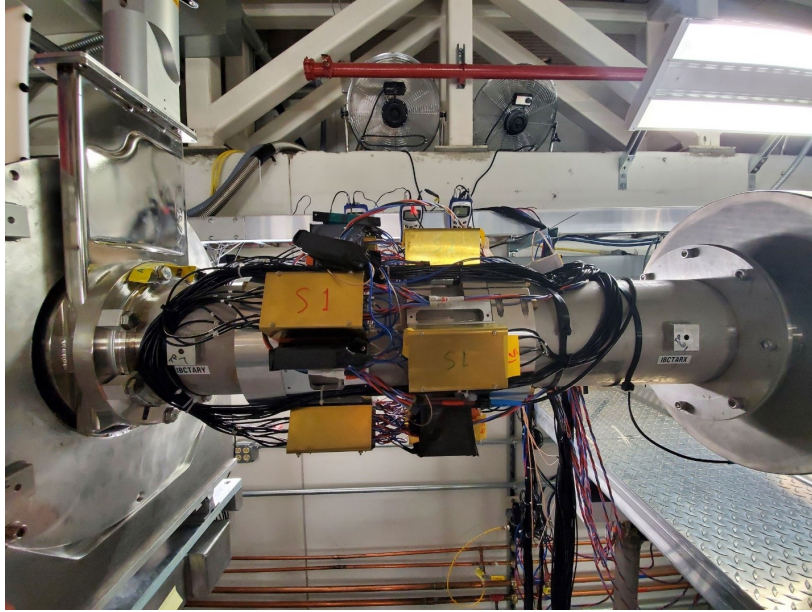


Figure 4.10: The electronic system of the Halo detector is made up of a FPGA box connected to 32 identical SiPMs, each connected to its own independent channel amplifier. Four step-up power supplies are each connected to eight SiPMs/amplifier pairings to supply the proper voltage bias for the SiPMs to operate. Additionally, a raspberry pi computer is connected to the FPGA to read and manage the digitized rates.

Array (FPGA) box. Here the FPGA kept count of coincidence and anticoincidence signals every second and determined the rate of those signals.

The Halo system was controlled through a program known as halo-gtk, developed by Luca Barion. The program to control the detector ran off a designated Halo PC out in the DAQ area. It was used to view the data being collected live as well as record the data to text file for later analysis. The most important feature of the program was that it can determine the current position of the beam relative to the center axis of the beam line pipe as it passed through the target. It determined this position in real time and provided a visual representation in the graphical user interface.

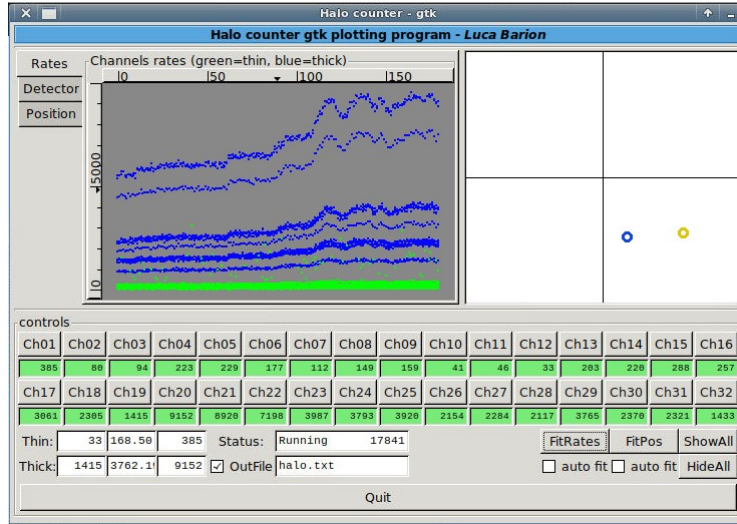


Figure 4.11: The halo-gtk in operation. The top right displays the beam location in real time when the accelerator is in operation. The top left has tabs which change the display on the left from displaying the channel rates over time, the rates per channel, or to the position of each event detected. The bottom displays individual channel rates of the detectors.

4.3 Target Loading and Unloading Procedure

The target loading procedure began by removing the ceiling tiles of Cave 2 by trained crane riggers. After the removal, the riggers moved HDice Work Platform into place. The platform spanned the length of Cave 2's roof. It provided users access to the lifting crane as well as the top of the IBC. After this occurred, the transfer cryostat was cooled down near the production dewar as it held the target to be used in the IBC. The TC was then attached to the PD and the target removal procedure described previously in Chapter 2 is performed. Once the target was secure in the TC, the TC was placed on a cart for transportation from the HDice Lab to the UITF.

The TC's liquid cryogen levels were checked continuously during the transfer from the HDice Lab to UITF. Cryogen refills were performed as necessary. To check the levels the instrumentation and electronic readouts accompanied the TC cart as it moved with the TC. Once in the Cave 2, the TC was positioned for lifting. The TC was attached to the North 25 Ton crane located in the Test Lab and lifted through the hole in the roof made by the tile removal. In order to successfully attach the TC to the IBC for target loading, gate valves were closed to separate the IBC from the beamline vacuum. After which the IBC could be detached from the beamline and oriented from a horizontal operating position to the vertical loading position.



Figure 4.12: Target loading at the UITF. The left shows the IBC as it was being rotated vertically for loading. The right shows the UITF ceiling tiles removed allowing the TC to be attached to the crane, lifted, and mounted to the vertical IBC.

Once the IBC was vertical, the TC was lowered down and mounted to the gate valve on the back of the IBC. To ensure the TC was in a vertical position for mounting, a retractable arm with counterweights on the TC frame was used to make adjustments via remote control. After the TC and IBC gate valves were connected, three stabilization chains were connected between the walls of Cave 2 and to the TC. The chains were used not just to secure the TC, but could be tightened to make small corrections to the vertical orientation of the TC when necessary.

After TC was attached to the IBC, the space between each of the cryostat's gate valves was pumped down to vacuum allowing the valves to be opened. The TC's helium tube was lowered down from within the TC to within the IBC. The target, which was threaded onto the helium tube and lowered with it, was threaded into the IBC coldfinger following the same procedure as used during transfers between the other cryostats. Once the target was threaded into the IBC and the helium tube threads was released, the tube was retracted and the gate valves closed. The space between the gate valves was then back filled with Nitrogen gas instead of atmosphere. At this point the chains were removed, the TC was disconnected from the IBC, and the TC was placed back on its transport cart by the crane to be wheeled back to the HDIce Lab. At

this point, the riggers were able to remove the access walkway above the IBC and reposition the roof shielding tiles back on Cave-2.

During target removal from the IBC, the procedure is the same, except in reverse order. Regardless of whether a target was being installed or removed, the process always ended with resetting the IBC to its horizontal operating position. The IBC was then rolled forward and reconnected to the beam line through the gate valve connections. The space between all these connections were pumped to vacuum before any gate valves were opened for beam operation. The TC was then relocated to the HD Ice Lab for storage.

4.4 Experimental Runs at UTF

The experimental run plan required to have the UTF commissioned by the end of September 2020. This meant the electron beam energy and position needed to be determined. Then from October 2020 to March 2021, four targets were used at UTF for the eHD experiment. While two of the targets were polarized target studies with electron beams, the other two targets were unpolarized and used for HD temperature studies. The dates of these run periods are found in Table 4.1.

Experimental Run	Start Date	End Date
Run 1	September 11, 2020	October 2, 2020
Run 2A	October 27, 2020	November 11, 2020
Run 3A	November 20, 2020	November 30, 2020
Run 3B	December 8, 2020	December 17, 2020
Run 2B	February 27, 2021	March 13, 2021

Table 4.1: The eHD Run Schedule.

Run 1 successfully achieved the goals of delivering a MeV beam through the entire beam line ending in the beam dump, verifying Cave 2 YAG viewers worked, calibrating the BPMs, and fine tuning beam on operating procedures. This was necessary for the subsequent electron beam runs to take place. The next run was Run 2A, which used an unpolarized HD target. As targets took a minimum of 3 months to reach a frozen spin state, Run 2A acted as a beam operating practice without the risk of wasting one of the two polarized targets. More importantly, Run 2A was used to study the response of HD to electron irradiation.

Run 3A took place following Run 2A and it used polarized target #60. The target was subjected to different beam conditions and holding fields with the target responses being measured through the use of NMR. Next followed Run 3B using target #66 and it had a couple differences. The average target holding field was lower. This will be explained further in Section 4.4.4. The other difference was that during 3B, it was possible to introduce a duty factor or modulation on the electron beam. Doing so allowed for possible time correlations between beam heating and the target's polarization to be studied.

After Run 3B was completed, it was decided to condense another unpolarized target to be used in an additional electron beam run. This run was called Run 2B as it was the second unpolarized target run. The goal of the run was to study the HD temperature within the target during the same beam conditions as in Run 3B. A detailed description of each run period is in the following sections.

4.4.1 Run 1: Aperture Target

The first experimental run was to calibrate the entire system so that electron-beam can be delivered through the in-beam cryostat in a reliable and consistent manner. This experimental run allowed the calibration of beam position monitors and the verification of the simulations completed for the experimental runs. Prior to Run 1, the accelerator group was able to produce 9.7MeV beam that exited the QCM and terminated in the waist high beam dump. This beam dump was located just before the vertical chicane and allowed refinements to be made prior to passing beam through the IBC.

At the start of Run 1, the beam leaving the QCM was directed up the vertical chicane to the IBC. Before the beam could enter the IBC, several beam line studies and calibrations were required. A Faraday cup, located right before the IBC, was placed into the beam line to block the beam from entering the IBC. This allowed for studies to be done with the viewers, BPMs, and beam current monitors. As mentioned earlier this chapter, the YAG viewers in the UITF had only been used with KeV beam energies, so it was necessary to observe their sensitivity with MeV energies of varying currents first. The studies began with a beam of 20nA current. Then the current was decreased in increments until reaching 0.25nA to ensure the equipment still functioned under "low" current conditions.

After confirming the YAG viewers worked, the raster could be tested. This was done by taking a beam concentrated along the beam axis and expanding the it out to form a circular

beam spot, which could be observed on the MeV region YAG viewers. After confirming the YAG viewers and raster worked together, a study to determine an Earth magnetic field correction to be applied to the beam was conducted. This allowed for additional magnetic coils to be added to the beam line and set to the correct field strengths to counteract the Earth's natural magnetic field's effect on low current electron beams.

After completing the studies and making the appropriate corrections to the beam line equipment, the beam could be studied going through the IBC. Steering magnets along with the viewers were used to center the beam before entering the IBC. During this time, the beam operator also ensured the beam energy was a stable 9.7MeV. Once a stable beam was centered, the accelerator operator would remove the cup and allow the beam to pass to the target.

The target loaded inside the IBC during Run 1 was the aperture target. Unlike the targets used for the remaining eHD experiment, the aperture target contained no HD crystal. This target did not require any aluminum wires for cooling since there was no HD present. The other key difference involved the replacement of the Kel-F shells. The inner shell was removed entirely, while the outer shell was replaced with a thin copper shell. The circular face of the copper shell had four arcing slots (apertures) at a radius of 7.75mm cut out along with a 2mm diameter hole in the center of the target as seen in Figure 4.13.



Figure 4.13: The aperture target used in Run 1.

These slots were used to determine the position of an unrastered beam on the target. The beam position was calibrated by passing the beam over the center hole of the aperture target and viewing the passing beam on the beam dump YAG viewer. After the beam was centered, it was steered away radially from the center towards the arc slots.

When the beam was not passing through one of the apertures, the electrons would scatter off

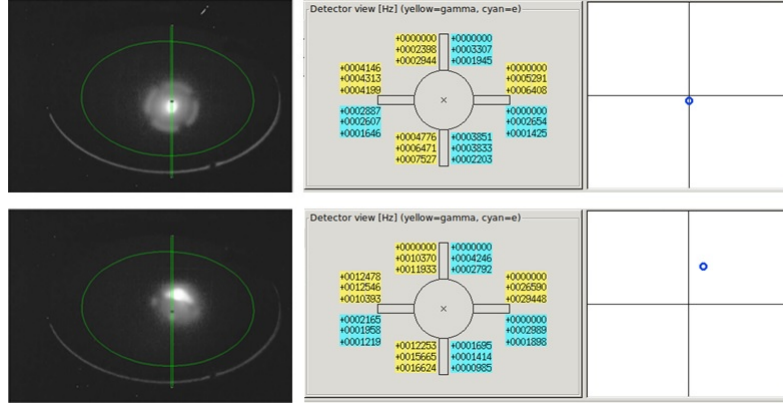


Figure 4.14: The HALO detector output was calibrated by putting the beam through the arcs of the aperture target using the halo-gtk during Run 1. The left panels show the beam position on the YAG viewers which were used to verify the position determined using the halo-gtk program, seen in the right panels.

the copper shell instead. The scattering sent electrons outward where they were detected by the scintillators of the Halo system. Figure 4.14 shows an example of the Halo calibration. When the beam passed through the slot, the rates would drop significantly and the beam would show up on the beam dump viewer. As the beam reached the edge of each open arc, the Halo rates should significantly increase. By performing this procedure for each open arc, the Halo counters were calibrated and the Halo asymmetries determined. These asymmetries and Halo rates were verified and compared to simulations allowing the beam position monitor built into the Halo system to be calibrated for the later runs. Doing so meant that if the beam drifted outside of the determined parameters, the Halo system would immediately shut down the beam. This prevented the beam from drifting and resting on the copper target ring. If this occurred, the copper ring would rapidly heat up resulting in the target heating and consequently depolarizing.

Next to be calibrated was the amplitude gain of the raster. The beam was frequency modulated by the raster to spread out as a circular pattern over the target face. Its dimensions and spiraling pattern distribution were controlled through the modulation of the beam current amplitude. Two raster components were responsible for the modulation. One component modulated the beam vertically, while the other did horizontally. The vertical and horizontal components being uncoupled created an elliptical pattern rather than a circular one when the raster was not calibrated.

To ensure a circular rastered beam pattern, the horizontal and vertical raster magnets were displaced and so required varying field strengths to create a circular beam spot on target. The

HARP was used to set the relative horizontal/vertical strengths. A circular pattern downstream on the target was created from the ratio of the vertical and horizontal amplitude modulations. A maximum radius for the circular beam pattern was then determined.

How fast the beam fell at the edge of the pattern was due to the beam dispersion. Beam operators set the raster size by looking at the image of the aperture target on the dump YAG viewer, and adjusted the raster currents to put the outer edges of the beam at the outer edges of the arcs. After establishing and recording the parameters for a rastered beam, preparations for HDice Run 2 could be made. The Cave 2 roof tiles were removed and the IBC disconnected from the beamline. This allowed for the aperture target to be removed from the IBC and an unpolarized HD target to be installed using the transfer procedure described in Section 4.3. After the install, the IBC was horizontally rotated and reconnected to the beam line.

4.4.2 Run 2A: Unpolarized Target

The second experimental run tested low current electron beams on an unpolarized HD target. The HD material did not go through the polarization and aging process. Instead the condensed target went directly from the PD to the IBC, skipping a stay in the DF. As a result the unpolarized target had a short T_1 . Additionally, the target polarization could grow up to 2% in the 1.1 T field holding field and 50 mK target temperature produced by the IBC.

This experimental run tested the new experimental system and allowed an analysis of the interaction between the electron beam and the HD material. Before loading the unpolarized target, the IBC refrigerator system's cooling power was measured so the energy deposition into the target could be determined. To make the measurements, a beam with previously determined parameters was established through the IBC and the flow of liquid helium through the mixing chamber was adjusted until a stable base temperature was established. The IBC mixing chamber had a heater attached directly to it that allowed additional heat to be applied to the chamber. Doing so allowed for simulated heating tests for beams of different currents to be compared to actual beam heating of those currents. The tests included the mixing chamber temperature (MC temperature) being recorded as heat was applied incrementally to the chamber. The simulated energy deposition of a 9.7MeV beam through the IBC was 0.74MeV, or 0.74mW/nA. This is to be compared with a projected energy loss of 0.70 MeV, predicted by the NIST ESTAR code for 10 MeV electrons passing through the target. A cooling curve for the IBC was determined and the energy deposition was verified.

After the cooling systems tests were performed, the IBC solenoids, dump solenoid, and Earth field correction coils were powered on. The Faraday cup before the IBC was placed into the beam line to prevent the beam from entering the IBC before the operator could align it. The beam was sent to the Faraday cup and the viewers were used to align the beam before entering the IBC. Afterwards, the Faraday cup was removed, the beam passed through the IBC, and terminated in the dump. The beam alignment through the IBC target region was monitored using the Halo system. A viewer in the beam dump allowed the beam alignment to be monitored at the point of beam termination.

In addition to allowing for beam alignment at the IBC entrance, the Faraday cup could be placed in the beam line to allow for the beam to be rastered and its quality checked. Afterwards, the rastered beam would be sent through the IBC and its distribution was monitored using the Halo detector. By completing this last step, all the parameters required to send the beam through the target and into the beam dump were set. Following the procedure in Section 4.3, the target was loaded and calibration of the NMR system took place.

The NMR system at UITF needed to be calibrated and tuned before attempting to study any signals taken. Calibration required using the FRS, described in Section 5.4.2. Tuning the NMR response involved performing FRS measurements with a fixed RF frequency while sweeping the magnetic holding field of the cryostat. Additional tuning of the NMR system was done through making changes to the cables connecting the NMR rack equipment to the transmitter and receiver coils of the IBC. Physical characteristics like cable capacitance, resistance, length, and temperature affected the NMR measurements. Three sets of cables were prepared prior to target installation.

Combinations of cables with fast response scans, followed by NMR measurements were made in order to determine the best to optimize the NMR measurements. Optimizing the measurements meant tuning the system to maximize the signal-to-noise ratio, while minimizing any background signals and determining the minimal RF power for scanning. Once all the parameters were determined, a NMR measurement was taken to verify the calibration.

The NMR measurement required an average of a large number of sweeps taken to produce a NMR signal with a good signal-to noise ratio for the target hydrogen nuclei. The base target temperature was ~ 70 mK with a holding field strength of 0.9 Tesla. These conditions produced a signal, but it was significantly smaller than that seen in a polarized target and thus the need to clean up the signal using an average of many sweeps. First, the NMR calibration was performed

NMR Run #	Date & Time	Run Condition #	Condition	Days Since Injection	Average Beam Current (pA)	Temperature (K)	Magnetic Field (T)
69722683	10/25/20 6:52	1	No Beam	9	0	0.066	1.04
69878386	10/27/20 2:35	1	No Beam	11	0	0.067	1.04
70505136	11/3/20 4:00	1	No Beam	17	0	0.066	1.04
70592536	11/4/20 4:53	1	No Beam	19	0	0.066	1.04
70661375	11/4/20 20:55	2	125pA Beam	19.5	125	0.072	1.04
70676079	11/5/20 3:11	3	Simulated 125pA	20	0	0.067	1.04
70734409	11/5/20 18:09	4	250pA Beam	20.5	250	0.078	1.04
70760320	11/6/20 3:24	5	Simulated 250pA	21	0	0.073	1.04
70844088	11/7/20 3:06	6	Simulated 500pA	22	0	0.098	1.04
70911093	11/7/20 18:15	7	500pA Beam	23	500	0.095	1.04
70941010	11/8/20 5:39	8	Simulated 500pA	23.5	0	0.098	1.04

Table 4.2: Run 2A summary of conditions in which NMR measurements were taken at the UTF. The simulated beam conditions were taken during overnight, no beam periods after running a particular beam current condition. The Mixing Chamber heater was turned on and adjusted to increase the Mixing Chamber temperature until it matched the same temperature reached during the actual beam interactions. This in turn would heat the HD sample up to the temperature it was during beam on operations.

with the both IBC solenoids turned on and the dump solenoid turned off. Afterwards, the dump solenoid was powered on and NMR calibration measurement was repeated.

NMR measurements for the hydrogen nuclei thermal equilibrium signals were made at both the IBC base temperature ~ 70 mK and at a target temperature of 205mK to simulate high beam current conditions. During an electron beam run, the increasing HD temperature would be measured to determine the beam energy deposition on the target. The beam conditions of Run 2A are found in Table 4.2. Each day during the experimental run, calibration measurements were taken and any necessary changes to the running parameters were made to optimize the measurements performed routinely on the target during electron irradiation. Measurements were taken during beam operation to track the polarization of the target material. All NMR signal measurements taken during Run 2A are located in Appendix 6.1.

The exothermic recombination of HD species produced by electron irradiation could increase the target temperature. These observed temperature spikes were more frequent at higher currents. Several electron beam conditions of varying beam current were conducted to measure effects of the beam on an unpolarized HDice target temperature.

The results of these runs are discussed in Section 6.1.2. Once testing on the unpolarized target had finished, it was removed from the IBC. Then preparations were made for the polarized target used in Run 3A. The target's polarization during experimental Run 2A was extrapolated to the behavior of electrons on a polarized HD target to give some understanding before using

a polarized, frozen spin target.

4.4.3 Run 3A: Polarized Target

The third experimental run tested low current electron beams on a polarized, frozen-spin HD target. Its goal was to determine the longitudinal polarization relaxation times (T_1 values) of the HD target material under different electron beam conditions. These polarization relaxation times are how long the polarization of the target material survives. The relationship between target polarization and the T_1 time was defined in Equation 2.1. Monitoring the behavior of the polarization during the experimental run was used to analyze the effects of various depolarization mechanisms previously determined to affect the target material. Since the g14 experiment, several solutions have been implemented to limit the effects of the depolarization mechanisms and extend the polarization relaxation time of the HD target. After the third experimental run the effectiveness of the implemented solutions could be determined.

The polarization of hydrogen in the target #60 (used during Run 3A) should have been close to 60%, while the polarization of the deuterium should have reached around 20%. Unfortunately, this was not the case due to issues during the target aging process. In addition, a He^3 capillary in the DF became blocked, which required the dilution cooling had to be turned off during June 2020. This caused the target in the DF to slowly warm up to a temperature of $\sim 1\text{K}$. Between these two events, approximately a third of target #60's polarization had decayed away before the start of the run in November 2020. The initial polarization was $\sim 39\%$ instead of the maximum possible of 60% with the DF setup.

Run 3A began by taking the polarization calibration NMR scan in the PD before loading the target into the IBC using the same TC transfer procedure used in Run 2A. Target #60 had an outer diameter of 20mm and a length of 12.5mm. To simulate the effects of a 10GeV, 2nA beam from Hall B, an additional 4mW heater was applied to the mixing chamber while testing a rastered 9.7MeV beam with various current conditions. The parameters for this run were determined from Runs 1 and 2A. In addition to testing different current conditions, the strength of the target's magnetic holding field and HD temperatures were also tested. NMR measurements were taken intermittently through the different condition settings to monitor the polarization and see how it was affected.

The different conditions were tested by establishing stable beam and changing the beam current settings as well the mixing chamber heater settings after performing several NMR

measurements. Before the first beam went through the polarized target, the Adiabatic Fast Passage was performed on the target to flip the spin direction of the target nuclei. This was done to eliminate any hyperfine mixing that could have led to target depolarization. The procedure is described in Section 5.3.

After the AFP procedure and with the Faraday cup in, it was safe to establish a 9.7MeV beam up to the entrance of the IBC. The beam position parameters were then verified using the viewers and BPMs. With all the solenoids on that contributed to the target holding field, the beam raster was turned on and the rastered beam sent through the IBC. The dump viewer was used to confirm the position and shape of the beam after leaving the IBC. Following the confirmation at the dump viewer, several NMR calibration scans were taken to establish a good noise-to-signal ratio.

Once the beam position was verified at the beam dump, the rastered beam with a specific current could be tested with the target. A description of the various operating conditions and when each was used can be found in Table C.1. During each target irradiation period, the beam position was continuously monitored using the BPMs, YAG viewers, and Halo counters. Target polarization was monitored periodically using NMR. In Run 3A, the center target holding field during irradiation was set to 1.1 Tesla. The NMR measurements taken required the holding field to be lowered to 0.89 Tesla. As a result the average holding field during Run 3A was 1.04 Tesla.

By the end of the experimental beam periods of Run 3A, the target's polarization was used up. The depleted target was then transferred out of the DF to the IBC to recollect the HD sample within the target cell. This was done the same way as it was done in Run 2A to prepare for the next polarized target.

4.4.4 Run 3B: Polarized Target

Part B of the third experimental run also tested low current electron beams on a polarized, frozen-spin HD target. During this time it became possible to impose a duty factor on to the beam. The duty factor limited a portion of the beam from reaching the target. These newly available conditions were tested in addition to retesting the same beam conditions in Run 3A with a second polarized target. The goal of Run 3B was to determine the polarization relaxation times of the HD target material under the different electron beam conditions.

Like with the previous run, monitoring the behavior of the polarization was used to analyze

the effects of various depolarization mechanisms affecting the target material. During the aging process in the DF, RF pulses were used to test taking a NMR measurement using the new NMR setup with the DF. The issue that occurred during early 2020 was that large RF pulses were accidentally used resulting in some target depolarization. This loss was in addition to that mentioned for target #60, where a line blockage in the DF cooling system necessitated shutting down of that system. This resulted in the targets aging at the elevated temperature of $\sim 1\text{K}$ instead of 10mK and reducing the maximum achievable amount of polarization. Instead of target #66 having an initial 60% polarization for hydrogen, the initial polarization was $\sim 33\%$. This was about 6% less starting polarization than target #60.

Run 3B began by taking the polarization calibration NMR scan in the PD and then loading the target into the IBC with the TC just like Run 3A. In addition to studying the duty factor effects, NMR measurements were taken intermittently to monitor the polarization and see how similar conditions compared between runs. Before the first beam went through the polarized target, an Adiabatic Fast Passage was performed on the target to flip the spins and eliminate hyperfine mixing in target #66. This procedure is described in Section 5.3. After the AFP procedure the Faraday cup was inserted to establish a 9.7MeV beam up to the entrance of the IBC. Beam position parameters were verified using viewers and BPMs. With all the holding field solenoids powered on, the beam raster was turned on and a rastered beam was sent through the IBC. The viewer in the dump was used to confirm the position and shape of the beam at the end of the beam line. Following confirmation at the dump viewer, NMR calibration scans were taken to establish a good noise-to-signal ratio.

With the beam position verified and the NMR calibration complete, a specific beam condition could be tested. A description of the various beam conditions and when each was used can be found in Table C.2. During each target irradiation period, the beam position was continuously monitored using BPMs, viewers, and Halo counters. Target #66's polarization was monitored intermittently using NMR. A notable difference between Runs 3A and 3B, involved a different center target holding field during beam irradiation. The decision was made to set the holding field to 0.89 Tesla during the run. In Run 3A the NMR measurements taken required the holding field to be lowered from 1.1 Tesla to 0.89 Tesla . Ramping the solenoids down to the lower field for NMR scans took almost half the beam on run times resulting in an average holding field of 1.04 Tesla . For Run 3B, it was decided to keep the holding field at 0.89 Tesla for most beam conditions to avoid all the field changes during a run.

By the end of the experimental beam periods of Run 3B, the target's polarization was depleted. It was then transferred out of the DF to the IBC for HD recollection. This was done the same way as it was with the previous targets and to prepare for Run 2B's unpolarized target.

Target #66 electron irradiation used the same beam currents as in Run 3A. With the addition of applying a duty factor onto the beam, continuous beam current conditions could be compared to average beam currents of the same value. Duty factors would limit a portion of the beam it from reaching the target. This was done by an accelerator operator by using a USER MODE utility that introduced 1 gap within a 5 ms interval, by blocking the laser pulses at the electron gun. Two modes used with the utility were:

- 3.333 ms ON + 1.667 ms OFF \Leftrightarrow DF= $\frac{2}{3}$
- 1.667 ms ON + 3.333 ms OFF \Leftrightarrow DF= $\frac{1}{3}$

By applying these modes, up to three separate beam conditions could be studied for the same average beam current, but different peak currents. Using an average beam current of 125pA as an example, the three conditions that could be compared were: 125pA CW (continuous current), a peak current of 375pA at 1/3 DF, and a peak current of 188pA at 2/3 DF. The oscilloscope readout of one Halo detector in Figure 4.15 demonstrates the duty factor beam blocking affect during beam operations.

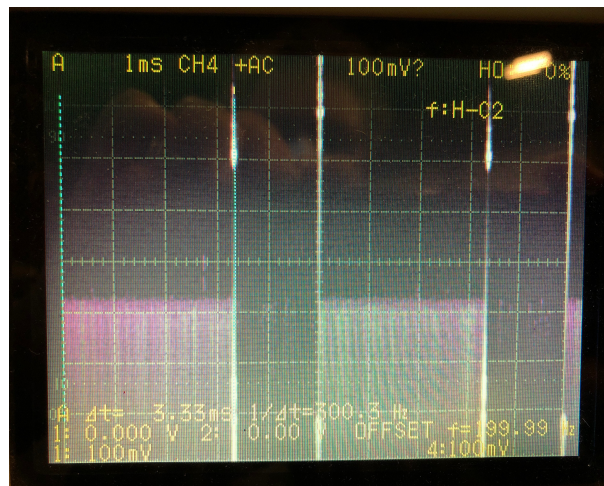


Figure 4.15: Oscilloscope output of signals from one Halo detector, triggered by the gun laser, during DF = 2/3 operations.

4.4.5 Run 2B: Unpolarized Target

Run 3B added the capability to impose and test the effects of a duty factor applied to the beam. As a result there was a necessity to expand upon the studies done in Run 2A by examining the additional temperature effects of a duty-factored beam on another HD target. This provided the additional information needed to interpret the Run 3B data taken with reduced duty factor, by measuring the HD temperature at the same reduced duty factor conditions of Run 3B. As a result, an additional run was added to the HDice experiment in the UITF. Since the target used was unpolarized like in Run 2A (originally called Run 2 before the additional run), the run was designated as Run 2B.

The operating procedure for Run 2B was similar to that in Run 2A except that it included the addition of different duty factor beam conditions from Run 3B. As with the previous runs, Run 2B began by loading the target and resetting the beam line. Before disconnecting the IBC for loading, all gate valves were closed and the Faraday cup was inserted in. The roof tiles of Cave 2 were removed allowing the IBC to be rotated so that the TC could be mounted to it using the North 25 ton crane. Like the previous targets, the Run 2B target was loaded following the procedure described in Section 4.3. Once the target was loaded into the IBC and the TC removed, the IBC was rotated to be reconnected to the beam line. Cave 2's roof tiles were then returned to allow for usage.

<u>NMR Run #</u>	<u>Date</u>	<u>Time</u>	<u>Run Condition #</u>	<u>Days Since Injection</u>	<u>Temperature (K)</u>	<u>Magnetic Field (T)</u>
80868010	3/2/2021	22:23-8:59	1	9.5	0.070	0.8817
80918878	3/3/2021	23:06-7:43	2	10.5	0.070	0.8817
81001775	3/4/2021	22:35-8:04	3	11.5	0.255	0.8817
81041576	3/5/2021	23:05-07:44	4	12.5	0.071	0.8817
81088195	3/6/2021	22:30 - 11:35	5	13.5	0.245	0.8817
81214068	3/7/2021	21:46-7:34	6	14.5	0.071	0.8817
81343255	3/8/2021	23:23-7:40	7	15.5	0.131	0.8817
81390015	3/9/2021	23:05-7:35	8	16.5	0.071	0.8817
81475331	3/10/2021	23:24-8:09	9	17.5	0.133	0.8817
81602590	3/11/2021	22:18-7:42	10	18.5	0.259	0.8817
81645335	3/12/2021	23:51 - 8:36	11	19.5	0.070	0.8817
81774759	3/13/2021	22:59 - 10:56	12	20.5	0.070	0.8817

Table 4.3: Run 2B summary of overnight beam off conditions for NMR measurements taken at the UITF.

All the solenoids used in aligning the beam through the IBC were set to the optimum running values and NMR calibration scans were performed. This was done before beam operation to establish a good signal-to-noise ratio. With the Faraday cup inserted, a rastered 9.7MeV beam

was established. Next, the beam position was verified using viewers and BPMs. Then the Faraday cup was removed allowing the rastered beam to pass through the IBC, which the alignment was monitored using the dump viewer and Halo BPM. During the beam operation, several NMR measurements were performed to monitor the target polarization. This entire procedure was repeated for each set of beam conditions tested. These conditions are listed in Tables 4.3 and 4.4.

NMR Run #	Date & Time	Run Condition #	Condition	Days Since Injection	Average Beam Current (pA)	Magnetic Field (T)
81088195	3/5/2021 11:29	1	250pA CW Beam	10	250	0.8817
81343255	3/8/2021 10:20	2	250pA peak, 2/3 duty, 167pA Average	11	167	0.8817
81368360	3/8/2021 5:19	3	250pA peak, 1/3 duty, 83pA Average	12	83	0.8817
81435289	3/9/2021 11:54	4	83pA CW beam	15	83	0.8817
81515334	3/10/2021 10:08	5	125pA, 2/3 duty cycle, 83pA Average	15.5	83	0.8817
81693190	3/12/2021 11:33	6	125pA CW	16.5	125	0.8817
81001775	3/4/2021 11:29	7	188pA peak, 2/3 duty cycle, 125pA Average	17.5	125	0.8817
80918878	3/3/2021 12:27	8	250pA CW Beam	18	250	0.8817
81545401	3/10/2021 18:30	9	375pA CW	18.5	375	0.8817
81774759	3/10/2021 10:12	10	375pA peak, 1/3 duty cycle, 125pA Average	19.5	125	0.8817
81602590	3/11/2021 10:23	11	500pA peak, 2/3 duty cycle, 333pA Average	20	333	0.8817

Table 4.4: Run 2B summary of conditions in which beam on NMR measurements were taken at the UITF.

After testing all the desired beam conditions, the NMR measurements taken incorporated the effects of a duty-factored electron beam into the eHD experimental studies. All NMR signal measurements taken during Run 2B are located in Appendix 6.1. Following the completion of all tests in Run 2B, the procedure described in Section 4.3 was used to transferred the target back to the PD to recollect the HD gas.

Chapter 5

Polarimetry

5.1 Polarimetry Overview

Polarimetry refers to the study of a material's electron or atomic nuclei spin polarization. Spin is the intrinsic total angular momentum of a particle. Associated with each nuclear spin is a nuclear magnetic moment that produces magnetic interactions with the surrounding environment. Individual protons, neutrons, and electrons all have an associated non-zero magnetic moment in their ground states. As a result, these particles will be in either one of the $2S + 1$ spin states. Due to the interactions between external magnetic fields and the sample particles' magnetic moments, the polarization of the sample can be oriented and maintained. The strength of the holding field determines the amount of polarization that can take place.

If an external magnetic field is not present, spin states are degenerate and have the same energy. When an external magnetic field is applied to the sample material, a separation of the spin states at different energy levels can be observed. This effect, named the Zeeman effect, was first discovered by Pieter Zeeman in 1896. It can be seen Figure 5.1. The energy relative to the ground state is given by:

$$E_m = -m\gamma\hbar B, \quad (5.1)$$

where \hbar is the reduced Planck's constant, γ is the gyromagnetic ratio of the nucleus or electron, B is the external magnetic field, and $m = -S, -S + 1, \dots, S - 1, S$. Information on the occupancy of the different magnetic substates is provided by the spin polarization. The polarization is a

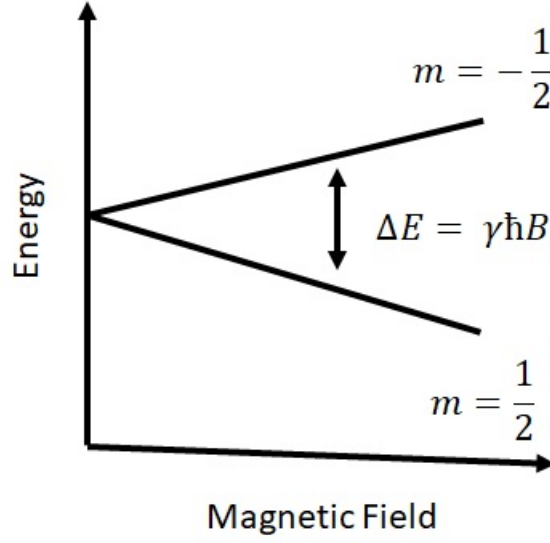


Figure 5.1: The $S = 1/2$ energy level splitting.

unitless quantity with a range from -1 to 1 and its general form is defined as:

$$P = \frac{1}{S} \sum_{i=-S}^S i \frac{N_i}{N}, \quad (5.2)$$

where N is the total number of particles in the sample material, N_i is the number of particles in the spin state i . The occupancy ratio of a spin state, i , is defined as N_i/N . The polarization of a sample is zero for the case where all spin states are equally populated. In the case of studying just protons and electrons, like the eHD target, Equation 5.2 reduces to:

$$P = \frac{N_{+\frac{1}{2}} - N_{-\frac{1}{2}}}{N_{+\frac{1}{2}} + N_{-\frac{1}{2}}}. \quad (5.3)$$

A sample material at a given temperature, under the influence of an external magnetic field, typically has some minimal amount of polarization. This polarization is known as the thermal equilibrium polarization, TE. At TE conditions, the spin state population follows the statistical Boltzmann distribution, where the occupancy ratio of the spin state is defined as:

$$\frac{N_m}{N} = \frac{g_m \exp\left(\frac{-E_m}{kT}\right)}{\sum_{i=-S}^S g_i \exp\left(\frac{-E_i}{kT}\right)}, \quad (5.4)$$

where $g_m(g_i)$ represents the degeneracy of spin state $m(i)$, $E_m(E_i)$ as defined by Equation 5.1 represents the energy of spin state $m(i)$, k is the Boltzmann constant, T is the sample material

temperature, and $m = -S, -S + 1, \dots, S - 1, S$.

The TE polarization can then be found using Equations 5.1, 5.2, and 5.4 to be:

$$P_{TE} = \frac{1}{S} \frac{\sum_{i=-S}^S i g_i \exp\left(\frac{i\gamma\hbar B}{kT}\right)}{\sum_{i=-S}^S g_i \exp\left(\frac{i\gamma\hbar B}{kT}\right)}. \quad (5.5)$$

The TE polarization is dependent upon an applied B and T as seen in Equation 5.5. Both decreasing the sample temperature and increasing the magnetic field are causes for an increase in TE polarization. For the case of the hydrogen nuclei and electrons of the HD target, spin $S = 1/2$, Equation 5.5 reduces to:

$$P_{TE} = \frac{1 - \exp\left(-\frac{\gamma\hbar B}{2kT}\right)}{1 + \exp\left(-\frac{\gamma\hbar B}{2kT}\right)} = \tanh\left(\frac{\gamma\hbar B}{2kT}\right). \quad (5.6)$$

For the deuterium in the sample material, spin $S = 1$ and Equation 5.5 then becomes:

$$P_{TE} = \frac{1 - \exp\left(-\frac{2\gamma\hbar B}{kT}\right)}{1 + \exp\left(-\frac{\gamma\hbar B}{kT}\right) + \exp\left(-\frac{2\gamma\hbar B}{kT}\right)} = \frac{4 \tanh\left(\frac{\gamma\hbar B}{2kT}\right)}{3 + \tanh^2\left(\frac{\gamma\hbar B}{2kT}\right)}. \quad (5.7)$$

The polarization of target material's nuclei can be measured via nuclear magnetic resonance by using a magnetic field and stimulating transitions between the energy levels in said nuclei via a RF field.

5.2 Nuclear Magnetic Resonance

Nuclear magnetic resonance is a valuable tool used to find the polarization of a HD target. It is a physical phenomenon where nuclei in a constant magnetic holding field are perturbed by a weaker, oscillating field in transverse direction relative to holding field and respond by producing an electromagnetic signal detectable by an antenna coil. This response signal frequency is characteristic of the magnetic field found at the nucleus. The hydrogen atoms in the target have nuclear spins and associated nuclear magnetic moments. As discussed in Section 5.1, the degenerate energy levels of target nuclei can be separated in the presence of a magnetic field. When placed in a magnetic field, the atoms in the target align themselves to be pointed either in the direction of this field or the opposite, depending upon the sign of magnetic moment.

The nuclear spins of the target material, aligned along a static magnetic field in a cryostat,

are subjected to a radio frequency magnetic field, transverse to B_0 , which oscillates at the nominal Larmor frequency, where γ is the gyromagnetic ratio of the nucleus (42.576 MHz/tesla for Hydrogen). Viewed semi-classically, an RF pulse tips a fraction of the aligned spins into the transverse plane. The transverse spins then precess about the B_0 direction at the Larmor frequency. The rotating magnetic field generated by the magnetic moments of the precessing spins induces an oscillating current in another RF receiver coil, which constitutes the NMR signal. The RF energy is just Planck's constant multiplied by the RF frequency,

$$E_{RF} = h\omega. \quad (5.8)$$

The energy gap can be calculated by taking the difference between two consecutive energy levels and is equivalent to the product of the gyromagnetic ratio, reduced Planck's constant, and the applied magnetic field strength:

$$\Delta E = E_{m+1} - E_m = \gamma\hbar B. \quad (5.9)$$

Equations 5.8 and 5.9 can be combined to solve for a specific Larmor frequency, ν_{Larmor} , by the following:

$$\omega_{Larmor} = \frac{\gamma B}{2\pi}. \quad (5.10)$$

The Larmor frequency is found simply by multiplying the strength of the external magnetic applied field by the gyromagnetic ratio of the atom.

During the eHD experiment, NMR signal measurements were made before and after the polarization process. The measurements were taken in the PD and IBC as both cryostats were configured to work with the auxiliary NMR rack systems. When the HD target was condensed in the PD, the first set of target NMR measurements were taken. At this point of the target creation process, NMR measurements can be taken using either of two methods. Either a frequency sweep could be done with a constant applied external magnetic field or the magnetic field is swept while at a constant radio frequency.

For newly condensed targets, both methods are used. This allowed for two separate ways to analyze and cross check target polarization values. After the PD NMR was complete, the targets were moved into the DF to start the polarization process. Once the target was moved to the DF, it was subjected to a constant magnetic field for the rest of its life to maintain its

polarization. In the IBC, the frequency was held constant and the field was swept to take NMR measurements. In principle either a field sweep or frequency sweep could be used. Holding the field constant while sweeping the frequency avoids eddy-current heating. But, that is only significant at the low temperatures obtained in the DF. In any case, the available LabView code developed by the JLab support group had too much overhead (in time) when sweeping frequency, so much more data was collected with the field-sweep mode. Thus, in the end, field-sweep was used as the default in all cryostats.

After the aging process was complete, the target cell was transferred back into the PD with the target temperature kept at 2-4 Kelvin for a polarization measurement via field swept NMR, and compared with the TE signal measured right after the target condensation. Once the polarization was confirmed to be adequate, the target cell was left in the PD for temporary storage until preparations for the target transfer to the IBC were complete. Once in the IBC, NMR measurements were taken throughout the experimental run to track target depolarization under an electron beam. In in depth description of the NMR measurement procedure is found in Section 5.5.

5.3 Adiabatic Fast Passage

Adiabatic Fast Passage (AFP) is an NMR technique used to reverse or flip the polarization of sample nuclei. AFP is carried out by applying RF to each HD molecule at exactly the Larmor frequency. However, this frequency is not the same numerical value for all HD spread over the volume of the target. This is due to field non-uniformities across the target, which is why the NMR resonance peak has a width. To perform an AFP, the RF is set to the gyromagnetic ratio of hydrogen (42.576 MHz/Tesla) multiplied by the central magnetic field (in Tesla). Then starting below that nominal field value, the field is swept over the resonance condition exactly once with the RF frequency fixed. Doing so ensures that all the HD molecules throughout the target volume see the resonance condition exactly once. Performing the AFP more than once will drive the transition the other way and result in polarization loss.

The AFP procedure used to flip the spins of both eHD polarized targets involves turning on a RF transition signal and sweeping it across a range of the magnetic holding field that avoided the transition fields of H and D in the sample material. This procedure can vary with the parameters of the magnetic field along with the RF signal rates and powers while sweeping

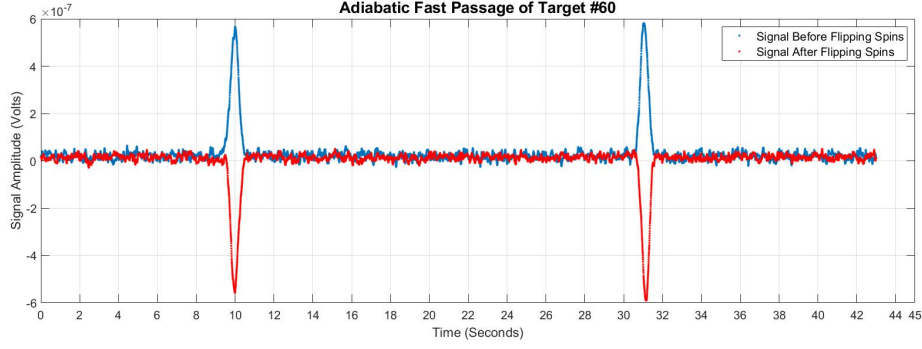


Figure 5.2: NMR Signals before and after performing the Adiabatic Fast Passage on Target #60.

across the desire range.

Each RF induced transition causes a loss of polarization. In some cases, like with the HD target, the RF transitions used may not be entirely efficient. This leads to possible polarization losses. Additionally, the RF power required to perform the AFP might be too much resulting in the target heating up and losing some polarization. Regular NMR measurements are typically performed with a much smaller power of around 10^{-5} Watts resulting in very few induced transitions among the sample nuclei. There is virtually no polarization loss due to the small number induced transitions during regular NMR scans.

5.4 NMR Setup

The most important tool for understanding how an electron beam affects a frozen-spin, highly polarized HDice target was nuclear magnet resonance. NMR was responsible for tracking each polarized target's polarization throughout the electron beam tests. An understanding of the NMR apparatus used at UTF is important for signal data processing.

5.4.1 NMR Apparatus

Two nuclear magnetic resonance systems were used to scan the HDice targets during the eHD experiment. One NMR system was installed next to the PD where it could be connected to that dewer's NMR solenoid and NMR coils. It was used to measure the TE signal of each target as well as polarized signal after the target has aged in the DF. The other system was located in Cave 2 of the UTF, where it was connected to the IBC for polarization tracking of beam-on and beam-off conditions, TE signals at different temperature and holding field, and AFP for

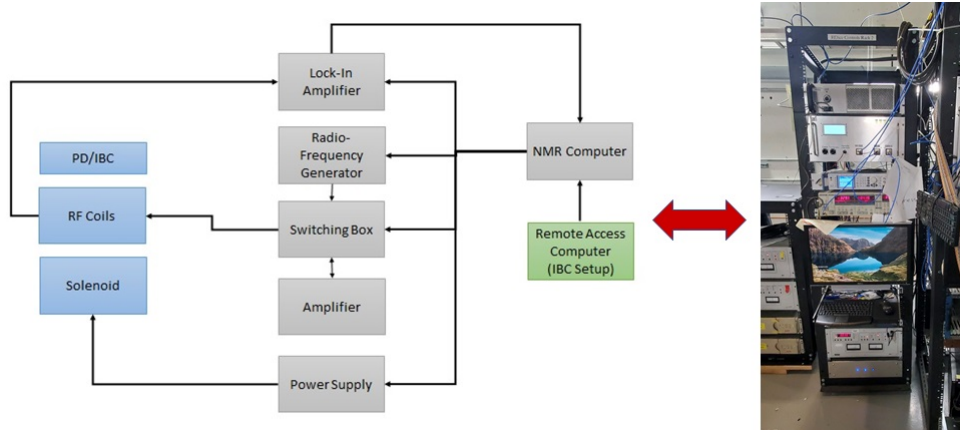


Figure 5.3: The NMR rack located in Cave 2 of the UTF. On the left is the schematic and on the right is a photo of the actual rack. From bottom to top the rack contains the main solenoid power supply, NMR computer, lock-in amplifier, radio-frequency generator, switching box, and amplifier.

flipping proton polarization. The systems had similar hardware configurations, but different LabView software for operation. In the event of a system failure during the experimental run, the PD NMR rack could be interchanged for IBC NMR rack. Each rack system consisted of several devices.

One such device was an Oxford IPS120-10 power supply. It was used to provide current to the main solenoid of the dewar where the NMR measurement took place. Target polarization was maintained throughout the entire experiment due to the magnetic field provided by the IBC's main solenoid. The field direction was along the beam axis (defined as the Z-axis). The solenoids were connected to their respective power supplies with standard high current insulated copper cables.

Each NMR rack also had a Rohde and Schwarz SMB100A signal generator that provided the radio frequency signal used to induce transitions between the energy levels split by the main magnetic field. The signal frequency depends on the strength of the main field. For the eHD experiment, NMR measurements were taken at a main field strength of approximately 0.9T (High Field) and 0.4T (Low Field). The corresponding frequencies were approximately 38MHz and 19MHz.

Another component was a module switching box that could attenuate the RF signal from 0 to -63 dBm. The box also provided a switch between the regular NMR circuit and the spin transfer circuit used in the AFP spin flipping procedure mentioned earlier. A set of Molex-141

air-core, ultra-low-loss coaxial cables were used to connect the NMR system to the two RF coils in the IBC and PD. The first acted as a transmitter that carried an RF signal from the signal generator to NMR coil in the IBC. It created the RF magnetic field oriented perpendicular (along the x-axis) to the main field.

The second coil was the receiver responsible for providing a measurement of the RF response along the y direction of the target cell's HD material. To minimize any magnetic flux from the transmitter to the receiver coil, the coils were in a cross coil configuration. Some flux still existed due to the capacitance between coils, which is inevitable, also provides the path for RF. This resulted in a signal being induced on the receiver coil by the transmitter coil and would require phase corrections during analysis to isolate the pure signals.

A lock-in amplifier, Stanford Research Systems SR844, was used to extract the NMR signal from the generated RF signal and provided the acquisition to this signal data. A computer located in Cave 2 was connected directly to the NMR system interfaced all NMR device components together. The interface was provided through a LabView program designed for the eHD experiment by Jefferson Lab's Detector Support Group. This program provided the controls to operate the NMR system as well as collect and store the NMR data. While the beam was running, radiation prevented anyone from entering Cave 2 to access the NMR computer. In order to run the NMR program while the beam was in operation, a second computer in the Control Room area was used to remotely connect to the computer in Cave 2 through an Ethernet connection.

5.4.2 Fast Resonance Scan

The Fast Resonance Scan (FRS) was used to measure the frequency dependency of the RLC circuit because it provides several resonances at different frequencies. This can be observed in Figure 5.4. A FRS scan worked by measuring both the phase and magnitude between the input/output RF signals of the circuit response for the different resonances. This information was important as it determined the frequency that provided the best signal-to-noise ratio. The first peak on the left in Figure 5.4 is the resonance associated with the coil. Each other peak represents resonances corresponding to standing waves in the cables. They correspond to the cable lengths being $\frac{1}{2}$ integer multiples of the RF wavelength; from left to right these are $\frac{1}{2}\lambda$, $\frac{3}{2}\lambda$, and $\frac{5}{2}\lambda$. Initially, the $\frac{5}{2}\lambda$ was desired to be used as it corresponds to a holding field of 1.1 Tesla, which is the largest the IBC can provide and would improve the polarization loss rates.

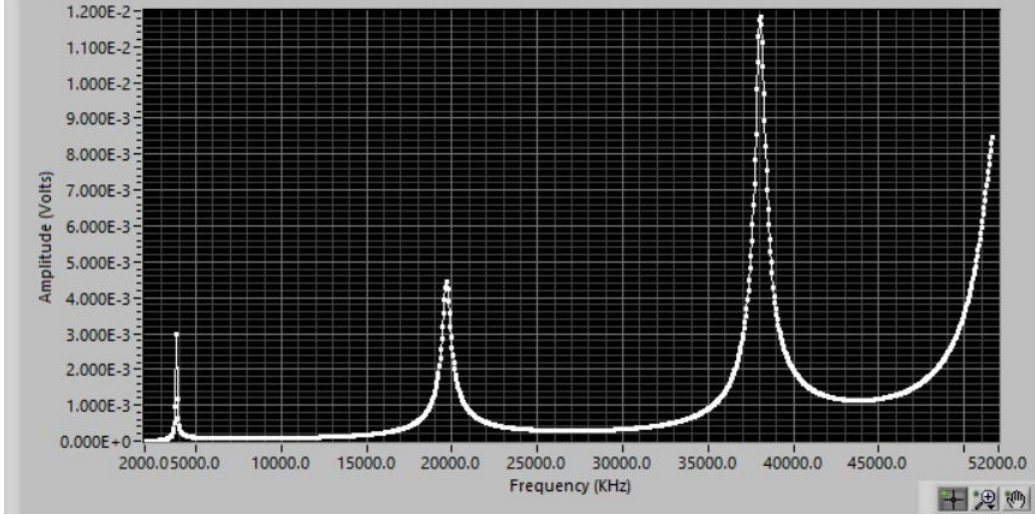


Figure 5.4: Fast Resonance Scan example in the IBC during the eHD experiment. Each peak represents resonances corresponding to standing waves in the cables.

However, there was a large background present during scans at $\frac{5}{2}\lambda$. This background made taking NMR measurements at 1.1T not plausible.

To minimize the background noise in the measurement during Run 3A, the holding field was lowered from 1.1T TO 0.89T during scans and then raised back up after each scan was complete. This resulted in an average holding field of 1.04T during Run 3A beam operations. Besides the background issue, the ramping process was also time consuming during Run 3A. It was decided in Run 3B to keep the holding field always at 0.89T, corresponding to the $\frac{3}{2}\lambda$ resonance. By doing so, no time was wasted with adjusting the solenoids during beam on operations allowing for longer studies with the same beam conditions as in Run 3A.

The FRS scan was performed at the start of each experimental day as it could detect any change to the circuit that, which would require a new calibration. An example of how the circuit could change day to day involved the ambient temperature of the UITF. During the week days, other people and operations took place in the surrounding test lab and would result in the temperature of the cables increasing. The capacitance of coax cables is dependent on temperature, which would shift the resonance frequency as ambient temperature changes and leads to RF amplitude reduction. This would result in slight shifts in the resonance frequency, which were taken into account after each new FRS.

In addition to the circuit response depending on temperature, the NMR signal amplitude depended on the magnitude of the circuit response. Using one of the resonance frequencies maximized the signal. Most importantly, it stabilized the RF signal since the gain change is

minimal around the RF peak. The target holding field was then chosen to met the conditions of Equation 5.10 with the desired resonance frequency. Fast Resonance Scans do not require a holding field be present. However, the magnetic field was present for the polarized target as each required a holding field to maintain polarization.

5.4.3 Field Scan

The field scan was the NMR procedure used to perform an NMR measurement. This method requires the RF field to be fixed at an optimal setting by fixing the frequency and the holding field of the cryostat sweeps past the resonance magnetic field. Within the target material, the nuclear spins align with the holding field, B_0 . These spins were then subjected to a RF magnetic field, B_{RF} , which was transverse to the holding field. The RF field oscillates at the nominal Larmor frequency, where Equation 5.10 becomes:

$$\omega_{Larmor} = \frac{\gamma B_0}{2\pi}, \quad (5.11)$$

where

$$\frac{\gamma}{2\pi} = 42.5776 MHz/T. \quad (5.12)$$

Equation 5.12 is the gyromagnetic ratio of the hydrogen nucleus. The RF field tilts a portion of the spins out of alignment with the holding field into the transverse plane. These transverse spins would then precess about the direction of the holding field, B_0 , at the Larmor frequency. The magnetic moments of the precessing spins generated a rotating magnetic field, which in turn induced an oscillating current in the RF receiver coil. This induced current was the desired NMR signal to be measured.

The field scan would take place after first using the FRS to calibrate the NMR system. Afterwards the field scan would begin by ramping the magnetic field down. During this down sweep time the data acquisition simultaneously took place. Once the down sweep was complete, the magnetic would ramp back up with the data acquisition continuing. The data of each sweep, collected from the lock-in amplifier, was stored in the amplifier's internal data buffers until it was copied to the local disc of the NMR control PC. By ramping the field down and then back up to the initial field setting each sweep, the resonance condition was passed twice per sweep allowing two separate signal measurements. During field scans the NMR absorption (lock-in amplifier X-Channel) and dispersion (lock-in amplifier Y-Channel) spectra are examined instead

for an NMR signal measurement. The FRS differs from the field scan in that the magnitude and phase of the circuit response signal are monitored.

5.5 Measuring NMR Signals

The process of making a final measurement of NMR signals began first with a raw NMR measurement. As stated in Section 5.4.3, each NMR measurement produced four signal measurements. This in turn allowed for a weighted mean to be taken for improved accuracy and reduced error. However, to take the weighted mean, some of the raw signals required additional processing due to the difference between the absorption and dispersion spectra. The following is an overview of the signal processing procedure required to make a final measurement for each scan with the following subsections describing these steps in further detail:

- The phase angle between the detected signal and lock-in amplifier's reference signal was determined through the use of a phase angle test.
- A baseline correction was made to correct systematic effects.
- For the dispersion spectra, Kramer-Kronig relations were used to convert into an equivalent absorption signal as described in Section 5.5.2.
- Once all signals were absorption spectra, the Discrete Fourier Transform was used on each to filter noise. The signal data was converted from the time domain to the frequency domain, where most of the high frequency noise was easily removed. This was done by removing frequencies above 40 Hertz. The remaining spectra was then back converted to time space through the use of the Inverse Discrete Fourier Transform, described in Section 5.5.4.
- The noise filtered signal then has a quadratic background fitted and removed to remove some of the remaining systematic background or possible artifacts from the Discrete Fourier Transform.
- The noise that remained was then removed by fitting the background (data with the signal region removed) to either a periodic background or up to a 9th order polynomial, and removing it. A procedure was developed to determine which fit was the best suited for each NMR scan.

5.5.1 Treating Raw Signal Data

Each signal measurement was represented by absorption and dispersion spectra of the NMR response of the HD sample nuclei to the RF pulse sent via the transmission coil. The absorption spectra and dispersion spectra were also referred to as Channel-X and Channel-Y respectively after their corresponding lock-in amplifier channels (see Figure 5.5). Each of the 4 NMR signal spectra produced by scans were used to determine the overall polarization of an eHD target for every NMR measurement.

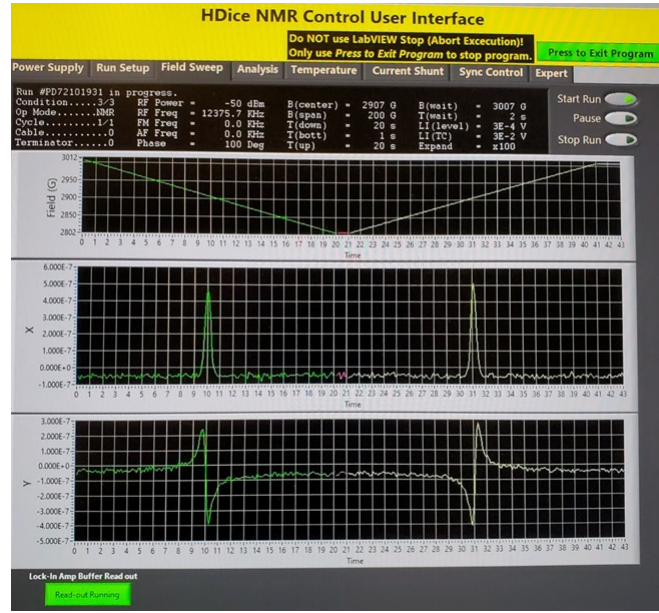


Figure 5.5: Field Scan in the IBC during the eHD experiment.

The area under the NMR signal peak of each of the four signal spectra was proportional to their individual polarization values. An example of the shape of an NMR signal curve can be seen in Figure 5.7. The area under the curve also required a scaling factor to calibrate the NMR system gain. To do this, a scan is performed on the target in the PD before (thermal equilibrium condition) and after target polarization to determine the initial target polarization, described in Section 2.5.1. A thermal equilibrium measurement was made for the Run 3 polarized targets in the PD, while the same measurements were made on the Run 2 unpolarized targets while installed in the IBC. More on the differences between thermal equilibrium measurements is discussed in Section 5.6.4.

During the thermal equilibrium NMR scan, the signal is extremely small compared to a scan of a fully polarized target ($\sim 0.4\%$ vs $\sim 40\%$). As a result, 450 scans that could be further broken down into 1800 individual signal measurements to be averaged, were performed to reduce the

noise enough to make an overall signal measurement.

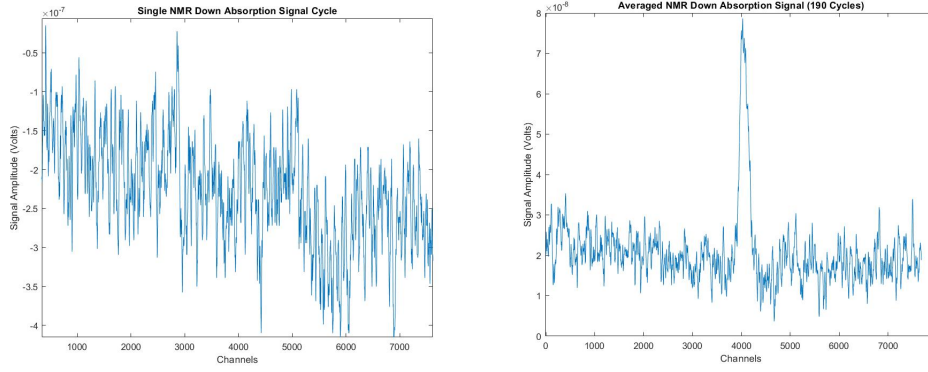


Figure 5.6: The difference between a single NMR sweep (left) and multiple sweeps averaged together (right) during a scan to cancel the noise and isolate the signal.

The scans of the polarized target had a notable difference to the thermal equilibrium scans. After the HD material within the target cell became highly polarized, the aligned HD nuclear spins generated a magnetic field of around a few gauss, which was comparable to the line width of the NMR signal. This resulted in a distortion in the shape of the NMR signal, demonstrated in Figure 5.7.

The left panels show the initial shape of the NMR signal during thermal equilibrium measurements of Targets #60 and #66. The background noise is significantly more noticeable due to the thermal equilibrium polarization being about $\sim 1\%$, despite using 450 scans to improve this. Single scans taken after each eHD target had fully polarized can be seen on the right. Here it can be observed that a distinct lump formed on the left side of the polarized signals, which was caused by the magnetic field generated by the aligned HD spins.

The IBC NMR set up for polarized targets had significantly more noise compared to the PD due to several sources of electrical interference. Before extracting any polarization values from the raw NMR signals, these signals required the removal of noisy backgrounds to prepare the signal for analysis. The analysis of each measurement required taking into account several factors and making the relevant corrections to obtain a final polarization value. Since the amount of distortion depended on the degree of polarization, determining a fitting function that could analytically provide the area of the NMR signal response for all values of the target polarization proved very difficult. An alternative procedure that could be used universally for all polarization levels was developed to remove excess background noise from each signal and calculate the area under the curve.

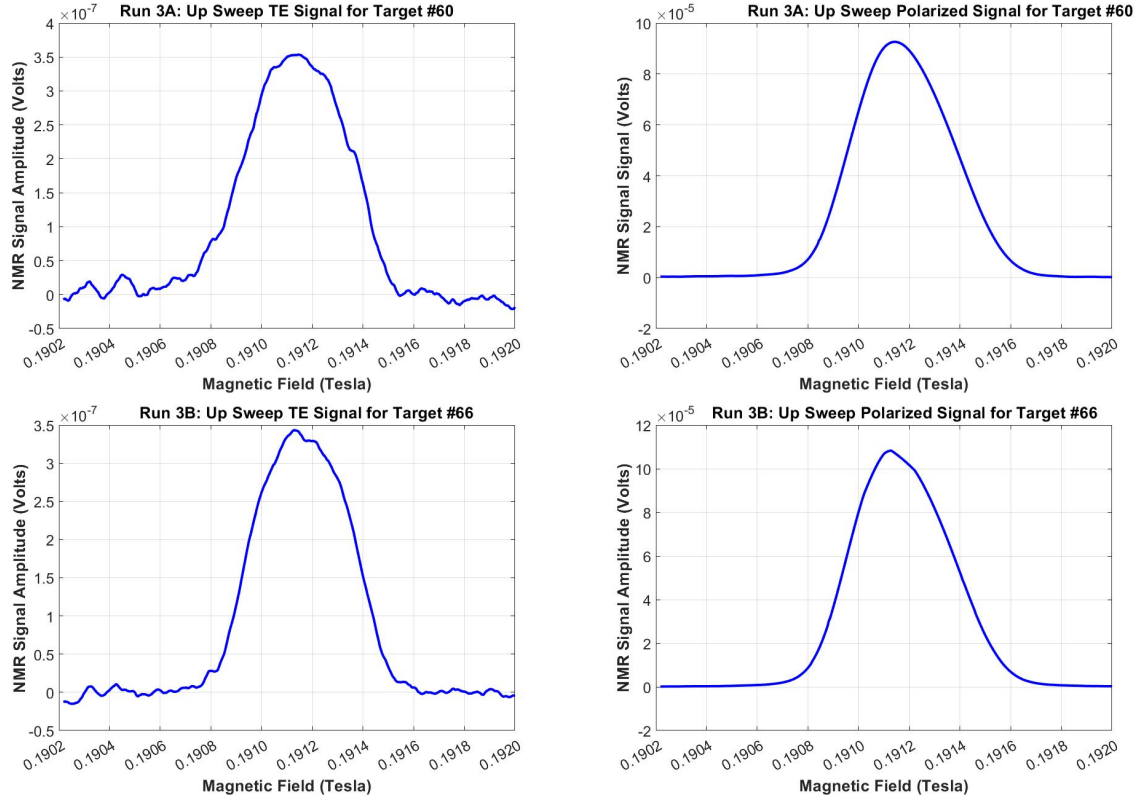


Figure 5.7: Comparison of target TE up absorption signals with polarized target up absorption signals. The top row corresponds to Run 3A’s target #60, while the bottom corresponds to target #66 of Run 3B. The TE signals on the left panels are an average of 450 sweeps in the PD, prior to polarization in the DF. These pre-frozen-spin line shapes are broadened by jitter in the timing of the 450 sweeps. The right panels are single sweeps in the PD after the HD has reached a frozen-spin state.

The signal measurement in the PD after polarization is compared to a scan in the IBC immediately after the target transfer. After the transfer and before any beam time, the target’s polarization should be the same in both the PD and IBC, minus an approximate 1% loss. This small loss, which has been documented [14], occurs during the transfer of a target between the cryostats due to transfer fields and target temperature conditions in the TC not being absolutely perfect.

5.5.2 Kramers-Kronig Relations

The Kramers-Kronig relations connect the real and imaginary parts of a complex function. This is extremely beneficial as it provides a way for NMR scans to provide twice the signal measurements for each scan due to each signal measurement being represented by an absorption

and dispersion spectra. These spectra are shown in Figure 5.8. The utility of the KK transform is the ability to take a dispersion spectrum, with long tails that flip sign over the resonance, and transform it into an absorption-like shape that can be easily integrated. This is because it does not change sign and it does not have long tails. Longer tails would cause the integration to include a lot of noise.

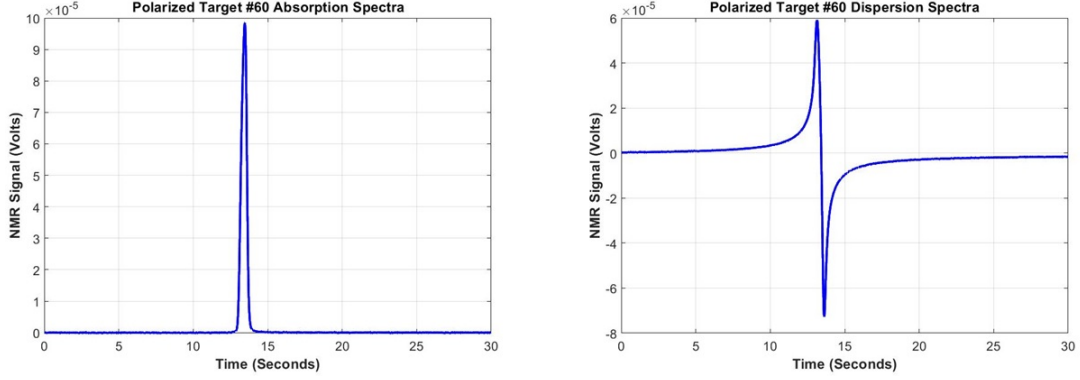


Figure 5.8: Example of an NMR signal being broken up into its absorption (left plot) and dispersion spectra (right plot). Both signals are from a single sweep in the PD over the hydrogen line in target #60, with $P_H = 38\%$, just prior to the start of Run 3A.

The response function $\chi(\omega)$ of a system has real and imaginary parts:

$$\chi(\omega) = \Re\chi(\omega) + i\Im\chi(\omega) \quad (5.13)$$

The Kramers-Kronig relations connect real and imaginary parts. The relations are analogous to the Hilbert transform [19] and have for expression:

$$\Re\chi(\omega) = \frac{1}{\pi} P \int_{-\infty}^{\infty} \frac{\Im\chi(\omega')}{\omega' - \omega} d\omega', \quad (5.14)$$

$$\Im\chi(\omega) = -\frac{1}{\pi} P \int_{-\infty}^{\infty} \frac{\Re\chi(\omega')}{\omega' - \omega} d\omega', \quad (5.15)$$

where P denotes the Cauchy principal value. Like with the Fourier transform, the Discrete Kramers-Kronig Relations are more adapted to a sampled signal. The discrete relationship takes the following forms:

$$\Re\chi(\omega_j) \approx \frac{1}{\pi} \lim_{N \rightarrow \infty} \sum_{i=-N, i \neq j}^N \frac{\Im\chi(\omega_i)}{\omega_i - \omega_j} \Delta\omega_i, \quad (5.16)$$

$$\Im\chi(\omega_j) \approx \frac{-1}{\pi} \lim_{N \rightarrow \infty} \sum_{i=-N, i \neq j}^N \frac{\Re\chi(\omega_i)}{\omega_i - \omega_j} \Delta\omega_i. \quad (5.17)$$

For a known range of data, the above equations simplify to:

$$\Re\chi(j) \approx \frac{1}{\pi} \sum_{i=i_{min}, i \neq j}^{i_{max}} \frac{\Im\chi(i)}{i - j} \Delta i, \quad (5.18)$$

$$\Im\chi(j) \approx \frac{-1}{\pi} \sum_{i=i_{min}, i \neq j}^{i_{max}} \frac{\Re\chi(i)}{i - j} \Delta i. \quad (5.19)$$

These relationships allowed for the dispersion signals made of a finite data sample to be converted into absorption signals. These converted absorption signals allowed for additional measurements to ultimately determine the target's polarization. These signals provided additional statistics for the overall NMR signal measurement, which helped reduce noise. The weighted average of all these signals provided a measurement with less noise and thus, smaller error compared to using just one individual absorption signal.

5.5.3 Phase Test and Correction

NMR scans produce NMR signals that are made up of an absorption and a dispersion spectra representing a real and imaginary parts of the signals. These parts of the signal are separated by choosing a phase in the RF lock-in amplifier. When the NMR settings are perfect, the absorption and dispersion spectra are completely separate. When separate, the integral of the imaginary (absorption) signal output is maximized while the integral of the real (dispersion) signal output is minimized to zero as seen in Figure 5.8.

During the eHD experiment, the NMR settings were optimized, but not perfect. One such setting was the phase angle. If the phase is off, it results the absorption and dispersion spectra mixing together. It was then necessary to examine the amount of mixing for these scans to determine a phase correction angle for spectra separation. Due to the phase selection of the lock-in amplifier providing a simple rotation in the complex plane, the correction is just as simple. The following equations describe the relationship between absorption and dispersion spectra:

$$x' = \cos(\theta)x + \sin(\theta)y, \quad (5.20)$$

$$y' = \cos(\theta)y - \sin(\theta)x \quad (5.21)$$

where x' is the absorption spectra after being phase corrected, y' is the dispersion spectra after phase correction, x is the absorption spectra, y is the dispersion spectra, and θ is the phase between the two spectra.

A phase rotation of the signals using Equations 5.20 and 5.21, can be made to correct the mixing. To determine the phase correction angle to apply, a simple test was devised using the area under the curve. When the phase is correct the absorption signal appears to be a Lorentzian curve.. The tails of the curves are aligned to the X-axis. The area under the absorption signal curve would be maximum when the phase is correct. When the phase is off, part of the dispersion signal mixes into the absorption resulting in a distortion to the signal curve. This distortion causes the curve before or after the peak to dip below the X-axis. Due to the dip below the X-axis, any contribution to the total area under the curve is negative. This results in the net area being smaller than when the signal resembles a Lorentzian.

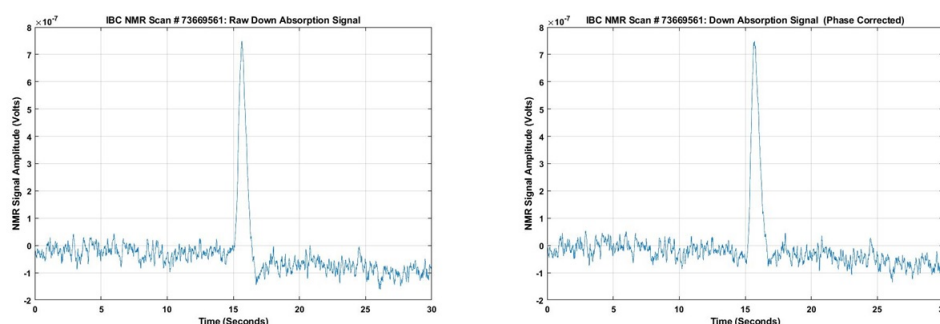


Figure 5.9: On the left plot is an example of when there is a phasing issue. The plot of the left is of the raw signal data. The right plot shows the absorption signal after applying a -13° phase rotation to isolate the pure absorption signal.

Once a phase correction has been applied, the tails on the sides of the peak are used to fit a baseline. The phase rotated data has the baseline subtracted from it resulting in the tails straightening and aligning to the X-axis. This allows now for the area under the signal peak to be easily calculated and compared with the areas using other angles.

After a phase correction has been applied to the raw signal data, one or more baseline corrections are required before being able to calculate the area under the curve. As seen in Figure 5.9, the signal appears to have a downwards slope and the tails are not aligned to the X-axis. In this specific case, applying a linear baseline correction will remove the slope and align the tails.

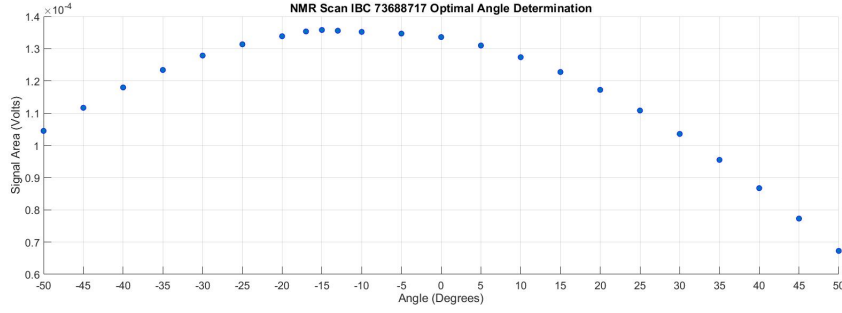


Figure 5.10: The plot above shows the results of the Phase test. The phase correction angle producing the maximum signal area is -15° for NMR Scan IBC 73688717.

The tails of the phase corrected signal data are used to determine the baseline correction. To do this, the 1500 data channels containing the peak data are removed, leaving only the tails. A linear fit is applied to the tail data. The equation from the fit is then used as the baseline subtraction. After the subtraction, the tails are aligned along the X-axis while shifting the peak the same amount. The baseline subtraction and consequent shifting of the peak now makes it possible to measure the area under the peak for each angle being tested. The area values could then be compared to determine the angle producing the largest area as seen in Figure 5.10.

5.5.4 Discrete Fourier Transform Filtering

The Fourier Transform is the mathematical tool that allows a waveform in the time domain to be transformed into a waveform in the frequency domain, while the inverse Fourier transform does the reverse. There are benefits for using the Fourier Transform such as applying operations that are simpler to apply to a function in the frequency domain compared to doing so in the time domain, and being able to observe trends only available in one domain. For the eHD experiment, the most important reason for using the Fourier Transform was its ability to convert NMR signals into the frequency domain for the purpose of removing high frequency noise. The Fourier Transform can be expressed as:

$$\hat{f}(v) = \int_{-\infty}^{\infty} f(t) e^{-i2\pi vt} dt, \quad (5.22)$$

where $f(v)$ is a wave function in frequency space and $f(t)$ is the wave function in time space. From this expression, the Inverse Fourier Transform is:

$$f(t) = \int_{-\infty}^{\infty} \hat{f}(v) e^{i2\pi vt} dv. \quad (5.23)$$

In the case of NMR signals with a finite number of data points, a more useful version of the Fourier Transform can be used. This version is known as the Discrete Fourier Transform (DFT). It converts a sequence of N samples equally spaced in a time domain function, x_N , into a sequence in the frequency domain [20]. Like the standard Fourier Transform having an inverse counterpart, the DFT has an Inverse Discrete Fourier Transform (IDFT). The DFT and IDFT can be expressed as the following:

$$X_k = \sum_{n=0}^{N-1} x_n \cdot e^{(-i\frac{2\pi}{N}kn)} = \sum_{n=0}^{N-1} x_n \cdot [\cos(\frac{2\pi}{N}kn) - i \cdot \sin(\frac{2\pi}{N}kn)], \quad (5.24)$$

$$X_k = \sum_{n=0}^{N-1} x_n \cdot e^{(-i\frac{2\pi}{N}kn)} = \sum_{n=0}^{N-1} x_n \cdot [\cos(\frac{2\pi}{N}kn) - i \cdot \sin(\frac{2\pi}{N}kn)]. \quad (5.25)$$

There are advantages in switching from the time to frequency domain and back. This includes being able to see trends available in the frequency domain that are not easily observable in the time domain, applying mathematical operations to simpler functions in the frequency domain compared to the time domain, and being able to filter out high frequency noise from a signal. Noise filtering is done by first converting the signal from the time domain to the frequency domain using DFT Equation 5.24. Then the high frequency bands can be isolated and removed before performing the IDFT by using Equation 5.25 to transform back to the time domain resulting in a cleaner signal. The steps of the signal processing can be seen in Figure 5.11. Subfigure 5.11d compares the filtered signal (red) with the raw signal (blue), demonstrating the effectiveness at noise filtering with the Discrete Fourier Transform. Despite how much noise was removed from the signal, additional baseline corrections were usually required to further clean up the signal.

5.5.5 Baseline Correction

During the phase test, a simple linear baseline correction was applied to align the signal tails to the x-axis so that the area under the curve could be easily measured. After determining the

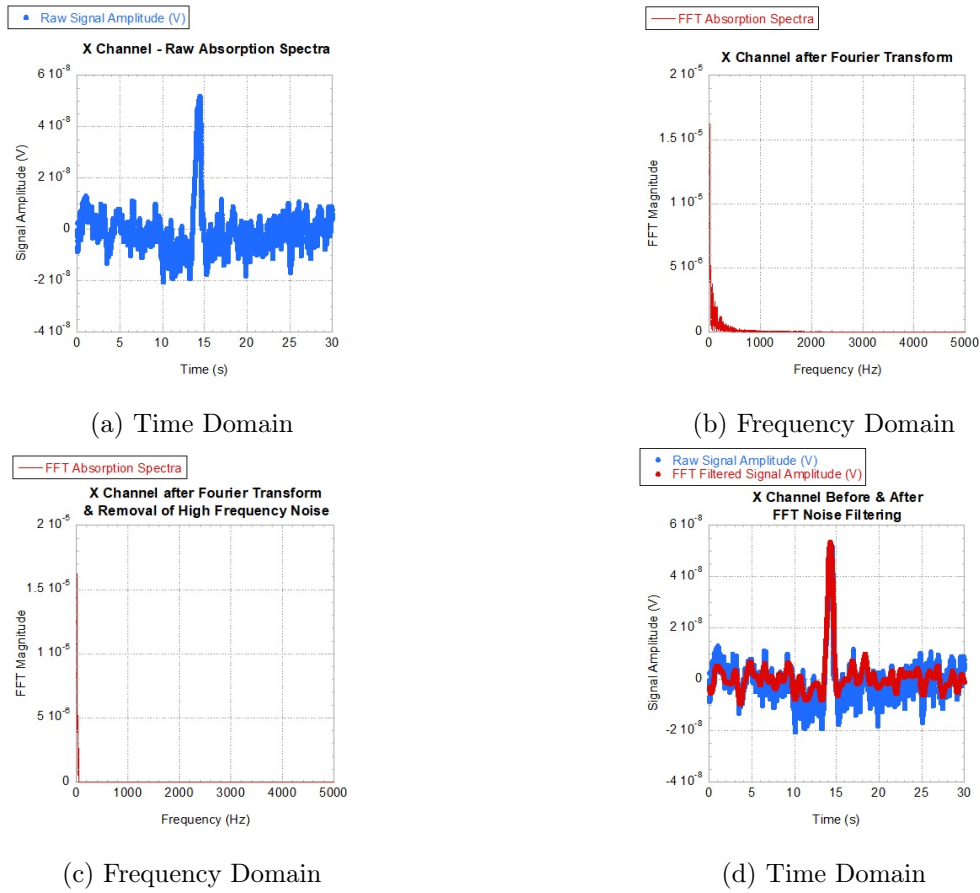


Figure 5.11: Noise filtering of raw NMR absorption signal. (a) Start with a raw signal. (b) The raw signal is converted to the frequency domain using the DFT. (c) High frequency noise is removed. (d) The filtered signal is converted back to the time domain.

phase correction angle that produces the largest area, the correction is applied and the phase corrected data has the higher order noise removed. At this point the NMR signals are almost ready to measure. The last remaining step is to apply a second baseline correction to ensure the tails are aligned along the x-axis again.

Sometimes the tails would shift slightly while being DFT noise filtered, requiring a second baseline correction. However, the more pressing reason for the second baseline cut was to address more complicated noise patterns resulting from other daily electrical activities in the Test Lab surrounding UITF. Certain device usage, like using one of the Test Lab cranes during eHD beam runs, would create repeating noise patterns in the NMR signal scan. Depending on when and which devices were used, the pattern could repeat many times over entire scan or it could just distort the tails away from the x-axis randomly. To mitigate the larger noise issues, a procedure was developed to determine what type of baseline correction was necessary.

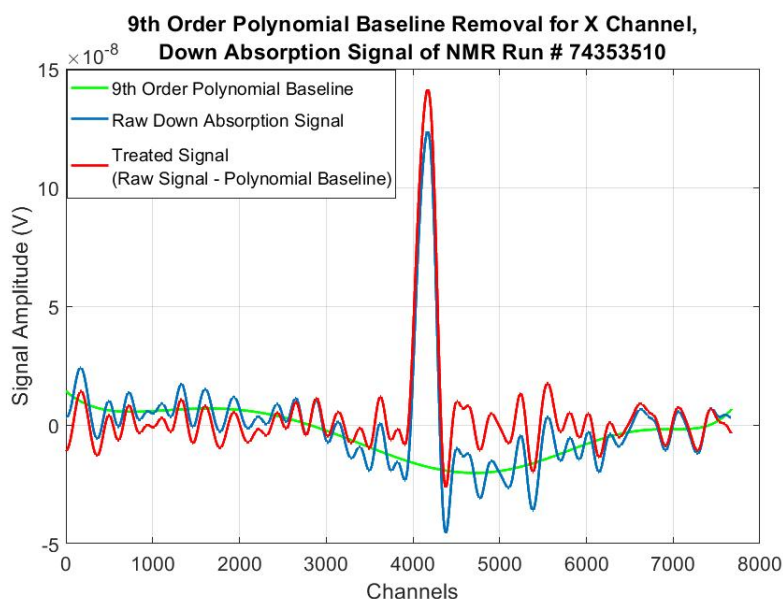


Figure 5.12: Polynomial baseline corrections to the raw NMR signals. Up to a *9th* order polynomial fit (green) is applied to the tails of the raw data (blue). The fitted baseline is then subtracted out from the raw data resulting in a cleaner, treated signal (red).

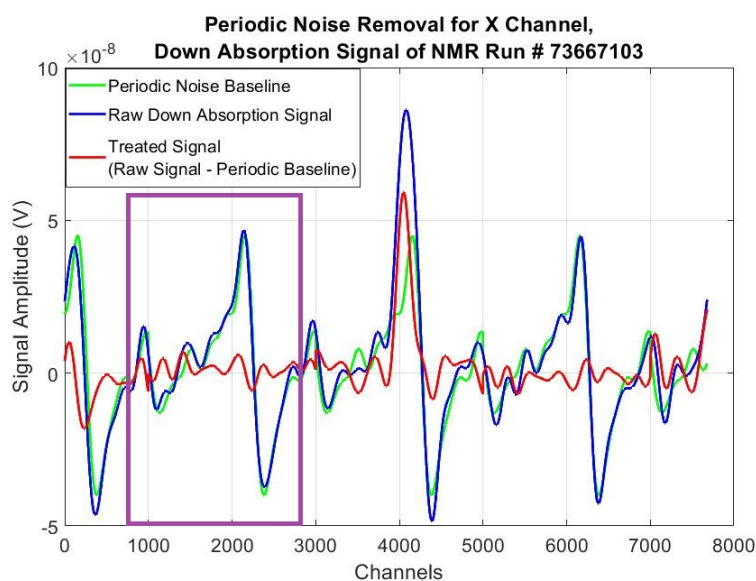


Figure 5.13: Periodic baseline corrections to the raw NMR signals. The determined repeating noise pattern is approximately 1900 channels wide, highlighted in the purple box. This pattern is isolated and repeated (green) to fit the periodic background of the raw signal tails (blue). The fit is then removed from the raw data resulting in a cleaner, treated signal (red) for analysis.

The baseline corrections made came from either using the tail data to fit up to a ninth order polynomial as the baseline or by constructing a baseline out of repeating a section of the tails.

Both baselines would be subtracted from the signal data, the area under the curves measured with the error, and then using a Chi Squared test with the error values to determine which fit resulted in the better noise removal. The full Chi Squared test method used is demonstrated in Appendix A.1. Figures 5.12 and 5.13 shows examples of when each fit was used to treat the raw signals.

5.6 Signal Integration

After each NMR spectra has been treated to remove background noise and systematic offsets, a polarization value could then be extracted from each of the spectra. As mentioned earlier, the polarization is proportional to the area under the signal curve. Initially, the integration of the signal peak to find that area under the treated curve was done by using the trapezoid theorem to create slices of the total area under the curve that were easily summed together. To improve the accuracy of this value, a more robust procedure was developed. This integration procedure was known as the sliding window technique [21].

5.6.1 Sliding Window Technique

Each of the signal spectra represented the NMR response of the HD sample nuclei as the magnetic field was swept past the resonance condition. This response was measured as a voltage and recorded by the Lock-In amplifier. This voltage was generated when the magnetic field value triggered the response, which was after a certain period of time since the start of the NMR scan.

The sliding window was a set interval of time within the NMR scan. Within the interval, the voltage values were summed together as part of the process to estimate the area under the signal curve. The width of the sliding window was set to be 600 data channels or approximately 25% larger than the full width of the NMR signal peak to ensure the entire signal was covered.

The sliding window technique started with summing up all the voltages within the window at the beginning of the spectra. Afterwards, the sliding window is shifted over the spectra by a single unit with the voltages within the window once again being summed together. This step was repeated until the right edge of the sliding window reached the end of the spectra. This procedure resulted in a list of voltage summations across the signal peak, which was then plotted against the initial time for each series of summations. The plot represented transforming the signal peak into a plateau made up of many summations (or measurements) of the signal peak

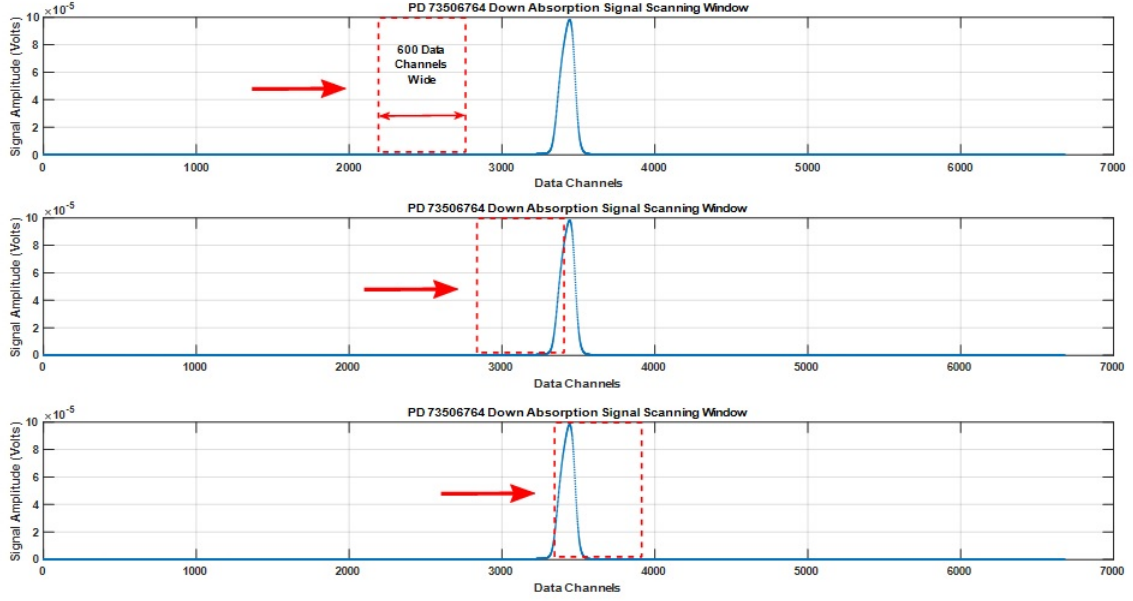


Figure 5.14: The sliding window technique as used on an NMR scan from the PD. A window 600 data channels wide was swept across the signal data. The window started from the left and swept right in intervals of 1 data channel. During each interval, the 600 points were summed together representing the area value under the curve within the specific windowed region.

region. By taking a weighted mean of the points of the sliding window plateau, the area under of the NMR signal peak was accurately measured. The sliding process can be seen in Figure 5.14 and the resulting plateau can be see in Figure 5.15. Amplitude variations in the plateau region reflect the noise within the window and their variance provides a consistent method of estimating the noise contribution to the uncertainty. The following subsections explain the steps of the sliding window technique in greater detail.

5.6.2 Peak Center Determination and Raw Signal Measurement

Due to there being residual background noise in all the measured spectra, the location of where the start and end of each signal peak was unclear. The sliding window technique provided a solution to the aforementioned issue as it incorporated the region outside the signal, which by definition should have no voltage. In practice, there was still some noise in these regions after the spectra was treated leading to non-zero values. However, the sliding window technique would effectively average out the noise in the non-peak region while keeping the signal intact.

The sliding window began away from the peak to ensure the entire peak gets scanned due

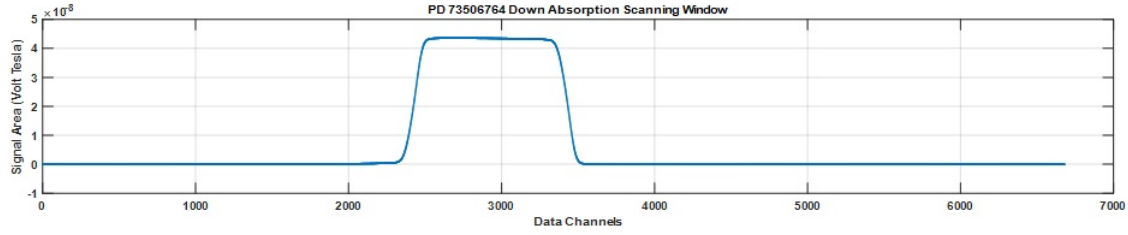


Figure 5.15: The results of the sliding window technique on PD Scan #73506764. The plateau in the center consists of the many individual area under the curve measurements performed by the window. Taking a weighted mean of the center points provides a NMR signal measurement with less error than just a single measurement.

to not being able to determine exactly where the peak started. The sliding window result plot ended up forming a downward dipping plateau. Each end of the plateau corresponded to the beginning and end of the signal peak from the original spectra scan plot. The center of this plateau approximated the sliding window properly over the center of the NMR signal peak. As the sliding window was set purposely larger than the base width of the signal peak, the points around the center of the plateau were also valid measurements of the peak area. By taking an average of the points around the flattish center of the plateau, the area under the NMR signal peak can be approximated with reduced error.

In order to sum up the points of the plateau, the center needed to be determined. This was done by using the sides of the sliding window plateau. Both sides of the plateau were fitted to separate linear fits. These linear fits would intersect centered above the plateau, which offered a good approximation where the center of the sliding window plateau was located. This is demonstrated in Figure 5.16. With the center of the plateau determined, the center point and the adjacent 50 points on both sides (for a total of 101) were used to determine an average value. This was due to the fact that each NMR spectra was composed of thousands of measurements across the resonance condition. At the same time, the top of the sliding window plateau was then composed of hundreds of individual sliding window summations across the NMR signal peak. Now an initial signal value was determined and ready to undergo additional processing.

5.6.3 RF Power Scaling

As mentioned previously, the area under the signal peak is correlated to the polarization of the HD sample within the target using the TE polarization that same sample. The TE

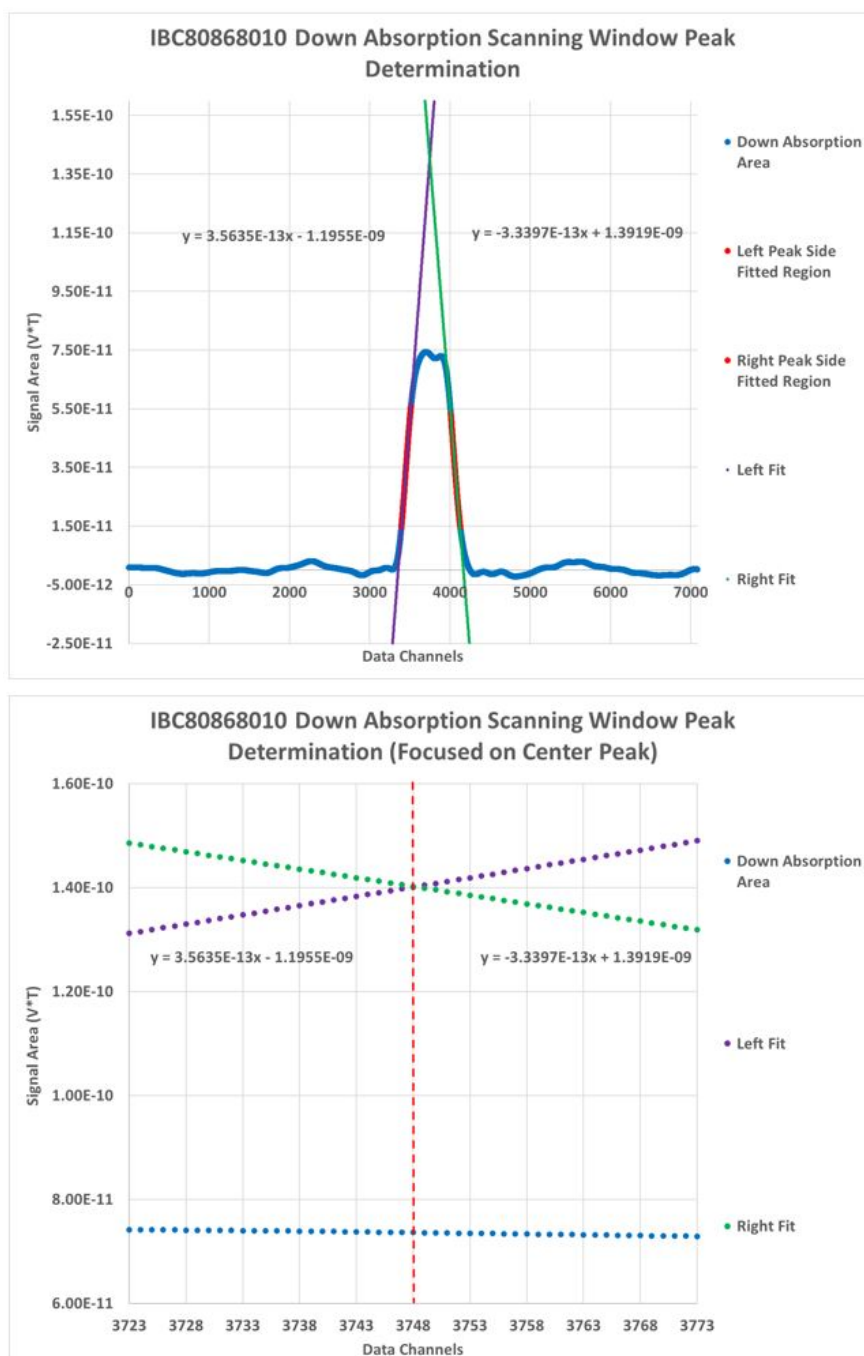


Figure 5.16: Center Peak Determination: The top plot shows the sliding window results where linear fits were applied to the sides of the plateau to locate the plateau center. In the plot below is the same plot, but zoomed in to show the center determination (dashed red line).

polarization was measured in the PD prior to fully polarizing a target in the DF and was dependent upon the temperature of the HD sample material and the magnetic holding field strength. After the target achieved its frozen spin state in the DF, it was transferred back to the PD for a polarized target NMR scan. Before the measurements could be compared

properly, they needed to be scaled to account for the different RF power levels used during the eHD experimental run. The RF levels required to scan for a signal needed to be adjusted as the polarization levels changed within the target.

The power levels of the RF pulses sent through the transmission coil were measured in terms of decibel-milliwatts (dBm). This is a unit of power used to express decibels with a reference of 1 mW being equal to 0 dBm [22]. This means that 10 dBm would be a factor of 10 increase in the power, while 20 dBm would 100 times larger in power. The following relationship describes how to convert the power between units of mW and dBm:

$$P_{mW} = (1mW) * 10^{\frac{P_{dBm}}{10}} \quad (5.26)$$

When a second NMR measurement was taken at a different power level, then the ratio of the two power levels became:

$$\frac{P_{mW1}}{P_{mW2}} = \left(\frac{1mW}{1mW} \right) \left(\frac{10^{\frac{P_{dBm1}}{10}}}{10^{\frac{P_{dBm2}}{10}}} \right) = 10^{\left(\frac{P_{dBm1} - P_{dBm2}}{10} \right)}, \quad (5.27)$$

where P_{mW1} was the first or "reference" power measurement, while P_{mW2} was the second power measurement. Equation 5.27 could then be used to compare the thermal equilibrium NMR measurement with the NMR measurement taken after completing the HD target polarization process. The thermal equilibrium measurements for both polarized targets were taken with a RF power setting of -40dBm. Polarized target scans taken in the PD after aging in the DF had a RF power setting of -20dBm. From the equation above, a difference of 20dBm between NMR measurements resulted in the actual power increasing by 100 fold.

Each NMR scan measured the signal in volts from a receiving coil in the PD using a lock-in amplifier. Changing the RF power settings affected the measured voltage by the square root of the change in power. Combining this with the fact that the scaling factor between the two power levels was a factor of 100, the scaling factor between two NMR measurements was 10. The RF scaling factor between NMR measurements thus was expressed as the square root of the ratio of the power levels as seen in the equation below:

$$s = \sqrt{\frac{P_{mW1}}{P_{mW2}}} = \sqrt{10^{\left(\frac{P_{dBm1} - P_{dBm2}}{10} \right)}} = 10^{\left(\frac{P_{dBm1} - P_{dBm2}}{20} \right)}, \quad (5.28)$$

where s is the scaling factor between NMR measurements taken at different power levels.

5.6.4 TE Signal Measurement and Polarization Calculation

The electrons in the HD sample were highly polarized by cooling the sample to a low temperature in a high magnetic field. During the period when the spins were in thermal equilibrium with the lattice, their polarization was given by the Brillouin function [23] as seen already in Equation 5.6. Before each polarized target began the polarization process in the DF, the targets' thermal equilibrium polarization was measured in the PD. Table 5.1 shows the Run 3 target TE polarization values calculated using Equation 5.6.

eHD Target #	NMR Run #	Temperature (K)	Magnetic Field (T)	P_{TE} (%)
66	PD-I 35072489	1.5180	0.1882	1.2668×10^{-4}
60	PD-I 42251681	1.6520	0.1882	1.1640×10^{-4}

Table 5.1: Thermal equilibrium polarization values from PD for eHD Targets #66 and #60.

After the TE polarization has been determined for a target, it was associated with the area under the NMR signal peak of the TE scan. An NMR signal area measurement taken of a polarized target was converted to polarization value by using the ratio of the area under that signal peak of that particular NMR measurement with the area under the NMR signal peak of the TE NMR signal measurement. This is expressed as the following:

$$P = s * P_{TE} * \left(\frac{A}{A_{TE}} \right), \quad (5.29)$$

where P is the average polarization value of the target HD sample, s is the RF Power scaling factor between two NMR measurements discussed in the previous section, P_{TE} is the TE polarization of the hydrogen molecules, A is the area under the polarized target NMR signal peak, and A_{TE} is the area under the thermal equilibrium signal peak. Both targets #60 and #66 required separate TE measurements due to slight differences in the average HD temperature during the scan. Appendix A.1 describes how the error on each determined polarization value was determined.

Run 2B provided an opportunity to cross check the initial polarization for Run 3A's target #60 by measuring the TE polarization in the IBC itself. This was due to using the same target cell and HD gas sample in both experimental runs. The TE polarization was measured following the same method as in the PD. Both the PD and IBC used the same NMR rack, but different sets of NMR coils. The PD TE measurement used with Equation 5.29 determined the initial polarization to be $39.33 \pm 0.51\%$, while the IBC yielded $37.80 \pm 0.93\%$. Although both the PD

and IBC measurements are in agreement, the IBC measurement has about twice the error. The IBC measurements included noise generated by electronic equipment like the overhead cranes being used in the surrounding Test Lab. As a result, the PD measurements were preferred for determining the initial polarization of a fully polarized eHD target.

Chapter 6

Analysis

6.1 HDice Runs 2A and 2B

Due to the lengthy process of constructing new polarized eHD targets and availability of the liquid helium supply for the QCM to run beam at UITF, preliminary tests with electron beams were done with an unpolarized target. Using an unpolarized target offered practice to develop safe running routines with beam for the polarized target runs, the opportunity to study the HD temperature under various beam conditions, and test the NMR system with an HD sample in UITF. All of which was done with a relatively expendable target that could be condensed and transferred into the IBC in about a week as opposed to over three months.

Run 2A began with the first unpolarized target, target #62. During the run, several electron beam studies were performed in preparation for Run 3A. Run 2A allowed for a check of how the electron beam was rastered as it passed through the IBC at various beam currents, a study of the HD target temperature during beam on operation, and calibration of the liquid helium flow in the IBC. Both Run 2A and 3A tested the same beam conditions.

Due to additional beam controls being added after Run 3A, Run 3B studied additional beam conditions. This resulted in an additional run being added to the experiment using an unpolarized target to study the new conditions introduced in Run 3B. This became known as Run 2B with the "2" referencing the use of an unpolarized target and the "B" referencing the new beam conditions. Run 2B allowed for a target temperature study using the 3B parameters. It used target cell #60 and the same HD gas that was previously used in target #62.

6.1.1 Aspects of Runs 2A & 2B

For both Run 2A and 2B, an unpolarized target was loaded into the IBC while in the UITF. The IBC temperature was more than an order of magnitude lower than that of the PD, and as a result the thermal equilibrium signal generated there was considerably larger than in the PD. Target cell #62 was used during Run 2A with cell #60 was used in Run 2B. Both target HD crystals were condensed from the same sample of gas. Table 6.1 provides the technical details of both target cells.

eHD Non-Polarized Targets		
Ring Number	60	62
Ring Material	4N8-MOF Cu	4N8-MOF Cu
Wire Material	5N8 (5N) Al	5N8 (5N) Al
Wire OD	0.0030"	0.0030"
Number of Wires	960	960
Wire Solder	Indalloy 250 (60/40)	Indalloy 250 (60/40)
H_2 Concentration, $\frac{C(H_2)}{C(HD)}$	$8.3 \pm 1.7\%$	$8.3 \pm 1.7\%$
D_2 Concentration, $\frac{C(D_2)}{C(HD)}$	$1.5 \pm 0.2\%$	$1.5 \pm 0.2\%$

Table 6.1: Characteristics of eHD Targets #62 and #60 used in Runs 2A and 2B respectively.

Experimental Run 2B followed and tested the new beam conditions introduced during Run 3B. To ensure the target used had a short relaxation time to reach thermal equilibrium polarization quickly, the same gas impurity concentrations used during Run 2A were desired. This resulted in condensing the HD crystal from the same gas used to form the crystal from the previous unpolarized target. Additionally, Run 2B used the same target cell that was used in Run 3B, #60. It became available when Run 3B finished and the HD ice was evaporated for collection.

6.1.2 HD Temperature Monitoring

While the focus of Run 2A was primarily calibrating the beam through the target, testing the IBC cooling systems, and NMR system, there was an opportunity to do preliminary HD temperature studies. However, Run 2B was dedicated to further expanding upon these studies using the beam conditions used during Run 3B. These studies included how varying beam

conditions, adjusting the liquid helium flow rates of the IBC, and time affected the temperature of the HD target material as it was monitored.

The target temperature was originally intended to be monitored through the Mixing Chamber as the target is cooled through direct thermal connect with it. The Mixing Chamber temperature was directly monitored by two temperature sensors mounted on its side. However, there was some uncertainty in how accurate the measurement was for the target especially during beam activity. The unpolarized targets, unlike the polarized, were transferred to the IBC within a week of being condensed. This meant the targets did not wait in the DF for the period long enough for the ortho-H₂ and para-D₂ to decay. Instead the impurities continue to decay to their ground states while the targets were in the IBC during their respective runs. The decay process resulted in heat being generated within the HD crystal, which in turn increased its temperature.

The heat generated by beam interaction was removed by the aluminum cooling wires in the target, but there was a desire to investigate the additional effect the decay heat on the wires cooling ability. Although a temperature sensor could not be placed directly on the target to measure the temperature, NMR measurements were capable of being used to do so. The concentrations of H₂ and D₂ in the target ensured very short relaxation times resulting in their polarization quickly reaching the thermal equilibrium level of $\sim 1\%$. This level was determined by the IBC holding field and the temperature of the HD. Curie's Law states that for a paramagnetic material (like the H in HD, but unlike H₂ since its diamagnetic in its ground state), the magnetic susceptibility is inversely proportional to temp:

$$\chi = \frac{C}{T}. \quad (6.1)$$

The magnetization, or anything that measures it like NMR, is:

$$M = \frac{\chi}{B}. \quad (6.2)$$

Thus, the product of the magnetization and temperature of the material is a constant for a fixed field. The benefit to this relationship is that when beam off signal measurements are used in the product, the temperature of the target HD was able to be determined during beam on activity. During the no beam scans, it was assumed the temperature of the HD target material was the same as the Mixing Chamber. Therefore a study of the Run 2A and 2B overnight (no

beam) NMR scans was performed.

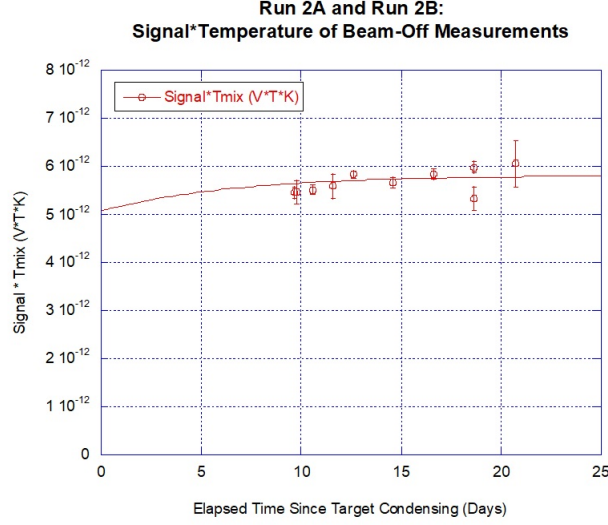


Figure 6.1: Runs 2A and 2B beam-off NMR Signal Measurements * temperature of the HD. The Run 2A data was normalized to the Run 2B. The fit is from using Equation 6.27.

As time elapses after the target is condensed, the amount of ortho-H₂ decreases. This causes the decay heat to decrease. As it decreases, both the temperature of the target and mixing chamber temperatures decrease. The decreasing temperatures cause the polarization to increase slowly over time. The product of this increase in HD temperature and beam off NMR signal was correlated with the product of a beam on signal to determine the HD temperature during beam on conditions. Equation 6.3 shows the relationship of the two products as determined by Curie's Law, while Equation 6.4 shows how the HD temperature of for the beam on runs were determined.

The relationship between the products of the signals and temperatures is expressed by:

$$S_{(beam-on)} * T_{HD(beam-on)} = S_{(beam-off)} * T_{HD(beam-off)}, \quad (6.3)$$

resulting in

$$T_{HD(beam-on)} = \frac{S_{(beam-off)} * T_{HD(beam-off)}}{S_{(beam-on)}}, \quad (6.4)$$

where S stands for an NMR signal with the subscripts designating the type of signal. Similarly, T_{HD} is the temperature of the HD with the same subscripts for designation purposes. The value of $S_{(beam-off)} * T_{HD(beam-off)}$ was extrapolated from the fitted trend line in Figure 6.1 by using

the time from the target condensed to when the beam on measurement took place. Dividing the extrapolated value by the signal of the beam on measurement resulted in finding the HD temperature for a given current beam.

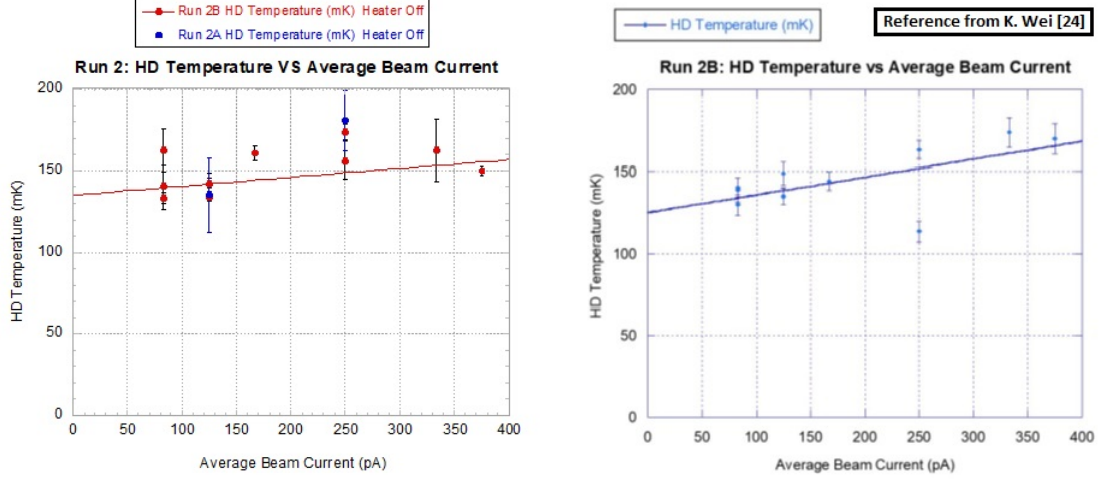


Figure 6.2: Comparison of HD temperature versus average beam current during Run 2 with the IBC Mixing Chamber at ~ 70 mK and the Mixing Chamber heater off. The left plot shows derived temperature calibration curve using data from Run 2A and 2B. The plot on the right is the calibration curve previously derived by Kevin Wei [24] using Run 2B data only.

The different Run 2B beam currents and their determined HD temperatures are plotted in Figure 6.2. The plots in this figure provide an estimate of the HD target material temperature as a function of the beam current being used with the eHD target in the IBC. The linear fit can thus be used as a temperature calibration curve used in estimating the temperature of the HD target material for specific beam currents. The HD temperature calibration curve was constructed mostly with Run 2B data, as the HD temperature study was the primary focus of this run. Run 2A had two different beam currents tested with the same conditions as in Run 2B and thus the data could be combined with Run 2B to construct the curve as seen in plot on the left in Figure 6.2. The plot to the right shows a temperature calibration curve previously derived by Kevin Wei [24]. Despite the previous work not including the Run 2A data points, the calibration curves agree well with each other. This is due to the measurements of the Run 2A 125pA and 250pA beam conditions being the same, within error, of the same current Run 2B measurements. Thus the calibration curve isn't effected much at all by the addition of the Run 2A points.

6.2 HDice Runs 3A and 3B

Both Runs 3A and 3B used polarized targets at UITF. Run 3A studied beams of continuous currents on target, while Run 3B expanded upon this by including average currents of different duty factors. However, both targets had issues with the raster settings. This resulted in different regions receiving different doses from the beam.

6.2.1 Aspects of Run 3A

Experimental Run 3A had polarized target #60 installed in the IBC for testing with varying electron beam conditions. A summery of target #60's physical characteristics can be found in Table 6.2. The initial polarization of the target prior to any beam time in the IBC was measured to be $39.12 \pm 0.35\%$.

Ring Number	60
Ring Material	4N8-MOF Copper
Wire Material	5N8 (5N) Aluminum
Wire OD	0.0030"
Number of Al wires	960
In/Pb wire coating	Indalloy 205 (60/40)
Operating Field	1.1T
Raster Scale (At Operating Field)	1.00
NMR Field	0.9T
Raster Scale (At NMR Field)	1.20

Table 6.2: Summery of Target #60 information.

Electrons beams were produced at various currents during Run 3A and tested on target #60. Additionally, various temperatures and magnetic holding field strengths were tested with the polarized target while installed in the IBC. Each Run 3A beam condition used for testing the polarized target is listed in Table C.1. After verifying the run settings for each beam condition and sending beam through the target, several NMR measurements were periodically taken. These measurements were used to monitor the behavior of the target's polarization during beam exposure.

Besides analyzing the target's polarization, it was important to study the accumulated dose on the HD target material by beam operations. This was done through the use of pico-ammmeters located right before the IBC and at the end of the beam line in the beam dump. The average current was monitored and recorded by the pico-ammmeters. The measurements taken were used to determine the total accumulated dose on the target during the various beam conditions of Run 3A.

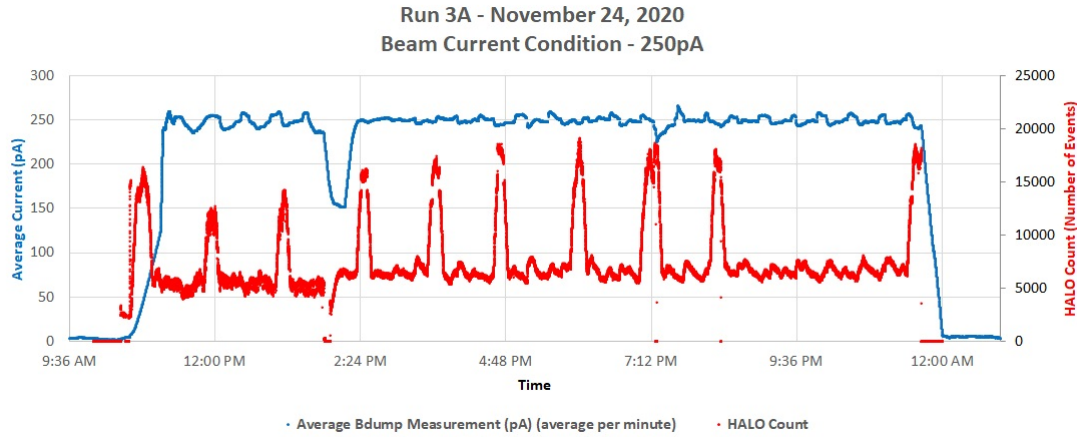


Figure 6.3: Sample of monitored HALO counts and accumulated dose as a function of time from the pico-ammmeter during Run 3A . This data was taken for the second 250pA beam condition of Run 3A on November 24, 2020. The red spikes correspond to time periods where NMR measurements were taken.

Figure 6.3 is an example of how the average beam current was recorded by the pico-ammmeters. Also included in the plot are the corresponding HALO counts for the second 250nA beam period. The red spikes of the HALO counts correspond to the times when NMR measurements were taken. This meant ramping the field down from 1.1T to 0.9T and increasing the raster scale to better fill the target. The latter condition had a larger beam spread on target and consequently higher HALO rates (red spikes) as more electrons spread out into the detectors. These rates were used to determine the average magnetic holding field.

Along with the accumulated dose, the temperature of the HD target material was monitored. During the experimental run this was done by using a temperature sensor on the Mixing Chamber in the IBC. The mixing chamber and target are in direct thermal contact with each other, so the HD temperature was taken to be the same as the temperature of Mixing Chamber when the beam was off. This allowed adjustments to be made to the liquid helium flow rate

of the IBC's cooling system. When beam was delivered to the target, the measurement of the HD temperature was no longer simply taken as the mixing chamber temperature. Additional temperature studies were performed during Runs 2A and 2B to develop a calibration used with the Mixing Chamber temperature measurements to determine the HD temperature for specific average beam currents (see Section 6.1.2).

6.2.2 Results with eHD Target #60

Each NMR measurement of Run 3A was used to extract a polarization value of the HD material within target #60. These values were first plotted versus the date/time and then by the accumulated dose from the electron beam runs. Figure 6.4 shows the polarization as well as the accumulated dose of Run 3A as a function of time. The polarization values here are weighted from the four separate signal measurements each NMR scan provides as discussed in the previous chapter.

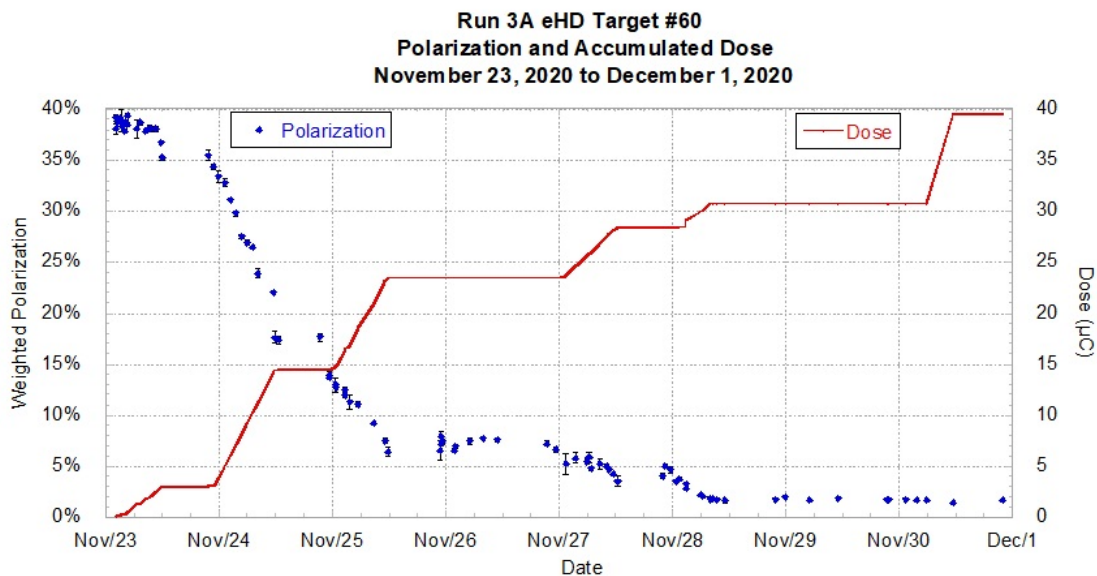


Figure 6.4: Target #60 polarization and accumulated dose as a function of time.

In Figure 6.5 there are doses where the polarization drops suddenly. These drops correspond to overnight periods where there was no beam going through the target when the polarization drops over this time due to a lowered T_1 . These drops can be seen in Figure 6.4 as well, though slightly harder to observe due to the drop occurring over the overnight time period versus occurring all at the same dose.

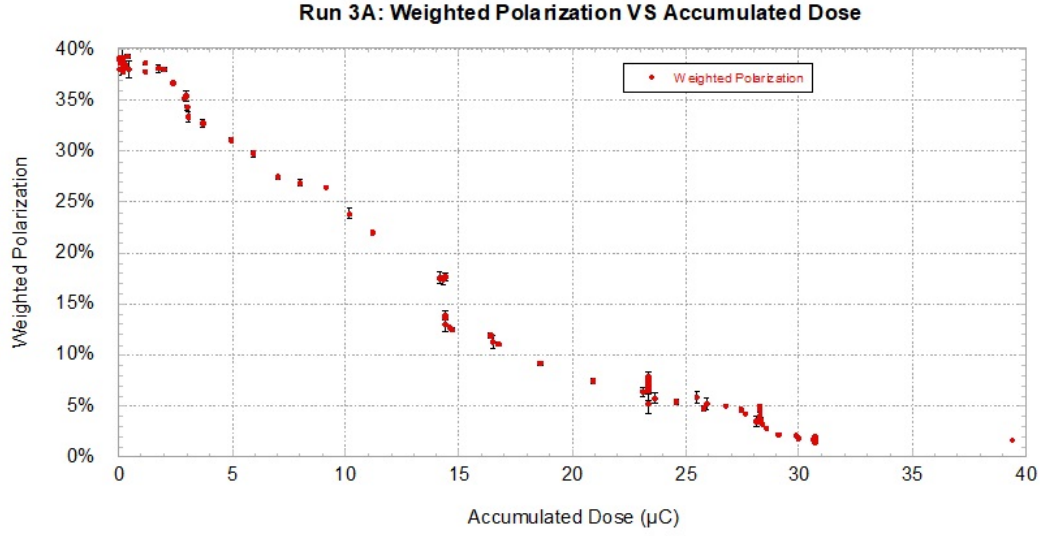


Figure 6.5: Run 3A initial polarization versus accumulated dose.

6.2.3 Aspects of Run 3B

Experimental Run 3B had polarized target #66 installed in the IBC for testing with varying electron beam conditions. This run differed from 3A in that new beam current controls became available to use allowing for additional beam conditions to be tested with the second polarized target. These controls allowed for beam blanking, which could "chop" a continuous beam into pieces, delivering an average current equivalent to the desired current of a continuous beam. For example, instead of a continuous wave 125pA electron beam (like used in Run 3A), a 167pA beam being blanked one-third of the time could be used to produce an average 125pA electron beam current.

Ring Number	66
Ring Material	4N8-MOF Copper
Wire Material	5N8 (5N) Aluminum
Wire OD	0.0030"
Number of Al wires	960
In/Pb wire coating	Indalloy 205 (60/40)
Operating and NMR Field	0.9T
Raster Scale	1.20

Table 6.3: Summery of Target #66 information.

In this case, the remaining two-thirds of the beam reaches the target and is referred to as being two-third duty factor or "2/3 DF". The beam blanking pattern for 2/3 DF can be seen in Figure 4.15. Run 3B allowed for the comparison of the continuous electron beam currents with average beam currents of different duty factors. This allowed to see whether the polarization lose was dependent entirely on accumulated dose or if duty factor could effect the lose rate.

A summery of target #66's physical characteristics can be found in Table 6.3. The initial polarization of the target in the IBC prior to any beam time in the IBC was measured to be $32.72 \pm 0.41\%$ of the HD material. Each Run 3B beam condition used for testing the polarized target is listed in Table C.2. Just as in Run 3A, after verifying the run settings for each beam condition and sending beam through the target, several NMR measurements were taken. These measurements were used to monitor the behavior of the target's polarization during beam exposure.

Like with Run 3A, it was also important to study the accumulated dose on the HD target material by beam operations. The pico-ammmeters located right before the IBC and at the end of the beam line in the beam dump were again used to measure the average current. These measurements were used to determine the total accumulated dose on the target during the various beam conditions of Run 3B.

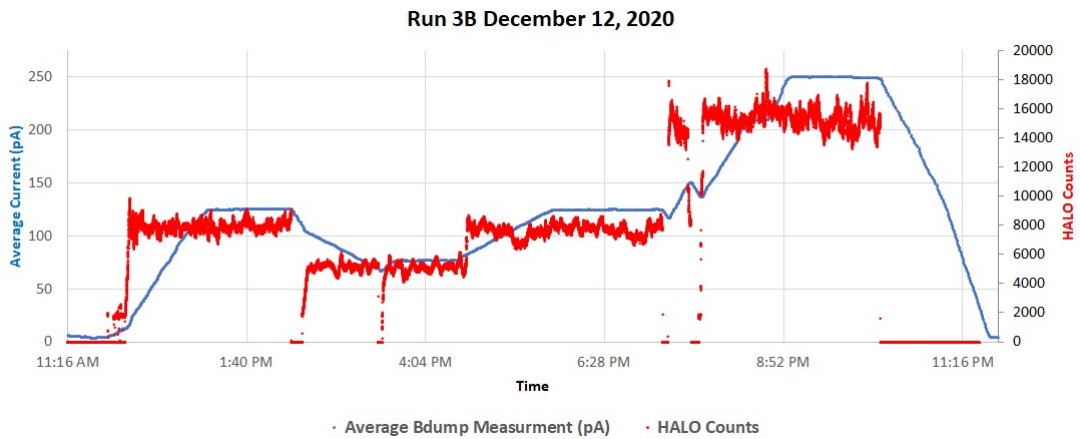


Figure 6.6: Sample of monitored HALO counts and accumulated dose as a function of time from the pico-ammmeter during Run 3B. This data was taken during the third 125pA, third 83pA, fourth 125pA, and the 250pA beam conditions of Run 3B on December 12, 2020.

Figure 6.6 is an example of the average beam current was recorded by the pico-ammeters and the corresponding HALO counts for the multiple beam-on periods during December 12, 2020. The red spikes of the HALO counts demonstrate periods where the beam drifted out of alignment resulting in part of the beam scattering off the copper target ring. When the beam was out of alignment, the HALO counts would increase as more particles scattered. The measured average beam current would decrease in response to less electrons reaching the beam dump due to the increased scattering. Beam operators would adjust the beam alignment in response to the spikes to ensure the beam went back through the center of the HD sample. There are also two instances of the electron beam cutting out. During the 83pA and 250pA conditions, the beam cut out temporarily before being reset.

Just as with target #60, the temperature of the HD target material was monitored throughout each beam condition. This was done during the experimental run, in part, by using the Mixing Chamber temperature sensor. The HD temperature was taken to be the same as the temperature of Mixing Chamber when the beam was off. When beam was delivered to the target, the measurement from the Mixing Chamber temperature sensor no longer accurately measured the temperature of the target. Again, the temperature calibration derived from the additional temperature studies performed during Runs 2A and 2B was used with the Mixing Chamber temperature measurements to determine the HD temperature for specific average beam currents (see Section 6.1.2).

6.2.4 Results with eHD Target #66

The results of extracting the polarization values from the NMR measurements of Run 3B can be plotted versus either the date and time each NMR measurement taken, or the accumulated dose of the target when the measurement was taken.

Figure 6.7 shows the accumulated dose of Run 3B as a function of time along with the weighted polarization values. Note that the periods where the polarization drops suddenly in Figure 6.8 where there was no beam activity yet the polarization of the target drops over time due to a lowered T_1 . This is the same effect with target #60 described in the previous section.

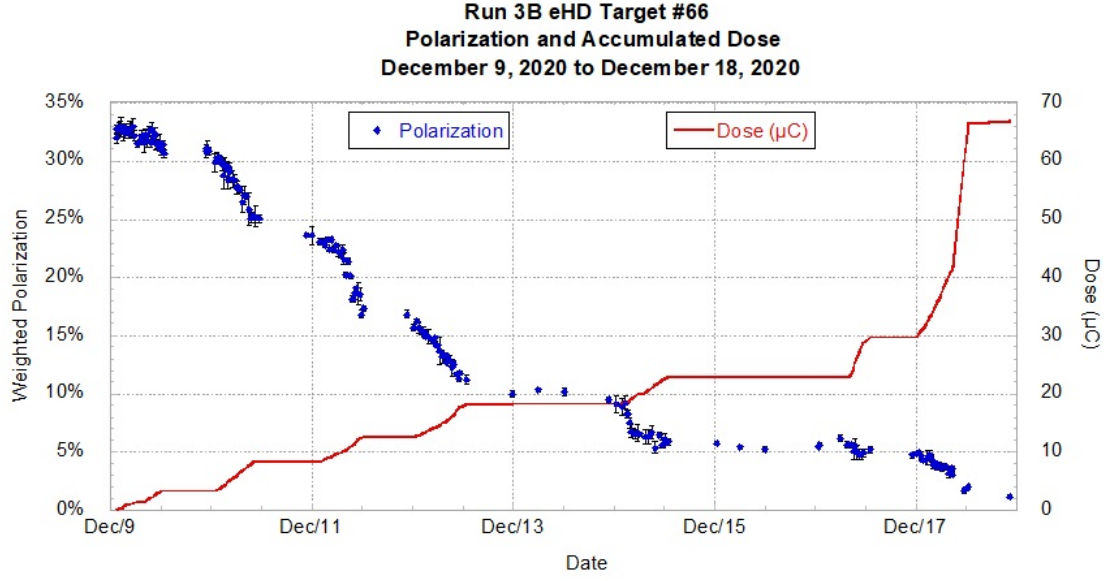


Figure 6.7: Run 3B initial polarization versus experimental run time.

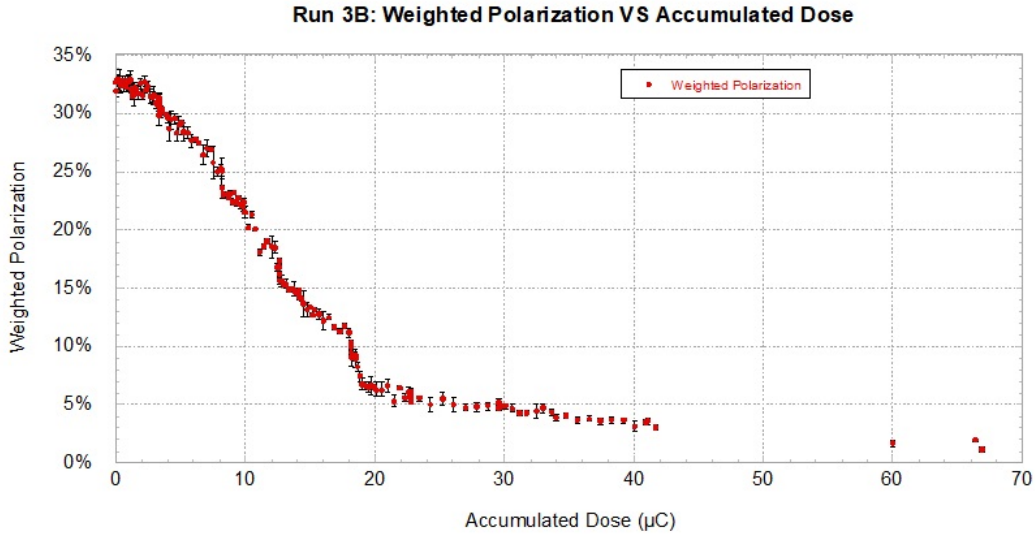


Figure 6.8: Run 3B initial polarization versus accumulated dose.

6.2.5 Spiral Raster Correction

The initial target polarization vs accumulated dose plots in Run 3A and 3B, seen in Figures 6.5 and 6.8, show the polarization decreasing in two distinct trends. For both polarized targets, the polarization loss rate was steady until the total target accumulated dose between $\sim 17 \mu C$ and $20 \mu C$. After receiving this dose, the polarization loss rate decreases. The rastered beam profile did not have sharp boundaries. This is already evident in the shape of the beam spot

at the dump after the target, Figure 4.9, and is clearly seen in a HARP scan of the beam just before entering the IBC (Figure 6.9). Although the central region is relatively flat, apart from small undulations, there are significant tails, and this resulted in regions of significantly differing accumulated dose.

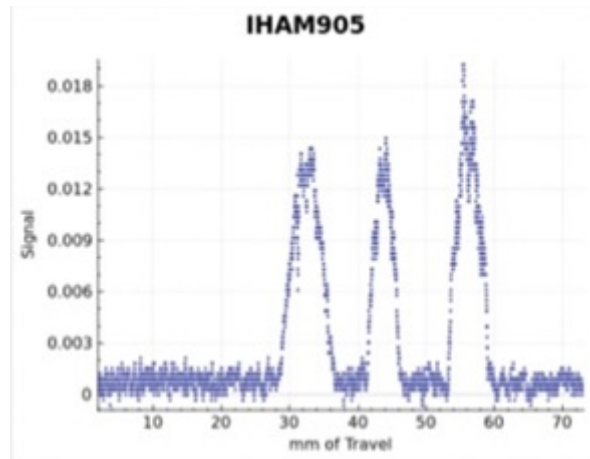


Figure 6.9: The radiation intensity near a HARP BPM just before the entrance to the IBC, plotted as a function of the position of three thin wires that are passed through the beam, at different angles to the beam axis.

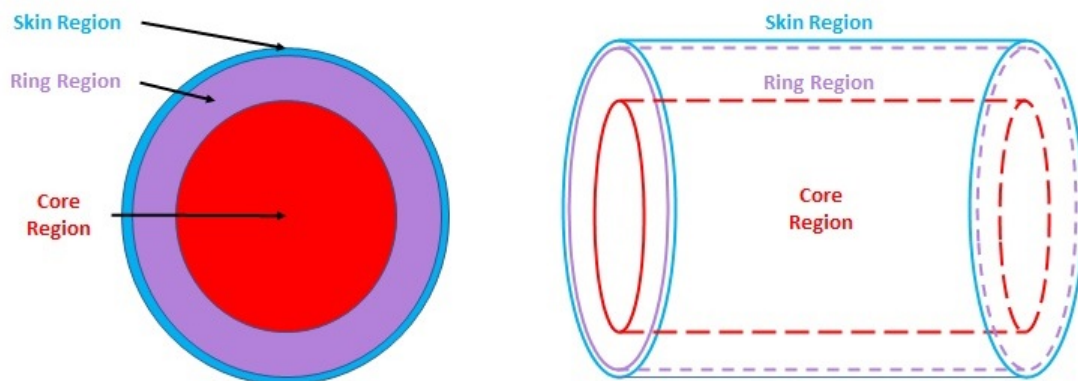


Figure 6.10: The image on the left shows a cross-sectional view of the target, where the regions experiencing different dose rates are labeled as Skin, Ring, and Core Regions. The figure to the right is a side view of the target regions.

The targets were broken down into three distinct regions. An uniform core concentrated at the center of the target was surrounded by an outer region, called the ring. The difference between each region was the core consistently received a larger dose from receiving more beam

flux during each beam run as compared to the ring region. Outside of the ring was a third region referred to as the skin. The skin effectively received no dose compared to either of the other regions. This means the HD material within the skin region lost no polarization throughout the beam runs. It explains why each polarized target continued to have NMR signals indicating remaining polarized material despite the core and ring regions being completely used up.

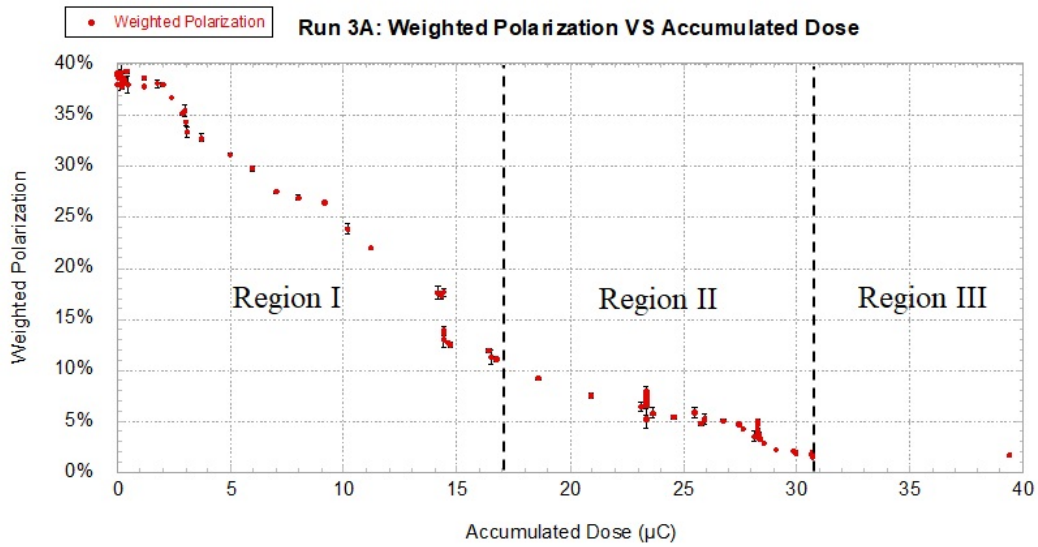


Figure 6.11: Run 3A demonstrated changes in the rate of polarization loss in different regions, separated by the vertical black dashed lines.

The target region breakdown is illustrated in Figure 6.10. Region I in Figures 6.11 and 6.12 represent the core, ring, and skin contributions total target polarization. Region II is where the core contributions has already died or complete depolarized, leaving just the ring and skin polarized material providing any NMR signals. In the last region, called Region III, only the polarized skin material remains to provide an NMR signal. The skin region of Run 3A and 3B effectively received no irradiation compared to the other regions, regaining polarized throughout the experiment. As a result, there was always some amount of polarized material causing the total target polarization to never be fully depleted. When the core and ring regions of both 3A and 3B were depleted, the lowest the total polarization reached was $\sim 1.6\%$ due to the skin contribution.

The distribution of the rastered beam was separated into just the core and surrounding ring region. This was done by determining when the polarization loss rate changes suddenly at a total accumulated dose at $19.46\mu\text{C}$ for target #60 and $19.94\mu\text{C}$ for target #66. At this point,

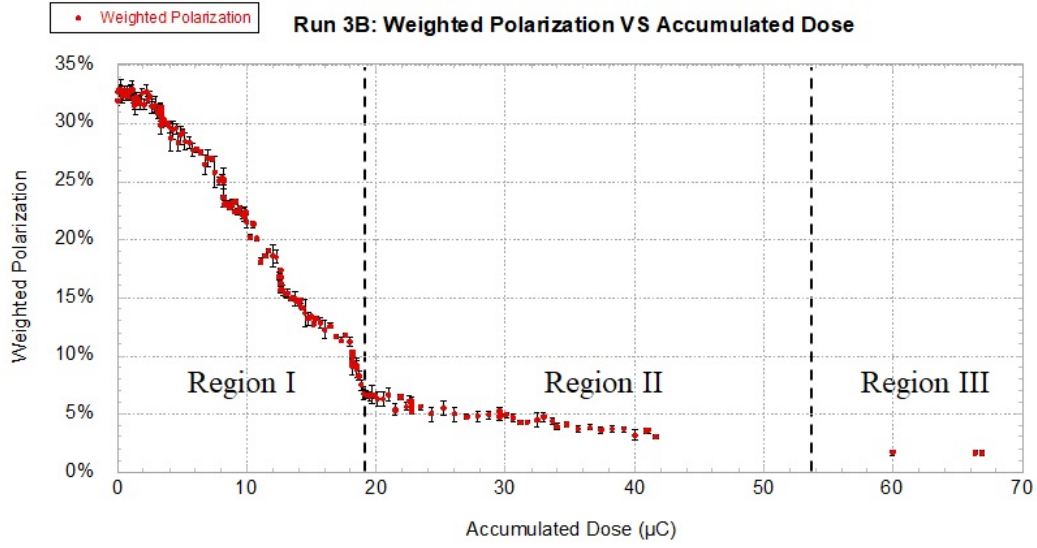


Figure 6.12: Run 3B demonstrated changes in the rate of polarization loss in different regions, separated by the vertical black dashed lines.

the core polarization was completely used up. After that dose, only the HD material within the ring and skin still had some amount of polarized HD material. The polarization loss rate in the ring region was not only different, but it was smaller due to receiving less beam irradiation than the core for each run condition. Eventually the ring region would lose all of its polarization. At this point, the skin was the only region providing a contribution to the NMR signal and it was simple to measure and then remove to isolate the core and ring regions separately.

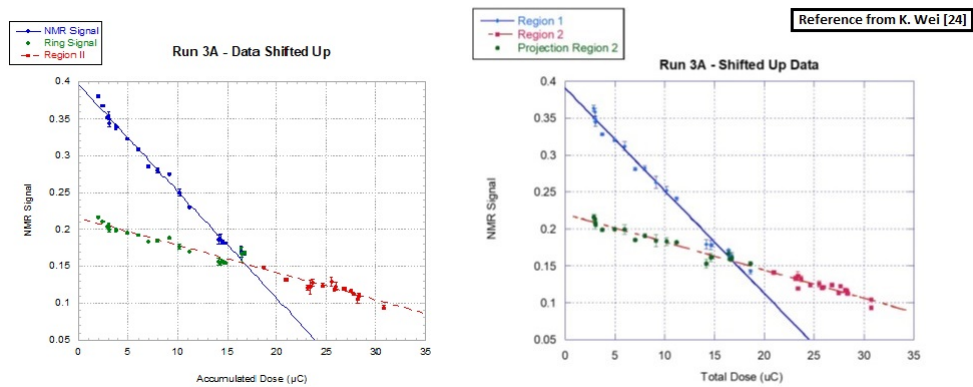


Figure 6.13: Run 3A shifted NMR Signal data with the projected ring only signals within Region I. The left plot shows the results of extrapolating the ring signals from the data and methods described within this chapter. On the right, the plot shows the previous work done determining the ring signals in Region I done by Kevin Wei [24].

Separating the regions began with studying the NMR polarization measurements at the end of each experimental run at UITF. It was observed that after accumulating dose, the polarization stopped decreasing and remained constant instead of being fully depleted. The only way a signal larger than the TE signal could be present is if there was still polarized material in the target that was not receiving any dose. Region III was defined by the NMR measurements that are constant despite the total target dose accumulating. Without a polarization loss rate in Region III, the skin contribution to the total signal is constant here as well as the other regions. The skin constant skin contribution was found easily by itself in Region III and then subtracted from the total signal contribution in Region II.

The difference is between the two is the ring contribution to the total signal. A linear fit was applied to region II to represent the ring and skin contributions. It was then extrapolated backwards into Region I (see Figures 6.13 and 6.14). Next, the Region II fit could be subtracted from Region I to separate out the core only contribution to Region I. Once the core, ring, and skin contributions are separated from the total signal, then could then be converted to actual polarization values for each region of the target. The core and ring regions of each target essentially became separate two targets to study for each target loaded in the IBC.

In addition to using the fit from Region II to isolate the core signal contribution in Region I, the fit can be used to extrapolate the NMR polarization values for the ring within Region I, as seen in Figures 6.13 and 6.14. The extrapolated values come from using the initial total target NMR signal values with the fit values to scale the ring signal values in Region I. The plots also project the dose in which the core region's polarization is entirely depleted. For Run 3A, target #60's core region was determined depleted by $16.99 \pm 0.68 \mu\text{C}$. Both the previous work done and this work agree with determining the core depletion to occur when the target's total accumulated dose reaches approximately $17.0 \mu\text{C}$. This is where the Region I and II fits intersect.

Figure 6.14, demonstrates the ring signal projection for the Run 3B polarized target. Unlike Run 3A, the projected core depletion in 3B was $19.55 \pm 0.35 \mu\text{C}$. This is almost $2.5 \mu\text{C}$ larger than the previous run. A better metric for comparison between Run 3A and 3B is instead to use the accumulated dose in a region per region area of the target. In order to make those comparisons of the core dose per core area or the ring region equivalent, the target region areas needed to be determined. In addition to this, the total accumulated dose needed to be broken into separate core and ring contributions. Section 6.2.6 discusses the procedure for determining

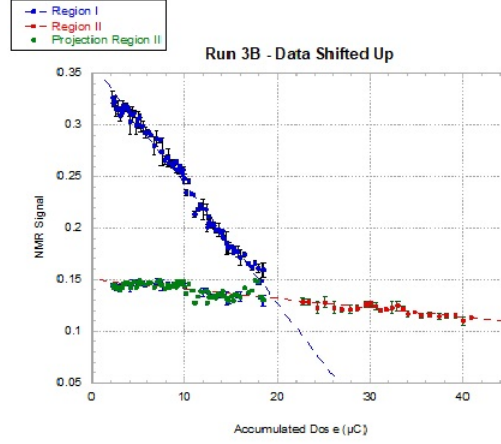


Figure 6.14: Run 3B shifted NMR Signal data with the projected ring only signals within Region I plotted.

these necessary pieces of information along and continues with the comparison of the regions.

6.2.6 Dose Determination

After establishing that the beam flux was not the same throughout the different sections of the target, it was necessary to examine the differences in accumulated doses in each to further study how the polarization changes with dose. To do so, the beam off periods were removed and polarization values after each period were shifted up. Shifting up was to account for the polarization loss that occurred during the overnight, no beam activity periods. This was to simulate continuous beam operation for each polarized target. After this was done, the two main polarization loss trends became easily observable. The weighted mean polarization values in these plots are then instead treated as the NMR signal magnitudes. A linear fit was applied to the groups of signals in Region I and Region II. This can be seen in Figures 6.13 and 6.14.

The determined linear trends could then be used to estimate the polarization loss rate in each region. The blue linear fits represent the polarization loss rate of both the core and ring sections until target #60's total accumulated dose reached $\sim 17.0\mu\text{C}$ and target #66's reached $\sim 19.5\mu\text{C}$. After these doses, each of the targets' core sections were fully depolarized. Then the red fits represent the polarization loss rate of just the ring sections of the targets. The polarization loss rate of the ring sections were separated from the rates of the core sections within Region I by taking the ratio of the two linear fits and multiplying that by total signal measurements in Region I. Doing so projected data points of the ring sections within Region I.

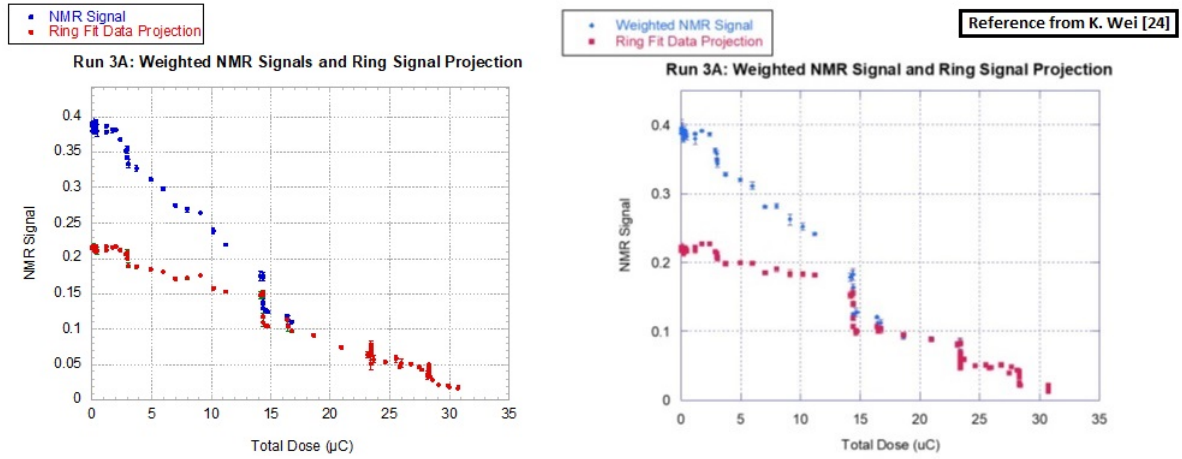


Figure 6.15: Run 3A NMR signals with overnight data and the projected ring signals. The left plot is of the signals derived from Section 6.2.6, while the right plot is a reference of previous work done by K. Wei [24].

The Run 3A projections can be seen in Figure 6.13 as the green data points. This figure also shows the ring projections in Region I are in agreement with those previously determined by Kevin Wei [24] for target #60. Run 3B's ring projections are demonstrated for the first time in 6.14. With the ring projections determined along Region II's extended fit, the overnight periods could be reinserted by shifting the data points down after at each overnight period an amount proportional to what the signal drop was originally.

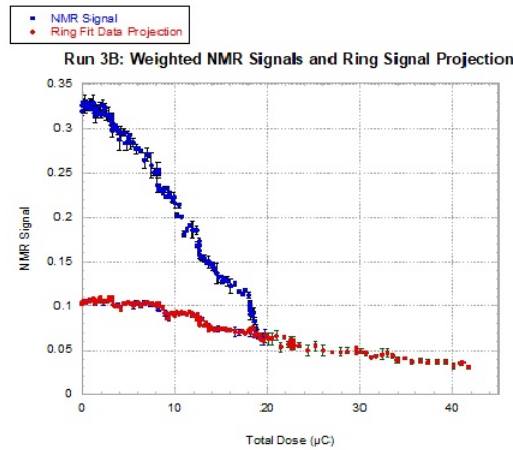


Figure 6.16: Run 3B NMR Signals with overnight data and the projected ring signals are plotted on the right.

There is no transfer of polarization between the core and ring regions of the eHD targets

because the spin-spin relaxation time of frozen-spin targets, known as T2, is essentially infinite. With this in mind and the previous work to separate the regions of the target with the fits, the next goal is to break up the total accumulated dose from the electron beam on the target into parts for the different regions. The core accumulated dose at a different rate than the ring because the core always saw a uniform beam across its region during beam operations, while the ring region wasn't as uniformly covered. As mentioned earlier in the chapter, the skin region effectively never accumulated any dose resulting in the total target polarization never being completely depleted. To separate the core and ring accumulated doses from the total, it is important to note that before ever seeing beam, the eHD target is uniformly polarized. This initial polarization is thus the same for each region before decreasing at different rates due to receiving different doses from the beam. Despite losing polarization from the different doses, the lose rate should be the same rate per unit dose of the region over area of the region. Lastly, the core and ring sections of the polarized targets are proportional to the initial NMR signals measured of the two main fitted trends. Using all this information, thus the areas of the core and ring can be expressed as:

$$A_C = \left(\frac{S_C^0}{S_T^0} \right) * A_T \quad (6.5)$$

$$A_R = \left(\frac{S_R^0}{S_T^0} \right) * A_T, \quad (6.6)$$

where A^T is the total cross-sectional area of the target, A^C is the area of core region, A^R is the ring region area, S_T^0 is the total initial measure NMR signal, S_C^0 is the core contribution of the total NMR signal, and S_R^0 is the ring contribution to the total signal.

$$D_C = f * D_R \quad (6.7)$$

$$D_T = D_C + D_R \quad (6.8)$$

$$D_T = (1 + f) * D_R \Rightarrow D_R = \frac{1}{(1 + f)} * D_T \quad (6.9)$$

$$D_T = \frac{(f + 1)}{f} * D_C \Rightarrow D_C = \frac{f}{(f + 1)} * D_T, \quad (6.10)$$

where D_T is the accumulated dose of the total target, D_C is the dose accumulated in the core only, D_R is the accumulated dose in just the ring region, and f is the proportionality constant between the core dose and ring dose. The polarization in the core section is proportional to

the ratio of the core NMR signal contribution with it's initial signal value. Likewise, the ring section is proportional to the ratio of the Ring NMR signal contribution with it's initial signal value.

$$\langle P_C \rangle = \left(\frac{S_C}{S_C^0} \right) * \langle P_C \rangle_i \quad (6.11)$$

$$\langle P_R \rangle = \left(\frac{S_R}{S_R^0} \right) * \langle P_R \rangle_i, \quad (6.12)$$

where P_C is the polarization of the core region, P_R is the polarization of the ring region, S_C is the signal contribution from the core region, and S_R is the signal contribution from the ring region.

The polarization loss rates of the core and ring sections, with respect to the dose per unit area of each respective section, should be the same:

$$\frac{d\langle P_C \rangle}{d(\frac{D_C}{A_C})} = \frac{d\langle P_R \rangle}{d(\frac{D_R}{A_R})}, \quad (6.13)$$

The total cross sectional area of the target is simply their sum, $A_T = A_C + A_R$. Multiplying the polarization decay rates by an amount of their respective dose per unit area results in the polarization change in each of the sections after receiving that amount of each respective dose per unit area:

$$\frac{d\langle P_C \rangle}{d(\frac{D_C}{A_C})} * \frac{D_C}{A_C} = d\langle P_C \rangle - d\langle P_C \rangle_i = \left(\frac{S_C}{S_C^0} \right) * \langle P_C \rangle_i - \langle P_C \rangle_i \quad (6.14)$$

$$\frac{d\langle P_R \rangle}{d(\frac{D_R}{A_R})} * \frac{D_R}{A_R} = d\langle P_R \rangle - d\langle P_R \rangle_i = \left(\frac{S_R}{S_R^0} \right) * \langle P_R \rangle_i - \langle P_R \rangle_i. \quad (6.15)$$

Solving for the polarization decay rate results in the following expressions:

$$\frac{d\langle P_C \rangle}{d(\frac{D_C}{A_C})} * \frac{D_C}{A_C} = \left(\frac{A_C}{D_C} \right) (\langle P_C \rangle_i) \left(\frac{S_C}{S_C^0} - 1 \right) \quad (6.16)$$

$$\frac{d\langle P_R \rangle}{d(\frac{D_R}{A_R})} * \frac{D_R}{A_R} = \left(\frac{A_R}{D_R} \right) (\langle P_R \rangle_i) \left(\frac{S_R}{S_R^0} - 1 \right) \quad (6.17)$$

The two polarization decay rates should be the same and result in the following:

$$\left(\frac{A_C}{D_C} \right) (\langle P_C \rangle_i) \left(\frac{S_C}{S_C^0} - 1 \right) = \left(\frac{A_R}{D_R} \right) (\langle P_R \rangle_i) \left(\frac{S_R}{S_R^0} - 1 \right) \quad (6.18)$$

Going further, an expression relating D_C to D_R can be derived:

$$D_C = \left[\left(\frac{A_C}{A_R} \right) \left(\frac{\langle P_C \rangle_i}{\langle P_R \rangle_i} \right) \left(\frac{\left(\frac{S_C}{S_C^0} - 1 \right)}{\left(\frac{S_R}{S_R^0} - 1 \right)} \right) \right] D^R \quad (6.19)$$

This expression can be combined with 6.7 to solve for each target section's proportionality constant f:

$$f = \left(\frac{A_C}{A_R} \right) \left(\frac{\langle P_C \rangle_i}{\langle P_R \rangle_i} \right) \left(\frac{\left(\frac{S_C}{S_C^0} - 1 \right)}{\left(\frac{S_R}{S_R^0} - 1 \right)} \right) \quad (6.20)$$

The target is uniformly polarized at the start of Run 3A and 3B. Each section has the same initial polarization. This means, $\langle P_C \rangle_i = \langle P_R \rangle_i$ and $\frac{\langle P_C \rangle_i}{\langle P_R \rangle_i} = 1$.

$$f = \left(\frac{A_C}{A_R} \right) \left(\frac{\left(\frac{S_C}{S_C^0} - 1 \right)}{\left(\frac{S_R}{S_R^0} - 1 \right)} \right) = \left(\frac{S_C^0}{S_R^0} \right) \left(\frac{\left(\frac{S_C}{S_C^0} - 1 \right)}{\left(\frac{S_R}{S_R^0} - 1 \right)} \right) = \frac{(S_C - S_C^0)}{(S_R - S_R^0)} \quad (6.21)$$

From this expression the term to either side of the equation with respect to their section can be separated and then differentiated with respect to the total dose:

$$f * (S_R - S_R^0) = (S_C - S_C^0) \quad (6.22)$$

$$f * \left(\frac{dS_R}{dD_T} - \frac{dS_R^0}{dD_T} \right) = \left(\frac{dS_C}{dD_T} - \frac{dS_C^0}{dD_T} \right) \quad (6.23)$$

The initial NMR measurement signals are used as constants. This results in their derivatives being equal to zero and reduces Equation 6.23 to:

$$f * \left(\frac{dS_R}{dD_T} \right) = \left(\frac{dS_C}{dD_T} \right) = \left(\frac{dS_T}{dD_T} - \frac{dS_R}{dD_T} \right) \quad (6.24)$$

The proportionality constant f can be solved for to give an expression in terms of the polarization loss rates:

$$f = \frac{\left(\frac{dS_T}{dD_T} \right)}{\left(\frac{dS_R}{dD_T} \right)} - \frac{\left(\frac{dS_T}{dD_T} \right)}{\left(\frac{dS_T}{dD_T} \right)} = \frac{\left(\frac{dS_T}{dD_T} \right)}{\left(\frac{dS_R}{dD_T} \right)} - 1. \quad (6.25)$$

The result is that the f constant defines the division of the dose between the core and ring. It is derived from the slopes of Regions I and II, using the polarization decay rate in the first region as dS_T/dD_T and the second region's decay rate as dS_R/dD_T .

Run #	3A	3A (Reference)	3B
dS_T/dD_T	$-0.0139 \pm 1.11\text{E-}04$	$-0.0139 \pm 3.5\text{E-}4$	$-0.0116 \pm 7.17\text{E-}05$
dS_R/dD_T	$-0.0037 \pm 1.66\text{E-}04$	$-0.0038 \pm 4.4\text{E-}4$	$-0.00121 \pm 5.49\text{E-}05$
f constant	2.75 ± 0.01	2.66 ± 0.07	11.87 ± 0.04
D_C/D_T	0.733 ± 0.023	0.727 ± 0.014	0.922 ± 0.066
D_R/D_T	0.267 ± 0.056	0.273 ± 0.005	0.078 ± 0.007
S_T^0	0.389 ± 0.002	0.390 ± 0.008	$0.360 \pm 8.37\text{E-}4$
S_C^0	0.172 ± 0.003	0.171 ± 0.011	0.179 ± 0.007
S_R^0	0.208 ± 0.007	0.207 ± 0.007	$0.083 \pm 1.2\text{E-}3$
S_{skin}^0	0.016 ± 0.002	0.012 ± 0.003	0.016 ± 0.002
A_C	$1.262 \pm 0.060 \text{ cm}^2$	$1.243 \pm 0.086 \text{ cm}^2$	$1.608 \pm 0.216 \text{ cm}^2$
A_R	$1.457 \pm 0.03 \text{ cm}^2$	$1.505 \pm 0.064 \text{ cm}^2$	$1.057 \pm 0.155 \text{ cm}^2$
Target Diameter	$1.90 \pm 0.01 \text{ cm}$	$1.90 \pm 0.01 \text{ cm}$	$1.90 \pm 0.01 \text{ cm}$
Core Diameter	$1.28 \pm 0.02 \text{ cm}$	$1.30 \pm 0.03 \text{ cm}$	$1.45 \pm 0.02 \text{ cm}$

Table 6.4: Properties of the core and ring sections of Runs 3A, 3A (Reference) [24], and 3B.

Table 6.4 provides a summary of values derived from the expressions above for both Runs 3A and 3B. In addition, a 3A reference column is provided for comparison to previous work done [24]. The target diameters were all the same value due to using the same size target cell, while the core diameter changed due to the target holding field and beam raster settings. The errors provided in the table were calculated using the error propagation techniques provided in Appendix A. Run 3A's values agree with previous work done. The same analysis methods used to analyze Run 3A were used to analyze Run 3B. The differences between the values from Run 3A differ from those of Run 3B are accounted for by the difference in raster settings.

6.2.7 Corrected eHD Run 3A Results for the Core and Ring Sections

The correction methods described in Section 6.2.6, were then applied to the NMR and dose data to separate eHD target #60 into two regions that could then be studied separately and compared to each other later. This allowed for additional studies. This section provides the results of separating the core and ring regions within the target.

The polarization loss rates in Figures 6.17 and 6.18 can be adjusted to simulate contin-

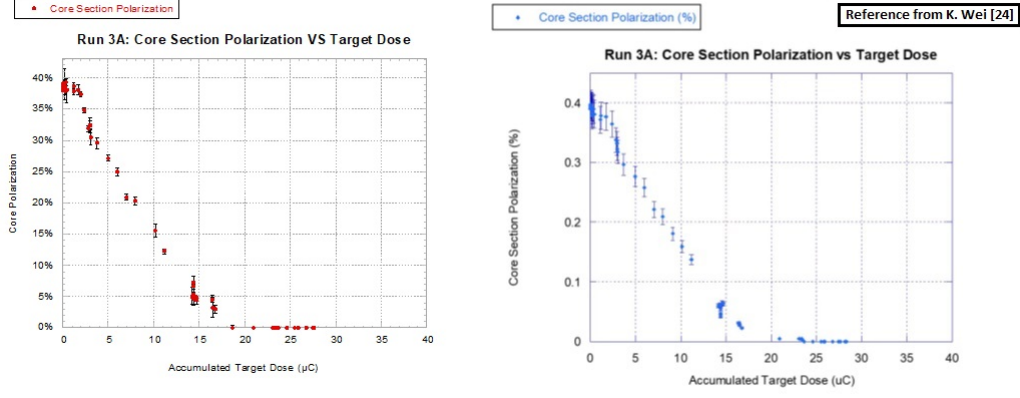


Figure 6.17: Run 3A core section polarization values as a function of accumulated total target dose. In both plots, the data were shifted up to simulate continuous running without overnight periods. The left plot is of the polarization values derived from Section 6.2.6, while the right plot is a reference of previous work done by K. Wei [24].

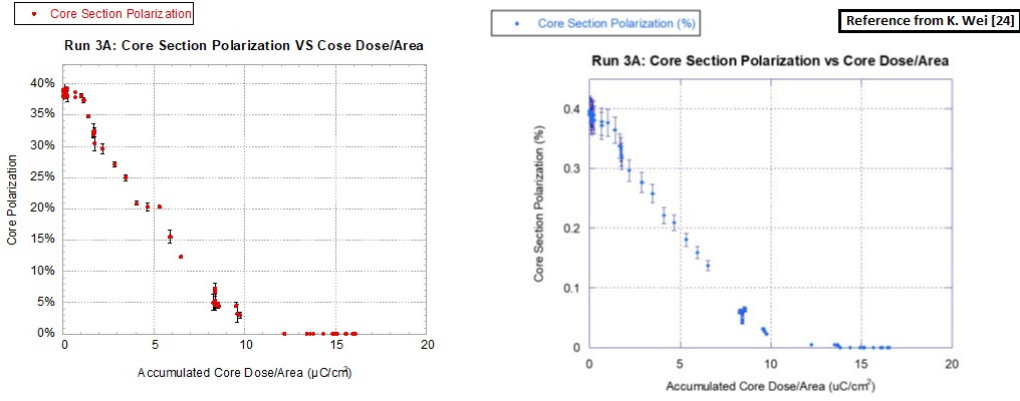


Figure 6.18: Run 3A core section polarization values as a function of the core section accumulated dose. In both plots, the data were shifted up to simulate continuous running without overnight periods. The left plot is of the polarization values derived from Section 6.2.6, while the right plot is a reference of previous work done by K. Wei [24].

uous beam on the target throughout the entire experimental run. This is done by removing the overnight periods of no beam activity and shifting all data points up after each period, compensating for the polarization drops that occurred each night during the no beam periods as seen in Figure 6.21. After shifting, the points show clear trends in polarization loss rates. The core section polarization drops to $1/e$ of its initial polarization value after accumulating $\sim 6\mu C/cm^2$ or $3.7E-13$ electrons/ cm^2 . It is also projected to lose the entire core polarization by $\sim 10\mu C/cm^2$. This agrees with the previous Run 3A (Reference) analysis.

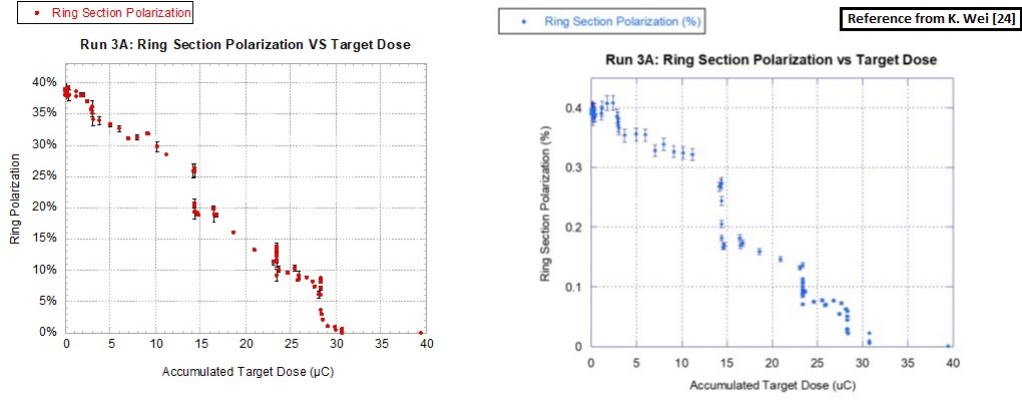


Figure 6.19: Run 3A ring section polarization values as a function of accumulated total target dose. The left plot is of the polarization values derived from Section 6.2.6, while the right plot is a reference of previous work done by K. Wei [24].

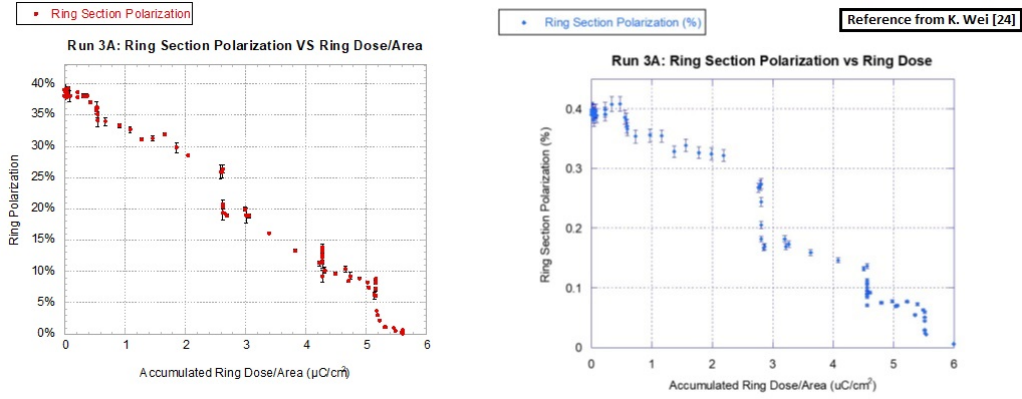


Figure 6.20: Run 3A ring section polarization values as a function of ring section accumulated dose. These plots show the ring data before removing the overnight scans and the data shifts to simulate continuous beam running. The left plot is of the polarization values derived from Section 6.2.6, while the right plot is a reference of previous work done by K. Wei [24].

Similar to the core section, the ring section data seen in Figures 6.19 and 6.20 includes the overnight NMR scans. Again, to simulate a continuous beam on the ring section, the overnight scans were removed with the remaining data shifted accordingly. This treated data can be seen plotted versus the ring dose per area in Figure 6.22. The plot confirms that the ring section demonstrates the same trends in polarization loss rate as the core section and that both sections were depleted of all polarization at approximately the same dose per area.

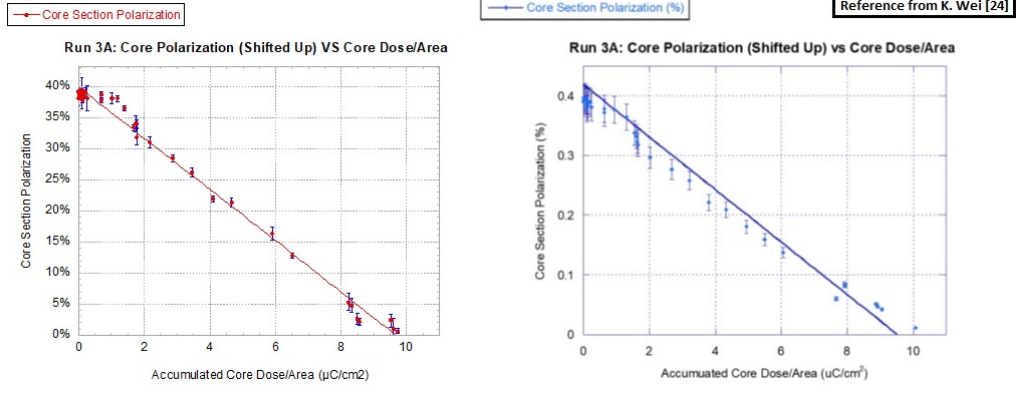


Figure 6.21: Run 3A core section polarization values as a function of the core section accumulated dose with the overnight periods removed and data shifts to simulate continuous beam use. The left plot is of the polarization values derived from Section 6.2.6, while the right plot is a reference of previous work done by K. Wei [24].

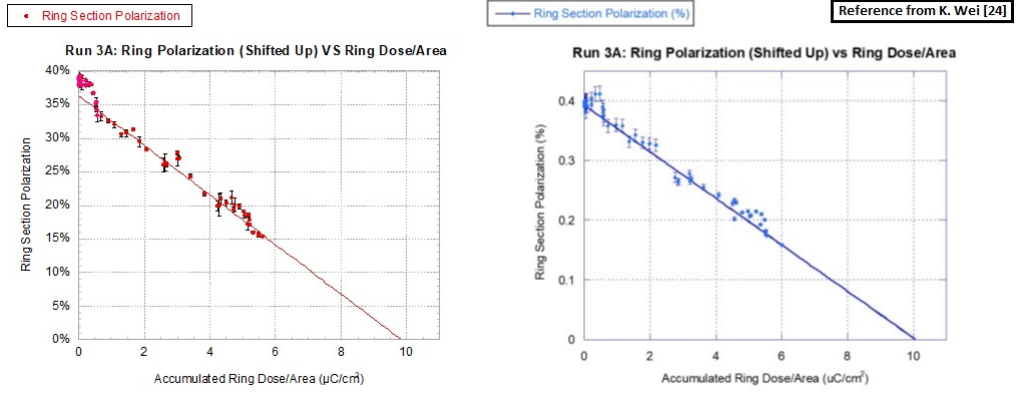


Figure 6.22: Run 3A ring section polarization values as a function of the ring section accumulated dose with the overnight periods removed and data shifts to simulate continuous beam use. The left plot is of the polarization values derived from Section 6.2.6, while the right plot is a reference of previous work done by K. Wei [24].

6.2.8 Corrected Run 3B Results for the Core and Ring Sections

The correction methods described in Section 6.2.6, were applied again for eHD target #66 to separate the NMR and dose data into core and ring regions. This section provides the results of separating the core and ring regions within the polarized target used in Run 3B.

The polarization loss rates in Figures 6.23 and 6.24 were adjusted like with Run 3A, to simulate continuous beam on the target throughout the entire experimental run. After removing the overnight data and shifting the rest accordingly, the points show again show clear trends in

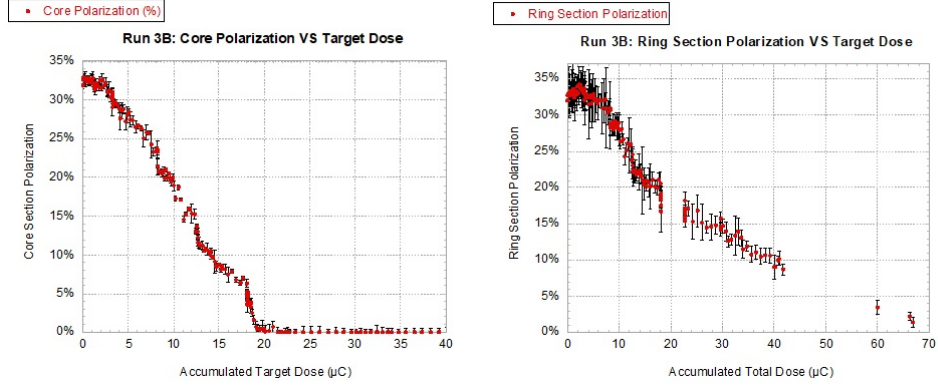


Figure 6.23: Run 3B core polarization versus total target accumulated dose on the left with the ring polarization versus total target accumulated dose on the right. Note the removal of the high and low holding field points were removed from the ring data.

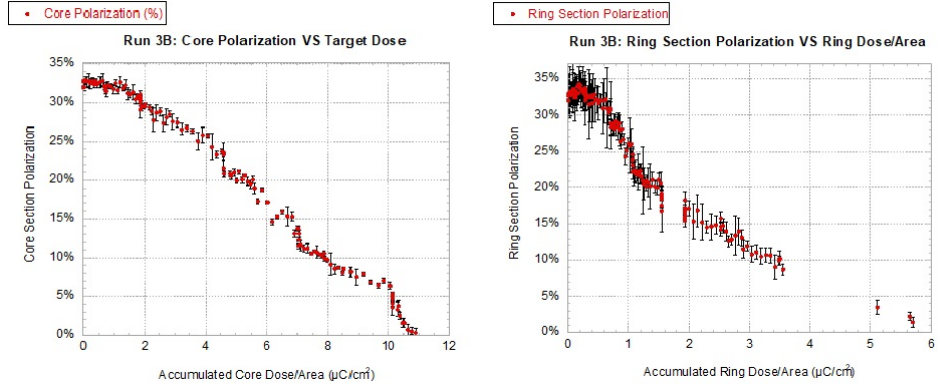


Figure 6.24: Run 3B core polarization versus accumulated core dose/area on the left with the ring polarization versus ring dose/area on the right. Note the removal of the high and low holding field points were removed from the ring data.

polarization loss rates.

The Run 3B core and ring polarizations drop to $1/e$ of their initial polarization values after accumulating $\sim 6\mu C/cm^2$ or $3.7E-13$ electrons/ cm^2 , demonstrating the same behavior as with the first polarized target. Each target section, as seen in Figure 6.25, are still projected to lose their entire polarization by $\sim 10\mu C/cm^2$. This agrees with what was observed by the previous target in Run 3A, confirming the polarization loss trends observed were the same for both the eHD targets. Even with the additional beam conditions tested in Run 3B, the rate of polarization loss still has a linear dependence with accumulated dose per area.

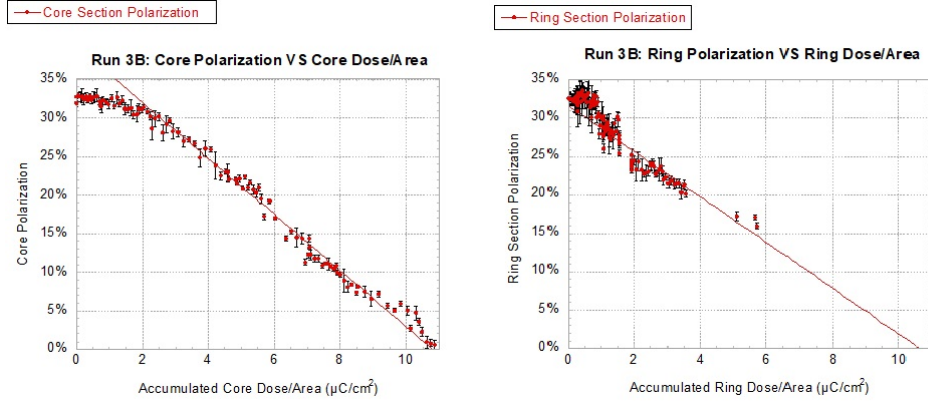


Figure 6.25: Run 3B core polarization versus core dose per area (left) and ring polarization versus ring section dose per area (right). Both plots have the overnight periods removed and data shifts to simulate continuous beam use.

6.2.9 Relaxation Time Determination

After the polarization values of an HD target were determined for a given beam current, the relaxation time of the HD material could be extracted by fitting the values to Equation 2.1. The T_1 values for beam off times were found the same way. An example of the beam on and beam off T_1 determinations can be seen in Figures 6.26 and 6.27 respectively.

Figure 6.26 has both the core and ring polarization values fitted separately to Equation 2.1 for the same beam current condition. The fitting process to determine the T_1 value was done through the following steps:

1. The average beam current and the total accumulated dose on the entire target were determined. After this, the doses for the core and ring regions of the target were calculated as done in Section 6.2.6. Figure 6.26 shows a beam condition of 250pA with the accumulated core and ring doses determined in Section 6.2.6. For beam conditions during Run 3A, $D_C/D_T = 0.733 \pm 0.023$ and $D_R/D_T = 0.267 \pm 0.056$. Taking the total accumulated dose and multiplying it by either of these rates determines the dose in the core and ring regions respectively.
2. The initial HD temperature within the target during the 0.25nA beam condition seen in Figure 6.26, was determined to be 149mK using the determined temperature curve from Section 6.1.2. This HD temperature was calibrated to the base running temperature of the IBC, 70mK. At base, the Mixing Chamber heater was off, contributing no additional

heat to the Mixing Chamber. Additional heat from the heater being on proportionally shifted the calibration by the difference between between the heater on Mixing Chamber temperature and the heater off (IBC base temperature). The result is then added to the HD temperature from the temperature calibration curve. For the 250pA being discussed, the heater was on. This results in the calibrated HD temperature being determined as $149mK + (161mK - 70mK) = 240mK$.

3. During this run condition, the average magnetic holding field for the HD target was 1.04T. Using this, along with the determined HD temperature and Equation 5.5, the Thermal Equilibrium polarization of the target was found to be 0.0044, or 0.44%. P_{TE} was fixed at this value in Equation 2.1 when fitting T_1 .

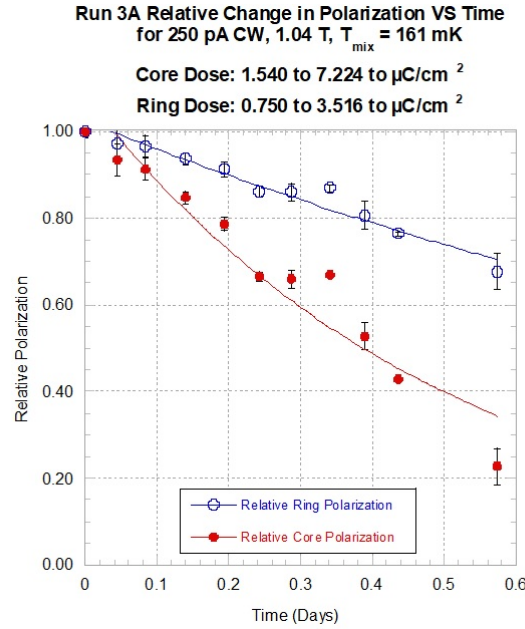


Figure 6.26: The polarization values from the run condition with 0.25 nA and at 161 mK (a temperature elevated by a resistive heater) are fitted to Equation 2.1 and divided by the initial polarization for the beam condition to find the relative change in polarization.

Polarization values measured during each beam condition for the ring and core were converted to relative polarization values by dividing each value by the initial polarization value of the condition. The Thermal Equilibrium polarization was calculated for each run condition just as it was done for the 250pA run condition. Like the polarization values, the Thermal Equilibrium polarization was also converted to a relative value by dividing it by the initial polarization value of the condition and then used with the fitting equation. By using the rela-

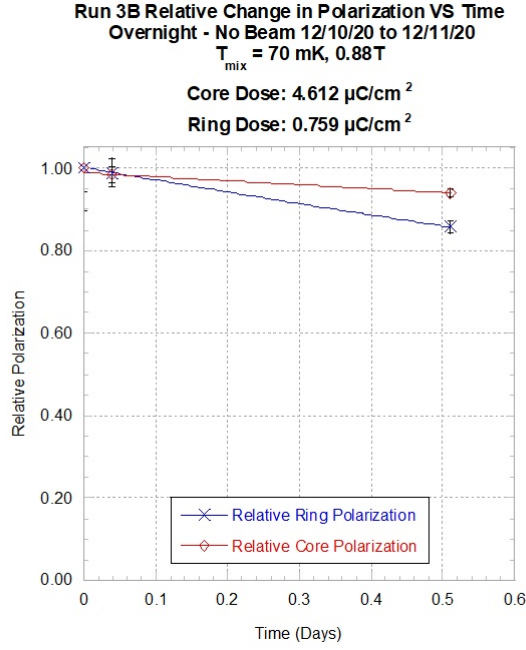


Figure 6.27: The relative change in polarization during a Run 3B overnight, no beam condition at the IBC base temperature. The polarization values were fitted to Equation 2.1 and divided by the initial polarization for that overnight condition to find the relative change in polarization.

tive polarization values plotted as a function of time, the relative change in polarization values were comparable between the results for the core and ring sections. The relaxation times (T_1 values) were then extracted from each run condition's relative change in polarization data. The remaining plots from which the T_1 values were derived by fitting the data to Equation 2.1 are located in Appendix F. Summaries of the T_1 values for each beam condition in Run 3A can be found in Tables 6.5, 6.6, 6.7, and 6.8. The Run 3B T_1 value summaries can be found in Tables 6.9, 6.10, 6.2.9, and 6.12.

Tmix (mK)	THD (mK)	B (T)	Core Dose/Area ($\mu\text{C}/\text{cm}^2$)	Core T_1 (Days)	Core T_1 Error (Days)
158	158	1.04	1.6809	9.154	2.644
161	161	1.04	8.128	0.942	0.018
70	70	1.04	13.19935	N/A	N/A
70	70	1.04	15.96453	N/A	N/A

Table 6.5 continued from previous page

Tmix (mK)	THD (mK)	B (T)	Core Dose/Area ($\mu\text{C}/\text{cm}^2$)	Core T_1 (Days)	Core T_1 Error (Days)
----------------------------	---------------------------	------------------------	--	---	---

Table 6.5: The Run 3A T_1 values from fitting the polarization data of the core section for the no beam run conditions are listed above. Due to the NMR measurements being taken during no beam periods, the temperature of the HD is the same as the Mixing Chamber. The core polarization is depleted entirely before the last two sets of measurements were taken so there are no T_1 values available.

Tmix (mK)	THD (mK)	B (T)	Ring Dose/Area ($\mu\text{C}/\text{cm}^2$)	Ring T_1 (Days)	Ring T_1 Error (Days)
160	160	1.04	0.601346	11.106	2.955
160	160	1.04	2.907785	1.608	0.038
70	70	1.04	4.722122	19.405	1.213
70	70	1.04	5.711374	4.267	0.181

Table 6.6: The Run 3A T_1 values from fitting the polarization data of the ring section for the no beam run conditions. The Mixing Chamber and HD temperatures are the same due to these being beam-off measurements.

Beam Current (nA)	Tmix (mK)	THD (mK)	B (T)	Starting Core Dose/Area ($\mu\text{C}/\text{cm}^2$)	Ending Core Dose/Area ($\mu\text{C}/\text{cm}^2$)	Core T_1 (Days)	Core T_1 Error (Days)
0.125	158	238	1.04	0.125869	0.261899	5.631	2.769
0.125	161	241	1.04	0.659262	1.680892	1.479	0.05
0.25	161	247	1.04	1.704599	7.994681	0.501	0.008
0.25	239	325	1.04	8.127888	10.49965	0.235	0.113
0.125	70	156	0.45	N/A	N/A	N/A	N/A

Table 6.7: The Run 3A T_1 values from fitting the polarization data of the core section for beam-on run conditions. There is no T_1 value for the core section after the fourth row because all the core polarization is gone by this run condition.

Beam Current (nA)	T _{mix} (mK)	THD (mK)	B (T)	Starting Ring Dose/Area ($\mu\text{C}/\text{cm}^2$)	Ending Ring Dose/Area ($\mu\text{C}/\text{cm}^2$)	Ring T_1 (Days)	Ring T_1 Error (Days)
0.125	158	238	1.04	0.04503	0.093685	7.113	3.823
0.125	161	241	1.04	0.235854	0.601346	1.759	0.07
0.25	161	247	1.04	0.609827	2.86013	1.533	0.063
0.25	239	325	1.04	3.311644	4.664572	1.067	0.06
0.125	70	156	1.04	4.722122	5.680883	0.637	0.082

Table 6.8: The Run 3A T_1 values from fitting the polarization data of the ring section for beam-on run conditions.

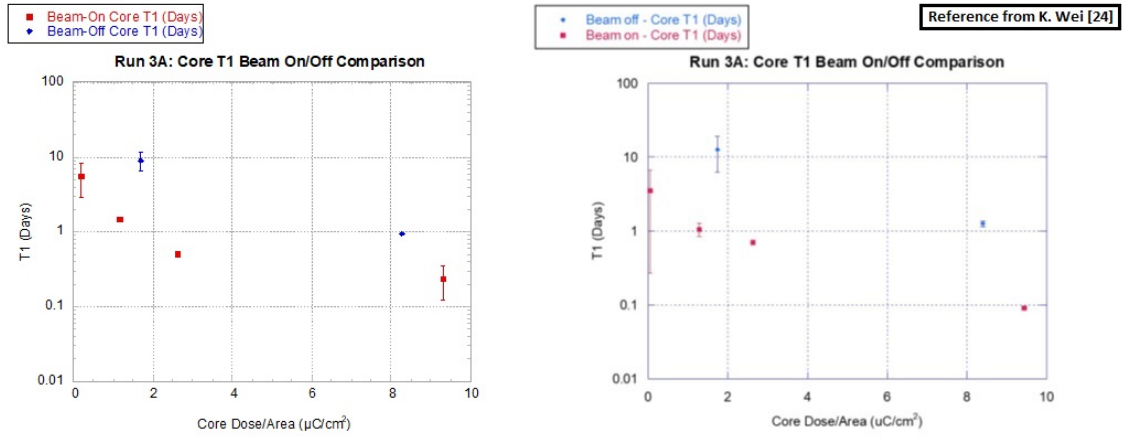


Figure 6.28: Comparing the T_1 values between the beam-on and beam-off NMR measurements of the core section of Run 3A.

Figures 6.28 and 6.29 are used to compare the T_1 values of the 3A core and ring target regions with those found previously for target #60. Each plot monitors the polarization relaxation time values for the beam on periods and overnight periods when the beam was off. The figures demonstrate that the T_1 values while the beam is on are almost an order of magnitude smaller compared to the values from the beam off periods. Also shown in the plots is how as dose accumulates within a section of the target, the T_1 values steadily decrease. Evidently, the electron beam creates charges within the HD crystal that serve as paramagnetic centers of depolarization.

Mano and Honig's previous work expected such a depolarization mechanism [11]. The is-

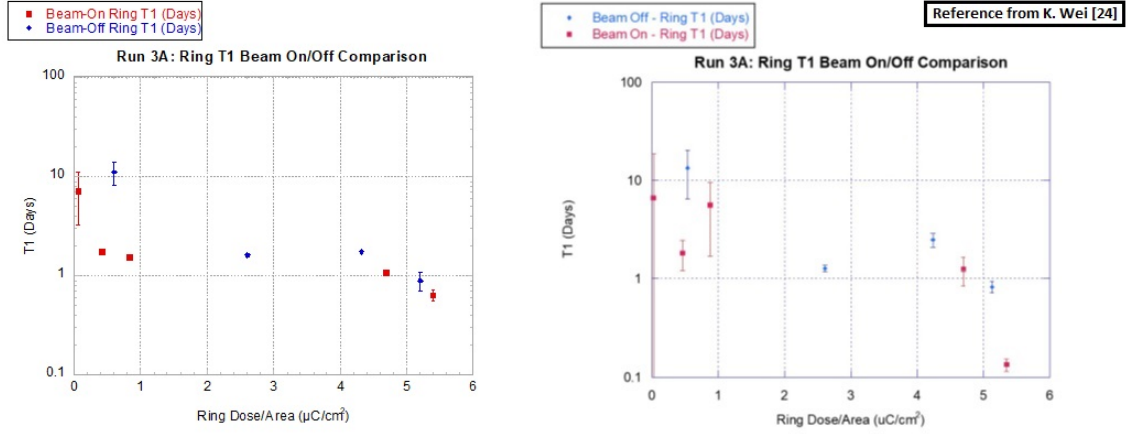


Figure 6.29: Comparing the T_1 values between the beam-on and beam-off NMR measurements of the Ring section of Run 3A.

sue with this depolarization mechanism is that if they neutralized immediately after the beam was removed, the expected overnight T_1 values should be higher. However, the targets continued losing polarization throughout the night indicating a secondary depolarization mechanism present after a day of beam operation. The overnight T_1 results are then interpreted such that additional depolarization occurs through a cloud of charge, coming from the beam and its associated secondaries, transiting the target. The ring data show similar trends to the core. As the ring region first received dose, the T_1 values were higher. As the dose accumulated, the T_1 values decrease towards being on the order of 1 day like in the core. The same trends observed in 3A were seen in 3B's core and ring sections as well. These trends can be seen in Figure 6.30.

Tmix (mK)	THD (mK)	B (T)	Core Dose/Area ($\mu\text{C}/\text{cm}^2$)	Core T_1 (Days)	Core T_1 Error (Days)
70	70	0.88	1.8473	N/A	N/A
70	70	0.88	4.612056	10.104	4.488
70	70	0.88	7.08296	2.8164	0.0371
70	70	0.88	10.17355	3.2602	1.19

Table 6.9: The Run 3B T_1 values from fitting the polarization data of the core section for beam-off run conditions.

T_{mix} (mK)	THD (mK)	B (T)	Ring Dose/Area ($\mu\text{C}/\text{cm}^2$)	Ring T_1 (Days)	Ring T_1 Error (Days)
70	70	0.88	0.30407	8.2913	5.3033
70	70	0.88	0.759159	3.2809	0.8719
70	70	0.88	1.163108	2.666	0.776
70	70	0.88	1.674599	11.861	7.47
70	70	0.88	2.096192	21.11	15.38

Table 6.10: The Run 3B T_1 values from fitting the polarization data of the ring section for beam-off run conditions.

<u>Beam</u> <u>Current</u> <u>(nA)</u>	<u>T_{mix}</u> <u>(mK)</u>	<u>THD</u> <u>(mK)</u>	<u>B</u> <u>(T)</u>	<u>Starting Core</u> <u>Dose/Area</u> <u>($\mu\text{C}/\text{cm}^2$)</u>	<u>Ending Core</u> <u>Dose/Area</u> <u>($\mu\text{C}/\text{cm}^2$)</u>	<u>Core T_1</u> <u>(Days)</u>	<u>Core T_1</u> <u>Error</u> <u>(Days)</u>
0.083nA Average, 0.25nA Peak	70	142	0.88	0	0.684181	5.631	2.769
0.125nA Average, 0.188nA Peak	72	149	0.88	0.731289	1.84729	3.7827	0.846
0.125nA Average, 0.188nA Peak	72	149	0.88	1.84729	2.154611	6.63	18.624
0.167nA Average, 0.250nA Peak	73	153	0.88	2.237049	4.612056	1.401	0.084
0.083nA Average, 0.125pA Peak	72	146	0.88	4.612056	5.556451	5.1703	2.3129
0.167nA Average, 0.250nA Peak	73	153	0.88	5.612531	7.066136	0.5116	0.033
0.125nA CW	73	150	0.88	7.08296	7.500199	0.91272	0.25028
0.083nA Average, 0.125nA Peak	74	148	0.88	7.591049	7.913512	4.1492	6.1007
0.125nA Average, 0.375nA Peak	78	155	0.88	7.935383	8.519181	0.41895	0.05346
0.250nA CW	78	163	0.88	8.585355	10.09336	0.44266	0.06731

Table 6.11: The Run 3B T_1 values from fitting the polarization data of the core section for beam-on run conditions.

	<u>Tmix</u>	<u>THD</u>	<u>B</u>	<u>Starting Ring</u>	<u>Ending Ring</u>		<u>Ring T_1</u>
<u>BeamCurrent(nA)</u>	<u>(mK)</u>	<u>(mK)</u>	<u>(T)</u>	<u>Dose/Area</u>	<u>Dose/Area</u>	<u>Ring T_1</u>	<u>Error</u>
				<u>($\mu\text{C}/\text{cm}^2$)</u>	<u>($\mu\text{C}/\text{cm}^2$)</u>	<u>(Days)</u>	<u>(Days)</u>
0.083nA Average, 0.25nA Peak	70	142	0.88	0.04503	0.093685	29.888	59.835
0.125nA Average, 0.188nA Peak	72	149	0.88	0.120372	0.30407	33.763	111.16
0.125nA Average, 0.188nA Peak	72	149	0.88	0.30407	0.354656	1.533	0.063
0.167nA Average, 0.250nA Peak	73	153	0.88	0.354656	0.759159	1.067	0.06
0.083nA CW	72	146	0.88	0.759159	0.914609	0.637	0.082
0.167nA Average, 0.250nA Peak	73	153	0.88	0.914609	1.147139	7.2857	4.6052
0.125nA CW	73	150	0.88	1.167355	1.234556	3.1329	2.9796
0.083nA Average, 0.125nA Peak	74	148	0.88	1.249511	1.302589	1.8492	132.4
0.125nA Average, 0.375nA Peak	78	155	0.88	1.306189	1.402284	1.9308	143.49
0.250nA CW	78	163	0.88	1.413177	1.661399	N/A	N/A
0.125nA CW, Low Field	73	150	0.45	1.704816	1.819292	0.53524	0.2337
0.125nA CW, High Field	70	147	1.04	1.837276	2.080776	13.879	46.152
0.5nA CW	70	171	0.88	2.096192	2.572051	0.59226	0.17679
0.333nA Average, 0.5nA Peak	81	171	0.88	2.733317	3.139758	0.63015	0.13648
0.5nA Average, 0.75nA Peak	101	202	0.88	3.210191	3.774114	0.79708	0.42591

Table 6.12: The Run 3B T_1 values from fitting the polarization data of the ring section for beam-on run conditions.

Plotting all the core section T_1 values from Run 3A and 3B, suggests a strong current dependence to T_1 . Figure 6.31 demonstrates that not only does the T_1 decrease with accumulated dose, but decreases faster with higher beam currents accompanied by a slower decrease with

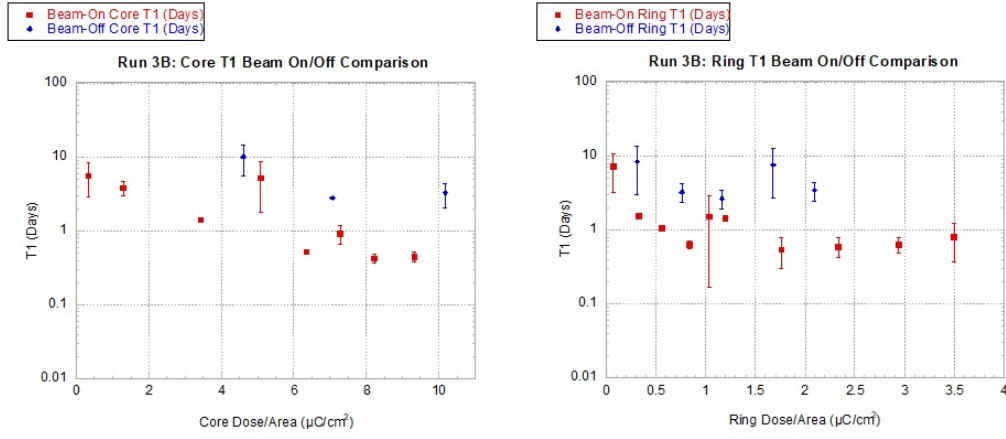


Figure 6.30: Comparing the T_1 values between the beam-on and beam-off NMR measurements of the core and ring sections of Run 3B. Note: Two T_1 values with errors larger than the values were suppressed.



Run 3A and 3B: All Beam-On Core T_1 Values

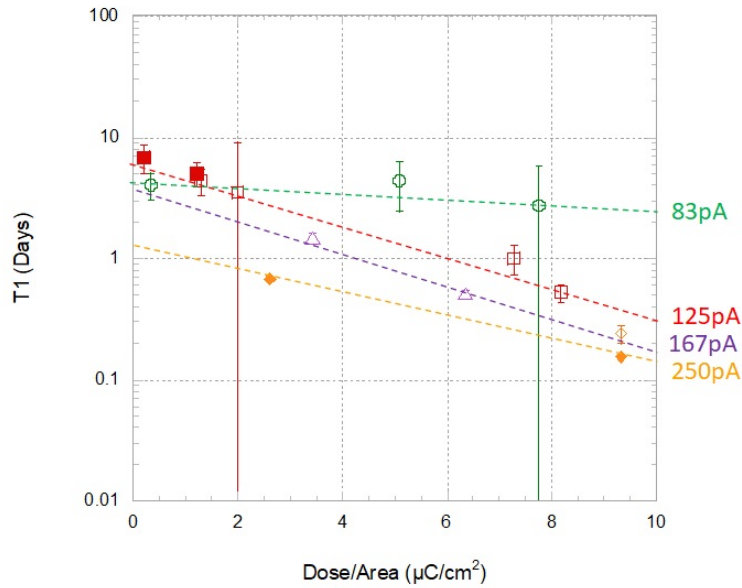


Figure 6.31: Comparing the Run 3A and 3B T_1 values between different beam-on currents. The effect of current on the T_1 can be seen in the plot.

dose. This effect was not apparent with just the Run 3A data alone, making Run 3B crucial in this observation. Figure 6.32 shows a comparison of projected core T_1 values at the same core dose for four different average beam currents. It further emphasizes the average beam current

dominates the T_1 alongside the accumulated dose.

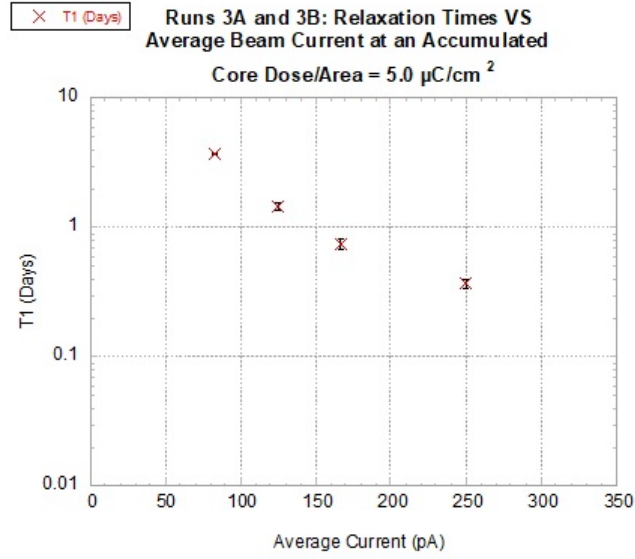


Figure 6.32: Relaxation times as function of average beam current at an accumulation of $5.0\mu C/cm^2$.

In addition to demonstrating that the average beam current affects the relaxation times just as the accumulated dose, Run 3B allowed the opportunity to observe if different beam duty factors, would also have an effect on the relaxation times. To first study if an effect exists, the average beam currents of 125pA were compared to 125pA peak currents. While there were six beam conditions with an average current of 125pA, only one condition had a different average current with same peak current at 125pA. This condition came from the average 83pA current, 125pA peak current. Figure 6.33 shows the relaxation times from the average current conditions and those of the peak currents.

From these figures alone, it is hard to clearly say if there is an effect. Fortunately, there were more 250pA average and peak current conditions that could be compared. Figures 6.34 shows the relaxation times from the average 250pA current conditions and those of the 250pA peak currents. It is much clearer from the 250pA case that there no obvious large effects from the duty factor. The time scale of the beam blanking available during Run 3B had no dramatic effect compared to the dominating factors of the accumulated dose and average beam current.

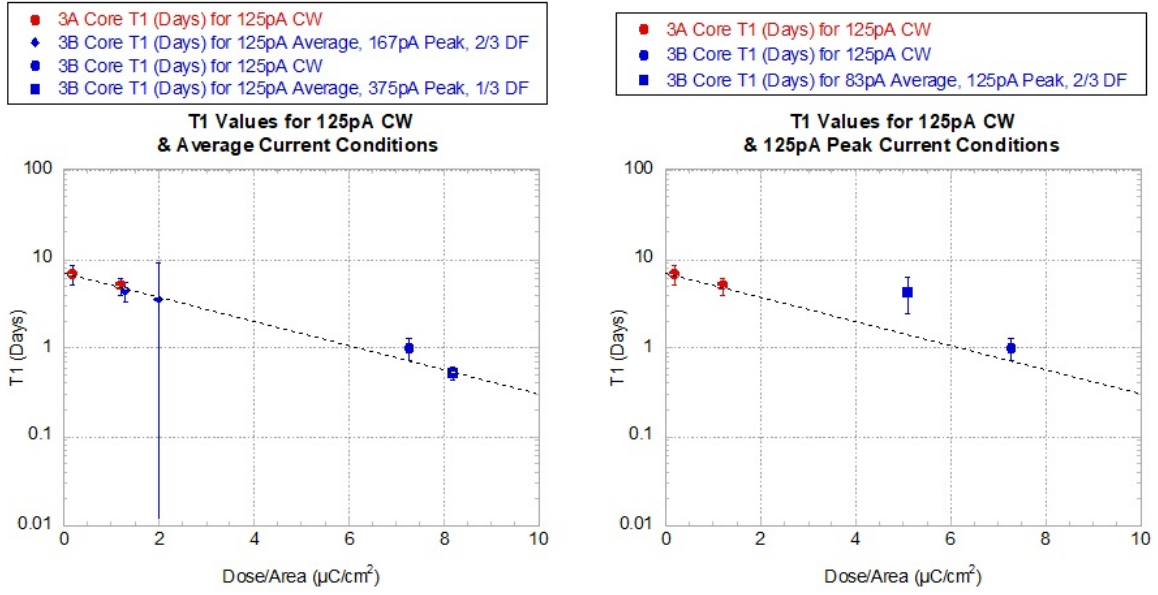


Figure 6.33: Comparison of relaxation time, T_1 values, from 125pA average beam current (top) and the 125pA peak beam current (bottom).

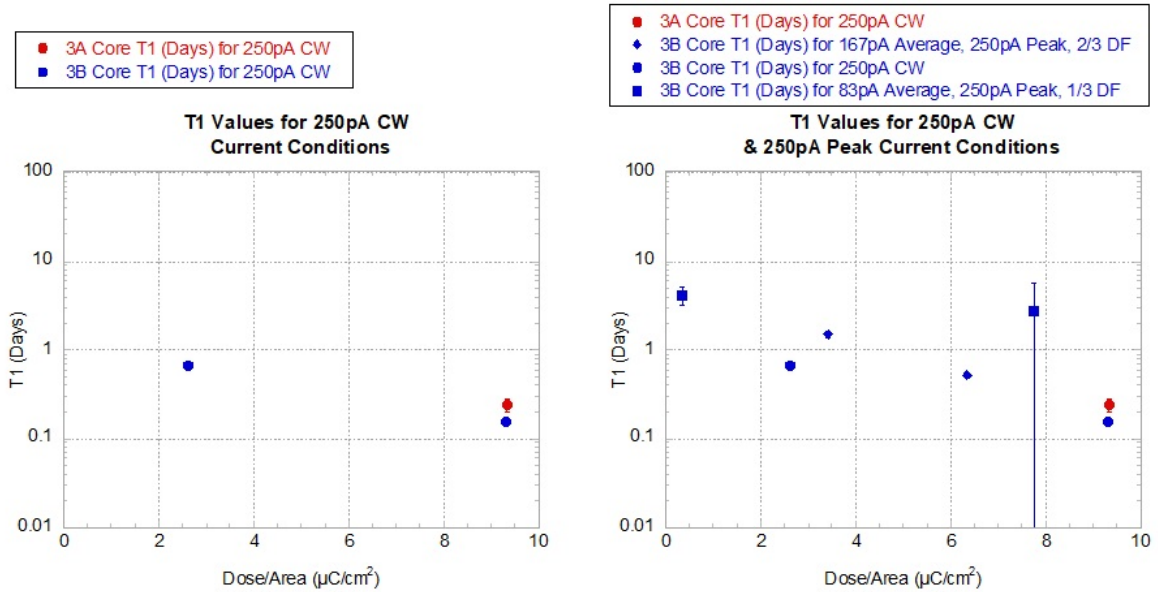


Figure 6.34: Comparison of relaxation time, T_1 values, from 250pA CW beam current (left) and the 250pA peak beam current (right).

6.2.10 Modeling the HD Polarization Loss in Run 3A

During Run 3A, both the core and ring sections of target #60 demonstrated a very small amount of polarization loss during the initial $\sim 1\mu\text{C}/\text{cm}^2$ accumulation. After this amount, the polarization decreased at a steady rate for each section of the target. This effect can be

observed in Figures 6.21 and 6.25. After the initial accumulation, a clear linear trend forms between the loss in polarization and the accumulated dose. Chapter 3 discussed the different possible depolarization mechanisms that could affect the target. The Run 3A results suggest that the polarization loss is dominated by the para-magnetic charge centers caused by the beam.

As discussed in Section 1.4, targets produced through DNP have been studied at great lengths and have found that the paramagnetic impurities of the targets dominate the spin relaxation. The targets used at UITS gave the opportunity to test the DNP model for spin relaxation, from the work of C. Keith [25]. Testing the model allowed to see if it could account for the polarization losses that occurred during the various beam conditions of the run. When the unpaired electrons' spins are not entirely polarized, the spins will flip between magnetic substates. This results in creating a time varying field with Fourier components at hydrogen's Larmor frequency. From Abragam and Goldman, this field produces a relaxation time of the general form [26]:

$$\frac{1}{T_1^H} = C_e \left(\frac{\mu_e}{\mu_p} \right) \left(\frac{\Delta B_p}{B} \right)^2 \left(\frac{1 - P_e^2}{\tau_e} \right) \quad (6.26)$$

where C_e is the unpaired electron concentration of the sample material, μ_e is the unpaired electrons' magnetic moment, μ_p is the proton's magnetic moment, ΔB_p is the nuclear line width, P_e is the unpaired electrons' polarization, and τ_e is the correlation time of the oscillating field in the sample material.

The correlation time of the field becomes proportional to the relaxation time of the unpaired electrons when the concentration of these electrons is low. For low temperatures, the relaxation time of these electrons can be determined through the process by when a spin flip is accompanied by either the absorption or emission of a phonon with energy $2\mu_e B$. During this process, the dependence on the magnetic holding field and temperature is demonstrated by the following [25]:

$$\frac{1}{T_1^e} \propto B^5 \coth \left(\frac{\mu_e B}{kT} \right), \quad (6.27)$$

now combining the above with Equation 6.26,

$$\frac{1}{T_1^H} \propto C_e \left(\frac{\mu_e}{\mu_p} \right) \left(\frac{\Delta B_p}{B} \right)^2 (1 - P_e^2) \left(B^5 \coth \left(\frac{\mu_e B}{kT} \right) \right) \quad (6.28)$$

$$T_1^H \propto \left(\frac{1}{B^3 C_e} \right) \left(\frac{\mu_e}{\mu_p} \right) \left(\frac{1}{\Delta B_p^2} \right) \left(\frac{1}{1 - P_e^2} \right) \left(\frac{1}{\coth \left(\frac{\mu_e B}{kT} \right)} \right). \quad (6.29)$$

The polarization of the unpaired electrons can be substituted for the TE polarization of the electrons for low temperatures given by Equation 5.5.

$$T_1^H \propto \left(\frac{1}{B^3 C_e} \right) \left(\frac{\mu_e}{\mu_p} \right) \left(\frac{1}{\Delta B_p^2} \right) \left(\frac{\tanh\left(\frac{\mu_e B}{kT}\right)}{(1 - \tanh^2\left(\frac{\mu_e B}{kT}\right))} \right) \quad (6.30)$$

$$T_1^H \propto \left(\frac{1}{2B^3 C_e} \right) \left(\frac{\mu_e}{\mu_p} \right) \left(\frac{1}{\Delta B_p^2} \right) \left(\tanh\left(\frac{2\mu_e B}{kT}\right) \right). \quad (6.31)$$

Material that is under frozen spin conditions $\mu_e B > kT$ and the relaxation time for the nucleons in the material is derived to have an exponential dependence on both the holding field and temperature:

$$T_1^H \propto \left(\frac{1}{B^3 C_e} \right) \exp\left(\frac{2\mu_e B}{kT}\right) \quad (6.32)$$

From here, a proportionality constant, called α , can be determined to equate each side of the equation:

$$T_1^H = \frac{1}{\alpha} \left(\frac{1}{B^3 C_e} \right) \exp\left(\frac{2\mu_e B}{kT}\right). \quad (6.33)$$

Time for each beam condition is related to the current and dose received. From $D_{rel} = I_e * t$, time can be rewritten as $t = \frac{D_{rel}}{I_e}$. After replacing time in Equation 6.33, the new expression can be inserted into Equation 2.1 to yield:

$$P(t) = (P_0 - P_{TE}) * \exp\left(-\frac{\left(\frac{D_{rel}}{I_e}\right)}{\frac{1}{\alpha} \left(\frac{1}{B^3 C_e}\right) \exp\left(\frac{2\mu_e B}{kT}\right)}\right) + P_{TE} \quad (6.34)$$

$$P(t) = (P_0 - P_{TE}) * \exp\left(\frac{-\alpha * D_{rel} * D_T * \beta}{I_e}\right) + P_{TE}, \quad (6.35)$$

where $\beta = B^3 \exp\left(\frac{-2\mu_e B}{kT}\right)$, with α absorbing the proportionality constant between C_e and D_T . Numerical values of α can be fitted using the above expression with the polarization values determined for the core and ring sections, as seen in Figure 6.35. However, Equation 6.35 above requires the polarization values used be measured under the same beam operating conditions. These include the same temperature, holding field, and beam current. Thus, a different numerical alpha was determined for each different beam current period.

The polarization values of Run 3A's core and ring sections can be simulated as a function of each section's accumulated dose per area, found in Section 6.2.6, by using the found α values in Equation 6.35. Given α is a proportionality constant, it shouldn't vary much between run

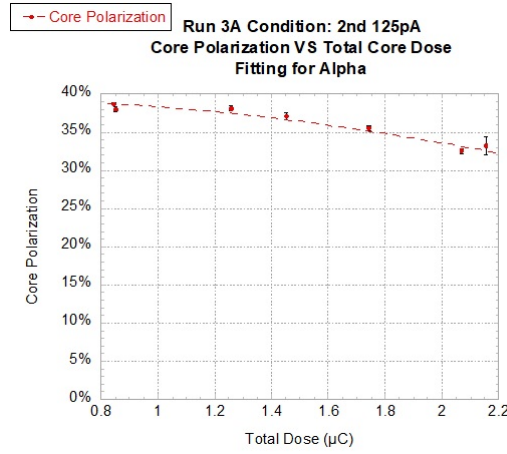


Figure 6.35: The fitted α values of Run 3A's core section, determined from the different beam conditions.

Beam Condition	Target Section	Alpha Value	Error
1 st 125 pA CW	Core	1260.2	205.3
2 nd 125 pA CW	Core	647.0	201.1
1 st 250 pA CW	Core	2244.9	153.1
2 nd 250 pA CW	Core	1049.7	40.0
1 st 250 pA CW	Ring	1849.0	69.0
2 nd 250 pA CW	Ring	2029.8	117.4
Weighted Mean	Global	948.3	32.0

Figure 6.36: The fitted α values of Run 3A's core and ring sections, determined from the different beam conditions.

conditions. However, there is an issue that arises out of the polarization behavior in each section for the first $\sim 1\mu\text{C}/\text{cm}^2$. At the start of being irradiated, the polarization effectively doesn't change. As a result any values of α determined for beam conditions during the initial dosage blow up towards infinity. Putting infinity for α in Equation 6.35, the exponential term goes to 1 and results in the polarization at some time being the same as the initial polarization. For this reason, any α values determined in the starting region were excluded when determining a global value of α that could be used for any beam condition once the polarization began decreasing. For the core section, this meant three separate beam conditions could be used to fit α before the core was depleted.

Regarding the ring section, only two beam conditions were usable. This was due to the ring

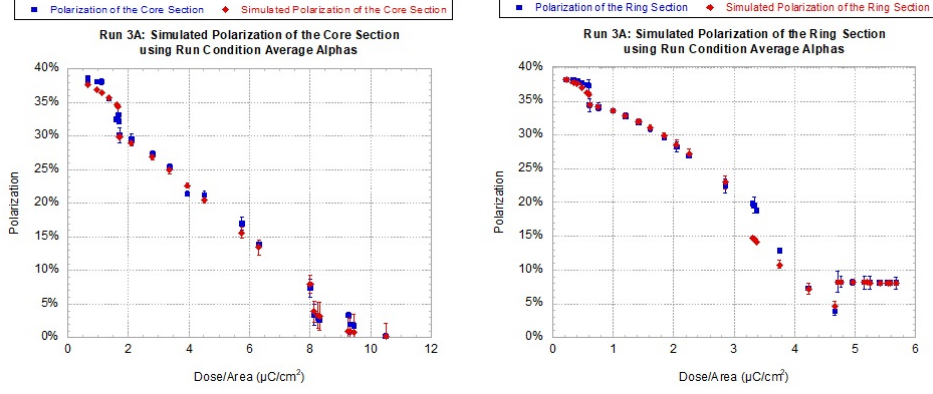


Figure 6.37: Run 3A core (left) and ring (right) sections measured polarization along with the simulated values from using the fitted α values found for each of the beam conditions.

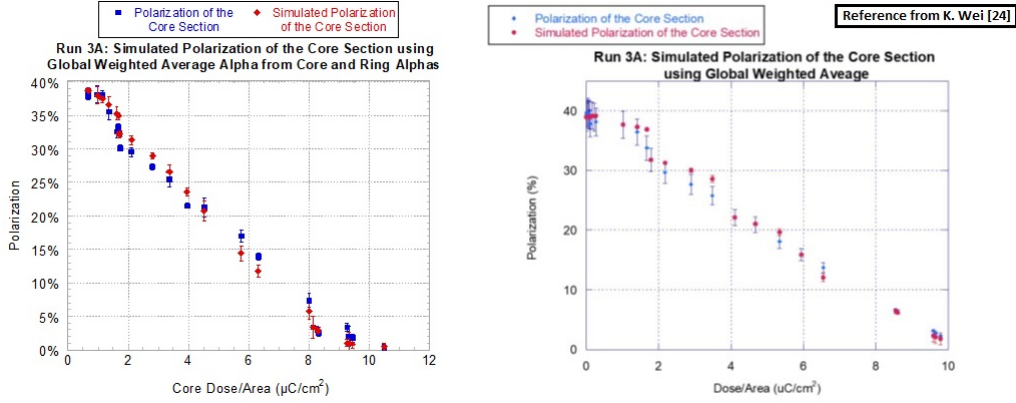


Figure 6.38: Run 3A core section measured polarization along with the simulated values from using the global α .

accumulating dose slower than the core. In addition to the region of little polarization change at the start of the run, the ring also had an issue during the last beam condition (125pA) of Run 3A. Here the polarization experienced a fast drop at the start of the condition and then remained steady before returning the the same loss rate as previous beam condition. It was discovered that the QCM at the UITF was not working correctly. This resulted in a dither in the beam, which would cause the ring region to not receive consistent irradiation across the surface area of the ring. Receiving different amounts of dose throughout the same beam condition accounts for the behavior of the polarization as well as why the model for simulating the ring polarization breaks down during the last condition. Luckily, the core section was well defined and received a consistent dose during each condition. As a result, the core didn't see polarization loss rate changes the ring saw at the end of Run 3A and the core ends up more

accurate with the model.

A global α could be taken as the weighted mean of the alphas from fitting Equation 6.35 to the polarization loss during each different beam condition as outlined earlier in the section. The weighted mean and error estimation method is described in detail in Appendix A. For Run 3A, Figure 6.36 shows the different values determined for α found for each beam condition of each section. This global value was then used to simulate the polarization of Run 3A. Figure 6.37 demonstrates simulating polarization values in each the core and ring sections when using the individual fitted α values derived from each beam condition. The simulated values fit well as the α values are tailored for each set of NMR measurements taken during a particular set of conditions. Likewise, the core and ring section's simulations using a global α value to simulate all the beam on measurements can be seen in Figures 6.38 and 6.39. The ring simulation works well until receiving around $3 \text{ } \mu\text{C}/\text{cm}^2$. At this point, the model starts to break down. This is due to the nonuniform irradiation of the ring section occurring midway through Run 3A. After $3 \text{ } \mu\text{C}/\text{cm}^2$, the ring section dose becomes too difficult to accurately measure from this non-uniformity. Proportionality constants are dependent on the dose information. Without accurate dose information, a proper alpha for each condition could not accurately be determined. Thus, the model works well for targets receiving consistent and uniform electron beam.

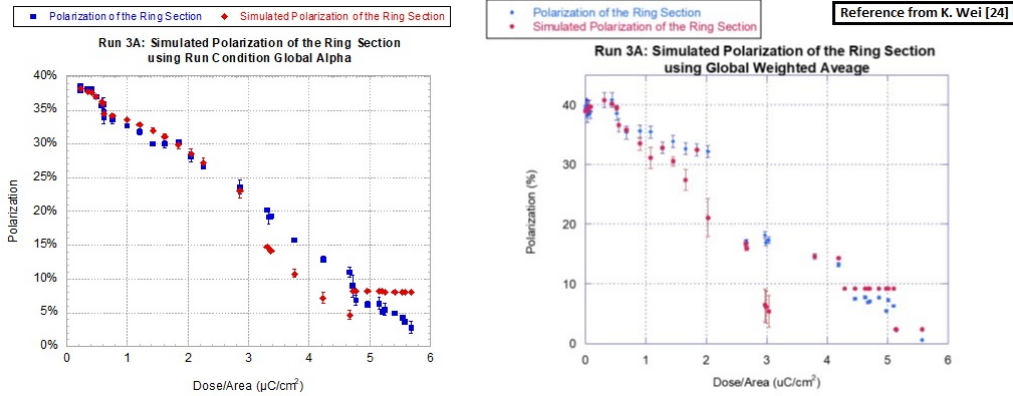


Figure 6.39: Run 3A ring section measured polarization along with the simulated values from using the global α .

The global α value used for simulating the core section polarization loss seen in Figure 6.38 was $948 \pm 32 \text{ (pA/S)}(1/\mu\text{C}^2)(1/T^3)$, while Figure 6.39 shows the ring section using this α . Comparing the plots in Figures 6.37, 6.38, and 6.39, the simulated polarization derived from using the global α is a good estimate of each target section's polarization. As stated earlier,

the simulated polarization agrees far better with the measured polarization values of the core section.

The most likely reason for why the simulated polarization of the core section agrees better with the measured values than those of the ring section involves the differences in how each section was irradiated. The core was uniformly irradiated over the entire core cross section and seen with the YAG viewer results. On the other hand, the ring section polarization values may not have been properly simulated due to the lack of irradiation uniformity.

A more accurate way to describe the ring section would be instead of one solid ring, the ring section is made up of many rings each with their own accumulated dose amount. The model used for simulating the values would work better if the ring section could be separated further into additional sections that could be modeled individually. However, the vertical beam motion that affected the illumination of the ring region had no simple periodic structure, and so accurate information on the distribution of dose across the ring was not available.

In addition to the ring section receiving different amounts of dose affecting the model, the simulated polarization values of the ring section are affected by inconsistent fitted α values from each beam condition. The values fluctuate in areas where the polarization values effectively stay the same. These areas were located at the beginning and last condition for Run 3A. The conditions in the middle region were well defined for the developed model. As a result the global weighted mean α did not include the fitted values for poorly defined regions. This is why in Figure 6.36, only the α values from fitting the polarization measurements from the first and second 250pA beam conditions were used to find a weighted mean for a global value.

After finding the weighted mean α values for each the core and ring, the weighted mean of those two values was taken as the new global α for the all of Run 3A. This global value was used to simulate the polarization value for both the core and ring section. Figure 6.40 shows that the global value works well. The simulated polarization values of the core section appear in good agreement with the measured values. The ring section agrees well, but not as much so as the core. Initially, the simulation agrees very well until after $\sim 4\mu C/cm^2$ when the model breaks down. This was due to the vertical instability of the beam throughout Run 3A.

The ring was not being uniformly irradiated at the end of the target polarization, which makes the dose information at during the last 8% not well known. Additionally, polarization values measured were higher as they are associated with a lower actual dose. With less irradiation than calculated in Section 6.2.6, the polarization appears to not decrease even when

accumulated dose. Thus this end region is poorly defined and the model collapses at the end of the ring section, which means that additional factors need to be taken into account in order to properly model the distribution of the beam. With the core section being well defined, the global weighted value from that section is more accurate than the ring value. Despite this, the global weighted value taken from both the core and ring, worked well for simulating most of the ring section's polarization.

While the ring results indicate the ring wasn't uniformly irradiated, the core results indicate that the beam was uniformly rastered over the entire core section. The model works for the whole core section. In summary, the use of a single constant, α , in Equation 6.35 adequately describes the full polarization history, indicating that depolarization is chiefly driven by the creation of paramagnetic centers.

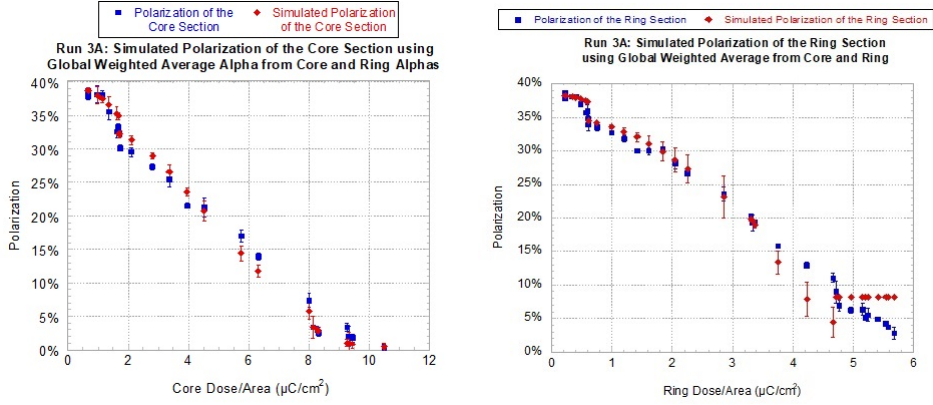


Figure 6.40: Run 3A measured polarization values along with the simulated values from using the global α , $948 \pm 32 \text{ (pA/S)}(1/\mu\text{C}^2)(1/T^3)$, from the weighted mean of the individual core and ring global α values. The core section is represented by the plot of the left with the ring section plotted on the right.

6.2.11 Modeling the HD Polarization Loss in Run 3B

In Run 3B the core made up more than 92% of target #66 and received at least a quasi-uniform beam irradiation. This helped produce a larger, stronger signal contribution from the core section. As a result, the increased accuracy in the NMR measurements made the trends in polarization loss easier to determine. Additionally, fitting the alphas for each beam condition became easier with the increased accuracy of the core polarization values. The ring section made up less than 8% of the target. As mentioned in Section 6.2.6, the ring region did not

Beam Condition	Target Section	Alpha Value	Error
1 st 83 pA Average	Core	3759.8	5745.4
1 st 125 pA Average	Core	8868.2	1597.9
2 nd 125 pA Average	Core	6090.6	983.6
1 st 167 pA Average	Core	332.7	17.5
2 nd 83 pA Average	Core	1711.2	563.6
2 nd 167 pA Average	Core	568.6	30.962
3 rd 125 pA Average	Core	603.5	100.0
2 nd 83 pA Average	Core	256.7	200.0
4 th 125 pA Average	Core	516.3	46.2
1 st 250 pA CW	Core	597.4	64.8
Weighted Mean	Global	4590.9	301.0757

Figure 6.41: The fitted α values of Run 3B's core section, determined from the different beam conditions.

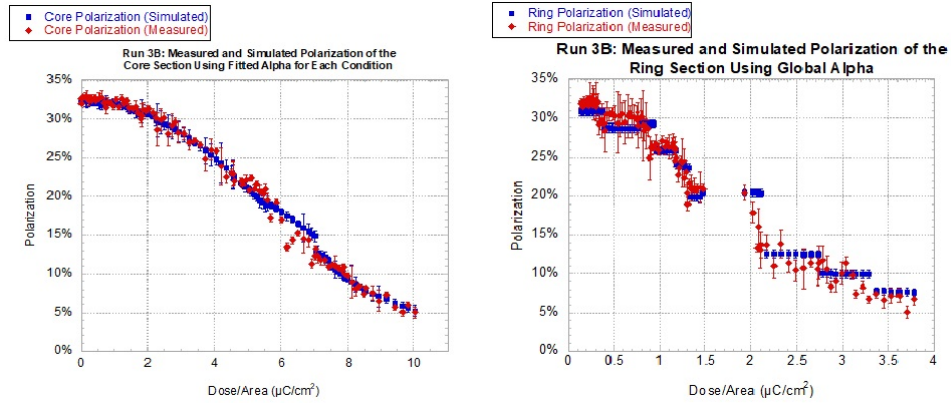


Figure 6.42: The left plot shows Run 3B's core section measured and simulated polarization values using each beam condition's fitted α . The ring section equivalent is on the right. The ring made up less than $\sim 7\%$ of the total target, which received much less dose than the core during each condition, and thus no polarization loss when beam was on. The overnight drops in polarization dominate the ring polarization loss.

receive a uniform dose across the entire region due to the beam dither coming from the QCM. This the ring section dose information and polarization values for Run 3B are less accurate.

Besides less accurate measurements, the slower accumulation in ring dose meant the polarization values for each beam measurement decreased at a slower rate compared the the core section counterparts. The slow change in polarization coupled with occasional signal measurements that fluctuated to a larger value than the previous one, results in negative or nonphysical

α values. The frozen-spin polarization could never increase in the IBC during the experimental run conditions. The thermal equilibrium polarization can still change, but never grew more than 0.6% given the IBC field and temperature conditions.

The model worked well for both the core and ring sections of the Run 3A target data. This was a result of the IBC holding field and beam raster setting resulting in a significant ring region. The different IBC field and beam raster configuration used in Run 3B filled the target more effectively. As a result, the dose conditions in the small Run 3B “ring” were inherently noisy. While comparisons with the Run 3B ring are included below, it is the simulation of the Run 3B core that is more significant.

As in Section 6.2.10, a global α of 4591 ± 301 (pA/S)($1/\mu C^2$)($1/T^3$) was found by taking the weighted mean of the individual fitted values. These values are located in Figure 6.41. In the Run 3B ring case, only the positive determined values and errors were used. This allowed for a global α to be used to roughly simulate the ring polarization values. The right plot of Figure 6.43 shows the simulated ring polarization values, while the left plot shows those belonging to the core. From the plots, it is clear that the model works well overall for simulating the data in Run 3B, much like it did for Run 3A. Using the global α for the ring section also generates an acceptable simulation, although the ring data has more noise.

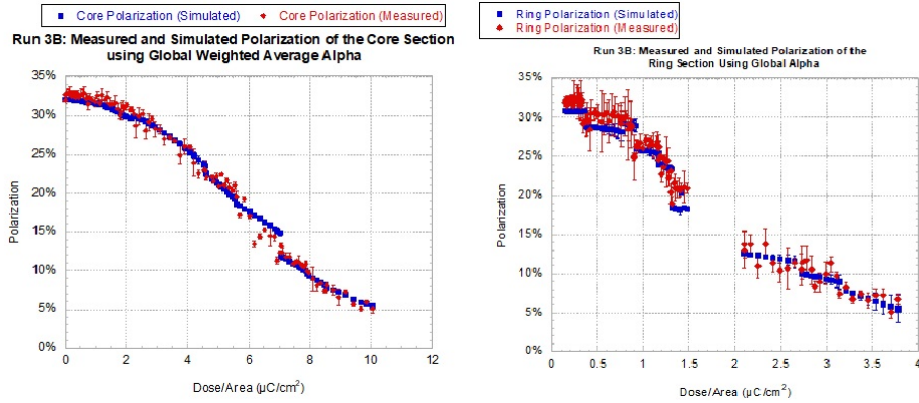


Figure 6.43: Run 3B’s target core and ring section measured and simulated polarization values using the global α .

6.2.12 Comparison to Mano and Honig

Prior to the eHD experiment, two solid HD targets were tested with electron beams by Mano and Honig [27]. The experiment took place at the Cornell Electron Synchrotron using a

10.4GeV beam. During the experiment, the targets used consisted of HD samples with low levels of ortho-H₂ and para-D₂ to polarize the targets as well as control the spin-lattice relaxation time, T_1^H . The targets were created with small relaxation times to allow for the targets to be quickly re-polarized. Besides a higher energy beam and short T_1^H values, the targets were held at a temperature of 4.2K and in a magnetic holding field of 0.28T.

For the first initial 10^{12} electrons/ cm^2 , or $0.16\mu C/cm^2$, no change in T_1^H was observed. For both targets, the initial T_1^H value and up until this dose was approximately 0.35 days. However, a substantial drop occurred at around maximum accumulated dose of $1.34\mu C/cm^2$. The T_1^H values dropped to ~ 0.010 days (measured at $1.36\mu C/cm^2$) for the first target and ~ 0.011 days (measured at $1.34\mu C/cm^2$) for the other. As seen in Section 6.2.9, the eHD target T_1^H values at the UITF were over five times larger in size for comparable doses. For Run 3A, the T_1^H was 5.05 days when measured at $1.21\mu C/cm^2$.

This was at least partly due to the eHD targets having better cooling so that the HD temperatures during beam on operations ranged from 0.070K to 0.325K, while Mano and Honig's targets were over an order in magnitude larger at $\sim 4K$. Additionally, the average magnetic holding field was roughly 3.7 times larger in comparison during Run 3A and about 3.1 times larger in Run 3B. This contributed to improving the T_1 along with the lower HD temperature.

Both eHD target T_1 and core polarization values can be accurately determined with the model developed in Section 6.2.10. As such, these values could then be compared to the the work of Mano and Honig. Equation 6.32 can be used to compare these results by:

$$\frac{T_1^{H_I}}{T_1^{H_{II}}} = \frac{\frac{1}{\alpha} \left(\frac{1}{B_I^3 C_e} \right) \exp \left(\frac{2\mu_e B_I}{k T_I} \right)}{\frac{1}{\alpha} \left(\frac{1}{B_{II}^3 C_e} \right) \exp \left(\frac{2\mu_e B_{II}}{k T_{II}} \right)}, \quad (6.36)$$

where $T_1^{H_I}$, B_I , and T_I are the relaxation time, magnetic holding field, and HD temperature values from Run 3A of the eHD experiment. The denominator terms $T_1^{H_{II}}$, B_{II} , and T_{II} are the equivalent values from Mano and Honig's experiment. In Equation 6.36, the global alpha determined in Section 6.2.10 was used, however the α terms cancel out when carrying through the division just like the C_e terms. What remains in the expression can then be used to develop a scaling factor between the T_1 values of the two experiments:

$$\frac{T_1^{H_I}}{T_1^{H_{II}}} = \frac{\left(\frac{1}{(B_I=1.04T)^3} \right) \exp \left(\frac{2\mu_e (B_I=1.04T)}{k(T_I=0.22K)} \right)}{\left(\frac{1}{(B_{II}=0.28T)^3} \right) \exp \left(\frac{2\mu_e (B_{II}=0.28T)}{k(T_{II}=4.2K)} \right)} \approx 10 \quad (6.37)$$

The scaling factor is calculated to be about 10. Multiplying this factor by the T_1 results of Mano and Honig scales both T_1 values up from ~ 0.01 days to ~ 0.10 days. Similarly, the conditions from Run 3A could be used (lower T_{HD} , smaller holding field) to find a scaling factor of ~ 79 . This results in scaling Mano and Honig's T_1 values from ~ 0.01 days to ~ 0.79 days. The initial and scaled T_1 values are plotted with all the eHD T_1 values in Figure 6.44. In the figure, the blue bar represents how much the T_1 values scale with the range of HD temperatures and holding fields available with the IBC. This allows for comparisons of results to be directly made between those measured under the conditions at the UTIF and measured under different field and temperature conditions at Cornell.

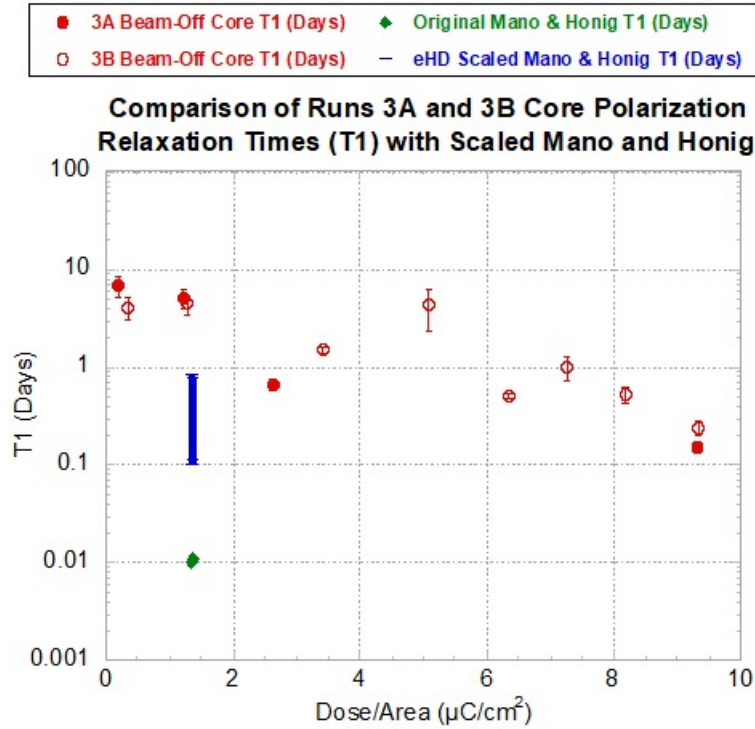


Figure 6.44: Run 3A and 3B core section relaxation times compared to those from Mano and Honig [27]. Equation 6.37 was used to scale those initial T_1 values to match the same HD temperature and magnetic field conditions during the eHD experiment. The blue bar represents scaling Mano and Honig's results between Run 3A and 3B conditions. Run 3A had a higher holding field, but higher T_{HD} due to running the mix heater on.

Despite the HD temperature and holding field scaling increasing the relaxation times of Mano and Honig, it doesn't adjust the times enough. The UITF beams passed through extremely thin aluminum windows before reaching the polarized HD targets. In contrast, the Cornell beam had to pass through substantially more material in the walls of the Mano and Honig cryostat. These

windows were part of the IBC. For the Cornell experiment, the cryostat used had substantially more window material in the way of the beam. The increased amount of material in between the target material and synchrotron beam could have resulted in an increased production of secondary electrons, increasing the overall dose. Thus it is possible, the actual doses in the Cornell experiment were higher than were measured. With a higher actual dose, the Mano and Honig points in Figure 6.44 would shift to the right and closer match the values seen in the eHD experiment.

6.2.13 Projected Performance with a Colder Target

In Sections 6.2.5 and 6.2.9, models were developed to determine the polarization within the core section as well as the core's different relaxation times under different accumulated doses. These models allow for additional projections of the Run 3A relaxation times based on improvements made to the conditions of the target. During Run 3A, the conditions weren't ideal. It was discovered that the HD temperature was larger than the temperature of the Mixing Chamber during beam on operations. Additionally, the target holding field needed to be lowered for NMR, due to UITF noise. This resulted in a lower average holding field during irradiation. During Run 3B, the holding field was kept at 0.88T in order to take more frequent NMR measurements during beam operations without incurring the overhead of cycling the field.

The combination of the elevated HD temperatures and lower fields affected the relaxation times during each beam condition, resulting in the target polarization being depleted at an increased rate. Equation 6.33 can be used to project the relaxation times had an ideal HD temperature and target holding field been maintained during Run 3A and 3B. Some degree of beam heating will always be caused as the beam interacts with the target. As such, for future experiments, a reasonable HD temperature to maintain would be 120mK. A reasonable holding field accompanying that temperature would be 1.25T. For comparison the average holding field was 1.04T with the HD temperature being determined from Figure 6.2 to be 150mK for the 250pA CW beam condition during Run 3A. Using ratio of relaxation times from Equation 6.33, with these Run 3A conditions and the ideal conditions previously mentioned, gives the following:

$$\frac{T_1^I}{T_1^{3A}} = \frac{\left(\frac{1}{(B_I)^3}\right) \exp\left(\frac{2\mu_e(B_I)}{k(T_{HD}^I)}\right)}{\left(\frac{1}{(B_{3A})^3}\right) \exp\left(\frac{2\mu_e(B_{3A})}{k(T_{HD}^{3A})}\right)} = \frac{\left(\frac{1}{(1.25T)^3}\right) \exp\left(\frac{2\mu_e(1.25T)}{k(0.120K)}\right)}{\left(\frac{1}{(1.04T)^3}\right) \exp\left(\frac{2\mu_e(1.04T)}{k(0.150K)}\right)} \approx 77 \quad (6.38)$$

where in the numerator T_1^I , B_I , and T_{HD}^I are the relaxation time, holding field, and HD

temperature under ideal conditions. The "I" denotes ideal. In the denominator T_1^{3A} , B_{3A} , and T_{HD}^{3A} are the relaxation time, holding field, and HD temperature under Run 3A conditions. The standard electron magnetic moment and Boltzmann constant values are used for μ_e and k .

During the 250pA CW condition in Run 3B, the average holding field was 0.88T. The HD temperature from the calibration curve in Figure 6.2 is the same as in Run 3A, 150mK. A similar ratio of relaxation times using Equation 6.33 can be expressed:

$$\frac{T_1^I}{T_1^{3B}} = \frac{\left(\frac{1}{(B_I)^3}\right) \exp\left(\frac{2\mu_e(B_I)}{k(T_{HD}^I)}\right)}{\left(\frac{1}{(B_{3B})^3}\right) \exp\left(\frac{2\mu_e(B_{3B})}{k(T_{HD}^{3B})}\right)} = \frac{\left(\frac{1}{(1.25T)^3}\right) \exp\left(\frac{2\mu_e(1.25T)}{k(0.120K)}\right)}{\left(\frac{1}{(0.88T)^3}\right) \exp\left(\frac{2\mu_e(0.88T)}{k(0.150K)}\right)} \approx 159 \quad (6.39)$$

where in the denominator T_1^{3B} , B_{3B} , and T_{HD}^{3B} are the relaxation time, holding field, and HD temperature under Run 3B conditions. The T_1 values would then increase by a factor of approximately 159.

The ratio of T_1 values has shown how much improvement lowering the HD temperature and increasing the holding field does, but this compares two beam on conditions. During Run 3B, the average beam off overnight HD temperature was 70mK with an average holding field of 0.88T. Comparing this condition with the same 250pA beam on condition yields:

$$\frac{T_1^{Beam-Off}}{T_1^{Beam-On}} = \frac{\left(\frac{1}{(B_{Beam-Off})^3}\right) \exp\left(\frac{2\mu_e(B_{Beam-Off})}{k(T_{HD}^{Beam-Off})}\right)}{\left(\frac{1}{(B_{Beam-On})^3}\right) \exp\left(\frac{2\mu_e(B_{Beam-On})}{k(T_{HD}^{Beam-On})}\right)} = \frac{\left(\frac{1}{(0.88T)^3}\right) \exp\left(\frac{2\mu_e(0.88T)}{k(0.070K)}\right)}{\left(\frac{1}{(0.88T)^3}\right) \exp\left(\frac{2\mu_e(0.88T)}{k(0.15K)}\right)} \approx 8.2 * 10^3. \quad (6.40)$$

The model predicts a T_1 without beam that is significantly larger than the T_1 with beam. This is in clear disagreement with the results of Figure 6.44. Evidently, the electron dose has altered the molecular structure of some lattice sites, which now relax the HD out of its initially pure frozen-spin state.

The potential T_1 enhancements from maintaining more ideal running conditions, Equations 6.38 and 6.39, could be useful for future targets. However, the beam-off T_1 is dominated by another polarization loss mechanism, and essentially imposes a limit on the gains in the beam-on T_1 that might be achieved with improvements in running conditions (mainly temperature). Thus, gains are possible with a colder target, although not as large as Equations 6.38 or 6.39 would suggest.

Chapter 7

Conclusions

7.1 Summary and Outlook

The response of solid polarized HD to electron beams has been measured under various conditions during the first experiment carried out at Jefferson Lab’s newly commissioned Upgraded Injector Test Facility (UITF). The measurements were conducted using an in-beam cryostat (IBC), a dilution refrigerator capable of operating in the dilution mode in both horizontal and vertical orientations. Targets were loaded into the IBC in a vertical orientation, and then rotated horizontally and reconnected to the beam line. During beam exposure, the target polarization was maintained by the IBC cooling system and the magnetic field produced by its internal solenoids. The hydrogen polarization was monitored throughout the exposure by the use of NMR coils surrounding the target.

A beam-current dependent temperature calibration of the HD was developed using the Thermal Equilibrium polarization values of HD targets with short relaxation-times (T_1). With a new fast-rastering system (14 KHz FM x 1 KHz AM) constructed specifically for the eHD experiment and the improvements made to the target cell design, the beam-on HD temperatures were kept below about 170 mK for various beam current conditions up to 400pA (Figure 6.2). While the raster beam pattern was distributed uniformly across the core section of each target, the outer edge of the raster pattern did not drop as abruptly as desired. This led to an outer ring region with varying uniformity and reduced accumulated dose (Figure 4.9).

The first of the eHD polarized targets used in the experiment had an initial polarization of $\sim 39\%$ (UITF run 3A). This was studied with electron beams under various current, temperature, and holding field conditions. During an initial dose accumulation of $\sim 1.9\mu C/cm^2$ the

polarization loss was insignificant. With higher dose, the target polarization dropped at a rate approximately proportional to dose, although with two distinct loss rates. These resulted from the nonuniform irradiation of the entire target and the corresponding *core* and *ring* contributions to the total NMR signal measurements, as seen in Figures 6.18 and 6.20. By $\sim 6\mu C/cm^2$ or $4 * 10^{13}$ *electrons/cm²*, both the polarization of the core and ring sections dropped to $\frac{1}{e}$ of their initial values as discussed in Section 6.2.7. Beam-on spin-relaxation rates (T_1) dropped with increasing dose. Beam-off T_1 values followed a similar trend with dose, although these were about an order of magnitude larger (Figure 6.44). The analysis of the Run 3A data agrees well with the previous work of K. Wei [24].

The second of the eHD polarized targets to interact with electron beams had an initial polarization of $\sim 33\%$ (UITF run 3B). Once again, the target depolarization was approximately proportional to dose with two observable loss rates; the initial dose accumulation of $\sim 1.9\mu C/cm^2$ saw a minimal polarization loss; and by $\sim 6\mu C/cm^2$, both the polarization of the core and ring sections had dropped to $\frac{1}{e}$ of their initial values, as discussed in Section 6.2.8.

Beam-on relaxation rates measured in the run 3B target dropped with accumulated dose, in agreement with the results of run 3A, and once again the beam-off T_1 values were about an order of magnitude larger. Run 3B provided data under a larger number of different currents. When combined with the run 3A results, it became evident that not only does the spin-relaxation rate drop with dose, but at a fixed dose T_1 also drops with increasing current (Figure 6.32). Additional measurements carried out during run 3B with a macroscopic duty factor imposed on the otherwise continuous UITF beam, with forced msecond-scale gaps, showed little correlation to polarization loss rates.

Combining the results of UITF runs 3A and 3B, a somewhat complex picture emerges of electron-beam interactions with polarized HD:

1. After an accumulated dose of $\sim 2\mu C/cm^2$, beam-off spin-relaxation rates drop from their immeasurably long pre-irradiation values to the order of weeks (Figure 6.44), reflecting the dose-dependent buildup of paramagnetic charge on molecules with altered structure within the HD lattice. The flipping of their spins between magnetic sub-states has Fourier components at the H-Larmor frequency that drives depolarization. The transverse spin-spin relaxation in HD (T_2) is known to be very long, so that local polarization changes do not easily spread through the lattice. This leads to the $\sim 2\mu C/cm^2$ threshold before depolarization becomes noticeable.

2. Beam-on T_1 values are typically an order of magnitude yet shorter, and fall with a similar dose dependence (Figure 6.44). Upon interruption of beam, the increase in T_1 to the beam-off value is almost immediate. This suggests that the lower beam-on T_1 values are driven by a buildup of static (and paramagnetic) charge within the insulating HD material. Milli-second scale gaps were introduced into the otherwise continuous UITF beam structure, to provide regular intervals in which such charge could be neutralized. These had little effect (Figures 6.33 and 6.34), which places a lower bound on the average time needed to neutralize the target.
3. At a fixed dose, there is an additional beam dependence of the T_1 on the average current (figure 6.31). There are at least two potential sources of this dependence: (a) higher currents raise the HD temperature and in doing so increase the mobility of trapped charge, which is then no longer coupled to the cold lattice, and only partially polarized with flipping spins; (b) a relativistic moving charge generates crossed electric and magnetic fields when boosted, and depolarization can result from with the interaction of the target with these magnetic fields. Overall, this a somewhat smaller effect and appears as fluctuations around the general dose dependent decay (figure 6.44).

Relaxation times of the eHD targets have been compared to those found in the only exiting published study performed using electron beam interactions with solid HD. This study was carried out at the Cornell synchrotron by Mano and Honig [27]. The present eHD experiment showed better performance, by five fold. The IBC's increased cooling capacity and eHD target cell design resulted in the increased relaxation times seen in Figure 6.44.

A model for polarization loss due to paramagnetic charges [25] was compared with the eHD data from the UITF experiment. Despite strong dependencies upon HD temperature and magnetic holding fields, the model was able to simulate the measured polarization values well within uncertainties, with the adjustment of only a single global parameter (Figure 6.40). The model suggests that with improvements to HD heat removal during beam-on operations and increased magnetic holding fields, it should be possible to increase the beam-on relaxation times by almost 10 fold (limited by the beam-off T_1 values). Such a situation would represent a significant performance improvement that could possibly have applications with secondary charged-hadron beams, given their limited flux. However, an improvement in the dose dependency of beam-off T_1 values found in the eHD targets is required for practical use in electron beam experiments

requiring large fluxes to compensate for the associated small electromagnetic cross sections. Further research and development is required to address this issue.

Appendix A

Error Analysis

A.1 Error Estimation on Polarization Calculation

The methods provided by Bevington [28] were used in calculating the the errors on the NMR signal measurements as well as propagating the error through the sliding window method. First, an optimal phase angle was determined by minimizing the mixing between the spectra from the X and Y channel NMR signal measurements. Afterwards, noise filtering through the use of the Fourier and Inverse Fourier transforms was applied to the spectra. Before filtering the dispersion spectra, it was necessary to convert the dispersion spectra into a real value absorption signal through the use of the Kramer-Kronig relations. After using the relations as a noise filter, the remaining noise can be fitted to either up to a 9th polynomial or a systematic periodic function. To determine which function is appropriate to use, the chi-squared values of the polynomial and periodic background fits of the remaining background noise were determined and compared to each other. The smaller of the two chi-squared values as well as which method to use was chosen.

The equations used for the chi-squared values are Equations A.1 and A.2. In the equations, the NMR signal background is the signal data with an estimate of the NMR signal peak width removed.

$$\chi_{polBKGD}^2 = \frac{1}{N-a} \sum \left[\frac{(\text{filterspectrum})_i - (\text{polynomialbackground})_i}{\delta(\text{filterspectrum})_i} \right]^2 \quad (\text{A.1})$$

$$\chi_{perBKGD}^2 = \frac{1}{N-a} \sum \left[\frac{(\text{filterspectrum})_i - (\text{periodicbackground})_i}{\delta(\text{filterspectrum})_i} \right]^2, \quad (\text{A.2})$$

where N is the number of data points across the NMR signal, a is the number of data points in NMR signal peak width, and $\delta(\text{filterspectrum})_i$ is the error on any one data point in the filtered spectrum. For an ideal signal, there would be no background noise resulting in a flat, zero baseline. The error on each point could then be determined by finding the difference between the signal spectra and the ideal baseline such that $\delta(\text{filterspectrum})_i = (\text{filterspectrum})_i$.

After determining a proper background fit, it was then removed from the filtered signal spectra. Then the sliding window method was applied to the result to calculate the area under the signal peak. The standard deviation of the background of the sliding window plateau was taken to determine the error on the area of the NMR signal peak measurement. This was done by finding the standard deviation of the right and left tails of the scanning window curve. The center plateau and sides of the curve were excluded, allowing only the tails to be compared to the zero baseline. Exclusion of the plateau region occurred by removing a portion equal to the width of the NMR signal peak. The sides of the plateau were excluded by removing a portion equal to the width of the sliding window. The resulting standard deviation of the sliding window summations, which was the error on the NMR signal peak area, was determined by:

$$\sigma^2 = \frac{1}{(N - (a + b))} \sum_{i \neq (\text{peak} \pm \frac{a+b}{2})}^N [(\text{slidingwindowsummations})_i]^2 \quad (\text{A.3})$$

where σ is the error on the NMR signal area measurement, N is the number of summations from the sliding window method, a is number of data points measured across the NMR signal peak width, and b is the number of data points that make up sliding window interval. During each NMR scan, each NMR measurement crosses the resonance condition twice providing two sets of absorption and dispersion spectra. The first set of spectra come from the down sweep of the scan, while the second set is from the up sweep. Each of the four spectra were analyzed separately due to each having their own calibrations. The down sweep spectra were first to be analyzed to determine the NMR signal area values under the signal peaks. These values were then combined by taking their weighted mean with their determined errors. To do this, the

weighted mean, \bar{S} , is given by the following equation:

$$\bar{S} = \frac{\left[\frac{S_{abs}}{\delta S_{abs}^2} + \frac{S_{disp}}{\delta S_{disp}^2} \right]}{\left[\frac{1}{\delta S_{abs}^2} + \frac{1}{\delta S_{disp}^2} \right]}, \quad (\text{A.4})$$

where S_{abs} is the absorption spectra signal area, S_{disp} is the dispersion spectra signal area, δS_{abs} is the error on S_{abs} and δS_{disp} is the error on S_{disp} . Then the error on the weighted mean, $\sigma_{\bar{S}}$ is:

$$\sigma_{\bar{S}} = \sqrt{\frac{1}{\left[\frac{1}{\delta S_{abs}^2} + \frac{1}{\delta S_{disp}^2} \right]}}. \quad (\text{A.5})$$

For an ideal NMR setup, the errors found on the absorption and dispersion spectra should overlap. Unfortunately this was not always the case. To ensure the combined error would cover the difference, an extra step was taken. This step was to convert the error on the weighted mean to the unbiased estimate uncertainty. The unbiased estimate uncertainty is defined as[29]:

$$\delta \bar{S}_{unbiased} = \sigma_{\bar{S}} * \sqrt{\chi^2} = \sigma_{\bar{S}} \sqrt{\left(\frac{S_{abs} - \bar{S}}{\delta S_{abs}} \right)^2 + \left(\frac{S_{disp} - \bar{S}}{\delta S_{disp}} \right)^2} \quad (\text{A.6})$$

where $\delta \bar{S}_{unbiased}$ represents the unbiased estimate uncertainty, the error on the weighted mean is $\sigma_{\bar{S}}$, and the chi-squared value (χ^2) from comparing the absorption and dispersion spectra values the weighted mean of the two. This step is included for all instances where $\chi^2 \geq 1$. For values less than 1, the error on the weighted mean was used to estimate the uncertainty instead.

After completing the process of finding the weighted mean of the down absorption and dispersion spectra with an error estimation, the process was repeated for the corresponding up spectra. With the weighted means and associated errors determined, they were converted from signal values to equivalent polarization values by using Equation 5.29. The polarization values found were then used study the behavior of each HD target's polarization separately. Eventually the down and up polarization values were combined by taking the weighted mean of the two with the error from the NMR measurements. This was done through the following equations:

$$P_{mean} = \frac{\left[\frac{P_{Down}}{\delta P_{Down}^2} + \frac{P_{Up}}{\delta P_{Up}^2} \right]}{\left[\frac{1}{\delta P_{Down}^2} + \frac{1}{\delta P_{Up}^2} \right]}. \quad (\text{A.7})$$

The error on P_{mean} was σ_{mean} , expressed as the following:

$$\sigma_{mean} = \sqrt{\frac{1}{\frac{1}{\delta P_{Down}^2} + \frac{1}{\delta P_{Up}^2}}}, \quad (\text{A.8})$$

where P_{mean} is the weighted mean of the down sweep (P_{Down}) and up sweep (P_{Up}) polarization values. The errors on the down and up polarization values are δP_{Down} and δP_{Up} , respectively.

Next, the χ^2 between the polarization values and their weighted mean was found using:

$$\chi_P^2 = \frac{1}{2} \left[\left(\frac{P_{Down} - P_{mean}}{\delta P_{Down}} \right)^2 + \left(\frac{P_{Up} - P_{mean}}{\delta P_{Up}} \right)^2 \right], \quad (\text{A.9})$$

where the chi-squared value of the down and up polarization values is denoted as χ_P^2 . If $\chi_P^2 \geq 1$, the error on the weighted mean does not change. For all other cases, the unbiased error estimate must be used in place of the error on the weighted mean. The unbiased error on the weighted mean is found by multiplying the error on the weighted mean by the square root of χ_P^2 , getting the following expression:

$$\delta P_{unbiased} = \sigma_{mean} * \sqrt{\chi_P^2} = \sigma_{mean} \sqrt{\frac{1}{2} \left[\left(\frac{P_{Down} - P_{mean}}{\delta P_{Down}} \right)^2 + \left(\frac{P_{Up} - P_{mean}}{\delta P_{Up}} \right)^2 \right]}, \quad (\text{A.10})$$

where the unbiased estimate uncertainty of the weighted mean polarization is denoted as $\delta P_{unbiased}$.

A.2 Error Estimation on Runs 3A and 3B Corrected Results

The error determined for each corrected polarization value in each section comes from the error in the method used to separate the total NMR signal measurements into core and ring sections parts. Beginning with the shifted, no overnight data, like that seen in Figure 6.21, the linear fits from the shifted up data were formed. Table 6.4 displays the values for the slopes of the fits as well as the error on the slopes obtained from the fitting program, KaleidaGraph. The slope errors were then projected to the beginning of the plot to determined the errors on the initial values of the total signal, core contribution to the total signal, and the ring's contribution (denoted as S_T^0 , S_C^0 , and S_R^0). The initial NMR signal uncertainties could then be used to determine other parameters the arise from the division between each target's core and ring sections.

The error between two measurements that are being either added or subtracted is given by Bevington [28] as the following:

$$\delta x^2 = \delta u^2 + \delta v^2 \quad (\text{A.11})$$

where x is a value derived from both u and v , such as $x = u + v$ or $x = u - v$. The errors on x , u , and v are denoted as δx , δu , and δv .

For determining the error between two values that are multiplied or divided, such as $x = u*v$ or $x = \frac{u}{v}$, the following expression was used:

$$\left(\frac{\delta x^2}{x^2}\right) = \left(\frac{\delta u^2}{u^2}\right) + \left(\frac{\delta v^2}{v^2}\right), \quad (\text{A.12})$$

where the errors on x , u , and v are δx , δu , and δv respectively.

Equations A.11 and A.12 were then used to determine the errors on the other parameters in Table 6.4 in addition to the errors on the polarization values. Due to the core and ring signal values being proportional to their polarization values, the corresponding polarization error values are also proportional to the error values on the corresponding NMR signals.

Appendix B

Unpolarized eHD Target Raw NMR Signal Area Data

The following tables contain the raw NMR signal measurements from Runs 2A and 2B. From these values, the temperature calibration work of Section 6.1 was done.

NMR Run #	NMR Start Date & Time	Down Absorption Signal (V*T)	Down Absorption Error (V*T)	Down Dispersion Signal (V*T)	Down Dispersion Error (V*T)
69722683	10/25/20 6:52	6.1182E-11	4.0240E-13	6.8365E-11	7.4898E-13
69878386	10/27/20 2:35	6.1057E-11	5.0923E-13	6.8102E-11	1.1380E-12
70505136	11/3/20 4:00	7.1352E-11	2.1001E-12	6.7475E-11	1.0331E-12
70592536	11/4/20 4:53	5.5185E-11	5.7017E-13	5.0420E-11	2.8122E-12
70661375	11/4/20 20:55	3.6200E-11	6.0124E-13	3.2658E-11	1.5452E-12
70676079	11/5/20 3:11	7.0745E-11	1.6585E-12	7.0585E-11	8.9305E-13
70734409	11/5/20 18:09	2.4717E-11	6.2172E-13	3.0803E-11	1.0537E-12
70760320	11/6/20 3:24	7.0883E-11	2.6102E-13	6.9053E-11	1.2624E-12
70844088	11/7/20 3:06	5.6401E-11	1.9915E-13	4.6776E-11	2.3721E-12
70911093	11/7/20 18:15	1.2390E-11	6.5071E-13	1.1437E-11	1.1590E-12
70941010	11/8/20 5:39	5.0192E-11	2.3797E-13	4.8728E-11	1.3142E-12

Table B.1: Summary of Run 2A raw down absorption and dispersion NMR signal measurements.

<u>NMR Run #</u>	<u>NMR Start Date & Time</u>	<u>Up Absorption Signal (V*T)</u>	<u>Up Absorption Error (V*T)</u>	<u>Up Dispersion Signal (V*T)</u>	<u>Up Dispersion Error (V*T)</u>
69722683	10/25/20 6:52	7.0999E-11	6.7595E-13	6.5924E-11	8.3002E-13
69878386	10/27/20 2:35	6.9079E-11	8.0187E-13	6.3679E-11	1.1954E-12
70505136	11/3/20 4:00	6.8978E-11	1.4437E-12	6.6546E-11	1.6917E-12
70592536	11/4/20 4:53	5.0429E-11	9.5084E-13	6.0486E-11	1.1730E-12
70661375	11/4/20 20:55	2.9514E-11	1.1627E-12	2.2392E-11	2.8462E-12
70676079	11/5/20 3:11	7.0745E-11	8.8898E-13	7.1877E-11	1.1449E-12
70734409	11/5/20 18:09	3.2798E-11	4.3010E-13	1.2058E-11	6.5366E-13
70760320	11/6/20 3:24	7.4289E-11	3.9456E-13	6.6848E-11	1.0204E-12
70844088	11/7/20 3:06	5.9432E-11	3.5194E-13	4.6776E-11	1.0511E-12
70911093	11/7/20 18:15	1.6200E-11	4.2540E-13	2.0813E-11	5.8428E-13
70941010	11/8/20 5:39	4.9355E-11	1.3395E-12	5.3533E-11	1.8702E-12

Table B.2: Summary of Run 2A raw up absorption and dispersion NMR signal measurements.

<u>NMR Run #</u>	<u>NMR Start Date & Time</u>	<u>Down Absorption Signal (V*T)</u>	<u>Down Absorption Error (V*T)</u>	<u>Down Dispersion Signal (V*T)</u>	<u>Down Dispersion Error (V*T)</u>
80868010	3/3/21 3:36	7.66703E-11	1.87381E-12	8.7454E-11	2.34937E-12
80918878	3/3/21 16:58	N/A	N/A	3.66255E-11	2.79818E-12
80958227	3/4/21 2:21	8.03511E-11	2.01192E-12	7.70546E-11	2.71906E-12
81001775	3/4/21 14:52	3.86362E-11	3.06967E-12	3.54555E-11	5.08204E-12
81041576	3/5/21 2:20	1.98526E-11	5.21062E-12	2.99893E-11	4.46196E-12
81088195	3/5/21 14:40	4.04109E-11	3.23537E-12	N/A	N/A
81129750	3/6/21 2:23	8.14685E-11	2.17733E-12	8.56128E-11	3.49168E-12
81214068	3/7/21 5:02	3.04165E-11	2.21081E-12	2.62909E-11	6.15936E-12
81263567	3/7/21 16:25	3.34622E-11	3.36238E-12	3.38988E-11	2.79448E-12
81297772	3/8/21 2:40	7.83169E-11	2.63977E-12	8.93988E-11	2.41625E-12
81343255	3/8/21 13:39	5.25894E-11	6.71071E-12	5.62338E-11	3.33561E-12
81368360	3/8/21 20:02	4.2148E-11	8.58137E-12	4.78993E-11	4.13651E-12
81390015	3/9/21 2:30	4.66994E-11	1.37297E-12	4.2679E-11	2.65667E-12
81435289	3/9/21 17:24	4.33987E-11	1.98181E-12	3.73835E-11	3.9308E-12
81475331	3/10/21 3:17	8.23117E-11	1.78383E-12	8.50665E-11	4.20688E-12
81515334	3/10/21 14:11	4.27332E-11	4.77876E-12	3.72864E-11	8.71762E-12
81562912	3/11/21 3:45	4.43333E-11	3.30625E-12	4.74974E-11	2.86881E-12
81602590	3/11/21 16:06	8.14685E-11	2.17733E-12	8.56128E-11	3.49168E-12
81645335	3/12/21 3:00	8.61545E-11	2.11026E-12	9.07724E-11	3.04416E-12
81693190	3/12/21 17:16	4.70002E-11	1.89806E-12	4.1096E-11	2.66284E-12
81737287	3/13/21 4:12	2.87899E-11	3.00364E-12	2.0939E-11	2.29066E-12
81774759	3/13/21 16:23	2.91985E-11	1.44001E-12	N/A	N/A
81820569	3/14/21 5:26	8.21931E-11	2.20793E-12	9.84738E-11	3.95552E-12
81545401	3/10/21 20:42	5.13844E-11	3.4714E-12	2.5808E-11	5.07933E-12

Table B.3: Summary of Run 2B raw down absorption and dispersion NMR signal measurements.

<u>NMR Run #</u>	<u>NMR Start Date & Time</u>	<u>Up Absorption Signal (V*T)</u>	<u>Up Absorption Error (V*T)</u>	<u>Up Dispersion Signal (V*T)</u>	<u>Up Dispersion Error (V*T)</u>
80868010	3/3/21 3:36	7.54723E-11	3.67792E-12	7.90737E-11	2.11509E-12
80918878	3/3/21 16:58	3.45359E-11	1.94595E-12	3.36724E-11	1.84304E-12
80958227	3/4/21 2:21	7.37626E-11	2.72474E-12	8.23413E-11	2.59195E-12
81001775	3/4/21 14:52	3.80997E-11	1.86341E-12	3.57016E-11	3.56562E-12
81041576	3/5/21 2:20	2.41345E-11	2.52564E-12	2.66773E-11	2.58533E-12
81088195	3/5/21 14:40	3.49877E-11	2.82394E-12	N/A	N/A
81129750	3/6/21 2:23	8.1914E-11	1.78051E-12	8.37389E-11	1.94445E-12
81214068	3/7/21 5:02	3.1774E-11	3.61343E-12	2.97153E-11	4.68407E-12
81263567	3/7/21 16:25	3.24398E-11	4.78112E-12	3.23699E-11	4.21583E-12
81297772	3/8/21 2:40	7.94212E-11	3.09127E-12	8.15941E-11	1.78777E-12
81343255	3/8/21 13:39	4.69971E-11	6.54747E-12	5.33703E-11	1.93861E-12
81368360	3/8/21 20:02	3.69227E-11	4.07E-12	4.08873E-11	4.5785E-12
81390015	3/9/21 2:30	4.92432E-11	1.98598E-12	4.64121E-11	3.46878E-12
81435289	3/9/21 17:24	4.05024E-11	3.00073E-12	4.7743E-11	1.47503E-12
81475331	3/10/21 3:17	7.2974E-11	3.82643E-12	8.44719E-11	2.68766E-12
81515334	3/10/21 14:11	5.00313E-11	4.36739E-12	3.1951E-11	4.80658E-12
81562912	3/11/21 3:45	4.1919E-11	3.59564E-12	5.07822E-11	2.75303E-12
81602590	3/11/21 16:06	8.1914E-11	1.78051E-12	8.37389E-11	1.94445E-12
81645335	3/12/21 3:00	8.1972E-11	1.51289E-12	7.55088E-11	1.75477E-12
81693190	3/12/21 17:16	4.57751E-11	3.41117E-12	4.18309E-11	4.40768E-12
81737287	3/13/21 4:12	2.58362E-11	2.25067E-12	2.50239E-11	2.57486E-12
81774759	3/13/21 16:23	2.40943E-11	3.20943E-12	4.34622E-11	1.52005E-12
81820569	3/14/21 5:26	8.78601E-11	2.19107E-12	8.06133E-11	3.85402E-12
81545401	3/10/21 20:42	3.62893E-11	6.45123E-12	N/A	N/A

Table B.4: Summary of Run 2B raw up absorption and dispersion NMR signal measurements.

Appendix C

Run 3A and 3B Run Conditions

The following tables contain the operating conditions during Run 3A and 3B.

Run Condition #	<u>Date & Time</u>	Average Beam Current (pA)	Mixing Chamber Temperature (K)	Magnetic Field (T)
1	11/23/20 13:54	40	160	1.04
1	11/23/20 14:08	40	160	1.04
1	11/23/20 14:15	40	160	1.04
1	11/23/20 14:23	40	160	1.04
1	11/23/20 14:39	40	160	1.04
1	11/23/20 14:57	40	160	1.04
1	11/23/20 15:07	40	160	1.04
1	11/23/20 15:22	40	160	1.04
2	11/23/20 15:37	0	160	1.04
2	11/23/20 16:03	0	160	1.04
3	11/23/20 16:16	125	160	1.04
3	11/23/20 16:31	125	160	1.04
3	11/23/20 16:43	125	160	1.04
4	11/23/20 18:33	0	166	1.04
4	11/23/20 19:09	0	166	1.04
5	11/23/20 20:28	125	160	1.04
5	11/23/20 22:36	125	160	1.04
5	11/23/20 23:36	125	160	1.04

6	11/23/20 23:55	0	160	1.04
6	11/24/20 9:47	0	160	1.04
7	11/24/20 10:48	250	160	1.04
7	11/24/20 11:53	250	160	1.04
7	11/24/20 13:05	250	160	1.04
7	11/24/20 14:25	250	160	1.04
8	11/24/20 15:36	250	166	1.04
8	11/24/20 16:40	250	166	1.04
8	11/24/20 17:57	250	166	1.04
9	11/24/20 19:09	250	240	1.04
9	11/24/20 20:15	250	240	1.04
10	11/24/20 23:33	250	79	1.04
11	11/24/20 23:46	0	160	1.04
11	11/25/20 0:47	0	160	1.04
11	11/25/20 9:24	0	160	1.04
11	11/25/20 11:24	0	160	1.04
11	11/25/20 11:30	0	160	1.04
12	11/25/20 12:38	250	240	1.04
12	11/25/20 12:44	250	240	1.04
12	11/25/20 14:37	250	240	1.04
12	11/25/20 14:43	250	240	1.04
12	11/25/20 15:36	250	240	1.04
12	11/25/20 17:37	250	240	1.04
13	11/25/20 20:34	250	160	1.04
13	11/25/20 23:08	250	160	1.04
14	11/25/20 23:45	0	73	1.04
14	11/26/20 10:47	0	73	1.04
15	11/26/20 10:59	0	70	1.04
15	11/26/20 11:08	0	70	1.04
15	11/26/20 11:20	0	70	1.04

15	11/26/20 13:53	0	70	1.04
15	11/26/20 13:59	0	70	1.04
15	11/26/20 17:03	0	70	1.04
15	11/26/20 20:01	0	70	1.04
15	11/27/20 9:27	0	70	1.04
15	11/27/20 11:24	0	70	1.04
16	11/27/20 13:19	125	70	1.04
16	11/27/20 15:26	125	70	1.04
16	11/27/20 17:45	125	70	1.04
16	11/27/20 18:25	125	70	1.04
16	11/27/20 18:43	125	70	1.04
16	11/27/20 20:34	125	70	1.04
16	11/27/20 22:06	125	70	1.04
16	11/27/20 23:35	125	70	1.04
16	11/27/20 23:49	125	70	1.04
17	11/28/20 0:27	0	70	1.04
17	11/28/20 9:52	0	70	1.04
17	11/28/20 10:27	0	70	1.04
18	11/28/20 11:35	0	100	1.04
18	11/28/20 11:41	0	100	1.04
19	11/28/20 12:41	125	70	1.04
19	11/28/20 13:25	125	70	1.04
19	11/28/20 17:08	125	70	1.04
19	11/28/20 17:33	125	70	1.04
20	11/29/20 17:04	0	70	1.04
20	11/29/20 23:10	0	70	1.04
20	11/30/20 9:25	0	70	1.04
20	11/30/20 13:19	0	70	1.04
21	11/30/20 15:49	0	70	1.04
21	11/30/20 15:56	0	70	1.04

22	11/30/20 23:27	1000	70	1.04
----	----------------	------	----	------

Table C.1: Run 3A summary of conditions in which NMR measurements were taken at the UTF.

Run Condition #	<u>Date & Time</u>	Average Beam Current (pA)	Mixing Chamber Temperature (mK)	Magnetic Field (T)
1	12/9/20 12:34	83	70	0.88
1	12/9/20 12:42	83	70	0.88
1	12/9/20 13:02	83	70	0.88
1	12/9/20 13:22	83	70	0.88
1	12/9/20 13:45	83	70	0.88
1	12/9/20 14:05	83	70	0.88
1	12/9/20 14:25	83	70	0.88
1	12/9/20 14:46	83	70	0.88
1	12/9/20 15:05	83	70	0.88
1	12/9/20 15:26	83	70	0.88
1	12/9/20 15:46	83	70	0.88
1	12/9/20 16:06	83	70	0.88
1	12/9/20 16:32	83	70	0.88
1	12/9/20 16:52	83	70	0.88
2	12/9/20 17:42	0	70	0.88
2	12/9/20 18:06	0	70	0.88
2	12/9/20 18:25	0	70	0.88
2	12/9/20 18:45	0	70	0.88
3	12/9/20 19:05	125	72	0.88
3	12/9/20 19:25	125	72	0.88
3	12/9/20 19:45	125	72	0.88
3	12/9/20 20:05	125	72	0.88
3	12/9/20 20:25	125	72	0.88
3	12/9/20 20:45	125	72	0.88

3	12/9/20 21:05	125	72	0.88
3	12/9/20 21:25	125	72	0.88
3	12/9/20 21:45	125	72	0.88
3	12/9/20 22:05	125	72	0.88
3	12/9/20 22:25	125	72	0.88
3	12/9/20 22:45	125	72	0.88
3	12/9/20 23:05	125	72	0.88
3	12/9/20 23:25	125	72	0.88
4	12/9/20 23:46	0	70	0.88
4	12/10/20 0:01	0	70	0.88
4	12/10/20 9:51	0	72	0.88
4	12/10/20 10:00	0	72	0.88
4	12/10/20 10:06	0	72	0.88
4	12/10/20 10:21	0	72	0.88
4	12/10/20 12:02	0	72	0.88
5	12/10/20 12:35	125	72	0.88
5	12/10/20 12:55	125	72	0.88
5	12/10/20 13:05	125	72	0.88
5	12/10/20 13:35	125	72	0.88
5	12/10/20 13:55	125	72	0.88
6	12/10/20 14:07	167	72	0.88
6	12/10/20 14:27	167	72	0.88
6	12/10/20 14:47	167	72	0.88
6	12/10/20 15:07	167	72	0.88
6	12/10/20 15:27	167	72	0.88
6	12/10/20 15:47	167	72	0.88
6	12/10/20 16:07	167	72	0.88
6	12/10/20 16:38	167	72	0.88
6	12/10/20 17:08	167	72	0.88
6	12/10/20 17:38	167	72	0.88

6	12/10/20 18:08	167	72	0.88
6	12/10/20 18:38	167	72	0.88
6	12/10/20 19:08	167	72	0.88
6	12/10/20 19:38	167	72	0.88
6	12/10/20 20:08	167	72	0.88
6	12/10/20 20:38	167	72	0.88
6	12/10/20 21:08	167	72	0.88
7	12/10/20 21:38	0	70	0.88
7	12/10/20 22:35	0	70	0.88
7	12/11/20 9:53	0	70	0.88
7	12/11/20 11:01	0	70	0.88
8	12/11/20 12:51	83	72	0.88
8	12/11/20 13:53	83	72	0.88
8	12/11/20 14:22	83	72	0.88
8	12/11/20 14:53	83	72	0.88
8	12/11/20 15:23	83	72	0.88
8	12/11/20 15:53	83	72	0.88
8	12/11/20 16:24	83	72	0.88
8	12/11/20 16:53	83	72	0.88
8	12/11/20 17:27	83	72	0.88
8	12/11/20 17:56	83	72	0.88
8	12/11/20 18:23	83	72	0.88
9	12/11/20 18:45	167	73	0.88
9	12/11/20 19:15	167	73	0.88
9	12/11/20 19:45	167	73	0.88
9	12/11/20 20:15	167	73	0.88
9	12/11/20 20:45	167	73	0.88
9	12/11/20 21:15	167	73	0.88
9	12/11/20 21:45	167	73	0.88
9	12/11/20 22:15	167	73	0.88

9	12/11/20 22:45	167	73	0.88
10	12/11/20 23:00	0	73	0.88
10	12/11/20 23:30	0	73	0.88
10	12/12/20 9:47	0	73	0.88
11	12/12/20 11:11	125	73	0.88
11	12/12/20 12:10	125	73	0.88
11	<u>12/12/20 12:40</u>	125	73	0.88
11	12/12/20 13:10	125	73	0.88
11	12/12/20 13:40	125	73	0.88
11	12/12/20 14:10	125	73	0.88
12	12/12/20 14:32	83	74	0.88
12	12/12/20 15:02	83	74	0.88
12	12/12/20 15:32	83	74	0.88
12	12/12/20 16:02	83	74	0.88
12	12/12/20 16:32	83	74	0.88
13	12/12/20 16:40	125	78	0.88
13	12/12/20 17:10	125	78	0.88
13	12/12/20 17:40	125	78	0.88
13	12/12/20 18:10	125	78	0.88
13	12/12/20 18:40	125	78	0.88
13	12/12/20 19:10	125	78	0.88
14	12/12/20 19:26	250	78	0.88
14	12/12/20 20:05	250	78	0.88
14	12/12/20 20:35	250	78	0.88
14	12/12/20 21:05	250	78	0.88
14	12/12/20 21:35	250	78	0.88
14	12/12/20 22:05	250	78	0.88
15	12/12/20 22:26	0	70	0.88
15	12/13/20 0:02	0	70	0.88
15	12/13/20 10:50	0	70	0.88

15	12/13/20 16:58	0	70	0.88
15	12/13/20 23:12	0	70	0.88
15	12/14/20 9:49	0	70	0.88
15	12/14/20 11:45	0	70	0.88
15	12/14/20 13:01	0	70	0.88
16	12/14/20 13:40	125	73	0.45
16	12/14/20 14:10	125	73	0.45
16	12/14/20 14:40	125	73	0.45
16	12/14/20 15:10	125	73	0.45
16	12/14/20 15:40	125	73	0.45
16	12/14/20 16:10	125	73	0.45
16	12/14/20 16:40	125	73	0.45
17	12/14/20 17:15	0	70	0.88
18	12/14/20 18:21	125	70	1.04
18	12/14/20 19:12	125	70	1.04
18	12/14/20 20:04	125	70	1.04
18	12/14/20 20:58	125	70	1.04
18	12/14/20 21:47	125	70	1.04
18	12/14/20 22:37	125	70	1.04
19	12/14/20 23:05	0	70	0.88
19	12/15/20 0:05	0	70	0.88
19	12/15/20 11:30	0	70	0.88
19	12/15/20 17:11	0	70	0.88
19	12/15/20 23:01	0	70	0.88
19	12/16/20 11:46	0	70	0.88
19	12/16/20 11:59	0	70	0.88
19	12/16/20 17:00	0	70	0.88
19	12/16/20 18:30	0	70	0.88
20	12/16/20 19:00	500	70	0.88
20	12/16/20 19:30	500	70	0.88

20	12/16/20 20:01	500	70	0.88
20	12/16/20 20:30	500	70	0.88
20	12/16/20 21:00	500	70	0.88
20	12/16/20 21:30	500	70	0.88
20	12/16/20 22:00	500	70	0.88
21	12/16/20 22:30	0	70	0.88
21	12/17/20 0:01	0	70	0.88
21	12/17/20 10:03	0	70	0.88
22	12/17/20 11:10	333	81	0.88
22	12/17/20 11:45	333	81	0.88
22	12/17/20 12:15	333	81	0.88
22	12/17/20 12:45	333	81	0.88
22	12/17/20 13:15	333	81	0.88
22	12/17/20 13:50	333	81	0.88
22	12/17/20 14:20	333	81	0.88
22	12/17/20 14:50	333	81	0.88
23	12/17/20 15:10	0	70	0.88
24	12/17/20 15:40	500	101	0.88
24	12/17/20 16:10	500	101	0.88
24	12/17/20 16:40	500	101	0.88
24	12/17/20 17:10	500	101	0.88
24	12/17/20 17:40	500	101	0.88
24	12/17/20 18:10	500	101	0.88
24	12/17/20 18:40	500	101	0.88
25	12/17/20 19:16	0	70	0.88
25	12/17/20 19:30	0	70	0.88
26	12/17/20 19:44	3000	166	0.88
27	12/17/20 22:26	1000	136	0.88
28	12/17/20 23:27	0	70	0.88
28	12/18/20 9:24	0	70	0.88

Table C.2: Run 3B summary of conditions in which NMR measurements were taken at the UITF.

Appendix D

Polarized eHD Target Raw NMR Signal Area Data

The following tables contain the raw NMR signal measurements from Runs 3A and 3B. From these values, the corresponding polarization values are determined.

NMR Run #	NMR Start Date & Time	Down Absorption Signal Area (V*T)	Down Absorption Error (V*T)	Down Dispersion Signal Area (V*T)	Down Dispersion Error (V*T)
72284094	11/23/20 13:55	2.2676E-10	1.2440E-12	2.3339E-10	1.3475E-12
72284887	11/23/20 14:08	2.4725E-10	2.0852E-12	2.2668E-10	2.1229E-12
72285297	11/23/20 14:14	2.4141E-10	1.3673E-12	2.4180E-10	1.0630E-12
72285817	11/23/20 14:23	2.3202E-10	1.0093E-12	2.3382E-10	1.0338E-12
72286758	11/23/20 14:39	2.4033E-10	2.1521E-12	2.3256E-10	1.5026E-12
72287850	11/23/20 14:57	2.3870E-10	1.2888E-12	2.3447E-10	1.0423E-12
72288449	11/23/20 15:07	2.2562E-10	1.8776E-12	2.4913E-10	1.4299E-12
72289342	11/23/20 15:22	2.3126E-10	9.9420E-13	2.2886E-10	1.7341E-12
72290224	11/23/20 15:37	2.4492E-10	2.3091E-12	2.2834E-10	1.5015E-12
72291836	11/23/20 16:03	2.3873E-10	2.1336E-12	2.4103E-10	3.3794E-12
72292576	11/23/20 16:16	2.4169E-10	1.0880E-12	2.4657E-10	1.9134E-12
72293488	11/23/20 16:31	2.2407E-10	7.4213E-13	2.4414E-10	1.1521E-12
72294229	11/23/20 16:43	2.2546E-10	1.3748E-12	2.5069E-10	3.6086E-12
72300827	11/23/20 18:33	2.2940E-10	9.2891E-13	2.4073E-10	1.4314E-12
72302990	11/23/20 19:09	2.3381E-10	1.2169E-12	2.3511E-10	1.1098E-12
72307682	11/23/20 20:28	2.3230E-10	1.7505E-12	2.3782E-10	1.3127E-12
72310626	11/23/20 21:17	2.2113E-10	2.5265E-12	2.2805E-10	1.2076E-12
72315376	11/23/20 22:36	2.2152E-10	9.0962E-13	2.4073E-10	1.4314E-12
72319018	11/23/20 23:36	2.2031E-10	3.1712E-12	2.1609E-10	1.8852E-12
72320158	11/23/20 23:55	2.0538E-10	1.4034E-12	2.2973E-10	1.4089E-12
72355672	11/24/20 9:47	2.2273E-10	2.0039E-12	2.0146E-10	1.4558E-12
72359305	11/24/20 10:52	2.0951E-10	1.6074E-12	2.0251E-10	1.5794E-12
72363235	11/24/20 11:47	1.9819E-10	1.2500E-12	2.0461E-10	7.4885E-13
72367510	11/24/20 13:09	1.9221E-10	1.8084E-12	1.9373E-10	1.6344E-12
72372320	11/24/20 14:25	1.9075E-10	1.6030E-12	1.8661E-10	1.2629E-12
72376586	11/24/20 15:36	1.6914E-10	3.0081E-12	1.6607E-10	1.3761E-12
72380455	11/24/20 16:41	1.6808E-10	1.4768E-12	1.6460E-10	1.9212E-12
72385067	11/24/20 17:57	1.5799E-10	1.1908E-12	1.6137E-10	9.0491E-13
72389354	11/24/20 19:09	1.5782E-10	2.4458E-12	1.4237E-10	1.4637E-12
72393348	11/24/20 20:15	1.3602E-10	1.0874E-12	1.3649E-10	1.3448E-12
72405214	11/24/20 23:33	1.0847E-10	9.8195E-13	1.2512E-10	1.7613E-12
72405969	11/24/20 23:46	1.1680E-10	1.4348E-12	1.0606E-10	1.6100E-12
72409640	11/25/20 0:47	1.1393E-10	1.2678E-12	1.0691E-10	3.7944E-12
72440652	11/25/20 9:24	8.9395E-11	3.3319E-12	8.5156E-11	1.1311E-12
72447879	11/25/20 11:24	9.1265E-11	1.5525E-12	8.4767E-11	8.5891E-13
72448218	11/25/20 11:30	8.5951E-11	1.5784E-12	7.6089E-11	1.6107E-12
72452315	11/25/20 12:38	7.8219E-11	2.0890E-12	7.9227E-11	2.5931E-12
72452645	11/25/20 12:44	7.2283E-11	1.3042E-12	7.9261E-11	1.3317E-12
72459423	11/25/20 14:37	7.0490E-11	1.4978E-12	7.5042E-11	1.5625E-12
72459783	11/25/20 14:43	6.9546E-11	1.6484E-12	5.2636E-11	1.5711E-12
72462990	11/25/20 15:36	6.7201E-11	1.0014E-12	6.0240E-11	1.3059E-12
72470244	11/25/20 17:37	5.8249E-11	7.5567E-13	5.0252E-11	1.3927E-12
72480881	11/25/20 20:43	3.2595E-11	1.0675E-12	4.4300E-11	1.6318E-12
72490119	11/25/20 23:08	7.2283E-11	1.3042E-12	6.9793E-11	1.4558E-12
72492353	11/25/20 23:45	7.2283E-11	1.3042E-12	7.9261E-11	1.3317E-12
72532055	11/26/20 10:47	7.0490E-11	1.4978E-12	7.5042E-11	1.5625E-12

Table D.1: Summary of the Run 3A NMR signal measurements from the down absorption and dispersion NMR signals, Part 1.

NMR Run #	NMR Start Date & Time	Down Absorption Signal Area (V*T)	Down Absorption Error (V*T)	Down Dispersion Signal Area (V*T)	Down Dispersion Error (V*T)
72532798	11/26/20 10:59	6.9546E-11	1.6484E-12	5.2636E-11	1.5711E-12
72533322	11/26/20 11:08	6.7201E-11	1.0014E-12	6.0240E-11	1.3059E-12
72534046	11/26/20 11:21	5.8249E-11	7.5567E-13	5.0252E-11	1.3927E-12
72543235	11/26/20 13:53	3.2595E-11	1.0675E-12	4.4300E-11	1.6318E-12
72543566	11/26/20 13:59	5.0519E-11	1.0943E-12	3.8007E-11	2.2039E-12
72554619	11/26/20 17:03	4.2548E-11	1.4716E-12	6.1521E-11	3.0512E-12
72565275	11/26/20 20:01	3.8177E-11	1.7858E-12	5.2732E-11	1.8531E-12
72576048	11/26/20 23:00	4.3389E-11	1.3095E-12	4.4660E-11	1.3981E-12
72613644	11/27/20 9:27	4.8571E-11	1.5877E-12	5.2732E-11	1.8531E-12
72620678	11/27/20 11:24	4.4021E-11	1.4619E-12	N/A	N/A
72627574	11/27/20 13:19	4.1885E-11	1.4214E-12	4.1838E-11	1.9062E-12
72635191	11/27/20 15:26	4.0161E-11	2.8285E-12	4.7208E-11	1.1006E-12
72643540	11/27/20 17:45	4.7706E-11	1.6583E-12	4.6548E-11	1.3279E-12
72645907	11/27/20 18:25	4.3587E-11	1.3361E-12	5.5902E-11	2.1785E-12
72647000	11/27/20 18:43	4.6835E-11	7.8187E-13	3.5376E-11	3.6202E-12
72653662	11/27/20 20:34	5.6745E-11	1.4145E-12	3.6476E-11	1.7467E-12
72659190	11/27/20 22:06	4.6359E-11	2.8464E-12	2.6547E-11	1.5617E-12
72664515	11/27/20 22:30	3.1691E-11	3.1286E-12	4.0894E-11	1.5370E-12
72665385	11/27/20 23:35	2.1824E-11	2.1159E-12	5.2494E-11	2.6095E-12
72667665	11/28/20 0:28	2.9917E-11	1.6917E-12	3.9958E-11	1.4592E-12
72701538	11/28/20 9:52	3.0309E-11	1.4281E-12	2.8881E-11	2.1650E-12
72703649	11/28/20 10:27	2.6515E-11	8.6371E-13	3.7692E-11	1.8344E-12
72708085	11/28/20 11:36	3.0837E-11	1.8353E-12	3.1202E-11	1.5908E-12
72711715	11/28/20 12:41	3.1177E-11	1.2467E-12	3.1720E-11	1.4731E-12
72714334	11/28/20 13:25	3.1177E-11	1.2467E-12	2.7151E-11	1.1645E-12
72719643	11/28/20 14:54	1.5052E-11	1.0538E-12	2.8967E-11	1.2322E-12
72720040	11/28/20 15:00	2.3840E-11	1.8838E-12	2.7972E-11	1.6494E-12
72728769	11/28/20 17:26	2.3587E-11	1.7510E-12	3.9804E-11	1.4880E-12
72732314	11/28/20 18:25	1.8739E-11	8.1976E-13	4.1177E-11	1.5102E-12
72737791	11/28/20 19:56	2.1217E-11	5.0372E-13	2.1012E-11	7.0270E-13
72738352	11/28/20 20:06	N/A	N/A	N/A	N/A
72739995	11/28/20 20:33	2.0460E-11	5.2687E-13	2.0663E-11	7.4584E-13
72743253	11/28/20 21:27	2.0261E-11	7.3900E-13	1.4699E-11	6.6470E-13
72748760	11/28/20 22:59	1.3733E-11	7.6122E-13	1.3085E-11	6.5269E-13
72787373	11/29/20 9:43	1.4879E-11	5.8754E-13	1.1411E-11	7.8599E-13
72795391	11/29/20 11:56	1.1828E-11	6.9689E-13	8.0416E-12	5.2398E-13
72813854	11/29/20 17:04	1.1079E-11	4.4518E-13	1.0713E-11	3.7650E-13
72835831	11/29/20 23:10	N/A	N/A	N/A	N/A
72872744	11/30/20 9:25	1.0585E-11	2.3060E-13	1.0868E-11	2.5497E-13
72874633	11/30/20 9:57	1.2223E-11	2.0340E-13	9.5094E-12	3.6952E-13
72886779	11/30/20 13:19	1.1503E-11	1.9067E-13	1.2425E-11	4.6518E-13
72895758	11/30/20 15:49	1.2729E-11	4.1039E-13	1.3227E-11	4.7370E-13
72896181	11/30/20 17:54	9.6793E-12	5.3156E-13	1.1374E-11	4.4466E-13
72923231	11/30/20 23:27	1.1779E-11	7.7948E-13	1.1196E-11	7.5858E-13
72961301	12/1/20 10:01	1.0920E-11	3.2807E-13	1.0448E-11	3.5660E-13

Table D.2: Summary of the Run 3A NMR signal measurements from the down absorption and dispersion NMR signals, Part 2.

Table D.3: Run 3A Raw NMR Up Sweep Signal Area Measurements

NMR Run #	NMR Start Date & Time	Up Absorption Signal Area (V*T)	Up Absorption Error (V*T)	Up Dispersion Signal Area (V*T)	Up Dispersion Error (V*T)
72284094	11/23/20 13:55	2.3329E-10	1.2363E-12	2.5830E-10	1.6484E-12
72284887	11/23/20 14:08	2.3983E-10	1.7916E-12	2.4434E-10	1.5333E-12
72285297	11/23/20 14:14	2.3459E-10	3.3461E-12	2.4745E-10	2.7758E-12
72285817	11/23/20 14:23	2.4315E-10	1.3024E-12	2.4489E-10	8.8957E-13
72286758	11/23/20 14:39	2.4090E-10	1.2914E-12	2.4534E-10	7.1071E-13
72287850	11/23/20 14:57	2.4745E-10	1.1250E-12	2.4454E-10	9.5759E-13
72288449	11/23/20 15:07	2.3177E-10	1.0655E-12	2.5479E-10	1.2657E-12
72289342	11/23/20 15:22	2.4443E-10	1.0754E-12	2.4207E-10	1.5380E-12
72290224	11/23/20 15:37	2.4493E-10	1.2726E-12	2.5388E-10	1.1884E-12
72291836	11/23/20 16:03	2.3835E-10	1.4433E-12	2.4261E-10	1.7534E-12
72292576	11/23/20 16:16	2.4001E-10	1.8766E-12	2.3651E-10	9.1702E-13
72293488	11/23/20 16:31	2.4809E-10	2.8415E-12	2.4314E-10	8.4034E-13
72294229	11/23/20 16:43	2.2992E-10	2.1720E-12	2.4234E-10	1.8042E-12
72300827	11/23/20 18:33	2.4133E-10	1.5145E-12	2.3910E-10	8.9355E-13
72302990	11/23/20 19:09	2.2788E-10	1.3705E-12	2.3751E-10	3.3663E-12
72307682	11/23/20 20:28	2.4443E-10	1.2510E-12	2.2751E-10	1.5401E-12
72310626	11/23/20 21:17	2.3803E-10	1.9567E-12	2.3826E-10	1.8376E-12
72315376	11/23/20 22:36	2.4133E-10	1.5145E-12	2.1931E-10	1.1596E-12
72319018	11/23/20 23:36	2.2858E-10	9.1762E-13	2.3665E-10	1.3302E-12
72320158	11/23/20 23:55	2.2031E-10	1.2502E-12	2.0516E-10	5.0458E-12
72355672	11/24/20 9:47	2.1345E-10	2.0147E-12	2.1176E-10	1.9900E-12
72359305	11/24/20 10:52	2.1504E-10	1.8246E-12	2.0199E-10	1.9952E-12
72363235	11/24/20 11:47	2.0747E-10	9.4662E-13	1.9652E-10	9.6693E-13
72367510	11/24/20 13:09	2.0152E-10	1.7191E-12	1.8468E-10	1.0335E-12
72372320	11/24/20 14:25	1.7916E-10	2.9958E-12	1.8323E-10	2.1047E-12
72376586	11/24/20 15:36	1.7846E-10	1.3679E-12	1.7506E-10	1.5721E-12
72380455	11/24/20 16:41	1.7633E-10	1.5622E-12	1.4330E-10	9.7851E-13
72385067	11/24/20 17:57	1.6480E-10	2.1919E-12	1.6445E-10	9.0007E-13
72389354	11/24/20 19:09	1.5062E-10	1.6118E-12	1.4394E-10	2.2960E-12
72393348	11/24/20 20:15	1.3753E-10	2.5068E-12	1.2990E-10	1.1016E-12
72405214	11/24/20 23:33	1.0549E-10	1.5536E-12	1.1411E-10	2.2927E-12
72405969	11/24/20 23:46	1.0057E-10	1.0881E-12	1.0753E-10	1.0401E-12
72409640	11/25/20 0:47	1.0837E-10	2.1004E-12	1.0244E-10	2.3777E-12
72440652	11/25/20 9:24	8.0756E-11	2.5401E-12	8.1636E-11	3.2803E-12
72447879	11/25/20 11:24	9.1268E-11	2.0146E-12	7.8301E-11	1.9190E-12
72448218	11/25/20 11:30	9.5772E-11	1.9355E-12	7.5630E-11	8.4024E-13
72452315	11/25/20 12:38	7.8399E-11	1.4342E-12	9.4139E-11	1.4694E-12
72452645	11/25/20 12:44	7.6889E-11	1.4781E-12	7.7910E-11	1.6995E-12
72459423	11/25/20 14:37	7.5351E-11	1.1009E-12	7.2534E-11	1.5447E-12
72459783	11/25/20 14:43	8.1127E-11	1.4727E-12	7.0238E-11	9.1983E-13
72462990	11/25/20 15:36	6.6763E-11	1.0631E-12	6.9804E-11	6.4039E-13
72470244	11/25/20 17:37	5.8125E-11	7.3508E-13	5.6122E-11	5.7244E-13
72480881	11/25/20 20:43	2.9917E-11	1.3023E-12	4.6611E-11	1.2997E-12
72490119	11/25/20 23:08	7.4188E-11	1.3070E-12	7.8643E-11	1.3616E-12
72492353	11/25/20 23:45	7.6889E-11	1.4781E-12	7.7910E-11	1.6995E-12
72532055	11/26/20 10:47	7.5351E-11	1.1009E-12	7.2534E-11	1.5447E-12

Table D.4: Summary of the Run 3A NMR signal measurements from the up absorption and dispersion NMR signals, Part 1.

NMR Run #	NMR Start Date & Time	Up Absorption Signal Area (V*T)	Up Absorption Error (V*T)	Up Dispersion Signal Area (V*T)	Up Dispersion Error (V*T)
72532798	11/26/20 10:59	8.1127E-11	1.4727E-12	7.0238E-11	9.1983E-13
72533322	11/26/20 11:08	6.6763E-11	1.0631E-12	6.9804E-11	6.4039E-13
72534046	11/26/20 11:21	5.8125E-11	7.3508E-13	5.6122E-11	5.7244E-13
72543235	11/26/20 13:53	2.9917E-11	1.3023E-12	4.6611E-11	1.2997E-12
72543566	11/26/20 13:59	3.4829E-11	2.3715E-12	4.0766E-11	1.6389E-12
72554619	11/26/20 17:03	5.3314E-11	3.8783E-12	3.6107E-11	1.7692E-12
72565275	11/26/20 20:01	4.6103E-11	2.2633E-12	5.1894E-11	1.9494E-12
72576048	11/26/20 23:00	3.7161E-11	2.0149E-12	5.5065E-11	9.7884E-13
72613644	11/27/20 9:27	4.6103E-11	2.2633E-12	4.4187E-11	1.6374E-12
72620678	11/27/20 11:24	3.2783E-11	2.0947E-12	4.4423E-11	8.1953E-13
72627574	11/27/20 13:19	4.5342E-11	2.1051E-12	4.9941E-11	2.5119E-12
72635191	11/27/20 15:26	3.9386E-11	1.1508E-12	5.5329E-11	1.1242E-12
72643540	11/27/20 17:45	5.3275E-11	3.2004E-12	5.0600E-11	3.5481E-12
72645907	11/27/20 18:25	5.4260E-11	1.7313E-12	4.2050E-11	2.5794E-12
72647000	11/27/20 18:43	4.7401E-11	3.3000E-12	5.4924E-11	1.3267E-12
72653662	11/27/20 20:34	3.9889E-11	3.4923E-12	4.4602E-11	1.2393E-12
72659190	11/27/20 22:06	4.6417E-11	4.8443E-12	2.8873E-11	2.7058E-12
72664515	11/27/20 22:30	4.3893E-11	3.0604E-12	2.9030E-11	1.0689E-12
72665385	11/27/20 23:35	4.0977E-11	1.8794E-12	1.5829E-11	2.8907E-12
72667665	11/28/20 0:28	4.2128E-11	1.2747E-12	3.1477E-11	1.4771E-12
72701538	11/28/20 9:52	4.1314E-11	3.1438E-12	2.4838E-11	9.9411E-13
72703649	11/28/20 10:27	3.3076E-11	3.5499E-12	2.3969E-11	3.0134E-12
72708085	11/28/20 11:36	2.8996E-11	1.0375E-12	3.7700E-11	1.1598E-12
72711715	11/28/20 12:41	2.7472E-11	1.9240E-12	2.4947E-11	1.1830E-12
72714334	11/28/20 13:25	2.7472E-11	1.9240E-12	2.4947E-11	1.1830E-12
72719643	11/28/20 14:54	2.8022E-11	1.7415E-12	1.9918E-11	1.0177E-12
72720040	11/28/20 15:00	2.6048E-11	1.9411E-12	N/A	N/A
72728769	11/28/20 17:26	3.4106E-11	1.1226E-12	4.0017E-11	9.2918E-13
72732314	11/28/20 18:25	2.7301E-11	9.1022E-13	3.1132E-11	9.1696E-13
72737791	11/28/20 19:56	2.2799E-11	5.5265E-13	2.1619E-11	3.3153E-13
72738352	11/28/20 20:06	2.4294E-11	1.0079E-12	1.9560E-11	7.1073E-13
72739995	11/28/20 20:33	1.8427E-11	6.7210E-13	2.0630E-11	4.4622E-13
72743253	11/28/20 21:27	1.6939E-11	5.1360E-13	1.8202E-11	4.7203E-13
72748760	11/28/20 22:59	1.4412E-11	6.7042E-13	N/A	N/A
72787373	11/29/20 9:43	1.3252E-11	3.2023E-13	1.2282E-11	4.2049E-13
72795391	11/29/20 11:56	1.0234E-11	5.3335E-13	1.3055E-11	2.6412E-13
72813854	11/29/20 17:04	1.7190E-11	3.2449E-13	6.5967E-12	4.0582E-13
72835831	11/29/20 23:10	1.0364E-11	3.9075E-13	1.3653E-11	6.0286E-13
72872744	11/30/20 9:25	1.0528E-11	1.9352E-13	1.1003E-11	2.5497E-13
72874633	11/30/20 9:57	8.3631E-12	4.3038E-13	1.0716E-11	5.8615E-13
72886779	11/30/20 13:19	9.4117E-12	2.9851E-13	1.0923E-11	4.6518E-13
72895758	11/30/20 15:49	1.0552E-11	3.2327E-13	9.7443E-12	4.7370E-13
72896181	11/30/20 17:54	9.7054E-12	2.9068E-13	1.0249E-11	4.4466E-13
72923231	11/30/20 23:27	1.7190E-11	3.2449E-13	6.5967E-12	4.0582E-13
72961301	12/1/20 10:01	1.0963E-11	3.2824E-13	1.0396E-11	1.7164E-13

Table D.5: Summary of the Run 3A NMR signal measurements from the down absorption and dispersion NMR signals, Part 2.

NMR Run #	NMR Start Date & Time	Down Absorption Signal Area (V*T)	Down Absorption Error (V*T)	Down Dispersion Signal Area (V*T)	Down Dispersion Error (V*T)
73654255	12/9/20 10:30	3.2688E-10	8.0289E-12	3.1251E-10	5.8753E-12
73661661	12/9/20 12:34	5.3553E-10	8.9903E-12	5.7822E-10	1.6914E-11
73662132	12/9/20 12:42	5.3265E-10	6.1208E-12	5.8690E-10	1.5576E-11
73663318	12/9/20 13:02	5.4783E-10	1.1440E-11	5.5677E-10	1.0699E-11
73664535	12/9/20 13:22	5.4244E-10	9.8158E-12	5.7540E-10	1.0500E-11
73665793	12/9/20 13:45	5.6314E-10	9.0496E-12	5.5363E-10	1.3004E-11
73667103	12/9/20 14:05	5.3768E-10	9.0361E-12	5.7772E-10	1.1457E-11
73668336	12/9/20 14:25	5.2379E-10	1.3332E-11	5.6354E-10	1.6494E-11
73669561	12/9/20 14:46	5.2855E-10	1.1510E-11	5.7901E-10	1.8481E-11
73670680	12/9/20 15:05	5.4630E-10	7.8680E-12	5.5722E-10	1.2523E-11
73671928	12/9/20 15:26	5.3595E-10	1.2184E-11	5.3634E-10	1.3850E-11
73673104	12/9/20 15:46	5.4706E-10	1.3173E-11	5.6673E-10	1.3655E-11
73674333	12/9/20 16:06	5.6269E-10	1.0763E-11	5.2857E-10	1.8367E-11
73675914	12/9/20 16:32	5.4122E-10	1.2135E-11	5.7916E-10	1.0957E-11
73677089	12/9/20 16:52	5.2037E-10	1.3284E-11	5.6396E-10	1.5161E-11
73680106	12/9/20 17:42	5.1289E-10	1.0601E-11	5.4213E-10	1.2213E-11
73681439	12/9/20 18:06	5.2801E-10	1.1383E-11	5.3163E-10	1.1917E-11
73682704	12/9/20 18:25	5.3387E-10	8.9850E-12	5.4518E-10	1.1238E-11
73683910	12/9/20 18:45	5.5682E-10	1.2246E-11	5.2710E-10	1.2415E-11
73685114	12/9/20 19:05	5.1759E-10	7.9122E-12	5.1173E-10	1.2402E-11
73686315	12/9/20 19:25	5.3117E-10	1.0731E-11	5.7935E-10	1.7995E-11
73687511	12/9/20 19:45	5.4044E-10	8.1288E-12	5.3815E-10	1.3472E-11
73688717	12/9/20 20:05	5.3053E-10	9.2364E-12	5.0837E-10	1.2753E-11
73689900	12/9/20 20:25	5.5622E-10	1.2474E-11	5.2981E-10	1.2986E-11
73691142	12/9/20 20:45	5.2651E-10	1.0399E-11	5.5420E-10	1.3885E-11
73692316	12/9/20 21:05	5.3933E-10	8.4130E-12	5.2882E-10	2.0389E-11
73693476	12/9/20 21:25	5.2588E-10	7.9318E-12	5.4609E-10	1.5068E-11
73694678	12/9/20 21:45	5.4783E-10	1.0764E-11	5.5685E-10	1.2383E-11
73695981	12/9/20 22:05	5.1690E-10	7.7088E-12	5.2256E-10	1.1865E-11
73697113	12/9/20 22:25	5.3421E-10	1.1919E-11	5.1263E-10	1.3301E-11
73698287	12/9/20 22:45	5.2470E-10	1.4089E-11	5.0809E-10	1.1003E-11
73699510	12/9/20 23:05	5.0350E-10	1.0236E-11	5.1657E-10	1.3406E-11
73700714	12/9/20 23:25	5.3301E-10	6.7964E-12	5.1050E-10	7.9113E-12
73701994	12/9/20 23:46	5.0862E-10	3.3134E-11	5.2029E-10	9.2519E-12
73702796	12/10/20 0:01	4.8881E-10	1.2039E-11	5.2169E-10	1.2018E-11
73738315	12/10/20 9:51	4.7839E-10	1.2092E-11	5.4430E-10	8.7242E-12
73738798	12/10/20 10:00	5.3514E-10	8.4671E-12	5.1062E-10	9.8142E-12
73739170	12/10/20 10:06	4.8807E-10	1.7106E-11	5.1264E-10	2.2615E-11
73740067	12/10/20 10:21	5.2013E-10	5.2923E-12	5.2266E-10	6.3833E-12
73746141	12/10/20 12:02	5.1618E-10	1.0336E-11	5.1427E-10	9.7787E-12
73748104	12/10/20 12:35	4.9382E-10	7.5501E-12	4.9686E-10	1.0131E-11
73749262	12/10/20 12:55	5.0349E-10	8.8731E-12	5.0370E-10	9.1176E-12
73750513	12/10/20 13:05	4.9992E-10	4.1956E-12	5.2319E-10	7.6024E-12
73751713	12/10/20 13:35	5.0558E-10	6.5827E-12	5.0015E-10	8.6019E-12
73752894	12/10/20 13:55	5.0523E-10	7.6625E-12	5.0304E-10	8.8994E-12
73753597	12/10/20 14:07	4.3762E-10	7.8632E-12	4.8792E-10	8.3882E-12
73754828	12/10/20 14:27	5.0048E-10	6.3367E-12	5.1230E-10	5.7675E-12
73756023	12/10/20 14:47	4.8325E-10	4.8136E-12	4.9493E-10	6.3533E-12
73757231	12/10/20 15:07	4.8128E-10	6.4712E-12	4.9135E-10	6.2408E-12
73758467	12/10/20 15:27	4.8696E-10	5.8106E-12	4.6264E-10	4.7294E-12

Table D.6: Summary of the Run 3B NMR signal measurements from the down absorption and dispersion NMR signals, Part 1.

NMR Run #	NMR Start Date & Time	Down Absorption Signal Area (V*T)	Down Absorption Error (V*T)	Down Dispersion Signal Area (V*T)	Down Dispersion Error (V*T)
73759634	12/10/20 15:47	4.9172E-10	5.1054E-12	4.9157E-10	9.5496E-12
73760856	12/10/20 16:07	4.7451E-10	6.5313E-12	5.0322E-10	8.3531E-12
73762701	12/10/20 16:38	4.3982E-10	5.2239E-12	5.1149E-10	4.4833E-12
73764517	12/10/20 17:08	4.2065E-10	8.6906E-12	4.7934E-10	8.2967E-12
73766296	12/10/20 17:38	4.6705E-10	5.1141E-12	4.6034E-10	1.0777E-11
73768089	12/10/20 18:08	4.5730E-10	5.6885E-12	4.6471E-10	7.4010E-12
73769864	12/10/20 18:38	4.6081E-10	6.7836E-12	4.4188E-10	7.9775E-12
73771702	12/10/20 19:08	4.5035E-10	1.0734E-11	4.2101E-10	1.1469E-11
73773484	12/10/20 19:38	4.6763E-10	7.1034E-12	4.4136E-10	6.6782E-12
73775299	12/10/20 20:08	4.3411E-10	5.6628E-12	4.6783E-10	4.4141E-12
73777084	12/10/20 20:38	3.9291E-10	7.4953E-12	4.3863E-10	9.4288E-12
73778876	12/10/20 21:08	4.2033E-10	4.3482E-12	4.3881E-10	5.8423E-12
73780683	12/10/20 21:38	4.3631E-10	5.1478E-12	4.2746E-10	7.5872E-12
73784111	12/10/20 22:35	4.0150E-10	6.1428E-12	4.3009E-10	7.3927E-12
73824795	12/11/20 9:53	3.9999E-10	5.5760E-12	3.8371E-10	6.5550E-12
73828919	12/11/20 11:01	4.1529E-10	6.1158E-12	3.9317E-10	6.8093E-12
73835429	12/11/20 12:51	3.8510E-10	4.3165E-12	4.0118E-10	6.8493E-12
73839182	12/11/20 13:53	3.8619E-10	6.5815E-12	3.8838E-10	7.9794E-12
73840955	12/11/20 14:22	3.5720E-10	4.7621E-12	4.0207E-10	5.5111E-12
73842810	12/11/20 14:53	3.7848E-10	4.6156E-12	3.8878E-10	6.3016E-12
73844564	12/11/20 15:23	3.8355E-10	6.8539E-12	3.5972E-10	6.2115E-12
73846491	12/11/20 15:53	3.6760E-10	6.2766E-12	4.0880E-10	6.1444E-12
73848274	12/11/20 16:24	3.7353E-10	4.6549E-12	3.6491E-10	5.4748E-12
73850033	12/11/20 16:53	3.8119E-10	8.3236E-12	3.7262E-10	8.9571E-12
73851829	12/11/20 17:27	3.7657E-10	5.0708E-12	3.7902E-10	5.3972E-12
73853763	12/11/20 17:56	3.4723E-10	5.7068E-12	3.9494E-10	8.6698E-12
73855396	12/11/20 18:23	3.5982E-10	1.7839E-11	3.6514E-10	1.9271E-11
73856716	12/11/20 18:45	3.7606E-10	9.4150E-12	3.6735E-10	8.4900E-12
73858507	12/11/20 19:15	3.3901E-10	5.0785E-12	3.2976E-10	5.7030E-12
73860350	12/11/20 19:45	3.5557E-10	9.5439E-12	3.5114E-10	8.7813E-12
73862143	12/11/20 20:15	3.4044E-10	4.4730E-12	3.2730E-10	6.9397E-12
73863949	12/11/20 20:45	3.3805E-10	7.4213E-12	3.4032E-10	4.0897E-12
73865773	12/11/20 21:15	3.2621E-10	7.0464E-12	2.8764E-10	7.1943E-12
73867513	12/11/20 21:45	3.2315E-10	4.3939E-12	3.0333E-10	8.0267E-12
73869332	12/11/20 22:15	3.1416E-10	4.5418E-12	3.3457E-10	5.6078E-12
73871131	12/11/20 22:45	3.0576E-10	6.3823E-12	2.9569E-10	8.4220E-12
73872051	12/11/20 23:00	2.7672E-10	4.3397E-12	2.7766E-10	6.5438E-12
73873771	12/11/20 23:30	2.9036E-10	7.2275E-12	2.8241E-10	8.3211E-12
73910822	12/12/20 9:47	2.7672E-10	4.3397E-12	2.7766E-10	6.5438E-12
73915872	12/12/20 11:11	2.5689E-10	4.9093E-12	2.5879E-10	6.5713E-12
73919418	12/12/20 12:10	2.5125E-10	4.3773E-12	2.8967E-10	4.9716E-12
73921249	12/12/20 12:40	2.5607E-10	5.8390E-12	2.4965E-10	7.8506E-12
73923057	12/12/20 13:10	2.5216E-10	6.0083E-12	2.7653E-10	7.3554E-12
73924806	12/12/20 13:40	2.3713E-10	7.5134E-12	2.6372E-10	7.9199E-12
73926632	12/12/20 14:10	2.3248E-10	4.6403E-12	3.0866E-10	8.1481E-12
73927893	12/12/20 14:32	2.7019E-10	6.1702E-12	2.3950E-10	5.7595E-12
73929762	12/12/20 15:02	2.5821E-10	5.8262E-12	2.5557E-10	9.6451E-12
73931530	12/12/20 15:32	2.4989E-10	4.2475E-12	2.3371E-10	6.8467E-12
73933326	12/12/20 16:02	2.4375E-10	6.9911E-12	2.3532E-10	6.6774E-12
73935076	12/12/20 16:32	2.5891E-10	5.7926E-12	2.2835E-10	8.3080E-12

Table D.7: Summary of the Run 3B NMR signal measurements from the down absorption and dispersion NMR signals, Part 2.

NMR Run #	NMR Start Date & Time	Down Absorption Signal Area (V*T)	Down Absorption Error (V*T)	Down Dispersion Signal Area (V*T)	Down Dispersion Error (V*T)
73935634	12/12/20 16:40	2.3167E-10	8.5454E-12	2.3742E-10	9.5634E-12
73937438	12/12/20 17:10	2.3466E-10	7.3036E-12	2.2927E-10	5.8939E-12
73939224	12/12/20 17:40	2.4054E-10	6.6406E-12	2.4787E-10	5.7497E-12
73941057	12/12/20 18:10	2.2150E-10	6.0251E-12	2.4409E-10	1.0217E-11
73942847	12/12/20 18:40	2.3345E-10	4.1783E-12	2.1390E-10	4.5385E-12
73944636	12/12/20 19:10	2.0988E-10	4.8318E-12	2.1041E-10	6.1794E-12
73945574	12/12/20 19:26	2.2169E-10	7.7058E-12	2.1676E-10	5.2321E-12
73947909	12/12/20 20:05	2.1043E-10	6.7666E-12	1.9857E-10	8.4838E-12
73949720	12/12/20 20:35	2.2339E-10	7.9184E-12	2.1424E-10	5.4023E-12
73951506	12/12/20 21:05	2.2312E-10	5.9165E-12	2.0377E-10	5.8814E-12
73953309	12/12/20 21:35	1.9781E-10	6.5913E-12	1.8309E-10	8.0697E-12
73955107	12/12/20 22:05	1.8891E-10	6.0598E-12	1.9358E-10	9.6040E-12
73956366	12/12/20 22:26	1.8382E-10	6.9512E-12	2.1189E-10	5.8358E-12
73962112	12/13/20 0:02	1.9568E-10	4.2076E-12	1.9355E-10	5.9988E-12
74000949	12/13/20 10:50	1.5726E-10	3.6949E-12	1.6968E-10	4.7670E-12
74023109	12/13/20 16:58	1.7709E-10	3.4788E-12	1.7225E-10	6.4890E-12
74045538	12/13/20 23:12	1.7294E-10	4.0981E-12	1.8079E-10	7.6097E-12
74083745	12/14/20 9:49	1.5877E-10	5.2108E-12	1.5318E-10	4.3044E-12
74090736	12/14/20 11:45	1.6787E-10	4.1607E-12	1.6062E-10	3.8599E-12
74095268	12/14/20 13:01	1.6787E-10	4.4220E-12	1.6062E-10	4.5646E-12
74097659	12/14/20 13:40	1.7172E-10	4.6036E-12	1.6005E-10	3.6928E-12
74099427	12/14/20 14:10	1.4376E-10	1.8398E-12	1.4241E-10	2.8536E-12
74101202	12/14/20 14:40	1.3685E-10	2.9500E-12	1.3010E-10	2.4356E-12
74103012	12/14/20 15:10	1.2344E-10	2.7131E-12	1.2842E-10	3.3171E-12
74104868	12/14/20 15:40	1.2191E-10	3.4591E-12	1.1502E-10	2.3132E-12
74106619	12/14/20 16:10	1.1943E-10	2.9754E-12	1.1551E-10	3.7199E-12
74108421	12/14/20 16:40	1.0751E-10	2.4595E-12	1.6128E-10	3.8053E-12
74110485	12/14/20 17:15	1.1911E-10	6.8784E-12	1.0469E-10	5.6306E-12
74114462	12/14/20 18:21	1.1289E-10	5.2646E-12	1.1918E-10	7.1070E-12
74117543	12/14/20 19:12	1.1352E-10	5.5890E-12	1.1976E-10	6.7809E-12
74120632	12/14/20 20:04	1.0535E-10	4.4423E-12	8.8131E-11	5.4837E-12
74123823	12/14/20 20:58	7.6438E-11	3.1354E-12	1.1034E-10	6.2290E-12
74126858	12/14/20 21:47	1.0697E-10	4.8475E-12	1.0124E-10	7.0102E-12
74129871	12/14/20 22:37	9.3589E-11	3.8013E-12	1.0239E-10	2.5054E-12
74131535	12/14/20 23:05	1.1251E-10	3.8468E-12	9.8811E-11	5.4837E-12
74135083	12/15/20 0:05	9.0890E-11	5.9596E-12	1.0854E-10	4.1765E-12
74176227	12/15/20 11:30	9.4666E-11	3.2964E-12	1.0582E-10	5.4690E-12
74196699	12/15/20 17:11	8.6074E-11	5.4064E-12	8.7806E-11	4.2754E-12
74217669	12/15/20 23:01	8.4352E-11	1.0105E-11	9.4005E-11	7.0109E-12
74263568	12/16/20 11:46	9.5722E-11	3.6816E-12	8.8708E-11	4.2647E-12
74264334	12/16/20 11:59	9.5722E-11	4.5640E-12	8.8708E-11	4.6313E-12
74282406	12/16/20 17:00	1.1070E-10	5.5523E-12	8.1074E-11	1.4261E-11
74287793	12/16/20 18:30	1.0209E-10	6.1393E-12	7.9244E-11	5.2703E-12
74289556	12/16/20 19:00	9.8018E-11	7.9054E-12	9.4858E-11	7.9205E-12
74291510	12/16/20 19:30	9.9481E-11	8.5325E-12	9.4736E-11	6.7352E-12
74293244	12/16/20 20:01	9.5761E-11	5.7874E-12	8.8824E-11	6.5256E-12
74295072	12/16/20 20:30	1.0775E-10	4.2796E-12	8.1096E-11	6.2295E-12
74296844	12/16/20 21:00	9.5761E-11	5.7874E-12	8.8824E-11	6.5256E-12
74298607	12/16/20 21:30	9.3393E-11	7.0638E-12	6.1758E-11	6.9367E-12
74300404	12/16/20 22:00	7.8939E-11	3.8764E-12	6.4777E-11	7.8945E-12

Table D.8: Summary of the Run 3B NMR signal measurements from the down absorption and dispersion NMR signals, Part 3.

NMR Run #	NMR Start Date & Time	Down Absorption Signal Area (V*T)	Down Absorption Error (V*T)	Down Dispersion Signal Area (V*T)	Down Dispersion Error (V*T)
74302198	12/16/20 22:30	8.6718E-11	7.4611E-12	7.5086E-11	1.2367E-11
74307638	12/17/20 0:01	8.9956E-11	4.9849E-12	6.7064E-11	1.2001E-11
74343823	12/17/20 10:03	8.5215E-11	5.9147E-12	7.3447E-11	9.2435E-12
74347821	12/17/20 11:10	8.7388E-11	4.2676E-12	7.3253E-11	7.0327E-12
74349910	12/17/20 11:45	8.6649E-11	1.4321E-11	7.0183E-11	1.3413E-11
74351696	12/17/20 12:15	8.3631E-11	5.7473E-12	5.7292E-11	1.6807E-11
74353510	12/17/20 12:45	7.2647E-11	4.1348E-12	7.1784E-11	8.3387E-12
74355311	12/17/20 13:15	7.3365E-11	3.7710E-12	5.7425E-11	1.1410E-11
74357470	12/17/20 13:50	8.9063E-11	4.9966E-12	6.0137E-11	1.0199E-11
74359219	12/17/20 14:20	8.8737E-11	5.3756E-12	6.5577E-11	1.0163E-11
74361024	12/17/20 14:50	8.6675E-11	7.1188E-12	5.2298E-11	1.2035E-11
74362207	12/17/20 15:10	7.0142E-11	6.5331E-12	5.5317E-11	1.3771E-11
74364013	12/17/20 15:40	8.9190E-11	5.4262E-12	4.3066E-11	5.4845E-12
74365804	12/17/20 16:10	6.6515E-11	1.2501E-11	5.8348E-11	1.1639E-11
74367612	12/17/20 16:40	6.9802E-11	6.5927E-12	5.6708E-11	8.7644E-12
74369414	12/17/20 17:10	6.1940E-11	5.6429E-12	5.5791E-11	1.5283E-11
74371202	12/17/20 17:40	6.9884E-11	8.8431E-12	6.2678E-11	1.2145E-11
74373013	12/17/20 18:10	7.4804E-11	6.9987E-12	3.7937E-11	1.0960E-11
74374803	12/17/20 18:40	6.1049E-11	1.4293E-11	4.9894E-11	1.6552E-11
74376968	12/17/20 19:16	5.9781E-11	3.5169E-12	5.6155E-11	7.8028E-12
74377850	12/17/20 19:30	5.5863E-11	6.5607E-12	6.1077E-11	9.6772E-12
74378596	12/17/20 19:44	5.9746E-11	3.0258E-12	4.7673E-11	3.5756E-12
74387679	12/17/20 22:26	3.3931E-11	9.4100E-12	2.3567E-11	7.9850E-12
74392011	12/17/20 23:27	3.4815E-11	4.2359E-12	2.9069E-11	4.8997E-12
74427842	12/18/20 9:24	3.7602E-11	7.4106E-12	2.6103E-11	6.0627E-12

Table D.9: Summary of the Run 3B NMR signal measurements from the down absorption and dispersion NMR signals, Part 4.

NMR Run #	NMR Start Date & Time	Up Absorption Signal Area (V*T)	Up Absorption Error (V*T)	Up Dispersion Signal Area (V*T)	Up Dispersion Error (V*T)
73654255	12/9/20 10:30	3.1414E-10	4.8894E-12	3.0742E-10	7.2497E-12
73661661	12/9/20 12:34	5.4398E-10	2.5061E-11	5.5163E-10	1.0642E-11
73662132	12/9/20 12:42	5.1646E-10	7.8180E-12	5.3636E-10	9.4061E-12
73663318	12/9/20 13:02	5.5012E-10	8.5854E-12	5.4300E-10	1.9796E-11
73664535	12/9/20 13:22	5.3825E-10	1.0726E-11	5.1481E-10	2.6422E-11
73665793	12/9/20 13:45	5.3661E-10	1.5537E-11	5.0981E-10	2.7748E-11
73667103	12/9/20 14:05	5.1745E-10	1.0000E-11	5.3348E-10	5.1551E-12
73668336	12/9/20 14:25	5.5928E-10	8.5556E-12	5.4775E-10	8.0895E-12
73669561	12/9/20 14:46	5.3445E-10	1.1164E-11	5.5460E-10	1.9230E-11
73670680	12/9/20 15:05	5.4315E-10	9.7076E-12	5.5817E-10	1.4772E-11
73671928	12/9/20 15:26	5.3563E-10	1.0614E-11	5.5129E-10	1.1320E-11
73673104	12/9/20 15:46	5.3475E-10	1.7242E-11	5.3158E-10	1.1130E-11
73674333	12/9/20 16:06	5.3535E-10	2.1610E-11	5.3146E-10	1.4465E-11
73675914	12/9/20 16:32	5.4781E-10	1.3732E-11	5.2845E-10	9.8675E-12
73677089	12/9/20 16:52	5.4303E-10	1.6009E-11	5.2523E-10	1.8264E-11
73680106	12/9/20 17:42	5.3040E-10	9.1180E-12	5.2093E-10	9.6350E-12
73681439	12/9/20 18:06	5.2353E-10	8.8594E-12	5.3238E-10	1.0471E-11
73682704	12/9/20 18:25	5.3345E-10	1.0474E-11	5.1691E-10	9.2196E-12
73683910	12/9/20 18:45	5.3970E-10	1.5748E-11	5.2404E-10	1.6153E-11
73685114	12/9/20 19:05	5.4656E-10	1.1011E-11	5.3396E-10	1.8156E-11
73686315	12/9/20 19:25	5.3334E-10	2.0392E-11	5.2381E-10	1.3611E-11
73687511	12/9/20 19:45	5.6967E-10	1.3134E-11	4.8879E-10	1.3378E-11
73688717	12/9/20 20:05	5.3400E-10	1.4400E-11	5.5194E-10	1.5442E-11
73689900	12/9/20 20:25	5.4063E-10	1.5123E-11	5.4991E-10	1.4913E-11
73691142	12/9/20 20:45	5.1901E-10	7.8006E-12	5.4849E-10	2.0619E-11
73692316	12/9/20 21:05	5.4652E-10	1.0526E-11	5.7144E-10	1.1907E-11
73693476	12/9/20 21:25	5.4150E-10	7.8807E-12	5.4170E-10	7.7936E-12
73694678	12/9/20 21:45	5.3552E-10	6.5390E-12	5.3167E-10	1.2663E-11
73695981	12/9/20 22:05	5.3068E-10	1.0777E-11	5.4700E-10	1.0860E-11
73697113	12/9/20 22:25	5.2617E-10	1.3601E-11	5.2551E-10	9.9586E-12
73698287	12/9/20 22:45	5.2303E-10	1.2478E-11	5.5211E-10	1.0978E-11
73699510	12/9/20 23:05	5.2826E-10	1.0592E-11	5.1681E-10	1.2750E-11
73700714	12/9/20 23:25	5.1813E-10	1.1802E-11	5.0854E-10	1.4140E-11
73701994	12/9/20 23:46	5.0620E-10	7.6648E-12	5.6696E-10	1.0737E-11
73702796	12/10/20 0:01	5.1187E-10	1.1781E-11	5.1904E-10	8.1564E-12
73738315	12/10/20 9:51	5.1303E-10	8.7135E-12	5.1497E-10	1.1187E-11
73738798	12/10/20 10:00	5.1019E-10	7.2793E-12	4.9808E-10	9.0386E-12
73739170	12/10/20 10:06	5.2149E-10	6.7958E-12	5.3655E-10	1.3994E-11
73740067	12/10/20 10:21	5.0532E-10	6.1175E-12	5.0954E-10	4.2900E-12
73746141	12/10/20 12:02	5.1727E-10	7.2675E-12	4.6622E-10	6.1143E-12
73748104	12/10/20 12:35	5.2155E-10	5.9418E-12	4.9828E-10	7.0699E-12
73749262	12/10/20 12:55	4.9868E-10	7.1248E-12	5.0994E-10	9.5953E-12
73750513	12/10/20 13:05	4.9806E-10	7.8252E-12	5.1801E-10	8.0067E-12
73751713	12/10/20 13:35	5.0631E-10	6.8350E-12	4.9131E-10	5.9610E-12
73752894	12/10/20 13:55	4.9041E-10	4.8681E-12	4.8991E-10	5.5290E-12
73753597	12/10/20 14:07	5.1278E-10	8.2396E-12	4.9629E-10	4.6594E-12
73754828	12/10/20 14:27	4.8611E-10	5.1264E-12	4.7065E-10	6.2970E-12
73756023	12/10/20 14:47	5.0747E-10	5.6330E-12	4.9655E-10	4.7641E-12
73757231	12/10/20 15:07	4.9340E-10	7.8692E-12	4.4358E-10	5.3752E-12
73758467	12/10/20 15:27	4.9582E-10	9.2490E-12	5.0121E-10	6.4302E-12

Table D.10: Summary of the Run 3B NMR signal measurements from the up absorption and dispersion NMR signals, Part 1.

NMR Run #	NMR Start Date & Time	Up Absorption Signal Area (V*T)	Up Absorption Error (V*T)	Up Dispersion Signal Area (V*T)	Up Dispersion Error (V*T)
73759634	12/10/20 15:47	4.7781E-10	6.6362E-12	4.9075E-10	8.1308E-12
73760856	12/10/20 16:07	4.5085E-10	9.4516E-12	4.6580E-10	6.8968E-12
73762701	12/10/20 16:38	4.6830E-10	6.2315E-12	4.6360E-10	5.4316E-12
73764517	12/10/20 17:08	4.7774E-10	5.9692E-12	4.5601E-10	7.9669E-12
73766296	12/10/20 17:38	4.7103E-10	8.6465E-12	4.5745E-10	3.6848E-12
73768089	12/10/20 18:08	4.2404E-10	1.0218E-11	4.6581E-10	5.0870E-12
73769864	12/10/20 18:38	4.4635E-10	1.2343E-11	4.1840E-10	5.6734E-12
73771702	12/10/20 19:08	4.6589E-10	7.5365E-12	4.6005E-10	5.2271E-12
73773484	12/10/20 19:38	4.3163E-10	7.7865E-12	4.5216E-10	4.3299E-12
73775299	12/10/20 20:08	4.1244E-10	5.0646E-12	4.0843E-10	4.2138E-12
73777084	12/10/20 20:38	4.3596E-10	5.8477E-12	4.1818E-10	4.1834E-12
73778876	12/10/20 21:08	4.3016E-10	4.9792E-12	4.1167E-10	3.9642E-12
73780683	12/10/20 21:38	3.9155E-10	7.5584E-12	4.1594E-10	7.7989E-12
73784111	12/10/20 22:35	4.1262E-10	8.0399E-12	4.3061E-10	6.5033E-12
73824795	12/11/20 9:53	3.9099E-10	3.0561E-12	4.0758E-10	5.2337E-12
73828919	12/11/20 11:01	4.0365E-10	9.2184E-12	3.7121E-10	4.3104E-12
73835429	12/11/20 12:51	3.8935E-10	5.3787E-12	3.7275E-10	4.9272E-12
73839182	12/11/20 13:53	3.7126E-10	6.0067E-12	4.0024E-10	6.6355E-12
73840955	12/11/20 14:22	3.9247E-10	4.4722E-12	3.7661E-10	4.6387E-12
73842810	12/11/20 14:53	3.9144E-10	8.6439E-12	3.9456E-10	5.2713E-12
73844564	12/11/20 15:23	3.6657E-10	8.8580E-12	3.8405E-10	6.8189E-12
73846491	12/11/20 15:53	3.7800E-10	7.2844E-12	3.9138E-10	5.5653E-12
73848274	12/11/20 16:24	3.8060E-10	6.0895E-12	3.7803E-10	5.6925E-12
73850033	12/11/20 16:53	3.8460E-10	4.1963E-12	3.7848E-10	4.9193E-12
73851829	12/11/20 17:27	3.5361E-10	8.3604E-12	3.6698E-10	6.5830E-12
73853763	12/11/20 17:56	3.8176E-10	7.5154E-12	3.6925E-10	7.1417E-12
73855396	12/11/20 18:23	3.7856E-10	7.4297E-12	3.7356E-10	9.7875E-12
73856716	12/11/20 18:45	3.5032E-10	5.7531E-12	3.5886E-10	7.6785E-12
73858507	12/11/20 19:15	3.3165E-10	9.4290E-12	3.5300E-10	8.1776E-12
73860350	12/11/20 19:45	3.3542E-10	7.2644E-12	3.6738E-10	4.3305E-12
73862143	12/11/20 20:15	3.2621E-10	7.8713E-12	3.3582E-10	5.1963E-12
73863949	12/11/20 20:45	3.1747E-10	1.0146E-11	2.9027E-10	6.0409E-12
73865773	12/11/20 21:15	3.2089E-10	7.9712E-12	3.1060E-10	5.5802E-12
73867513	12/11/20 21:45	3.1896E-10	6.4727E-12	3.1634E-10	7.1195E-12
73869332	12/11/20 22:15	3.2757E-10	9.1487E-12	2.7605E-10	5.5030E-12
73871131	12/11/20 22:45	3.1421E-10	7.3978E-12	3.2632E-10	9.4253E-12
73872051	12/11/20 23:00	2.9423E-10	8.2800E-12	2.8687E-10	5.1359E-12
73873771	12/11/20 23:30	2.8359E-10	9.9449E-12	2.9746E-10	8.0080E-12
73910822	12/12/20 9:47	2.9423E-10	8.2800E-12	2.8687E-10	5.1359E-12
73915872	12/12/20 11:11	2.7893E-10	6.6219E-12	2.5856E-10	5.3355E-12
73919418	12/12/20 12:10	2.7349E-10	5.1161E-12	2.7487E-10	4.4630E-12
73921249	12/12/20 12:40	2.7055E-10	6.5511E-12	2.7086E-10	5.8292E-12
73923057	12/12/20 13:10	2.6595E-10	7.5036E-12	2.4448E-10	4.7526E-12
73924806	12/12/20 13:40	2.4857E-10	6.9970E-12	2.7688E-10	6.9858E-12
73926632	12/12/20 14:10	2.5056E-10	5.2782E-12	2.3920E-10	5.0353E-12
73927893	12/12/20 14:32	2.4473E-10	5.0646E-12	2.5209E-10	5.6871E-12
73929762	12/12/20 15:02	2.2323E-10	8.4606E-12	2.4831E-10	7.9354E-12
73931530	12/12/20 15:32	2.4730E-10	8.9006E-12	2.4958E-10	8.5317E-12
73933326	12/12/20 16:02	2.5355E-10	8.5924E-12	2.4743E-10	6.1078E-12
73935076	12/12/20 16:32	2.4972E-10	8.9530E-12	2.4073E-10	5.6867E-12

Table D.11: Summary of the Run 3B NMR signal measurements from the up absorption and dispersion NMR signals, Part 2.

NMR Run #	NMR Start Date & Time	Up Absorption Signal Area (V*T)	Up Absorption Error (V*T)	Up Dispersion Signal Area (V*T)	Up Dispersion Error (V*T)
73935634	12/12/20 16:40	2.3612E-10	6.1824E-12	2.4542E-10	5.8999E-12
73937438	12/12/20 17:10	2.3959E-10	4.0503E-12	2.3748E-10	5.5845E-12
73939224	12/12/20 17:40	2.0121E-10	9.9835E-12	2.0798E-10	5.5115E-12
73941057	12/12/20 18:10	2.4536E-10	9.1448E-12	1.9745E-10	5.0576E-12
73942847	12/12/20 18:40	2.1612E-10	6.4973E-12	2.2705E-10	7.9057E-12
73944636	12/12/20 19:10	2.1355E-10	4.5238E-12	2.2140E-10	7.6975E-12
73945574	12/12/20 19:26	2.3607E-10	5.8398E-12	2.0896E-10	5.3601E-12
73947909	12/12/20 20:05	2.3728E-10	7.3801E-12	2.0871E-10	7.0462E-12
73949720	12/12/20 20:35	1.8313E-10	7.8896E-12	1.9789E-10	6.6514E-12
73951506	12/12/20 21:05	1.9328E-10	5.9368E-12	2.2165E-10	6.9583E-12
73953309	12/12/20 21:35	1.9657E-10	7.6695E-12	1.9999E-10	6.0579E-12
73955107	12/12/20 22:05	1.6768E-10	9.0911E-12	1.9482E-10	6.0578E-12
73956366	12/12/20 22:26	2.0964E-10	5.9669E-12	1.7467E-10	6.2983E-12
73962112	12/13/20 0:02	1.7865E-10	3.2408E-12	1.8936E-10	4.6014E-12
74000949	12/13/20 10:50	1.8094E-10	4.2992E-12	1.6519E-10	3.4858E-12
74023109	12/13/20 16:58	1.7262E-10	4.2506E-12	1.6585E-10	3.3691E-12
74045538	12/13/20 23:12	1.6844E-10	5.0670E-12	1.5933E-10	3.3531E-12
74083745	12/14/20 9:49	1.5470E-10	6.1352E-12	1.6388E-10	4.0002E-12
74090736	12/14/20 11:45	1.3568E-10	3.7552E-12	1.4757E-10	4.3882E-12
74095268	12/14/20 13:01	1.3568E-10	2.7350E-12	1.4757E-10	3.6126E-12
74097659	12/14/20 13:40	1.3471E-10	3.1170E-12	1.5063E-10	1.8094E-12
74099427	12/14/20 14:10	1.2778E-10	2.2078E-12	1.3639E-10	3.1634E-12
74101202	12/14/20 14:40	1.1675E-10	2.3549E-12	1.2591E-10	4.8283E-12
74103012	12/14/20 15:10	1.0112E-10	1.8214E-12	1.1402E-10	2.2230E-12
74104868	12/14/20 15:40	1.0168E-10	3.1888E-12	1.1137E-10	3.2985E-12
74106619	12/14/20 16:10	1.0091E-10	2.0968E-12	1.0560E-10	2.1299E-12
74108421	12/14/20 16:40	9.1748E-11	2.5142E-12	1.0631E-10	3.0704E-12
74110485	12/14/20 17:15	1.0463E-10	6.1992E-12	1.1266E-10	6.5072E-12
74114462	12/14/20 18:21	1.0390E-10	5.2359E-12	8.8264E-11	4.4430E-12
74117543	12/14/20 19:12	1.0449E-10	5.4522E-12	8.8590E-11	4.3863E-12
74120632	12/14/20 20:04	1.2566E-10	2.9291E-12	1.0591E-10	3.5310E-12
74123823	12/14/20 20:58	9.7327E-11	5.7908E-12	1.0586E-10	4.3079E-12
74126858	12/14/20 21:47	9.6851E-11	6.4069E-12	1.2234E-10	5.2540E-12
74129871	12/14/20 22:37	7.7061E-11	7.5060E-12	9.3388E-11	5.8332E-12
74131535	12/14/20 23:05	9.8787E-11	5.7383E-12	8.8763E-11	5.1301E-12
74135083	12/15/20 0:05	1.0503E-10	4.8027E-12	8.3898E-11	4.4008E-12
74176227	12/15/20 11:30	8.6107E-11	6.9886E-12	9.4851E-11	5.0591E-12
74196699	12/15/20 17:11	7.9471E-11	3.7817E-12	1.0842E-10	4.2980E-12
74217669	12/15/20 23:01	8.1541E-11	5.3883E-12	1.1178E-10	1.3354E-11
74263568	12/16/20 11:46	1.0049E-10	4.5193E-12	8.2801E-11	3.3046E-12
74264334	12/16/20 11:59	1.0049E-10	4.0768E-12	8.2801E-11	6.7663E-12
74282406	12/16/20 17:00	9.4930E-11	8.2124E-12	9.7010E-11	4.9241E-12
74287793	12/16/20 18:30	1.0349E-10	7.2374E-12	9.5394E-11	5.4693E-12
74289556	12/16/20 19:00	1.0813E-10	8.0053E-12	7.9004E-11	6.3768E-12
74291510	12/16/20 19:30	8.5970E-11	1.1653E-11	8.8591E-11	3.5748E-12
74293244	12/16/20 20:01	8.2690E-11	7.1423E-12	6.4402E-11	6.1864E-12
74295072	12/16/20 20:30	8.9372E-11	6.3359E-12	7.2531E-11	6.1570E-12
74296844	12/16/20 21:00	8.2690E-11	7.1423E-12	6.4402E-11	6.1864E-12
74298607	12/16/20 21:30	7.9039E-11	7.9236E-12	8.6977E-11	7.8612E-12
74300404	12/16/20 22:00	8.3930E-11	9.7964E-12	9.5529E-11	4.5747E-12

Table D.12: Summary of the Run 3B NMR signal measurements from the up absorption and dispersion NMR signals, Part 3.

NMR Run #	NMR Start Date & Time	Up Absorption Signal Area (V*T)	Up Absorption Error (V*T)	Up Dispersion Signal Area (V*T)	Up Dispersion Error (V*T)
74302198	12/16/20 22:30	7.8688E-11	1.1818E-11	7.9453E-11	7.1441E-12
74307638	12/17/20 0:01	9.3050E-11	1.2506E-11	8.8000E-11	8.2275E-12
74343823	12/17/20 10:03	8.4776E-11	6.8745E-12	7.0788E-11	4.5363E-12
74347821	12/17/20 11:10	8.1705E-11	5.2578E-12	7.4986E-11	5.3080E-12
74349910	12/17/20 11:45	8.6205E-11	4.2859E-12	7.8796E-11	4.4085E-12
74351696	12/17/20 12:15	8.8490E-11	1.3025E-11	6.3553E-11	5.5882E-12
74353510	12/17/20 12:45	6.9409E-11	9.0159E-12	6.2964E-11	7.7419E-12
74355311	12/17/20 13:15	6.7473E-11	4.7772E-12	7.5825E-11	3.8599E-12
74357470	12/17/20 13:50	6.8886E-11	7.1606E-12	4.9558E-11	8.6184E-12
74359219	12/17/20 14:20	7.0061E-11	1.0391E-11	6.6019E-11	5.1605E-12
74361024	12/17/20 14:50	6.8183E-11	8.0774E-12	6.9285E-11	1.2750E-11
74362207	12/17/20 15:10	7.2592E-11	1.2676E-11	5.6176E-11	6.8314E-12
74364013	12/17/20 15:40	6.6118E-11	6.9104E-12	7.1940E-11	5.3813E-12
74365804	12/17/20 16:10	6.6689E-11	5.7547E-12	5.4348E-11	6.9957E-12
74367612	12/17/20 16:40	6.8960E-11	1.1221E-11	5.6699E-11	8.9233E-12
74369414	12/17/20 17:10	5.7735E-11	9.3127E-12	6.0790E-11	1.1370E-11
74371202	12/17/20 17:40	6.4420E-11	5.8263E-12	4.7247E-11	8.5548E-12
74373013	12/17/20 18:10	6.0989E-11	7.1286E-12	5.8117E-11	4.9197E-12
74374803	12/17/20 18:40	5.8122E-11	9.6864E-12	4.4433E-11	9.5683E-12
74376968	12/17/20 19:16	4.8493E-11	6.0056E-12	6.4228E-11	4.9412E-12
74377850	12/17/20 19:30	6.8440E-11	7.5215E-12	5.0325E-11	1.1770E-11
74378596	12/17/20 19:44	4.7813E-11	2.9688E-12	4.9929E-11	4.3343E-12
74387679	12/17/20 22:26	3.1459E-11	6.8982E-12	2.6127E-11	5.4027E-12
74392011	12/17/20 23:27	3.5870E-11	3.8238E-12	2.8833E-11	4.5238E-12
74427842	12/18/20 9:24	1.5193E-11	4.3492E-12	2.3220E-12	7.6582E-12

Table D.13: Summary of the Run 3B NMR signal measurements from the up absorption and dispersion NMR signals, Part 4.

Appendix E

Polarized eHD Target Polarization Data

The following tables contain the polarization values derived from the raw NMR signal measurements from Runs 3A and 3B. From these values, the individual core and ring section values were derived in Chapter 6.

<u>NMR Run #</u>	<u>NMR Start Date & Time</u>	<u>Down Absorption Polarization (%)</u>	<u>Down Absorption Error (%)</u>	<u>Down Dispersion Polarization (%)</u>	<u>Down Dispersion Error (%)</u>
72284094	11/23/20 13:55	38.37	0.21	38.37	0.20
72284887	11/23/20 14:08	41.84	0.35	39.45	0.29
72285297	11/23/20 14:14	40.85	0.23	38.58	0.55
72285817	11/23/20 14:23	39.26	0.17	39.99	0.21
72286758	11/23/20 14:39	40.66	0.36	39.62	0.21
72287850	11/23/20 14:57	40.39	0.22	40.70	0.19
72288449	11/23/20 15:07	38.18	0.32	38.12	0.18
72289342	11/23/20 15:22	39.13	0.17	40.20	0.18
72290224	11/23/20 15:37	38.94	0.18	40.28	0.21
72291836	11/23/20 16:03	40.39	0.36	39.20	0.24
72292576	11/23/20 16:16	40.90	0.18	39.48	0.31
72293488	11/23/20 16:31	37.92	0.13	40.81	0.47
72294229	11/23/20 16:43	38.15	0.23	37.82	0.36
72300827	11/23/20 18:33	38.82	0.16	39.69	0.25
72302990	11/23/20 19:09	39.56	0.21	37.48	0.23
72307682	11/23/20 20:28	39.31	0.30	40.20	0.21
72310626	11/23/20 21:17	37.42	0.43	39.15	0.32
72315376	11/23/20 22:36	37.48	0.15	39.69	0.25
72319018	11/23/20 23:36	37.28	0.54	37.60	0.15
72320158	11/23/20 23:55	34.75	0.24	36.24	0.21
72355672	11/24/20 9:47	37.69	0.34	35.11	0.33
72359305	11/24/20 10:52	35.45	0.27	35.37	0.30
72363235	11/24/20 11:47	33.54	0.21	34.12	0.16
72367510	11/24/20 13:09	32.52	0.31	33.14	0.28
72372320	11/24/20 14:25	32.28	0.27	29.47	0.49
72376586	11/24/20 15:36	28.62	0.51	29.35	0.22
72380455	11/24/20 16:41	28.85	0.28	28.35	0.27
72385067	11/24/20 17:57	26.73	0.20	27.11	0.36
72389354	11/24/20 19:09	26.70	0.41	24.77	0.27
72393348	11/24/20 20:15	25.08	0.19	22.62	0.41
72405214	11/24/20 23:33	18.35	0.17	17.35	0.26
72405969	11/24/20 23:46	19.76	0.24	16.54	0.18
72409640	11/25/20 0:47	19.28	0.21	17.82	0.35
72440652	11/25/20 9:24	15.13	0.56	13.28	0.42
72447879	11/25/20 11:24	15.44	0.26	15.01	0.33
72448218	11/25/20 11:30	14.54	0.27	15.75	0.32
72452315	11/25/20 12:38	12.23	0.22	12.20	0.21
72452645	11/25/20 12:44	12.23	0.22	12.65	0.24
72459423	11/25/20 14:37	11.93	0.25	12.39	0.18
72459783	11/25/20 14:43	11.77	0.28	13.34	0.24
72462990	11/25/20 15:36	11.37	0.17	10.98	0.17
72470244	11/25/20 17:37	9.86	0.13	9.56	0.12
72480881	11/25/20 20:43	5.52	0.18	4.92	0.21
72490119	11/25/20 23:08	4.27	0.09	2.86	0.20
72492353	11/25/20 23:45	3.60	0.12	4.38	0.32
72532055	11/26/20 10:47	3.23	0.15	3.79	0.19
72532798	11/26/20 10:59	3.67	0.11	3.06	0.17
72533322	11/26/20 11:08	4.11	0.13	3.79	0.19
72534046	11/26/20 11:21	3.72	0.12	2.70	0.17
72543235	11/26/20 13:53	3.54	0.12	3.73	0.17

Table E.1: Summary of Run 3A polarization values from the raw down absorption and dispersion NMR signals, Part 1.

NMR Run #	NMR Start Date & Time	Down Absorption Polarization (%)	Down Absorption Error (%)	Down Dispersion Polarization (%)	Down Dispersion Error (%)
72543566	11/26/20 13:59	3.40	0.24	3.24	0.09
72554619	11/26/20 17:03	4.04	0.14	4.38	0.26
72565275	11/26/20 20:01	3.69	0.11	4.46	0.14
72576048	11/26/20 23:00	3.07	0.21	3.90	0.27
72613644	11/27/20 9:27	4.80	0.12	3.28	0.29
72620678	11/27/20 11:24	3.92	0.24	3.82	0.40
72627574	11/27/20 13:19	2.68	0.26	3.61	0.25
72635191	11/27/20 15:26	1.85	0.18	3.07	0.32
72643540	11/27/20 17:45	2.53	0.14	3.46	0.10
72645907	11/27/20 18:25	2.56	0.12	3.40	0.26
72647000	11/27/20 18:43	2.24	0.07	2.72	0.29
72653662	11/27/20 20:34	2.61	0.16	2.38	0.09
72659190	11/27/20 22:06	2.64	0.11	2.26	0.16
72664515	11/27/20 22:30	2.64	0.11	2.26	0.16
72665385	11/27/20 23:35	1.27	0.09	2.30	0.14
72667665	11/28/20 0:28	2.02	0.16	2.14	0.16
72701538	11/28/20 9:52	2.00	0.15	2.80	0.09
72703649	11/28/20 10:27	1.59	0.07	2.25	0.07
72708085	11/28/20 11:36	1.79	0.04	1.87	0.05
72711715	11/28/20 12:41	2.00	0.04	2.00	0.08
72714334	11/28/20 13:25	1.73	0.04	1.52	0.06
72719643	11/28/20 14:54	1.71	0.06	1.39	0.04
72720040	11/28/20 15:00	1.16	0.06	1.19	0.06
72728769	11/28/20 17:56	1.26	0.05	1.09	0.03
72732314	11/28/20 18:25	1.00	0.06	0.84	0.04
72737791	11/28/20 19:56	0.94	0.04	1.41	0.03
72738352	11/28/20 20:06	0.71	0.08	0.85	0.03
72739995	11/28/20 20:33	0.90	0.02	0.87	0.02
72743253	11/28/20 21:27	1.03	0.02	0.69	0.04
72748760	11/28/20 22:59	0.97	0.02	0.77	0.02
72787373	11/29/20 9:43	1.08	0.03	0.87	0.03
72795391	11/29/20 11:56	0.82	0.04	0.80	0.02
72813854	11/29/20 17:04	1.00	0.07	1.41	0.03
72835831	11/29/20 23:10	0.92	0.03	0.90	0.03
72872744	11/30/20 9:25	0.86	0.03	1.03	0.04
72874633	11/30/20 9:57	0.81	0.02	1.00	0.02
72886779	11/30/20 13:19	0.87	0.02	0.74	0.01
72895758	11/30/20 15:49	0.87	0.02	0.77	0.03
72896181	11/30/20 17:54	0.76	0.03	0.78	0.01
72923231	11/30/20 23:27	1.64	0.09	2.04	0.03
72961301	12/1/20 10:01	1.64	0.09	2.04	0.03

Table E.2: Summary of Run 3A polarization values from the raw down absorption and dispersion NMR signals, Part 2.

NMR Run #	NMR Start Date & Time	Up Absorption Polarization (%)	Up Absorption Error (%)	Up Dispersion Polarization (%)	Up Dispersion Error (%)
72284094	11/23/20 13:55	38.37	0.21	38.37	0.20
72284887	11/23/20 14:08	41.84	0.35	39.45	0.29
72285297	11/23/20 14:14	40.85	0.23	38.58	0.55
72285817	11/23/20 14:23	39.26	0.17	39.99	0.21
72286758	11/23/20 14:39	40.66	0.36	39.62	0.21
72287850	11/23/20 14:57	40.39	0.22	40.70	0.19
72288449	11/23/20 15:07	38.18	0.32	38.12	0.18
72289342	11/23/20 15:22	39.13	0.17	40.20	0.18
72290224	11/23/20 15:37	38.94	0.18	40.28	0.21
72291836	11/23/20 16:03	40.39	0.36	39.20	0.24
72292576	11/23/20 16:16	40.90	0.18	39.48	0.31
72293488	11/23/20 16:31	37.92	0.13	40.81	0.47
72294229	11/23/20 16:43	38.15	0.23	37.82	0.36
72300827	11/23/20 18:33	38.82	0.16	39.69	0.25
72302990	11/23/20 19:09	39.56	0.21	37.48	0.23
72307682	11/23/20 20:28	39.31	0.30	40.20	0.21
72310626	11/23/20 21:17	37.42	0.43	39.15	0.32
72315376	11/23/20 22:36	37.48	0.15	39.69	0.25
72319018	11/23/20 23:36	37.28	0.54	37.60	0.15
72320158	11/23/20 23:55	34.75	0.24	36.24	0.21
72355672	11/24/20 9:47	37.69	0.34	35.11	0.33
72359305	11/24/20 10:52	35.45	0.27	35.37	0.30
72363235	11/24/20 11:47	33.54	0.21	34.12	0.16
72367510	11/24/20 13:09	32.52	0.31	33.14	0.28
72372320	11/24/20 14:25	32.28	0.27	29.47	0.49
72376586	11/24/20 15:36	28.62	0.51	29.35	0.22
72380455	11/24/20 16:41	28.85	0.28	28.35	0.27
72385067	11/24/20 17:57	26.73	0.20	27.11	0.36
72389354	11/24/20 19:09	26.70	0.41	24.77	0.27
72393348	11/24/20 20:15	25.08	0.19	22.62	0.41
72405214	11/24/20 23:33	18.35	0.17	17.35	0.26
72405969	11/24/20 23:46	19.76	0.24	16.54	0.18
72409640	11/25/20 0:47	19.28	0.21	17.82	0.35
72440652	11/25/20 9:24	15.13	0.56	13.28	0.42
72447879	11/25/20 11:24	15.44	0.26	15.01	0.33
72448218	11/25/20 11:30	14.54	0.27	15.75	0.32
72452315	11/25/20 12:38	12.23	0.22	12.20	0.21
72452645	11/25/20 12:44	12.23	0.22	12.65	0.24
72459423	11/25/20 14:37	11.93	0.25	12.39	0.18
72459783	11/25/20 14:43	11.77	0.28	13.34	0.24
72462990	11/25/20 15:36	11.37	0.17	10.98	0.17
72470244	11/25/20 17:37	9.86	0.13	9.56	0.12
72480881	11/25/20 20:43	5.52	0.18	4.92	0.21
72490119	11/25/20 23:08	4.27	0.09	2.86	0.20
72492353	11/25/20 23:45	3.60	0.12	4.38	0.32
72532055	11/26/20 10:47	3.23	0.15	3.79	0.19
72532798	11/26/20 10:59	3.67	0.11	3.06	0.17
72533322	11/26/20 11:08	4.11	0.13	3.79	0.19
72534046	11/26/20 11:21	3.72	0.12	2.70	0.17
72543235	11/26/20 13:53	3.54	0.12	3.73	0.17

Table E.3: Summary of polarization values from the raw up absorption and dispersion NMR signals, Part 1.

<u>NMR Run #</u>	<u>NMR Start Date & Time</u>	<u>Up Absorption Polarization (%)</u>	<u>Up Absorption Error (%)</u>	<u>Up Dispersion Polarization (%)</u>	<u>Up Dispersion Error (%)</u>
72543566	11/26/20 13:59	3.24	0.09	4.11	0.08
72554619	11/26/20 17:03	4.38	0.26	3.76	0.26
72565275	11/26/20 20:01	4.46	0.14	4.02	0.09
72576048	11/26/20 23:00	3.90	0.27	2.93	0.22
72613644	11/27/20 9:27	3.28	0.29	3.31	0.09
72620678	11/27/20 11:24	3.82	0.40	2.14	0.20
72627574	11/27/20 13:19	3.61	0.25	2.16	0.08
72635191	11/27/20 15:26	3.07	0.32	2.99	0.09
72643540	11/27/20 17:45	3.46	0.10	2.34	0.11
72645907	11/27/20 18:25	3.40	0.26	1.84	0.07
72647000	11/27/20 18:43	2.72	0.29	1.78	0.22
72653662	11/27/20 20:34	2.38	0.09	2.80	0.09
72659190	11/27/20 22:06	2.26	0.16	1.85	0.09
72664515	11/27/20 22:30	2.26	0.16	1.85	0.09
72665385	11/27/20 23:35	2.30	0.14	1.48	0.08
72667665	11/28/20 0:28	2.14	0.16	1.50	0.13
72701538	11/28/20 9:52	2.80	0.09	2.97	0.07
72703649	11/28/20 10:27	2.25	0.07	2.31	0.07
72708085	11/28/20 11:36	1.87	0.05	1.61	0.02
72711715	11/28/20 12:41	2.00	0.08	1.45	0.05
72714334	11/28/20 13:25	1.52	0.06	1.53	0.03
72719643	11/28/20 14:54	1.39	0.04	1.35	0.04
72720040	11/28/20 15:00	1.19	0.06	0.76	0.03
72728769	11/28/20 17:56	1.09	0.03	0.91	0.03
72732314	11/28/20 18:25	0.84	0.04	0.97	0.02
72737791	11/28/20 19:56	1.41	0.03	0.49	0.03
72738352	11/28/20 20:06	0.85	0.03	1.01	0.04
72739995	11/28/20 20:33	0.87	0.02	0.82	0.02
72743253	11/28/20 21:27	0.69	0.04	0.80	0.04
72748760	11/28/20 22:59	0.77	0.02	0.81	0.03
72787373	11/29/20 9:43	0.87	0.03	0.72	0.04
72795391	11/29/20 11:56	0.80	0.02	0.76	0.03
72813854	11/29/20 17:04	1.41	0.03	0.49	0.03
72835831	11/29/20 23:10	0.90	0.03	0.77	0.01
72872744	11/30/20 9:25	1.03	0.04	0.81	0.05
72874633	11/30/20 9:57	1.00	0.02	0.83	0.01
72886779	11/30/20 13:19	0.74	0.01	0.90	0.01
72895758	11/30/20 15:49	0.77	0.03	0.89	0.01
72896181	11/30/20 17:54	0.78	0.01	0.75	0.01
72923231	11/30/20 23:27	2.04	0.03	2.22	0.04
72961301	12/1/20 10:01	2.04	0.03	2.22	0.04

Table E.4: Summary of Run 3A polarization values from the raw up absorption and dispersion NMR signals, Part 2.

<u>NMR Run #</u>	<u>NMR Start Date & Time</u>	<u>Down Absorption Polarization (%)</u>	<u>Down Absorption Error (%)</u>	<u>Down Dispersion Polarization (%)</u>	<u>Down Dispersion Error (%)</u>
73654255	12/9/20 10:30	32.11	0.48	34.74	0.35
73661661	12/9/20 12:34	32.08	0.54	34.63	1.01
73662132	12/9/20 12:42	31.90	0.37	35.15	0.93
73663318	12/9/20 13:02	32.81	0.69	33.35	0.64
73664535	12/9/20 13:22	32.49	0.59	34.47	0.63
73665793	12/9/20 13:45	33.73	0.54	33.16	0.78
73667103	12/9/20 14:05	32.21	0.54	34.60	0.69
73668336	12/9/20 14:25	31.37	0.80	33.75	0.99
73669561	12/9/20 14:46	31.66	0.69	34.68	1.11
73670680	12/9/20 15:05	32.72	0.47	33.38	0.75
73671928	12/9/20 15:26	32.10	0.73	32.13	0.83
73673104	12/9/20 15:46	32.77	0.79	33.95	0.82
73674333	12/9/20 16:06	33.70	0.64	31.66	1.10
73675914	12/9/20 16:32	32.42	0.73	34.69	0.66
73677089	12/9/20 16:52	31.17	0.80	33.78	0.91
73680106	12/9/20 17:42	30.72	0.63	32.47	0.73
73681439	12/9/20 18:06	31.63	0.68	31.84	0.71
73682704	12/9/20 18:25	31.98	0.54	32.66	0.67
73683910	12/9/20 18:45	33.35	0.73	31.57	0.74
73685114	12/9/20 19:05	31.00	0.47	30.65	0.74
73686315	12/9/20 19:25	31.82	0.64	34.70	1.08
73687511	12/9/20 19:45	32.37	0.49	32.23	0.81
73688717	12/9/20 20:05	31.78	0.55	30.45	0.76
73689900	12/9/20 20:25	33.32	0.75	31.73	0.78
73691142	12/9/20 20:45	31.54	0.62	33.20	0.83
73692316	12/9/20 21:05	32.30	0.50	31.68	1.22
73693476	12/9/20 21:25	31.50	0.48	32.71	0.90
73694678	12/9/20 21:45	32.81	0.64	33.35	0.74
73695981	12/9/20 22:05	30.96	0.46	31.30	0.71
73697113	12/9/20 22:25	32.00	0.71	30.71	0.80
73698287	12/9/20 22:45	31.43	0.84	30.43	0.66
73699510	12/9/20 23:05	30.16	0.61	30.94	0.80
73700714	12/9/20 23:25	31.93	0.41	30.58	0.47
73701994	12/9/20 23:46	30.47	1.98	31.16	0.55
73702796	12/10/20 0:01	29.28	0.72	31.25	0.72
73738315	12/10/20 9:51	28.65	0.72	32.60	0.52
73738798	12/10/20 10:00	32.05	0.51	30.59	0.59
73739170	12/10/20 10:06	29.23	1.02	30.71	1.35
73740067	12/10/20 10:21	31.15	0.32	31.31	0.38
73746141	12/10/20 12:02	30.92	0.62	30.80	0.59
73748104	12/10/20 12:35	29.58	0.45	29.76	0.61
73749262	12/10/20 12:55	30.16	0.53	30.17	0.55
73750513	12/10/20 13:05	29.94	0.25	31.34	0.46
73751713	12/10/20 13:35	30.28	0.39	29.96	0.52
73752894	12/10/20 13:55	30.26	0.46	30.13	0.53
73753597	12/10/20 14:07	26.21	0.47	29.22	0.50
73754828	12/10/20 14:27	29.98	0.38	30.69	0.35
73756023	12/10/20 14:47	28.95	0.29	29.64	0.38
73757231	12/10/20 15:07	28.83	0.39	29.43	0.37
73758467	12/10/20 15:27	29.17	0.35	27.71	0.28

Table E.5: Summary of Run 3B polarization values from the raw down absorption and dispersion NMR signals, Part 1.

<u>NMR Run #</u>	<u>NMR Start Date & Time</u>	<u>Down Absorption Polarization (%)</u>	<u>Down Absorption Error (%)</u>	<u>Down Dispersion Polarization (%)</u>	<u>Down Dispersion Error (%)</u>
73759634	12/10/20 15:47	29.45	0.31	29.44	0.57
73760856	12/10/20 16:07	28.42	0.39	30.14	0.50
73762701	12/10/20 16:38	26.34	0.31	30.64	0.27
73764517	12/10/20 17:08	25.20	0.52	28.71	0.50
73766296	12/10/20 17:38	27.98	0.31	27.57	0.65
73768089	12/10/20 18:08	27.39	0.34	27.84	0.44
73769864	12/10/20 18:38	27.60	0.41	26.47	0.48
73771702	12/10/20 19:08	26.98	0.64	25.22	0.69
73773484	12/10/20 19:38	28.01	0.43	26.44	0.40
73775299	12/10/20 20:08	26.00	0.34	28.02	0.26
73777084	12/10/20 20:38	23.53	0.45	26.27	0.56
73778876	12/10/20 21:08	25.18	0.26	26.28	0.35
73780683	12/10/20 21:38	26.13	0.31	25.60	0.45
73784111	12/10/20 22:35	24.05	0.37	25.76	0.44
73824795	12/11/20 9:53	23.96	0.33	22.98	0.39
73828919	12/11/20 11:01	24.88	0.37	23.55	0.41
73835429	12/11/20 12:51	23.07	0.26	24.03	0.41
73839182	12/11/20 13:53	23.13	0.39	23.26	0.48
73840955	12/11/20 14:22	21.40	0.29	24.08	0.33
73842810	12/11/20 14:53	22.67	0.28	23.29	0.38
73844564	12/11/20 15:23	22.97	0.41	21.55	0.37
73846491	12/11/20 15:53	22.02	0.38	24.49	0.37
73848274	12/11/20 16:24	22.37	0.28	21.86	0.33
73850033	12/11/20 16:53	22.83	0.50	22.32	0.54
73851829	12/11/20 17:27	22.56	0.30	22.70	0.32
73853763	12/11/20 17:56	20.80	0.34	23.66	0.52
73855396	12/11/20 18:23	21.55	1.07	21.87	1.15
73856716	12/11/20 18:45	22.53	0.56	22.00	0.51
73858507	12/11/20 19:15	20.31	0.30	19.75	0.34
73860350	12/11/20 19:45	21.30	0.57	21.03	0.53
73862143	12/11/20 20:15	20.39	0.27	19.60	0.42
73863949	12/11/20 20:45	20.25	0.44	20.38	0.24
73865773	12/11/20 21:15	19.54	0.42	17.23	0.43
73867513	12/11/20 21:45	19.36	0.26	18.17	0.48
73869332	12/11/20 22:15	18.82	0.27	20.04	0.34
73871131	12/11/20 22:45	18.31	0.38	17.71	0.50
73872051	12/11/20 23:00	16.57	0.26	16.63	0.39
73873771	12/11/20 23:30	17.39	0.43	16.92	0.50
73910822	12/12/20 9:47	16.57	0.26	16.63	0.39
73915872	12/12/20 11:11	15.39	0.29	15.50	0.39
73919418	12/12/20 12:10	15.05	0.26	17.35	0.30
73921249	12/12/20 12:40	15.34	0.35	14.95	0.47
73923057	12/12/20 13:10	15.10	0.36	16.56	0.44
73924806	12/12/20 13:40	14.20	0.45	15.80	0.47
73926632	12/12/20 14:10	13.93	0.28	18.49	0.49
73927893	12/12/20 14:32	16.18	0.37	14.35	0.34
73929762	12/12/20 15:02	15.47	0.35	15.31	0.58
73931530	12/12/20 15:32	14.97	0.25	14.00	0.41
73933326	12/12/20 16:02	14.60	0.42	14.09	0.40
73935076	12/12/20 16:32	15.51	0.35	13.68	0.50

Table E.6: Summary of Run 3B polarization values from the raw down absorption and dispersion NMR signals, Part 2.

<u>NMR Run #</u>	<u>NMR Start Date & Time</u>	<u>Down Absorption Polarization (%)</u>	<u>Down Absorption Error (%)</u>	<u>Down Dispersion Polarization (%)</u>	<u>Down Dispersion Error (%)</u>
73935634	12/12/20 16:40	13.88	0.51	14.22	0.57
73937438	12/12/20 17:10	14.06	0.44	13.73	0.35
73939224	12/12/20 17:40	14.41	0.40	14.85	0.34
73941057	12/12/20 18:10	13.27	0.36	14.62	0.61
73942847	12/12/20 18:40	13.98	0.25	12.81	0.27
73944636	12/12/20 19:10	12.57	0.29	12.60	0.37
73945574	12/12/20 19:26	13.28	0.46	12.98	0.31
73947909	12/12/20 20:05	12.60	0.41	11.89	0.51
73949720	12/12/20 20:35	13.38	0.47	12.83	0.32
73951506	12/12/20 21:05	13.36	0.35	12.21	0.35
73953309	12/12/20 21:35	11.85	0.39	10.97	0.48
73955107	12/12/20 22:05	11.32	0.36	11.60	0.58
73956366	12/12/20 22:26	11.01	0.42	12.69	0.35
73962112	12/13/20 0:02	11.72	0.25	11.59	0.36
74000949	12/13/20 10:50	9.42	0.22	10.16	0.29
74023109	12/13/20 16:58	10.61	0.21	10.32	0.39
74045538	12/13/20 23:12	10.36	0.25	10.83	0.46
74083745	12/14/20 9:49	9.51	0.31	9.17	0.26
74090736	12/14/20 11:45	10.05	0.25	9.62	0.23
74095268	12/14/20 13:01	10.05	0.26	9.62	0.27
74097659	12/14/20 13:40	10.29	0.28	9.59	0.22
74099427	12/14/20 14:10	8.61	0.11	8.53	0.17
74101202	12/14/20 14:40	8.20	0.18	7.79	0.15
74103012	12/14/20 15:10	7.39	0.16	7.69	0.20
74104868	12/14/20 15:40	7.30	0.21	6.89	0.14
74106619	12/14/20 16:10	7.15	0.18	6.92	0.22
74108421	12/14/20 16:40	6.44	0.15	9.66	0.23
74110485	12/14/20 17:15	7.13	0.41	6.27	0.34
74114462	12/14/20 18:21	6.76	0.32	7.14	0.43
74117543	12/14/20 19:12	6.80	0.33	7.17	0.41
74120632	12/14/20 20:04	6.31	0.27	5.28	0.33
74123823	12/14/20 20:58	4.58	0.19	6.61	0.37
74126858	12/14/20 21:47	6.41	0.29	6.06	0.42
74129871	12/14/20 22:37	5.61	0.23	6.13	0.15
74131535	12/14/20 23:05	6.74	0.23	5.92	0.33
74135083	12/15/20 0:05	5.44	0.36	6.50	0.25
74176227	12/15/20 11:30	5.67	0.20	6.34	0.33
74196699	12/15/20 17:11	5.16	0.32	5.26	0.26
74217669	12/15/20 23:01	5.05	0.61	5.63	0.42
74263568	12/16/20 11:46	5.73	0.22	5.31	0.26
74264334	12/16/20 11:59	5.73	0.27	5.31	0.28
74282406	12/16/20 17:00	6.63	0.33	4.86	0.85
74287793	12/16/20 18:30	6.11	0.37	4.75	0.32
74289556	12/16/20 19:00	5.87	0.47	5.68	0.47
74291510	12/16/20 19:30	5.96	0.51	5.67	0.40
74293244	12/16/20 20:01	5.74	0.35	5.32	0.39
74295072	12/16/20 20:30	6.45	0.26	4.86	0.37
74296844	12/16/20 21:00	5.74	0.35	5.32	0.39
74298607	12/16/20 21:30	5.59	0.42	3.70	0.42
74300404	12/16/20 22:00	4.73	0.23	3.88	0.47

Table E.7: Summary of Run 3B polarization values from the raw down absorption and dispersion NMR signals, Part 3.

NMR Run #	NMR Start Date & Time	Down Absorption Polarization (%)	Down Absorption Error (%)	Down Dispersion Polarization (%)	Down Dispersion Error (%)
74302198	12/16/20 22:30	5.19	0.45	4.50	0.74
74307638	12/17/20 0:01	5.39	0.30	4.02	0.72
74343823	12/17/20 10:03	5.10	0.35	4.40	0.55
74347821	12/17/20 11:10	5.23	0.26	4.39	0.42
74349910	12/17/20 11:45	5.19	0.86	4.20	0.80
74351696	12/17/20 12:15	5.01	0.34	3.43	1.01
74353510	12/17/20 12:45	4.35	0.25	4.30	0.50
74355311	12/17/20 13:15	4.39	0.23	3.44	0.68
74357470	12/17/20 13:50	5.33	0.30	3.60	0.61
74359219	12/17/20 14:20	5.32	0.32	3.93	0.61
74361024	12/17/20 14:50	5.19	0.43	3.13	0.72
74362207	12/17/20 15:10	4.20	0.39	3.31	0.82
74364013	12/17/20 15:40	5.34	0.33	2.58	0.33
74365804	12/17/20 16:10	3.98	0.75	3.49	0.70
74367612	12/17/20 16:40	4.18	0.39	3.40	0.52
74369414	12/17/20 17:10	3.71	0.34	3.34	0.92
74371202	12/17/20 17:40	4.19	0.53	3.75	0.73
74373013	12/17/20 18:10	4.48	0.42	2.27	0.66
74374803	12/17/20 18:40	3.66	0.86	2.99	0.99
74376968	12/17/20 19:16	3.58	0.21	3.36	0.47
74377850	12/17/20 19:30	3.35	0.39	3.66	0.58
74378596	12/17/20 19:44	3.58	0.18	2.86	0.21
74387679	12/17/20 22:26	2.03	0.56	1.41	0.48
74392011	12/17/20 23:27	2.09	0.25	1.74	0.29
74427842	12/18/20 9:24	2.25	0.44	1.56	0.36

Table E.8: Summary of Run 3B polarization values from the raw down absorption and dispersion NMR signals, Part 4.

<u>NMR Run #</u>	<u>NMR Start Date & Time</u>	<u>Up Absorption Polarization (%)</u>	<u>Up Absorption Error (%)</u>	<u>Up Dispersion Polarization (%)</u>	<u>Up Dispersion Error (%)</u>
73654255	12/9/20 10:30	32.58	0.29	32.94	0.43
73661661	12/9/20 12:34	32.58	1.50	33.04	0.64
73662132	12/9/20 12:42	30.93	0.47	32.13	0.56
73663318	12/9/20 13:02	32.95	0.51	32.52	1.19
73664535	12/9/20 13:22	32.24	0.64	30.84	1.58
73665793	12/9/20 13:45	32.14	0.93	30.54	1.66
73667103	12/9/20 14:05	30.99	0.60	31.95	0.31
73668336	12/9/20 14:25	33.50	0.51	32.81	0.48
73669561	12/9/20 14:46	32.01	0.67	33.22	1.15
73670680	12/9/20 15:05	32.53	0.58	33.43	0.88
73671928	12/9/20 15:26	32.08	0.64	33.02	0.68
73673104	12/9/20 15:46	32.03	1.03	31.84	0.67
73674333	12/9/20 16:06	32.07	1.29	31.83	0.87
73675914	12/9/20 16:32	32.81	0.82	31.65	0.59
73677089	12/9/20 16:52	32.53	0.96	31.46	1.09
73680106	12/9/20 17:42	31.77	0.55	31.20	0.58
73681439	12/9/20 18:06	31.36	0.53	31.89	0.63
73682704	12/9/20 18:25	31.95	0.63	30.96	0.55
73683910	12/9/20 18:45	32.33	0.94	31.39	0.97
73685114	12/9/20 19:05	32.74	0.66	31.98	1.09
73686315	12/9/20 19:25	31.95	1.22	31.37	0.82
73687511	12/9/20 19:45	34.12	0.79	29.28	0.80
73688717	12/9/20 20:05	31.99	0.86	33.06	0.92
73689900	12/9/20 20:25	32.38	0.91	32.94	0.89
73691142	12/9/20 20:45	31.09	0.47	32.85	1.24
73692316	12/9/20 21:05	32.74	0.63	34.23	0.71
73693476	12/9/20 21:25	32.43	0.47	32.45	0.47
73694678	12/9/20 21:45	32.08	0.39	31.85	0.76
73695981	12/9/20 22:05	31.79	0.65	32.76	0.65
73697113	12/9/20 22:25	31.52	0.81	31.48	0.60
73698287	12/9/20 22:45	31.33	0.75	33.07	0.66
73699510	12/9/20 23:05	31.64	0.63	30.96	0.76
73700714	12/9/20 23:25	31.03	0.71	30.46	0.85
73701994	12/9/20 23:46	30.32	0.46	33.96	0.64
73702796	12/10/20 0:01	30.66	0.71	31.09	0.49
73738315	12/10/20 9:51	30.73	0.52	30.85	0.67
73738798	12/10/20 10:00	30.56	0.44	29.83	0.54
73739170	12/10/20 10:06	31.24	0.41	32.14	0.84
73740067	12/10/20 10:21	30.27	0.37	30.52	0.26
73746141	12/10/20 12:02	30.98	0.44	27.93	0.37
73748104	12/10/20 12:35	31.24	0.36	29.85	0.42
73749262	12/10/20 12:55	29.87	0.43	30.54	0.57
73750513	12/10/20 13:05	29.83	0.47	31.03	0.48
73751713	12/10/20 13:35	30.33	0.41	29.43	0.36
73752894	12/10/20 13:55	29.37	0.29	29.34	0.33
73753597	12/10/20 14:07	30.71	0.49	29.73	0.28
73754828	12/10/20 14:27	29.12	0.31	28.19	0.38
73756023	12/10/20 14:47	30.40	0.34	29.74	0.29
73757231	12/10/20 15:07	29.55	0.47	26.57	0.32
73758467	12/10/20 15:27	29.70	0.55	30.02	0.39

Table E.9: Summary of Run 3B polarization values from the raw up absorption and dispersion NMR signals, Part 1.

NMR Run #	NMR Start Date & Time	Up Absorption Polarization (%)	Up Absorption Error (%)	Up Dispersion Polarization (%)	Up Dispersion Error (%)
73759634	12/10/20 15:47	28.62	0.40	29.40	0.49
73760856	12/10/20 16:07	27.00	0.57	27.90	0.41
73762701	12/10/20 16:38	28.05	0.37	27.77	0.33
73764517	12/10/20 17:08	28.62	0.36	27.31	0.48
73766296	12/10/20 17:38	28.21	0.52	27.40	0.22
73768089	12/10/20 18:08	25.40	0.61	27.90	0.30
73769864	12/10/20 18:38	26.74	0.74	25.06	0.34
73771702	12/10/20 19:08	27.91	0.45	27.56	0.31
73773484	12/10/20 19:38	25.85	0.47	27.08	0.26
73775299	12/10/20 20:08	24.70	0.30	24.46	0.25
73777084	12/10/20 20:38	26.11	0.35	25.05	0.25
73778876	12/10/20 21:08	25.77	0.30	24.66	0.24
73780683	12/10/20 21:38	23.45	0.45	24.91	0.47
73784111	12/10/20 22:35	24.71	0.48	25.79	0.39
73824795	12/11/20 9:53	23.42	0.18	24.41	0.31
73828919	12/11/20 11:01	24.18	0.55	22.23	0.26
73835429	12/11/20 12:51	23.32	0.32	22.33	0.30
73839182	12/11/20 13:53	22.24	0.36	23.97	0.40
73840955	12/11/20 14:22	23.51	0.27	22.56	0.28
73842810	12/11/20 14:53	23.45	0.52	23.63	0.32
73844564	12/11/20 15:23	21.96	0.53	23.00	0.41
73846491	12/11/20 15:53	22.64	0.44	23.44	0.33
73848274	12/11/20 16:24	22.80	0.36	22.64	0.34
73850033	12/11/20 16:53	23.04	0.25	22.67	0.29
73851829	12/11/20 17:27	21.18	0.50	21.98	0.39
73853763	12/11/20 17:56	22.87	0.45	22.12	0.43
73855396	12/11/20 18:23	22.68	0.45	22.38	0.59
73856716	12/11/20 18:45	20.98	0.34	21.49	0.46
73858507	12/11/20 19:15	19.86	0.56	21.14	0.49
73860350	12/11/20 19:45	20.09	0.44	22.01	0.26
73862143	12/11/20 20:15	19.54	0.47	20.11	0.31
73863949	12/11/20 20:45	19.02	0.61	17.39	0.36
73865773	12/11/20 21:15	19.22	0.48	18.60	0.33
73867513	12/11/20 21:45	19.10	0.39	18.95	0.43
73869332	12/11/20 22:15	19.62	0.55	16.53	0.33
73871131	12/11/20 22:45	18.82	0.44	19.55	0.56
73872051	12/11/20 23:00	17.62	0.50	17.18	0.31
73873771	12/11/20 23:30	16.99	0.60	17.82	0.48
73910822	12/12/20 9:47	17.62	0.50	17.18	0.31
73915872	12/12/20 11:11	16.71	0.40	15.49	0.32
73919418	12/12/20 12:10	16.38	0.31	16.46	0.27
73921249	12/12/20 12:40	16.21	0.39	16.22	0.35
73923057	12/12/20 13:10	15.93	0.45	14.64	0.28
73924806	12/12/20 13:40	14.89	0.42	16.58	0.42
73926632	12/12/20 14:10	15.01	0.32	14.33	0.30
73927893	12/12/20 14:32	14.66	0.30	15.10	0.34
73929762	12/12/20 15:02	13.37	0.51	14.87	0.48
73931530	12/12/20 15:32	14.81	0.53	14.95	0.51
73933326	12/12/20 16:02	15.19	0.51	14.82	0.37
73935076	12/12/20 16:32	14.96	0.54	14.42	0.34

Table E.10: Summary of Run 3B polarization values from the raw up absorption and dispersion NMR signals, Part 2.

NMR Run #	NMR Start Date & Time	Up Absorption Polarization (%)	Up Absorption Error (%)	Up Dispersion Polarization (%)	Up Dispersion Error (%)
73935634	12/12/20 16:40	14.14	0.37	14.70	0.35
73937438	12/12/20 17:10	14.35	0.24	14.22	0.33
73939224	12/12/20 17:40	12.05	0.60	12.46	0.33
73941057	12/12/20 18:10	14.70	0.55	11.83	0.30
73942847	12/12/20 18:40	12.95	0.39	13.60	0.47
73944636	12/12/20 19:10	12.79	0.27	13.26	0.46
73945574	12/12/20 19:26	14.14	0.35	12.52	0.32
73947909	12/12/20 20:05	14.21	0.44	12.50	0.42
73949720	12/12/20 20:35	10.97	0.47	11.85	0.40
73951506	12/12/20 21:05	11.58	0.36	13.28	0.42
73953309	12/12/20 21:35	11.77	0.46	11.98	0.36
73955107	12/12/20 22:05	10.04	0.54	11.67	0.36
73956366	12/12/20 22:26	12.56	0.36	10.46	0.38
73962112	12/13/20 0:02	10.70	0.19	11.34	0.28
74000949	12/13/20 10:50	10.84	0.26	9.89	0.21
74023109	12/13/20 16:58	10.34	0.25	9.93	0.20
74045538	12/13/20 23:12	10.09	0.30	9.54	0.20
74083745	12/14/20 9:49	9.27	0.37	9.82	0.24
74090736	12/14/20 11:45	8.13	0.22	8.84	0.26
74095268	12/14/20 13:01	8.13	0.16	8.84	0.22
74097659	12/14/20 13:40	8.07	0.19	9.02	0.11
74099427	12/14/20 14:10	7.65	0.13	8.17	0.19
74101202	12/14/20 14:40	6.99	0.14	7.54	0.29
74103012	12/14/20 15:10	6.06	0.11	6.83	0.13
74104868	12/14/20 15:40	6.09	0.19	6.67	0.20
74106619	12/14/20 16:10	6.04	0.13	6.33	0.13
74108421	12/14/20 16:40	5.50	0.15	6.37	0.18
74110485	12/14/20 17:15	6.27	0.37	6.75	0.39
74114462	12/14/20 18:21	6.22	0.31	5.29	0.27
74117543	12/14/20 19:12	6.26	0.33	5.31	0.26
74120632	12/14/20 20:04	7.53	0.18	6.34	0.21
74123823	12/14/20 20:58	5.83	0.35	6.34	0.26
74126858	12/14/20 21:47	5.80	0.38	7.33	0.31
74129871	12/14/20 22:37	4.62	0.45	5.59	0.35
74131535	12/14/20 23:05	5.92	0.34	5.32	0.31
74135083	12/15/20 0:05	6.29	0.29	5.03	0.26
74176227	12/15/20 11:30	5.16	0.42	5.68	0.30
74196699	12/15/20 17:11	4.76	0.23	6.49	0.26
74217669	12/15/20 23:01	4.88	0.32	6.70	0.80
74263568	12/16/20 11:46	6.02	0.27	4.96	0.20
74264334	12/16/20 11:59	6.02	0.24	4.96	0.41
74282406	12/16/20 17:00	5.69	0.49	5.81	0.29
74287793	12/16/20 18:30	6.20	0.43	5.71	0.33
74289556	12/16/20 19:00	6.48	0.48	4.73	0.38
74291510	12/16/20 19:30	5.15	0.70	5.31	0.21
74293244	12/16/20 20:01	4.95	0.43	3.86	0.37
74295072	12/16/20 20:30	5.35	0.38	4.34	0.37
74296844	12/16/20 21:00	4.95	0.43	3.86	0.37
74298607	12/16/20 21:30	4.73	0.47	5.21	0.47
74300404	12/16/20 22:00	5.03	0.59	5.72	0.27

Table E.11: Summary of 3B polarization values from the raw up absorption and dispersion NMR signals, Part 3.

<u>NMR Run #</u>	<u>NMR Start Date & Time</u>	<u>Up Absorption Polarization (%)</u>	<u>Up Absorption Error (%)</u>	<u>Up Dispersion Polarization (%)</u>	<u>Up Dispersion Error (%)</u>
74302198	12/16/20 22:30	4.71	0.71	4.76	0.43
74307638	12/17/20 0:01	5.57	0.75	5.27	0.49
74343823	12/17/20 10:03	5.08	0.41	4.24	0.27
74347821	12/17/20 11:10	4.89	0.31	4.49	0.32
74349910	12/17/20 11:45	5.16	0.26	4.72	0.26
74351696	12/17/20 12:15	5.30	0.78	3.81	0.33
74353510	12/17/20 12:45	4.16	0.54	3.77	0.46
74355311	12/17/20 13:15	4.04	0.29	4.54	0.23
74357470	12/17/20 13:50	4.13	0.43	2.97	0.52
74359219	12/17/20 14:20	4.20	0.62	3.95	0.31
74361024	12/17/20 14:50	4.08	0.48	4.15	0.76
74362207	12/17/20 15:10	4.35	0.76	3.36	0.41
74364013	12/17/20 15:40	3.96	0.41	4.31	0.32
74365804	12/17/20 16:10	3.99	0.34	3.26	0.42
74367612	12/17/20 16:40	4.13	0.67	3.40	0.53
74369414	12/17/20 17:10	3.46	0.56	3.64	0.68
74371202	12/17/20 17:40	3.86	0.35	2.83	0.51
74373013	12/17/20 18:10	3.65	0.43	3.48	0.29
74374803	12/17/20 18:40	3.48	0.58	2.66	0.57
74376968	12/17/20 19:16	2.90	0.36	3.85	0.30
74377850	12/17/20 19:30	4.10	0.45	3.01	0.70
74378596	12/17/20 19:44	2.86	0.18	2.99	0.26
74387679	12/17/20 22:26	1.88	0.41	1.56	0.32
74392011	12/17/20 23:27	2.15	0.23	1.73	0.27
74427842	12/18/20 9:24	0.91	0.26	0.14	0.46

Table E.12: Summary of 3B polarization values from the raw up absorption and dispersion NMR signals, Part 4.

Appendix F

T1 Fitted Plots

F.1 Run 3A Beam Off T1 Plots

The following plots are for Run 3A beam off conditions:

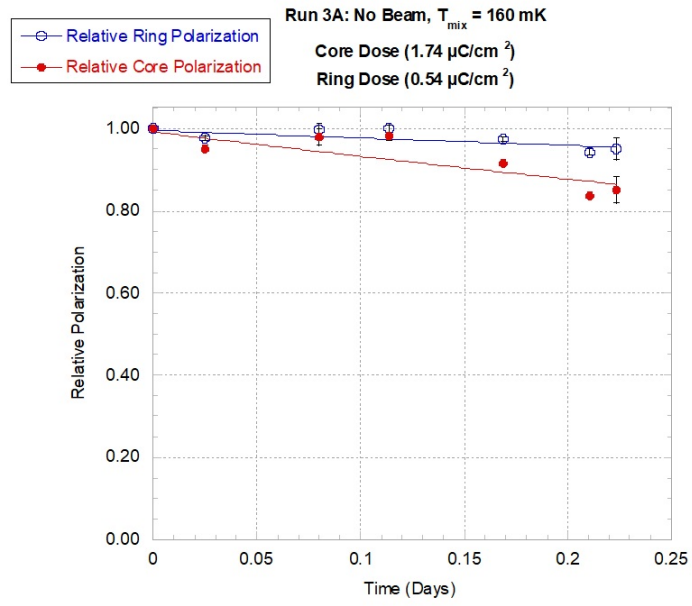


Figure F.1: The T1 extraction of the first no beam run condition at 160 mK. The fitted T1 value for the core section is 9.154 ± 2.644 days and 11.106 ± 2.955 days for the ring section.

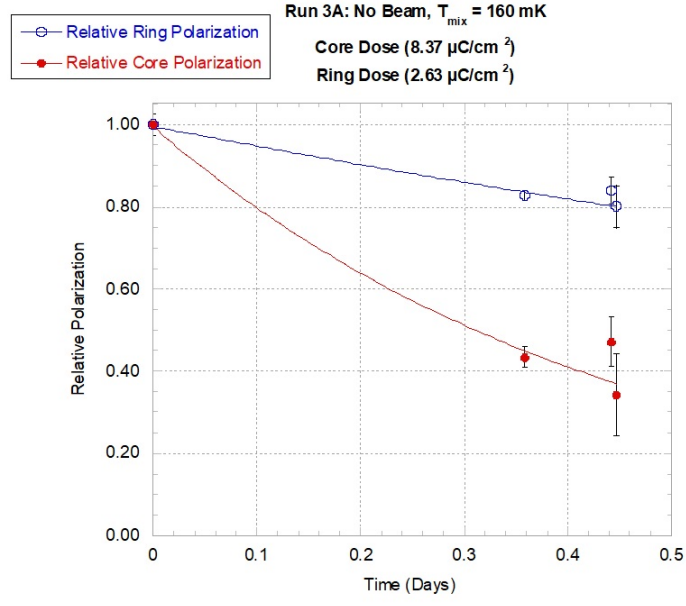


Figure F.2: The T_1 extraction of the second no beam run condition at 160 mK. The fitted T_1 value for the core section is 0.942 ± 0.018 days and 1.608 ± 0.038 days for the ring section.

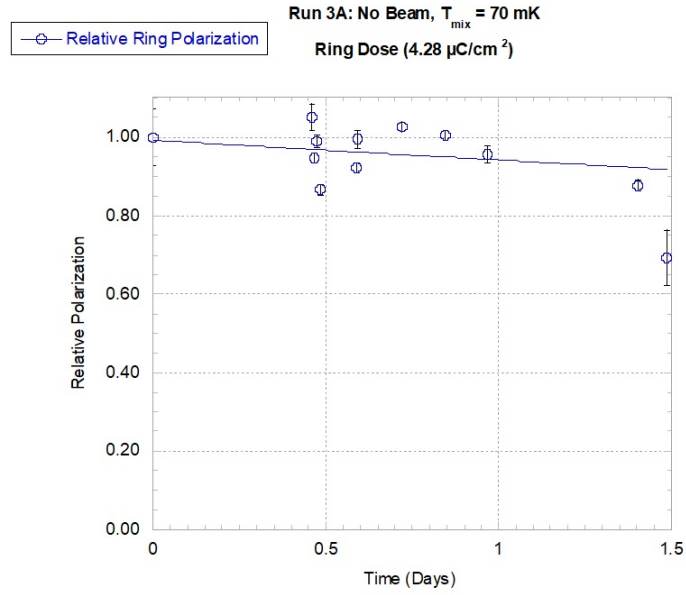


Figure F.3: The T_1 extraction of the third no beam run condition at 70 mK. By this point in the experimental run, the core section polarization was depleted, which leaves just the ring section polarization. The fitted T_1 value is 19.405 ± 1.213 days for the ring section.

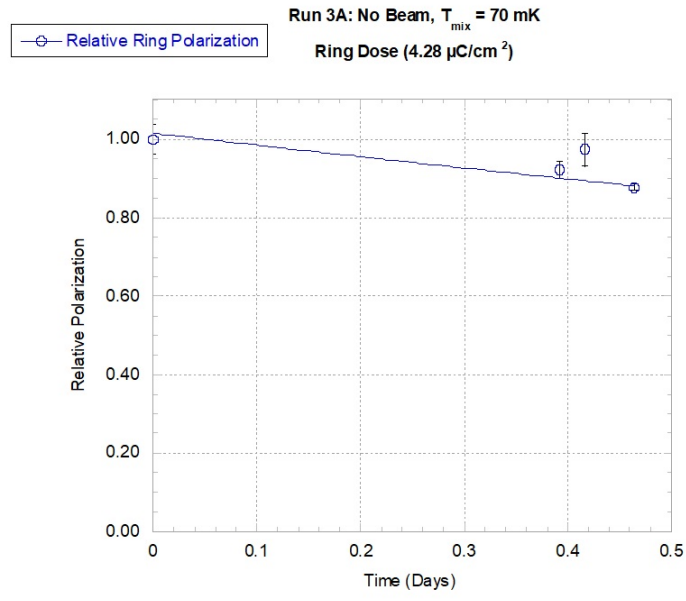


Figure F.4: The T_1 extraction of the fourth no beam run condition at 70 mK. By this point in the experimental run, the core section polarization was depleted, which leaves just the ring section polarization. The fitted T_1 value is 4.267 ± 0.181 days for the ring section.

F.2 Run 3A Beam On T1 Plots

The following plots are for Run 3A beam on conditions:

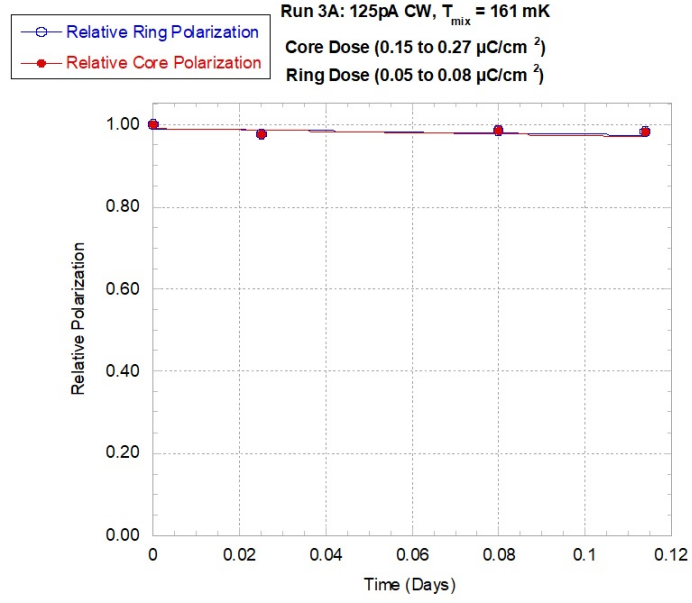


Figure F.5: The T_1 extraction of the first beam-on run condition with 125pA on the target at 160 mK. The fitted T_1 value for the core section is 5.631 ± 2.769 days and 7.113 ± 3.823 days for the ring section.

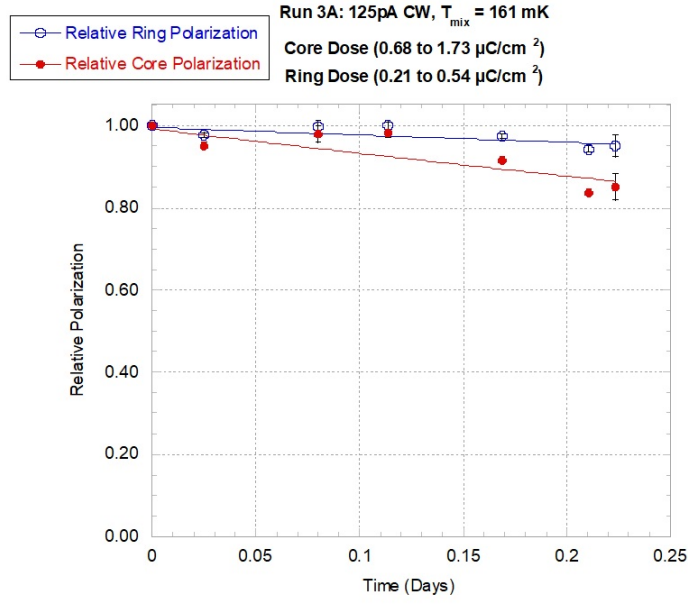


Figure F.6: The T_1 extraction of the second beam-on run condition with 125pA CW on the target at 160 mK. The fitted T_1 value for the core section is 1.479 ± 0.050 days and 1.759 ± 0.070 days for the ring section.

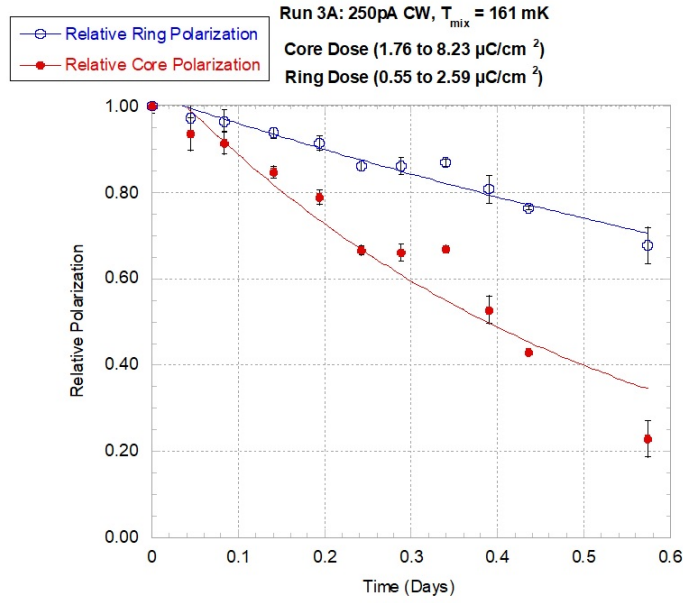


Figure F.7: The T_1 extraction of the first beam-on run condition with 250pA CW on the target at 160 mK. The fitted T_1 value for the core section is 0.501 ± 0.008 days and 1.533 ± 0.063 days for the ring section.

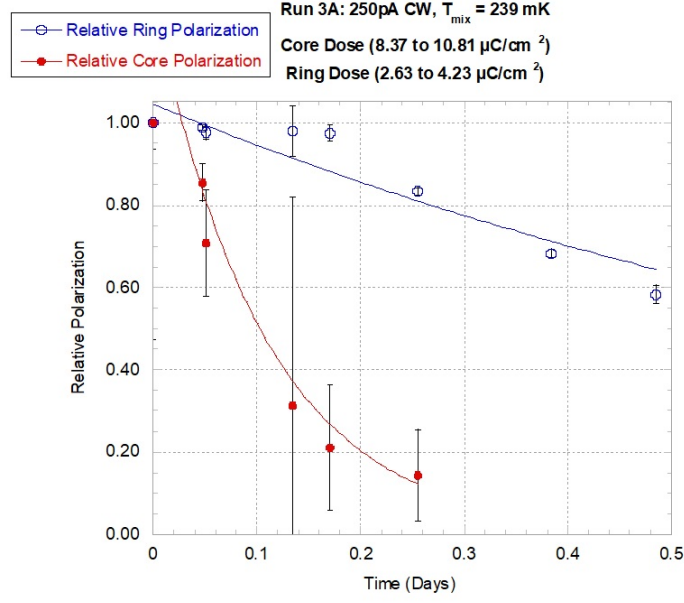


Figure F.8: The T_1 extraction of the second beam-on run condition with 250pA CW on the target at 239 mK. The fitted T_1 value for the core section is 0.235 ± 0.113 days and 1.067 ± 0.060 days for the ring section.

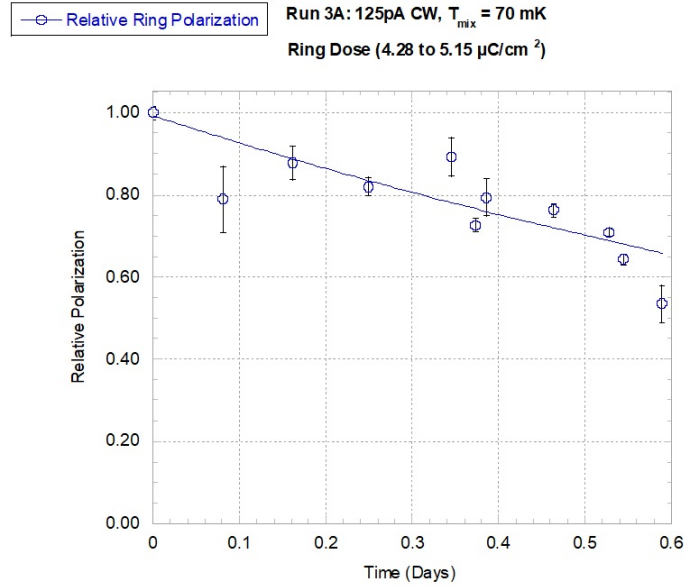


Figure F.9: The T_1 extraction of the third beam-on run condition with 125pA CW on the target at 70 mK. By this point in the experimental run, the core section polarization was depleted, which leaves just the ring section polarization. The fitted T_1 value is 1.759 ± 0.070 days for the ring section.

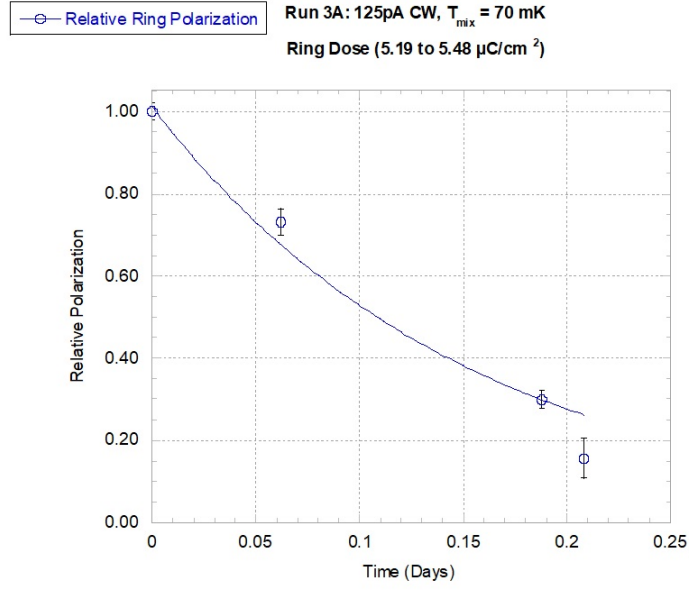


Figure F.10: The T_1 extraction of the fourth beam-on run condition with 125pA CW on the target at 70 mK. This run had an average magnetic holding field of 0.45T, instead of 1.04T like the rest of Run 3A. By this point in the experimental run, the core section polarization was depleted, which leaves just the ring section polarization. The fitted T_1 value is 1.759 ± 0.070 days for the ring section.

F.3 Run 3B Beam Off T1 Plots

The following plots are for Run 3B beam off conditions:

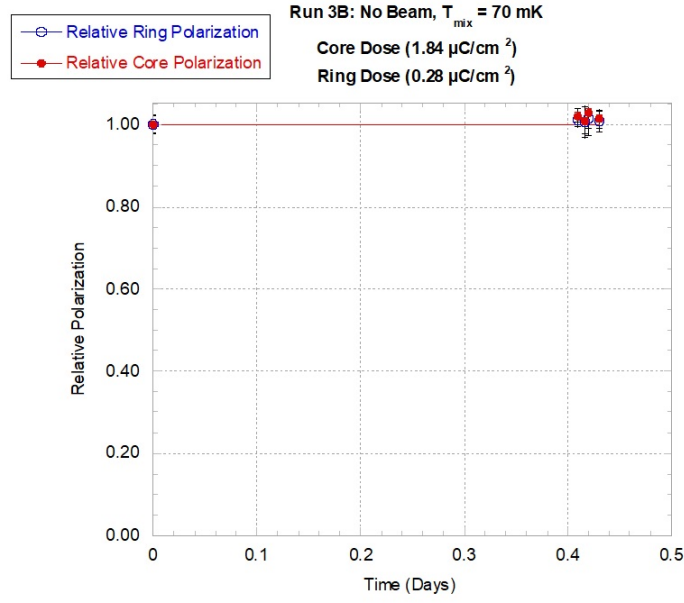


Figure F.11: The T_1 extraction of the first no beam run condition at 70 mK. The fitted T_1 values are not available due to the polarization effectively not changing with such a low accumulated dose. Without any measurable decrease in polarization, the T_1 values are infinite.

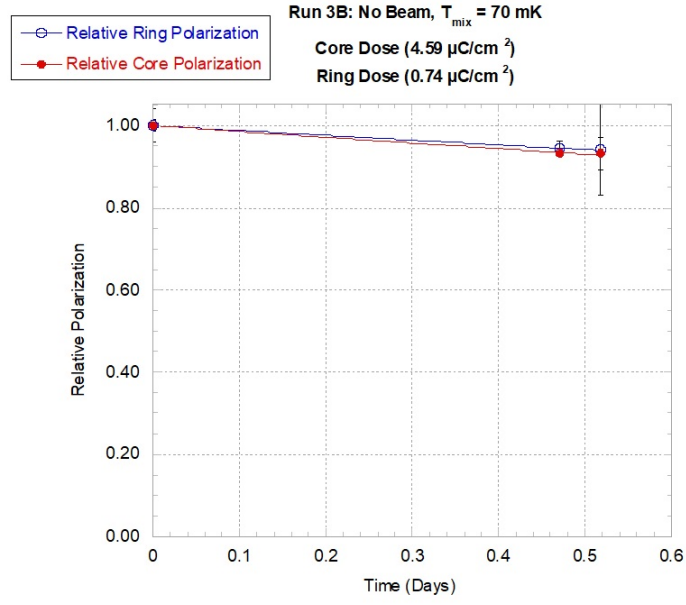


Figure F.12: The T_1 extraction of the second no beam run condition at 70 mK. The fitted T_1 value for the core section is 10.104 ± 4.488 days and 3.281 ± 0.872 days for the ring section.

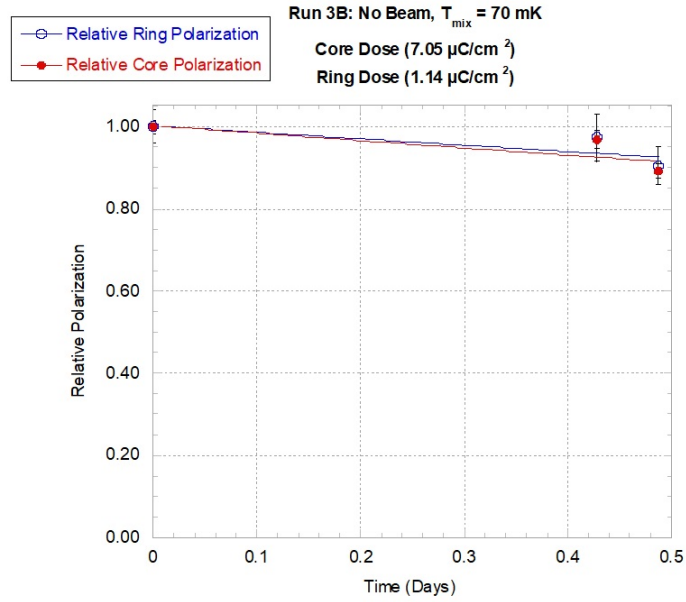


Figure F.13: The T_1 extraction of the third no beam run condition at 70 mK. The fitted T_1 value for the core section is 2.816 ± 0.037 days and 2.666 ± 0.776 days for the ring section.

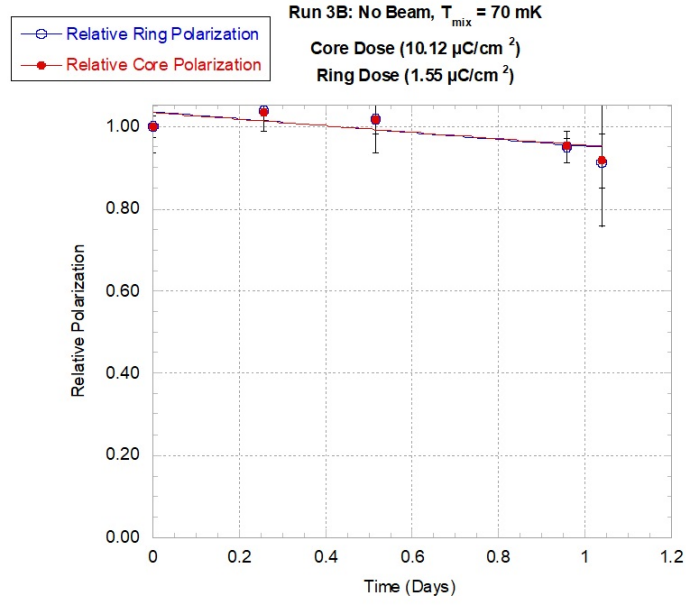


Figure F.14: The T_1 extraction of the fourth no beam run condition at 70 mK. The fitted T_1 value for the core section is 3.260 ± 1.190 days and 11.861 ± 7.47 days for the ring section.

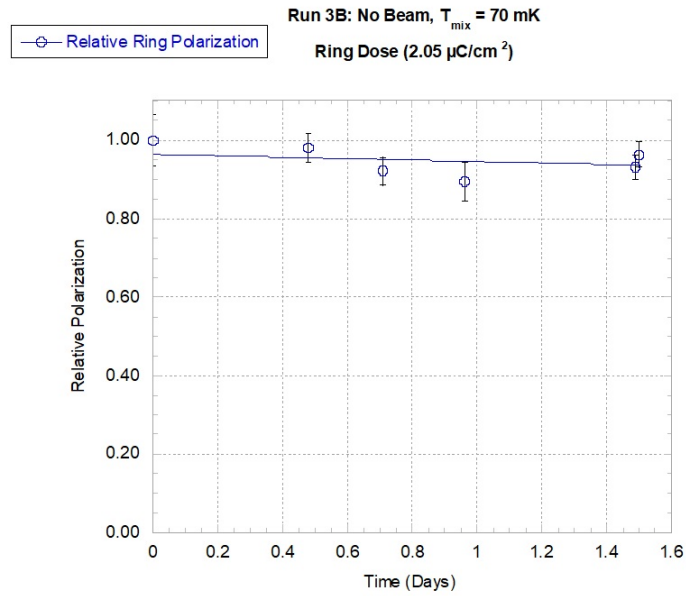


Figure F.15: The T_1 extraction of the fifth no beam run condition at 70 mK. By this point in the experimental run, the core section polarization was depleted, which leaves just the ring section polarization. The fitted T_1 value is 21.110 ± 15.380 days for the ring section.

F.4 Run 3B Beam On T1 Plots

The following plots are for Run 3B beam on conditions:

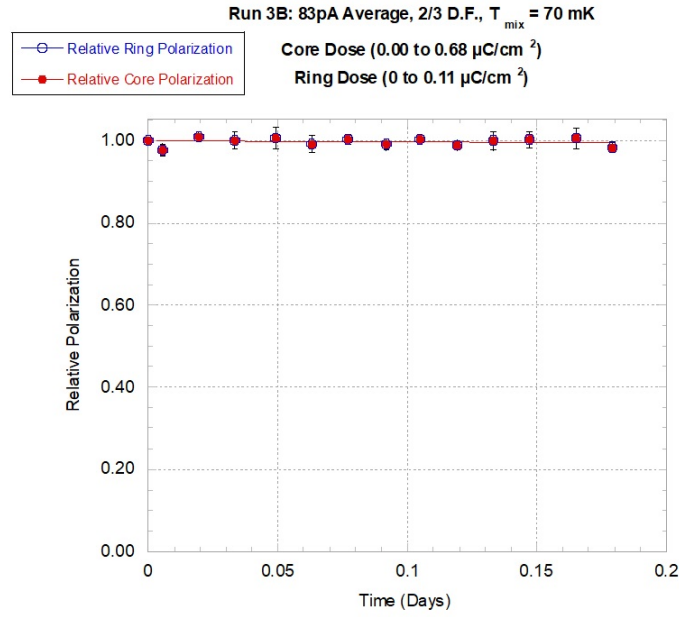


Figure F.16: The T_1 extraction of the first beam-on run condition of 83pA average, 250pA peak current on the target at 70 mK. The fitted T_1 value for the core section is 5.631 ± 2.769 days and 29.888 ± 59.835 days for the ring section.

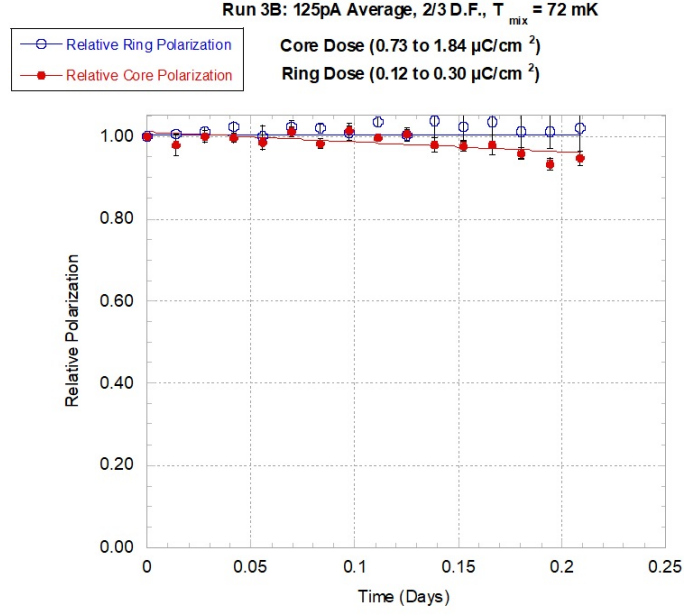


Figure F.17: The T_1 extraction of the second beam-on run condition of 125pA average, 188pA peak current on the target at 72 mK. The fitted T_1 value for the core section is 3.783 ± 0.846 days and 33.763 ± 111.160 days for the ring section.

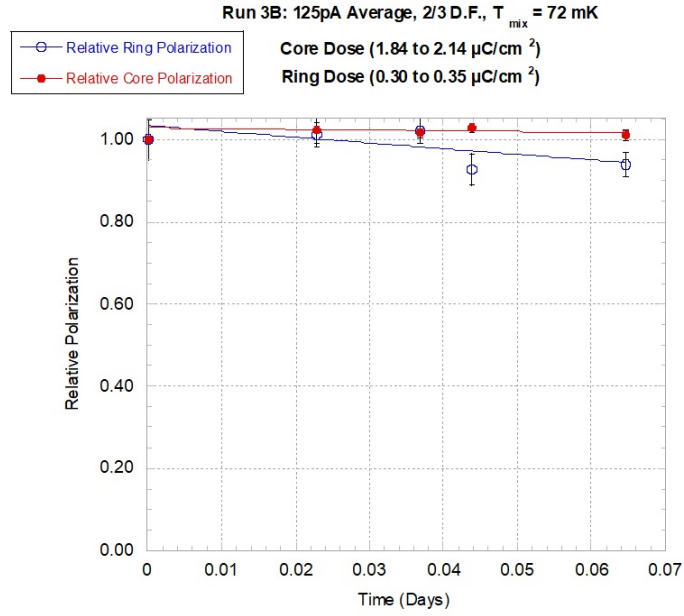


Figure F.18: The T_1 extraction of the third beam-on run condition of 125pA average, 188pA peak current on the target at 72 mK. The fitted T_1 value for the core section is 6.630 ± 18.624 days and 1.533 ± 0.063 days for the ring section.

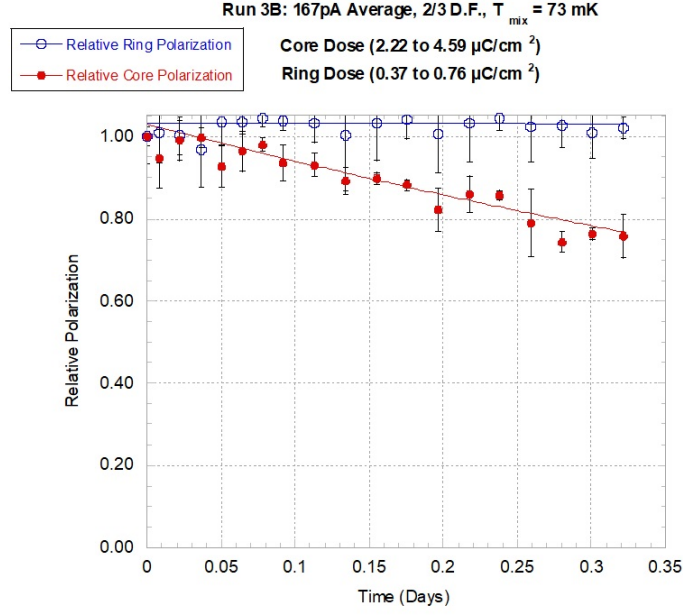


Figure F.19: The T_1 extraction of the fourth beam-on run condition of 167pA average, 250pA peak current on the target at 73 mK. The fitted T_1 value for the core section is 1.401 ± 0.084 days and 1.067 ± 0.06 days for the ring section.

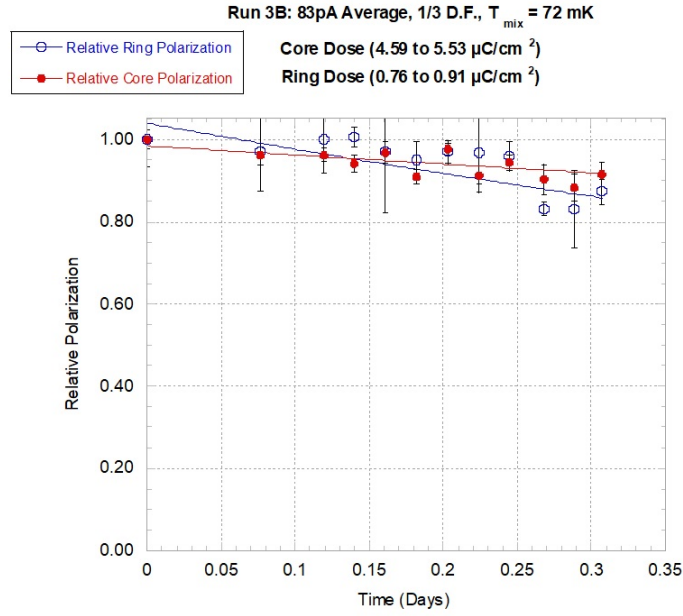


Figure F.20: The T_1 extraction of the fifth beam-on run condition of 83pA average, 250pA peak current on the target at 72 mK. The fitted T_1 value for the core section is 5.170 ± 2.313 days and 0.637 ± 0.082 days for the ring section.

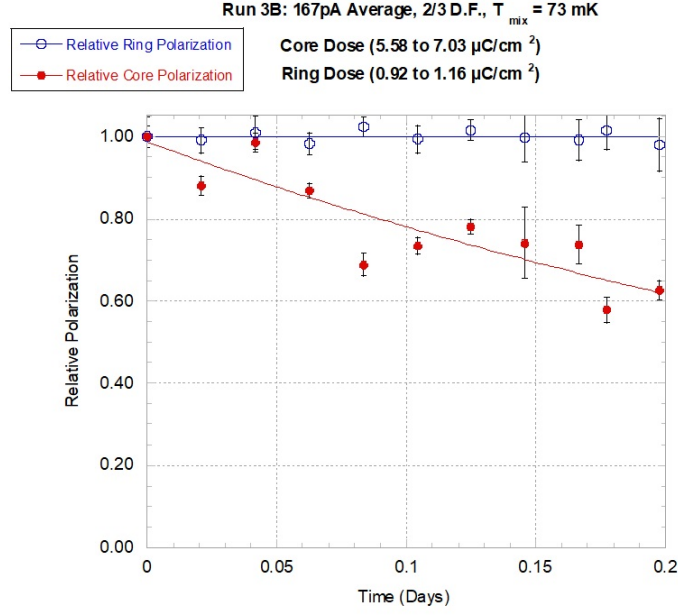


Figure F.21: The T_1 extraction of the sixth beam-on run condition of 167pA average, 250pA peak current on the target at 73 mK. The fitted T_1 value for the core section is 0.512 ± 0.033 days and 7.286 ± 4.605 days for the ring section.

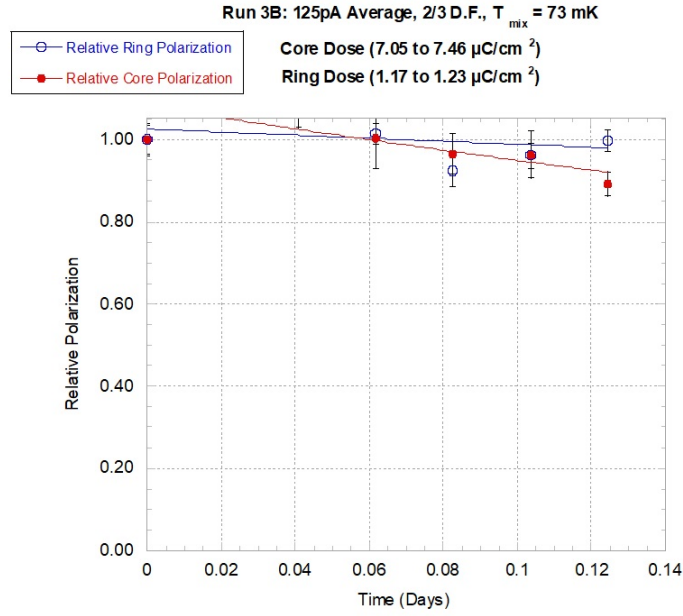


Figure F.22: The T_1 extraction of the seventh beam-on run condition of 125pA CW current on the target at 73 mK. The fitted T_1 value for the core section is 0.913 ± 0.250 days and 3.133 ± 2.980 days for the ring section.

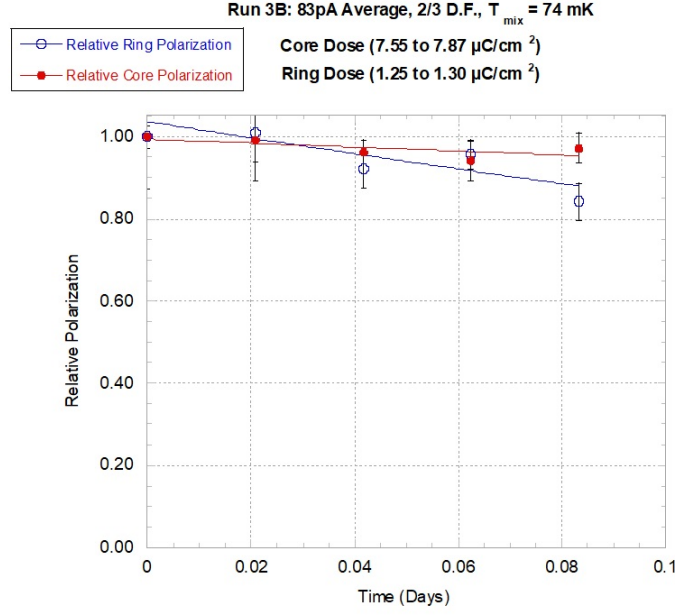


Figure F.23: The T_1 extraction of the eighth beam-on run condition of 83pA average, 125pA peak current on the target at 74 mK. The fitted T_1 value for the core section is 1.931 ± 6.101 days and 1.849 ± 132.400 days for the ring section.

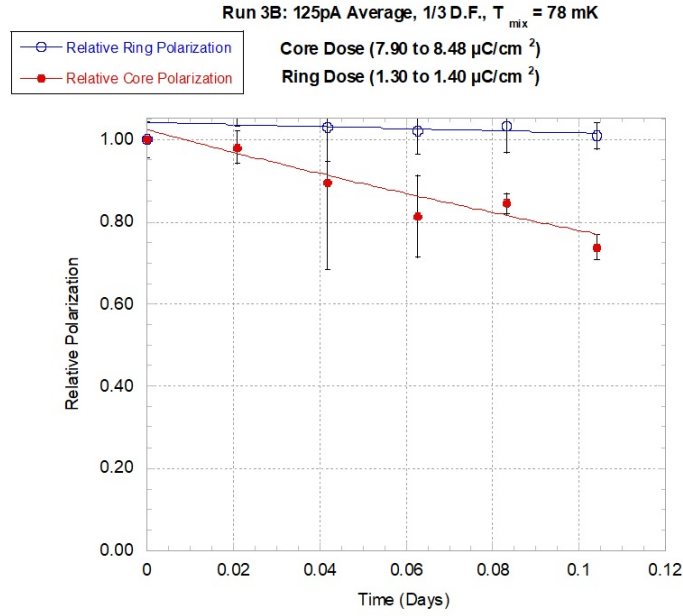


Figure F.24: The T_1 extraction of the eighth beam-on run condition of 125pA average, 375pA peak current on the target at 78 mK. The fitted T_1 value for the core section is 1.931 ± 6.101 days and 0.419 ± 0.0535 days for the ring section.

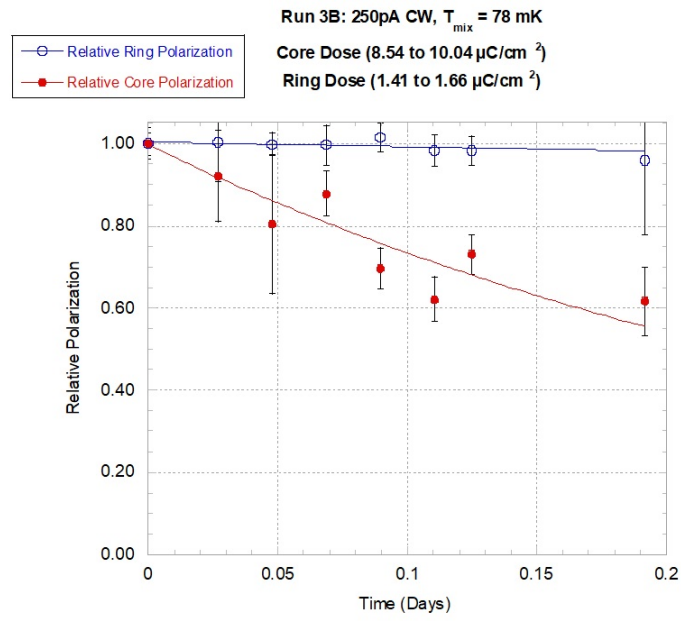


Figure F.25: The T_1 extraction of the ninth beam-on run condition of 250pA CW current on the target at 78 mK. The fitted T_1 value for the core section is 0.443 ± 0.067 days and not available due to no measurable change in polarization during the time period.

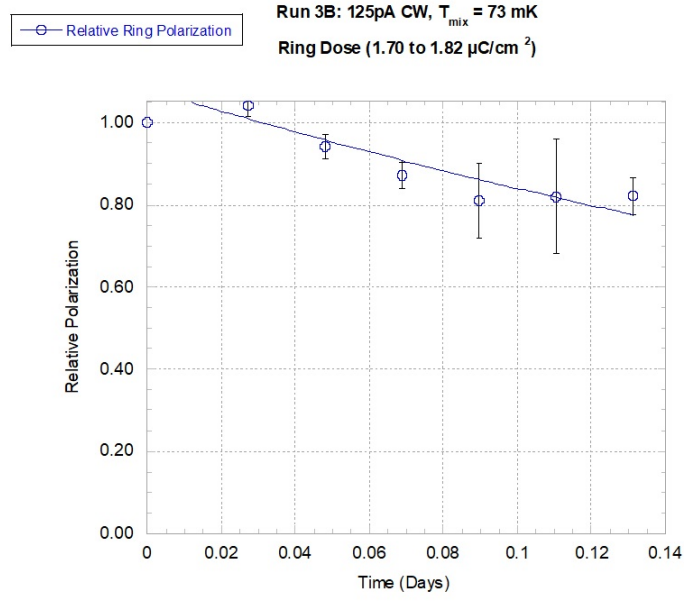


Figure F.26: The T_1 extraction of the ninth beam-on run condition of 125pA CW current on the target at 73 mK. Unlike most run conditions, this condition included setting the holding field to 0.45T. By this point in the experimental run, the core section polarization was depleted, which leaves just the ring section polarization. The fitted T_1 value is 0.535 ± 0.234 days for the ring section.

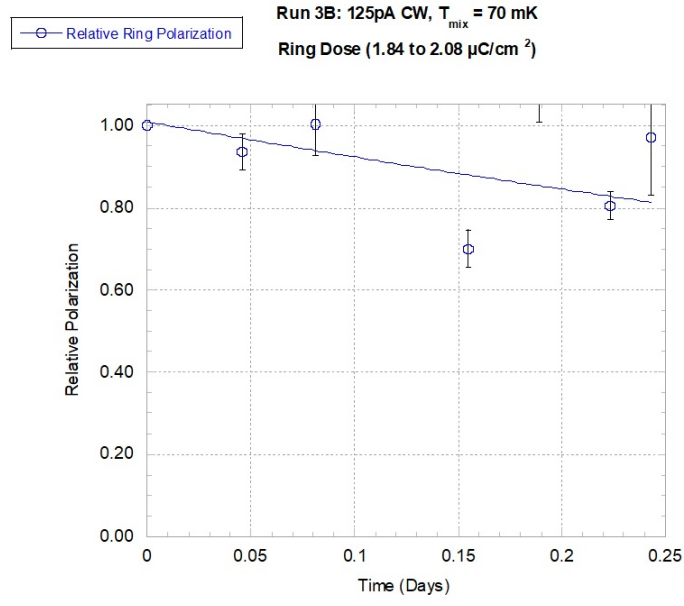


Figure F.27: The T_1 extraction of the ninth beam-on run condition of 125pA CW current on the target at 70 mK. Unlike most run conditions, this condition included setting the average holding field to 1.04T. By this point in the experimental run, the core section polarization was depleted, which leaves just the ring section polarization. The fitted T_1 value is 13.879 ± 46.152 days for the ring section.

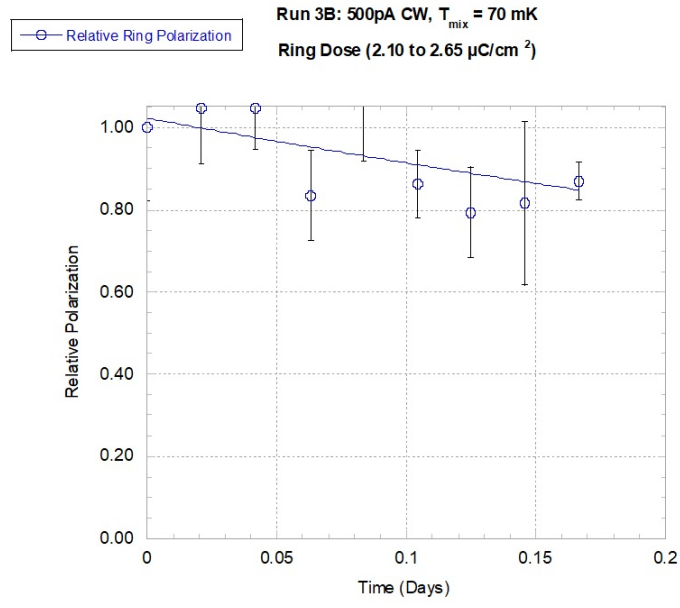


Figure F.28: The T_1 extraction of the ninth beam-on run condition of 500pA CW current on the target at 70 mK. By this point in the experimental run, the core section polarization was depleted, which leaves just the ring section polarization. The fitted T_1 value is 0.592 ± 0.177 days for the ring section.

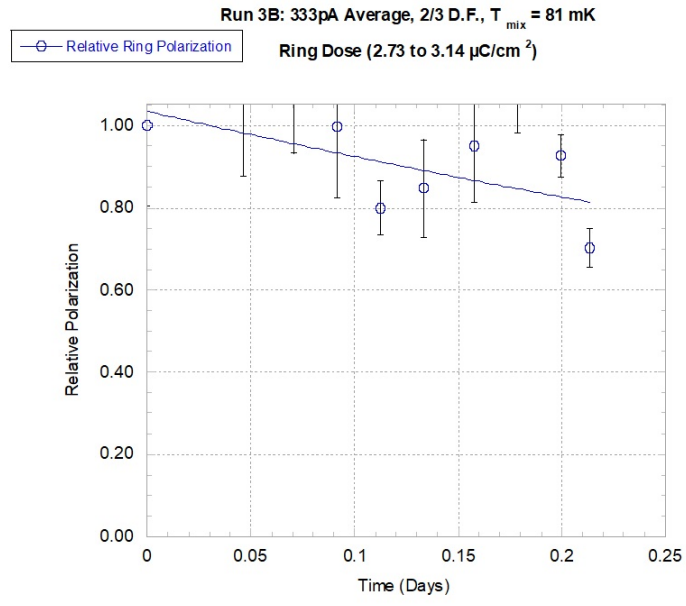


Figure F.29: The T_1 extraction of the ninth beam-on run condition of 333pA average, 500 peak current on the target at 81 mK. By this point in the experimental run, the core section polarization was depleted, which leaves just the ring section polarization. The fitted T_1 value is 0.630 ± 0.136 days for the ring section.

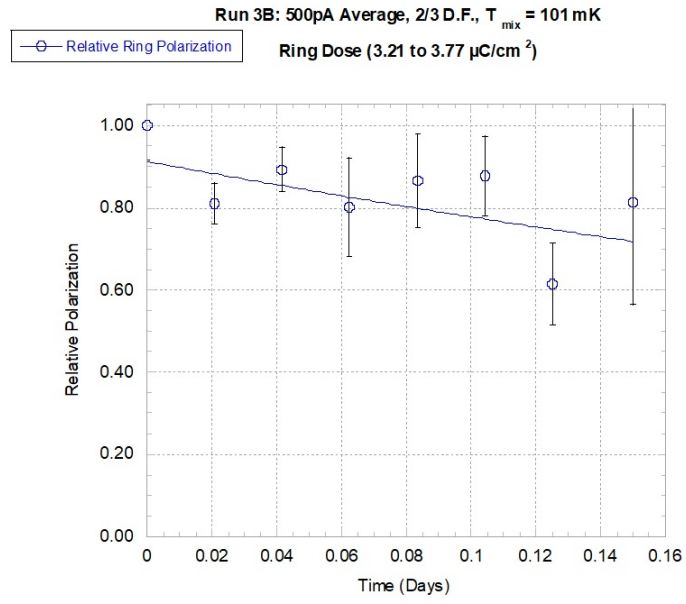


Figure F.30: The T_1 extraction of the ninth beam-on run condition of 500pA average, 750 peak current on the target at 101 mK. By this point in the experimental run, the core section polarization was depleted, which leaves just the ring section polarization. The fitted T_1 value is 0.797 ± 0.426 days for the ring section.

Bibliography

- [1] S Hoblit et al. “Measurements of $H \rightarrow D \rightarrow (\gamma \rightarrow, \pi)$ and Implications for the Convergence of the Gerasimov-Drell-Hern Integral”. In: *Physical review letters* 102.17 (2009), p. 172002.
- [2] Xiangdong Wei et al. “Hdice, highly-polarized low-background frozen-spin hd targets for clas experiments at jefferson lab”. In: *Journal of Physics: Conference Series*. Vol. 400. 5. IOP Publishing. 2012, p. 052042.
- [3] Jefferson Lab. *JLab Aerial - May 2016*. 2016. URL: <https://www.flickr.com/photos/jeffersonlab/32094641754/in/album-72157641132946535/>.
- [4] D Ho et al. “Beam-Target Helicity Asymmetry for $\gamma \rightarrow n \rightarrow \pi^- p$ in the N^* Resonance Region”. In: *Physical review letters* 118.24 (2017), p. 242002.
- [5] Joshua Pierce et al. “Dynamically polarized target for the g2p and gep experiments at jefferson lab”. In: *Nuclear Instruments and Methods in Physics Research Section A: Accelerators, Spectrometers, Detectors and Associated Equipment* 738 (2014), pp. 54–60.
- [6] Al Tobias. *Measurement of the proton and deuteron spin structure functions g1 and g2*. Tech. rep. Stanford Linear Accelerator Center, Menlo Park, CA (US), 2003.
- [7] WC Chen et al. “Polarized ^3He cell development and application at NIST”. In: *Journal of Physics: Conference Series*. Vol. 294. 1. IOP Publishing. 2011, p. 012003.
- [8] M Bassan et al. “Static and dynamic polarization of HD”. In: *Nuclear Instruments and Methods in Physics Research Section A: Accelerators, Spectrometers, Detectors and Associated Equipment* 526.1-2 (2004), pp. 163–167.
- [9] Hideki Kohri et al. “Polarized HD target for future LEPS experiments at SPring-8 in Japan”. In: *International Journal of Modern Physics E* 19.05n06 (2010), pp. 903–914.

- [10] MM Lowry et al. “Electrons on the HDice target: Results and analysis of test runs at JLab in 2012”. In: *Proceedings of the XVth International Workshop on Polarized Sources*. 2013, p. 15.
- [11] A Honig. “Highly spin-polarized proton samples-large, accessible, and simply produced”. In: *Physical Review Letters* 19.18 (1967), p. 1009.
- [12] Mool Chand Gupta. *Statistical thermodynamics*. New Age International, 2007.
- [13] Michael Lowry. *Production Cryostat Operations*. 2016. URL: <https://www.jlab.org/Hall-B/HDice/manuals/production01a.pdf>.
- [14] Christopher D Bass et al. “A portable cryostat for the cold transfer of polarized solid HD targets: HDice-I”. In: *Nuclear Instruments and Methods in Physics Research Section A: Accelerators, Spectrometers, Detectors and Associated Equipment* 737 (2014), pp. 107–116.
- [15] Michael Lowry. *Jülich Transfer Cryostat Operations*. 2020. URL: <https://www.jlab.org/Hall-B/HDice/manuals/transfer05.pdf>.
- [16] Michael Lowry. *Dilution Refrigerator Operations*. 2016. URL: <https://www.jlab.org/Hall-B/HDice/manuals/dilution01a.pdf>.
- [17] Michael Lowry. *Inbeam Cryostat Operations*. 2020. URL: <https://www.jlab.org/Hall-B/HDice/manuals/inbeam04.pdf>.
- [18] Michael M Lowry et al. “A cryostat to hold frozen-spin polarized HD targets in CLAS: HDice-II”. In: *Nuclear Instruments and Methods in Physics Research Section A: Accelerators, Spectrometers, Detectors and Associated Equipment* 815 (2016), pp. 31–41.
- [19] Edward Charles Titchmarsh et al. “Introduction to the theory of Fourier integrals”. In: (1937).
- [20] Steven L Brunton and J Nathan Kutz. *Data-driven science and engineering: Machine learning, dynamical systems, and control*. Cambridge University Press, 2019.
- [21] Vivien Laine. *Polarimetry of the polarized hydrogen deuteride HDice target under an electron beam*. 2013. URL: https://www.jlab.org/Hall-B/general/thesis/Laine_thesis.pdf.
- [22] Howard A Chinn, DK Gannett, and RM Morris. “A new standard volume indicator and reference level”. In: *Proceedings of the IRE* 28.1 (1940), pp. 1–17.

- [23] CD Keith et al. “The Jefferson Lab frozen spin target”. In: *Nuclear Instruments and Methods in Physics Research Section A: Accelerators, Spectrometers, Detectors and Associated Equipment* 684 (2012), pp. 27–35.
- [24] Kevin Wei. *The Response of Polarized Protons in Solid Hydrogen-Deuteride(HD) to Electron Beams*. 2021. URL: <https://collections.ctdigitalarchive.org/islandora/object/20002:860668045>.
- [25] CD Keith. *Frozen Spin Targets for Nuclear and Particle Physics*. 2016. URL: https://misportal.jlab.org/ul/publications/downloadFile.cfm?pub_id=14587.
- [26] Anatole Abragam and Maurice Goldman. “Principles of dynamic nuclear polarisation”. In: *Reports on Progress in Physics* 41.3 (1978), p. 395.
- [27] H Mano and A Honig. “Resistance of solid HD polarized-proton targets to damage from high-energy proton and electron beams”. In: *Nuclear Instruments and Methods* 124.1 (1975), pp. 1–10.
- [28] Philip R Bevington and D Keith Robinson. “Data reduction and error analysis for the physical sciences McGraw-Hill”. In: *New York 19692* (1969), p. 235.
- [29] JR Wolberg. “Applying the method of prediction analysis to the problem of peak separation”. In: *Nuclear Instruments and Methods* 56.2 (1967), pp. 209–212.